Publishing House ASV

begell house, inc. publishers

PAACH

Scientific coordination is carried out by the Russian Academy of Architecture and Construction Sciences (RAACS)

Volume 22 • Issue 3 • 2026

ISSN 2588-0195 (Online)
ISSN 2587-9618 (Print) Continues ISSN 1524-5845

International Journal for

Computational Civil and Structural Engineering

Международный журнал по расчету гражданских и строительных конструкций

https://ijccse.iasv.ru/

DOI: 10.22337/2587-9618
GICID: 71.0000.1500.2830

EXECUTIVE EDITOR

Vladimir I. Travush,
Full Member of RAACS, Professor, Dr.Sc.,
Vice-President of the Russian Academy
of Architecture and Construction Sciences;
Urban Planning Institute
of Residential and Public Buildings;
24, Ulitsa Bolshaya Dmitrovka, 107031, Moscow, Russia

EDITOR-IN-CHIEF

Vladimir N. Sidorov,
Full Member of RAACS, Professor, Dr.Sc., National Research Moscow State University of Civil Engineering; Russian University of Transport (RUT – MIIT); Moscow Institute of Architecture (State Academy); Perm National Research Polytechnic University; 26, Yaroslavskoe Shosse, 129337, Moscow, Russia

EDITORIAL DIRECTOR

Valery I. Telichenko,
Full Member of RAACS, Professor, Dr.Sc.,
The First Vice-President of the Russian Academy
of Architecture and Construction Sciences;
Honorary President of National Research
Moscow State University of Civil Engineering;
24, Ulitsa Bolshaya Dmitrovka, 107031, Moscow, Russia

MANAGING EDITOR

Nadezhda S. Nikitina,
Professor, Ph.D.,
Director of ASV Publishing House;
National Research Moscow State University
of Civil Engineering;
26, Yaroslavskoe Shosse, 129337, Moscow, Russia

ASSOCIATE EDITORS

Pavel A. Akimov,
Full Member of RAACS, Professor, Dr.Sc.,
Acting Rector of National Research
Moscow State University of Civil Engineering;
Vice-President of the Russian Academy
of Architecture and Construction Sciences;
Tomsk State University of Architecture and Building;
Russian University of Friendship of Peoples;
26, Yaroslavskoe Shosse, 129337, Moscow, Russia

Alexander M. Belostotsky,
Full Member of RAACS, Professor, Dr.Sc.,
Research & Development Center "STADYO";
National Research Moscow State University of Civil Engineering; Russian University of Transport (RUT – MIIT); Russian University of Friendship of Peoples;
Perm National Research Polytechnic University;
Tomsk State University of Architecture and Building;
Irkutsk National Research Technical University;
8th Floor, 18, ul. Tretya Yamskogo Polya,
125040, Moscow, Russia

Mikhail Belyi, Professor, Dr.Sc.,
Dassault Systèmes Simulia;
1301 Atwood Ave Suite 101W
02919 Johnston, RI, United States

Vitaly Bulgakov, Professor, Dr.Sc.,
Micro Focus;
Newbury, United Kingdom

Nikolai P. Osmolovskii, Professor, Dr.Sc.,
Systems Research Institute, Polish Academy of Sciences;
Kazimierz Pulaski University
of Technology and Humanities in Radom;
29, ul. Malczewskiego, 26-600, Radom, Poland

Gregory P. Panasenko, Professor, Dr.Sc.,
Equipe d'Analise Numerique; NMR CNRS 5585
University Gean Mehnet;
23 rue. P.Michelon 42023, St.Etienne, France

Scientific coordination is carried out by the Russian Academy of Architecture and Construction Sciences (RAACS)

PUBLISHER

ASV Publishing House
(ООО «Издательство АСВ»)
19/1,12, Yaroslavskoe Shosse, 120338, Moscow, Russia
Tel. +7(925)084-74-24; E-mail: iasv@iasv.ru; Интернет-сайт: http://iasv.ru/

ADVISORY EDITORIAL BOARD

Mojtaba Aslami, Ph.D,
Fasa University; Daneshjou blvd,
Fasa, Fars Province, Iran

Alexander T. Bekker,
Academician of RAACS,
Professor, Dr.Sc.,
Far Eastern Federal University;
Russian Academy of Architecture
and Construction Sciences;
8, Sukhanova Street, Vladivostok,
690950, Russia

Tomas Bock, Professor, Dr.-Ing.,
Technical University of Munich,
Arcisstrasse 21, D-80333
Munich, Germany

Jan Buynak, Professor, Ph.D.,
University of Žilina;
1, Univerzitná, Žilina, 010 26,
Slovakia

Vladimir T. Erofeev,
Full Member of RAACS,
Professor, Dr.Sc.,
Ogarev Mordovia State University;
68, Bolshevistskaya Str., Saransk
430005, Republic of Mordovia,
Russia

Victor S. Fedorov,
Full Member of RAACS,
Professor, Dr.Sc.,
Russian University of Transport
(RUT – MIIT);
9b9 Obrazcova Street, Moscow,
127994, Russia

Sergey V. Fedosov,
Full Member of RAACS,
Professor, Dr.Sc.,
Russian Academy of Architecture
and Construction Sciences;
24, Ul. Bolshaya Dmitrovka, 107031,
Moscow, Russia

Sergiy Yu. Fialko,
Professor, Dr.Sc.,
Cracow University of Technology;
24, Warszawska Street, Kraków,
31-155, Poland

Vladimir G. Gagarin,
Corresponding Member
of RAACS, Professor, Dr.Sc.,
Research Institute of Building
Physics of Russian Academy
of Architecture and Construction
Sciences;
21, Lokomotivny Proezd,
Moscow, 127238, Russia

Vyatcheslav A. Ilyichev,
Full Member of RAACS,
Professor, Dr.Sc.,
Russian Academy of Architecture
and Construction Sciences;
Podzemproekt Ltd.;
24, Ulitsa Bolshaya Dmitrovka,
Moscow, 107031, Russia

Marek Iwański, Professor, Dr.Sc.,
Kielce University of Technology;
7, al. Tysiąclecia Państwa Polskiego
Kielce, 25 – 314, Poland

Sergey Yu. Kalashnikov,
Corresponding Member of RAACS,
Professor, Dr.Sc.,
Volgograd State Technical
University; 28, Lenin avenue,
Volgograd, 400005, Russia

Semen S. Kaprielov,
Academician of RAACS,
Professor, Dr.Sc.,
Research Center of Construction;
6, 2nd Institutskaya St., Moscow,
109428, Russia

Vladimir V. Karpov,
Professor, Dr.Sc., Saint Petersburg
State University of Architecture and
Civil Engineering;
4, 2-nd Krasnoarmeiskaya Steet,
Saint Petersburg, 190005, Russia

Galina G. Kashevarova,
Corresponding Member
of RAACS, Professor, Dr.Sc.,
Perm National Research
Polytechnic University;
29 Komsomolsky pros., Perm,
Perm Krai, 614990, Russia

John T. Katsikadelis,
Professor, Dr.Eng, PhD, Dr.h.c.,
National Technical University of
Athens; Zografou Campus
9, Iroon Polytechniou str
15780 Zografou, Greece

Vitaly I. Kolchunov,
Full Member of RAACS,
Professor, Dr.Sc., Southwest State
University; Russian Academy of
Architecture and Construction
Sciences; 94, 50 let Oktyabrya,
Kursk, 305040, Russia

Dmitry V. Kozlov,
Full Member of RAACS
Dr. Sc. Engineering, Professor, Head
of the Department of Hydraulics and
Hydrotechnical Construction, NRU
MGSU, 26, Yaroslavskoe Shosse.,
129337, Moscow, Russia

Markus König, Professor
Ruhr-Universität Bochum;
150, Universitätsstraße, Bochum,
44801, Germany

Sergey B. Kositsin,
Advisor of RAACS,
Professor, Dr.Sc.,
Russian University of Transport
(RUT – MIIT); 9b9 Obrazcova
Street, Moscow, 127994, Russia

Sergey B. Krylov,
Full Member of RAACS,
Professor, Dr.Sc.,
Research Center of Construction;
6, 2nd Institutskaya St., Moscow,
109428, Russia

Sergey A. Kudryavtsev,
Corresponding Member of of
RAACS, Professor, Dr.Sc., Far
Eastern State Transport University;
47, Serysheva St., 680021,
Khabarovsk, Russia

Sergey V. Kuznetsov,
Professor, Dr.Sc.,
Ishlinsky Institute for Problems
in Mechanics of the Russian
Academy of Sciences;
101-1, Prosp. Vernadskogo,
Moscow, 119526, Russia

Vladimir V. Lalin,
Professor, Dr.Sc.,
Peter the Great Saint-Petersburg
Polytechnic University;
29, Ul. Politechnicheskaya,
Saint-Petersburg, 195251, Russia

Leonid S. Lyakhovich,
Full Member of RAACS,
Professor, Dr.Sc., Tomsk State University of Architecture and Building; 2, Solyanaya Sq., Tomsk, 634003, Russia

Rashid A. Mangushev,
Corresponding Member of RAACS, Professor, Dr.Sc., Saint Petersburg State University of Architecture and Civil Engineering;
4, 2-nd Krasnoarmeiskaya Steet, Saint Petersburg, 190005, Russia

Ilizar T. Mirsayapov,
Corresponding Member of RAACS, Professor, Dr.Sc., Kazan State University of Architecture and Engineering; 1, Zelenaya Street, Kazan, 420043, Republic of Tatarstan, Russia

Vladimir L. Mondrus,
Corresponding Member of RAACS, Professor, Dr.Sc., National Research Moscow State University of Civil Engineering;
Yaroslavskoe Shosse 26, Moscow, 129337, Russia

Valery I. Morozov,
Corresponding Member of RAACS, Professor, Dr.Sc., Saint Petersburg State University of Architecture and Civil Engineering;
4, 2-nd Krasnoarmeiskaya Steet, Saint Petersburg, 190005, Russia

Anatoly V. Perelmuter,
Foreign Member of RAACS, Professor, Dr.Sc., SCAD Soft;
Office 1,2, 3a Osvity street, Kiev, 03037, Ukraine

Alexey N. Petrov,
Advisor of RAACS, Professor, Dr.Sc., Petrozavodsk State University; 33, Lenina Prospect, Petrozavodsk, 185910, Republic of Karelia, Russia

Vladilen V. Petrov,
Full Member of RAACS, Professor, Dr.Sc.,
Yuri Gagarin State Technical University of Saratov;
77 Politechnicheskaya Street, Saratov, 410054, Russia

Jerzy Z. Piotrowski,
Professor, Dr.Sc.,
Kielce University of Technology;
al. Tysiąclecia Państwa Polskiego 7, Kielce, 25 – 314, Poland

Chengzhi Qi, Professor, Dr.Sc.,
Beijing University of Civil Engineering and Architecture;
1, Zhanlanlu, Xicheng District, Beijing, China

Vladimir P. Selyaev,
Full Member of RAACS, Professor, Dr.Sc., Ogarev Mordovia State University;
68, Bolshevistskaya Str., Saransk 430005, Republic of Mordovia, Russia

Eun Chul Shin,
Professor, Ph.D.,
Incheon National University;
(Songdo-dong)119 Academy-ro, Yeonsu-gu, Incheon, Korea

D.V. Singh,
Professor, Ph.D,
University of Roorkee;
Roorkee, India, 247667

Wacław Szcześniak,
Foreign Member of RAACS, Professor, Dr.Sc.,
Lublin University of Technology;
Ul. Nadbystrzycka 40, 20-618 Lublin, Poland

Tadatsugu Tanaka,
Professor, Dr.Sc.,
Tokyo University; 7-3-1 Hongo, Bunkyo, Tokyo, 113-8654, Japan

Josef Vican,
Professor, Ph.D,
University of Žilina;
1, Univerzitná, Žilina, 010 26, Slovakia

Zbigniew Wojcicki,
Professor, Dr.Sc.,
Wroclaw University of Technology;
11 Grunwaldzki Sq., 50-377, Wrocław, Poland

Artur Zbiciak, Professor, Dr.Sc.,
Warsaw University of Technology;
Pl. Politechniki 1, 00-661 Warsaw, Poland

Segrey I. Zhavoronok, Ph.D.,
Institute of Applied Mechanics of Russian Academy of Sciences;
Moscow Aviation Institute (National Research University);
7, Leningradsky Prt., Moscow, 125040, Russia

Askar Zhussupbekov,
Professor, Dr.Sc.,
Eurasian National University;
5, Munaitpassov street, Astana, 010000, Kazakhstan

TECHNICAL EDITOR

Taymuraz B. Kaytukov,
Advisor of RAACS,
Associate Professor, Ph.D.,
Vice-Rector of National Research Moscow State University of Civil Engineering;
Yaroslavskoe Shosse 26,
Moscow, 129337, Russia

EDITORIAL TEAM

Vadim K. Akhmetov, Professor, Dr.Sc., National Research Moscow State University of Civil Engineering; 26, Yaroslavskoe Shosse, 129337 Moscow, Russia

Pavel A. Akimov, Full Member of RAACS, Professor, Dr.Sc., Acting Rector of National Research Moscow State University of Civil Engineering; Vice-President of the Russian Academy of Architecture and Construction Sciences; Tomsk State University of Architecture and Building; Russian University of Friendship of Peoples; 26, Yaroslavskoe Shosse, 129337, Moscow, Russia

Alexander M. Belostotsky, Full Member of RAACS, Professor, Dr.Sc., Research & Development Center "STADYO"; National Research Moscow State University of Civil Engineering; Russian University of Transport (RUT – MIIT); Russian University of Friendship of Peoples; Perm National Research Polytechnic University; Tomsk State University of Architecture and Building; Irkutsk National Research Technical University; 8th Floor, 18, ul. Tretya Yamskogo Polya, 125040, Moscow, Russia

Mikhail Belyi, Professor, Dr.Sc., Dassault Systèmes Simulia; 1301 Atwood Ave Suite 101W 02919 Johnston, RI, United States

Vitaly Bulgakov, Professor, Dr.Sc., Micro Focus; Newbury, United Kingdom

Charles El Nouty, Professor, Dr.Sc., LAGA Paris-13 Sorbonne Paris Cite; 99 avenue J.B. Clément, 93430 Villetaneuse, France

Natalya N. Fedorova, Professor, Dr.Sc., Novosibirsk State University of Architecture and Civil Engineering (SIBSTRIN); 113 Leningradskaya Street, Novosibirsk, 630008, Russia

Darya Filatova, Professor, Dr.Sc., Probability, Assessment, Reasoning and Inference Studies Research Group, EPHE Laboratoire CHART (PARIS) 4-14, rue Ferrus, 75014 Paris

Vladimir Ya. Gecha, Professor, Dr.Sc., Research and Production Enterprise All-Russia Scientific-Research Institute of Electromechanics with Plant Named after A.G. Iosiphyan; 30, Volnaya Street, Moscow, 105187, Russia

Taymuraz B. Kaytukov, Advisor of RAACS, Associate Professor, Ph.D, Vice-Rector of National Research Moscow State University of Civil Engineering; 26, Yaroslavskoe Shosse, 129337, Moscow, Russia

Marina L. Mozgaleva, Professor, Dr.Sc., National Research Moscow State University of Civil Engineering; 26, Yaroslavskoe Shosse, 129337 Moscow, Russia

Nadezhda S. Nikitina, Professor, Ph.D., Director of ASV Publishing House; National Research Moscow State University of Civil Engineering; 26, Yaroslavskoe Shosse, 129337 Moscow, Russia

Nikolai P. Osmolovskii, Professor, Dr.Sc., Systems Research Institute Polish Academy of Sciences; Kazimierz Pulaski University of Technology and Humanities in Radom; 29, ul. Malczewskiego, 26-600, Radom, Poland

Gregory P. Panasenko, Professor, Dr.Sc., Equipe d'Analise Numerique NMR CNRS 5585 University Gean Mehnet; 23 rue. P.Michelon 42023, St.Etienne, France

Andreas Rauh, Prof. Dr.-Ing. habil. Carl von Ossietzky Universität Oldenburg, Germany School II - Department of Computing Science Group Distributed Control in Interconnected Systems D-26111 Oldenburg, Germany

Zhan Shi, Professor LPSM, Université Paris VI 4 place Jussieu, F-75252 Paris Cedex 05, France

Marina V. Shitikova, National Research Moscow State University of Civil Engineering, Advisor of RAACS, Professor, Dr.Sc., Voronezh State Technical University; 14, Moscow Avenue, Voronezh, 394026, Russia

Igor L. Shubin, Corresponding Member of RAACS, Professor, Dr.Sc., Research Institute of Building Physics of Russian Academy of Architecture and Construction Sciences; 21, Lokomotivny Proezd, Moscow, 127238, Russia

Vladimir N. Sidorov, Full Member of RAACS, Professor, Dr.Sc., National Research Moscow State University of Civil Engineering; Russian University of Transport (RUT – MIIT); Moscow Institute of Architecture (State Academy); Perm National Research Polytechnic University; 26, Yaroslavskoe Shosse, 129337, Moscow, Russia

Valery I. Telichenko, Full Member of RAACS, Professor, Dr.Sc., The First Vice-President of the Russian Academy of Architecture and Construction Sciences; National Research Moscow State University of Civil Engineering; 24, Ulitsa Bolshaya Dmitrovka, 107031, Moscow, Russia

Vladimir I. Travush, Full Member of RAACS, Professor, Dr.Sc., Vice-President of the Russian Academy of Architecture and Construction Sciences; Urban Planning Institute of Residential and Public Buildings; 24, Ulitsa Bolshaya Dmitrovka, 107031, Moscow, Russia

INVITED REVIEWERS

Akimbek A. Abdikalikov, Professor, Dr.Sc.,
Kyrgyz State University of Construction, Transport and Architecture n.a. N. Isanov;
34 Maldybayeva Str., Bishkek, 720020, Biskek, Kyrgyzstan

Vladimir N. Alekhin, Advisor of RAACS, Professor, Dr.Sc.,
Ural Federal University named after the first President of Russia B.N. Yeltsin;
19 Mira Street, Ekaterinburg, 620002, Russia

Irina N. Afanasyeva, Ph.D., University of Florida; Gainesville, FL 32611, USA

Ján Čelko, Professor, PhD, Ing., University of Žilina; Univerzitná 1, 010 26, Žilina, Slovakia

Tatyana L. Dmitrieva, Professor, Dr.Sc.,
Irkutsk National Research Technical University; 83, Lermontov street, Irkutsk, 664074, Russia

Petr P. Gaidzhurov, Advisor of RAACS, Professor, Dr.Sc.,
Don State Technical University; 1, Gagarina Square, Rostov-on-Don, 344000, Russia

Jacek Grosel, Associate Professor, Dr inz.
Wroclaw University of Technology; 11 Grunwaldzki Sq., 50-377, Wrocław, Poland

Stanislaw Jemioło, Professor, Dr.Sc.,
Warsaw University of Technology; 1, Pl. Politechniki, 00-661, Warsaw, Poland

Konstantin I. Khenokh, M.Ing., M.Sc.,
General Dynamics C4 Systems; 8201 E McDowell Rd, Scottsdale, AZ 85257, USA

Christian Koch, Dr.-Ing., Ruhr-Universität Bochum;
Lehrstuhl für Informatik im Bauwesen, Gebäude IA, 44780, Bochum, Germany

Gaik A. Manuylov, Professor, Ph.D.,
Moscow State University of Railway Engineering; 9, Obraztsova Street, Moscow, 127994, Russia

Alexander S. Noskov, Professor, Dr.Sc.,
Ural Federal University named after the first President of Russia B.N. Yeltsin;
19 Mira Street, Ekaterinburg, 620002, Russia

Ilya I. Ovchinnikov, Professor, Dr.Sc., Tyumen Industrial University; 38, Volodarsky St., 625000, Tyumen, Russia

Grzegorz Świt, Professor, Dr.hab. Inż.,
Kielce University of Technology; 7, al. Tysiąclecia Państwa Polskiego, Kielce, 25 – 314, Poland

AIMS AND SCOPE

The aim of the Journal is to advance the research and practice in structural engineering through the application of computational methods. The Journal will publish original papers and educational articles of general value to the field that will bridge the gap between high-performance construction materials, large-scale engineering systems and advanced methods of analysis.

The scope of the Journal includes papers on computer methods in the areas of structural engineering, civil engineering materials and problems concerned with multiple physical processes interacting at multiple spatial and temporal scales. The Journal is intended to be of interest and use to researches and practitioners in academic, governmental and industrial communities.

ОБЩАЯ ИНФОРМАЦИЯ О ЖУРНАЛЕ

International Journal for Computational Civil and Structural Engineering

(Международный журнал по расчету гражданских и строительных конструкций)

Международный научный журнал "International Journal for Computational Civil and Structural Engineering (Международный журнал по расчету гражданских и строительных конструкций)" (IJCCSE) является ведущим научным периодическим изданием по направлению «Инженерные и технические науки», издаваемым, начиная с 1999 года (ISSN 2588-0195 (Online); ISSN 2587-9618 (Print) Continues ISSN 1524-5845). В журнале на высоком научно-техническом уровне рассматриваются проблемы численного и компьютерного моделирования в строительстве, актуальные вопросы разработки, исследования, развития, верификации, апробации и приложений численных, численно-аналитических методов, программно-алгоритмического обеспечения и выполнения автоматизированного проектирования, мониторинга и комплексного наукоемкого расчетно-теоретического и экспериментального обоснования напряженно-деформированного (и иного) состояния, прочности, устойчивости, надежности и безопасности ответственных объектов гражданского и промышленного строительства, энергетики, машиностроения, транспорта, биотехнологий и других высокотехнологичных отраслей.

В редакционный совет журнала входят известные российские и зарубежные деятели науки и техники (в том числе академики, члены-корреспонденты, иностранные члены, почетные члены и советники Российской академии архитектуры и строительных наук). Основной критерий отбора статей для публикации в журнале − их высокий научный уровень, соответствие которому определяется в ходе высококвалифицированного рецензирования и объективной экспертизы, поступающих в редакцию материалов.

Журнал входит в Перечень ВАК РФ ведущих рецензируемых научных изданий, в которых должны быть опубликованы основные научные результаты диссертаций на соискание ученой степени кандидата наук, на соискание ученой степени доктора наук по научным специальностям и соответствующим им отраслям науки:

- 1.1.8 – Механика деформируемого твердого тела (технические науки),
- 1.2.2 – Математическое моделирование численные методы и комплексы программ (технические науки),
- 2.1.1 – Строительные конструкции, здания и сооружения (технические науки),
- 2.1.2 – Основания и фундаменты, подземные сооружения (технические науки),
- 2.1.5 – Строительные материалы и изделия (технические науки),
- 05.23.07 – Гидротехническое строительство (технические науки),
- 2.1.9 – Строительная механика (технические науки)

В Российской Федерации журнал индексируется Российским индексом научного цитирования (РИНЦ).

Журнал входит в базу данных Russian Science Citation Index (RSCI), полностью интегрированную с платформой Web of Science. Журнал имеет международный статус и высылается в ведущие библиотеки и научные организации мира.

Издатели журнала – *Издательство Ассоциации строительных высших учебных заведений /АСВ/* (Россия, г. Москва) и до 2017 года *Издательский дом Begell House Inc*. (США, г. Нью-Йорк). Официальными партнерами издания является *Российская академия архитектуры и строительных наук* (РААСН), осуществляющая научное курирование издания, и *Научно-исследовательский центр СтаДиО* (ЗАО НИЦ СтаДиО).

Цели журнала – демонстрировать в публикациях российскому и международному профессиональному сообществу новейшие достижения науки в области вычислительных методов решения фундаментальных и прикладных технических задач, прежде всего в области строительства.

Задачи журнала:

• предоставление российским и зарубежным ученым и специалистам возможности публиковать результаты своих исследований;

• привлечение внимания к наиболее актуальным, перспективным, прорывным и интересным направлениям развития и приложений численных и численно-аналитических методов решения фундаментальных и прикладных технических задач, совершенствования технологий математического, компьютерного моделирования, разработки и верификации реализующего программно-алгоритмического обеспечения;

• обеспечение обмена мнениями между исследователями из разных регионов и государств.

Тематика журнала. К рассмотрению и публикации в журнале принимаются аналитические материалы, научные статьи, обзоры, рецензии и отзывы на научные публикации по фундаментальным и прикладным вопросам технических наук, прежде всего в области строительства. В журнале также публикуются информационные материалы, освещающие научные мероприятия и передовые достижения Российской академии архитектуры и строительных наук, научно-образовательных и проектно-конструкторских организаций.

Тематика статей, принимаемых к публикации в журнале, соответствует его названию и охватывает направления научных исследований в области разработки, исследования и приложений численных и численно-аналитических методов, программного обеспечения, технологий компьютерного моделирования в решении прикладных задач в области строительства, а также соответствующие профильные специальности, представленные в диссертационных советах профильных образовательных организациях высшего образования.

Редакционная политика. Политика редакционной коллегии журнала базируется на современных юридических требованиях в отношении авторского права, законности, плагиата и клеветы, изложенных в законодательстве Российской Федерации, и этических принципах, поддерживаемых сообществом ведущих издателей научной периодики.

За публикацию статей плата с авторов не взымается. Публикация статей в журнале бесплатная. На платной основе в журнале могут быть опубликованы материалы рекламного характера, имеющие прямое отношение к тематике журнала.

Журнал предоставляет непосредственный открытый доступ к своему контенту, исходя из следующего принципа: свободный открытый доступ к результатам исследований способствует увеличению глобального обмена знаниями.

Индексирование. Публикации в журнале входят в системы расчетов индексов цитирования авторов и журналов. «Индекс цитирования» – числовой показатель, характеризующий значимость данной статьи и вычисляющийся на основе последующих публикаций, ссылающихся на данную работу.

Авторам. Прежде чем направить статью в редакцию журнала, авторам следует ознакомиться со всеми материалами, размещенными в разделах сайта журнала (интернет-сайт Российской академии архитектуры и строительных наук (http://raasn.ru); подраздел «Издания РААСН» или интернет-сайт Издательства АСВ (http://iasv.ru); подраздел «Журнал IJCCSE»): с основной информацией о журнале, его целями и задачами, составом редакционной коллегии и редакционного совета, редакционной политикой, порядком рецензирования направляемых в журнал статей, сведениями о соблюдении редакционной этики, о политике авторского права и лицензирования, о представлении журнала в информационных системах (индексировании), информацией о подписке на журнал, контактными данными и пр. Журнал работает по лицензии Creative Commons типа cc by-nc-sa (Attribution Non-Commercial Share Alike) – Лицензия «С указанием авторства – Некоммерческая – Копилефт».

Рецензирование. Все научные статьи, поступившие в редакцию журнала, проходят обязательное двойное слепое рецензирование (рецензент не знает авторов рукописи, авторы рукописи не знают рецензентов).

Заимствования и плагиат. Редакционная коллегия журнала при рассмотрении статьи проводит проверку материала с помощью системы «Антиплагиат». В случае обнаружения многочисленных заимствований редакция действует в соответствии с правилами COPE.

Подписка. Журнал зарегистрирован в Федеральном агентстве по средствам массовой информации и охраны культурного наследия Российской Федерации. Индекс в общероссийском каталоге РОСПЕЧАТЬ − 18076.

По вопросам подписки на международный научный журнал “International Journal for Computational Civil and Structural Engineering (Международный журнал по расчету гражданских и строительных конструкций)” обращайтесь в Агентство «Роспечать» (Официальный сайт в сети Интернет: http://www.rosp.ru/) или в издательство Ассоциации строительных вузов (АСВ) в соответствии со следующими контактными данными:

ООО «Издательство АСВ»

Юридический адрес: 129337, Россия, г. Москва, Ярославское ш., д. 26, офис 705;

Фактический адрес: 129337, Россия, г. Москва, Ярославское ш., д. 19, корп. 1, 5 этаж, офис 12 (ТЦ Соле Молл);

Телефоны: +7 (925) 084-74-24;

Интернет-сайт: www.iasv.ru. Адрес электронной почты: iasv@iasv.ru.

Контактная информация. По всем вопросам работы редакции, рецензирования, согласования правки текстов и публикации статей следует обращаться к главному редактору журнала академику РААСН *Сидорову Владимиру Николаевичу* (адреса электронной почты: sidorov.vladimir@gmail.com, sidorov@iasv.ru, iasv@iasv.ru, sidorov@raasn.ru) или к техническому редактору журнала советнику РААСН *Кайтукову Таймуразу Батразовичу* (адреса электронной почты: tkaytukov@gmail.com; kaytukov@raasn.ru). Кроме того, по указанным вопросам, а также по вопросам размещения в журнале рекламных материалов можно обращаться к генеральному директору ООО «Издательство АСВ» *Никитиной Надежде Сергеевне* (адреса электронной почты: iasv@iasv.ru, nsnikitina@mail.ru, ijccse@iasv.ru).

Журнал становится технологичнее. Издательство АСВ с сентября 2016 года является членом Международной ассоциации издателей научной литературы (Publishers International Linking Association (PILA)), осуществляющей свою деятельность на платформе CrossRef. Оригинальным статьям, публикуемым в журнале, будут присваиваться уникальные номера (индексы DOI – Digital Object Identifier), что значительно облегчит поиск метаданных и местонахождение полнотекстового произведения. DOI – это система определения научного контента в сети Интернет.

С октября 2016 года стал возможен прием статей на рассмотрение и рецензирование через онлайн систему приема статей Open Journal Systems на сайте журнала (электронная редакция): https://ijccse.iasv.ru.

Автор имеет возможность следить за продвижением статьи в редакции журнала в личном кабинете Open Journal Systems и получать соответствующие уведомления по электронной почте.

В феврале 2018 года журнал был зарегистрирован в Directory of open access journals (DOAJ) (это один из самых известных поисковых сервисов в мире, который предоставляет открытый доступ к материалам и индексирует не только заголовки журналов, но и научные статьи), в сентябре 2018 года включен в продукты EBSCO Publishing.

В ноябре 2020 года журнал начал индексироваться в международной базе Scopus.

Журнал International Journal for Computational Civil and Structural Engineering входит в первый уровень Единого государственного перечня научных изданий – «Белого списка» – Министерства Науки и высшего образования Российской Федерации (ЕГПНИ)

International Journal for
Computational Civil and Structural Engineering
(Международный журнал по расчету гражданских и строительных конструкций)
Volume 22, Issue 3 ***2026***

Scientific coordination is carried out by the Russian Academy of Architecture and Construction Sciences (RAACS)

CONTENTS

Destruction of Rockfill Slope Protections by Ice Jamming: Field and Theoretical Studies **14**
Dmitry V. Kozlov, Denis A. Krutov

Load-Transfer Mechanisms in Timber Connections Using Densified Wood and Steel Dowels: an Experimental and Numerical Study **23**
Trong Tuan Tran, Ngoc-Thang Nguyen

Experimental And Numerical Study of the "Bison" Power Deck Used as a Permanent Formwork **35**
Sergey M. Anpilov, Denis A. Panfilov, Alexander S. Bychkov

Thermal Buckling and Flexure in Laminated Composite and FGM Beams: a Bibliometric Revie **45**
Rahul D. Kapase, Sanjay Kulkarni

Optimization of the Main Rigidity Planes Position of Inhomogeneous Rod in Spatial Bending **63**
Andrey V. Mishchenko, Maxim S. Veshkin, Vladimir L. Mondrus, Leonid Yu. Stupishin

Numerical Modelling of Snow Loads. Verification and Validation for the Kemerovo Museum, Theatre and Education Complex **76**
Alexander M. Belostotsky, Nikita A. Britikov, Oleg S. Goryachevsky

Numerical Modeling of Plane Frame Vibrations Taking into Account Nonlocal in Time Elastic Properties of the Material **90**
Vladimir N. Sidorov, Elena. S. Badina, Roman O. Tsarev

Analysis and Comparison of the Effectiveness of Various Seismic Isolators in Reducing Seismic Movements Recorded in Peru **99**
Hubert S. Morales, Arnold S. Grados, Flor O. Vara

Main Parameters of a Butt Joint with Meander Outline for Box-Section Column in Frame Moment Connection for Seismic Applications **113**
Yurii S. Kost, Andrey S. Plyaskin, Tatiana L. Dmitrieva

Developing the Method for Creating the Map of Application Zones of the Building Envelope Based on Calculations of Protection Against Waterlogging **127**
Kirill P. Zubarev, Yulia A. Sapronova, Vladimir D. Fedoseev

Numerical Modeling Technique for the Hydrodynamic Stability of Swirling Flows **135**
Vadim K. Akhmetov

Analysis of the Roughness Parameters and Chemical Composition Transformation of the Protective Coating of a Pipeline During its Repair **144**
Vladimir A. Orlov, Sergey P. Zotkin, Maria A. Bolshakova

Lateral-Torsional Buckling Analysis of Asymmetric Thin-Walled Beams **155**
Olga A. Tusnina

Evaluation of the Buckling of Frame Structures Under Dynamic Loading, Taking into Account the Inertial Components of Internal Forces **175**
Vladimir N. Sidorov, Vadim K. Akhmetov, Dmitriy O. Klimushkin

Probabilistic Method of Structural Reliability Analysis by Sampling with Limited Statistical Data **189**
Sergey A. Solovev, Anastasia A. Soloveva

International Journal for
Computational Civil and Structural Engineering
(Международный журнал по расчету гражданских и строительных конструкций)
Volume 22, Issue 3 ***2026***

Scientific coordination is carried out by the Russian Academy of Architecture and Construction Sciences (RAACS)

СОДЕРЖАНИЕ

Разрушение ледовым припаем каменно-набросных откосных креплений: натурные и теоретические исследования **14**
Д.В. Козлов, Д.А. Крутов

Механизмы сопротивления соединений деревянных конструкций с нагелями из прессованной древесины и стальных: экспериментальные и численные исследования **23**
Т.Т. Чан, Нгок-Тханг Нгуен

Экспериментальное и численное исследование силового настила «БИЗОН», используемого в качестве несъемной опалубки **35**
С.М. Анпилов, Д.А. Панфилов, А.С. Бычков

Устойчивость и изгиб балок из слоистых композитов и функционально-градиентных материалов: обзор исследований **45**
Р.Д. Капасе, Санджай Кулкарни

Оптимизация положения главных плоскостей жесткости неоднородного стержня при пространственном изгибе **63**
А.В. Мищенко, М.С. Вешкин, В.Л. Мондрус, Л.Ю. Ступишин

Верификация и валидация численного моделирования снеговых нагрузок на примере музейного и театрально-образовательного комплекса в г. Кемерово **76**
А.М. Белостоцкий, Н.А. Бритиков, О.С. Горячевский

Численное моделирование колебаний плоских рам с учётом нелокальных во времени упругих свойств материала **90**
В.Н. Сидоров, Е.С. Бадьина, Р.О. Царев

Анализ и сравнение эффективности различных сейсмоизоляторов при сейсмических воздействиях, зарегистрированных в Перу **99**
Уберт С. Моралес, Арнольд С. Градос, Флор О. Вара

Основные параметры стыка с очертанием меандра коробчатой колонны для сейсмостойкого рамного узла **113**
Ю.С. Кость, А.С. Пляскин, Т.Л. Дмитриева

Разработка метода создания карты зон применения ограждающей конструкции здания на основе расчетов защиты от переувлажнения **127**
К.П. Зубарев, Ю.А. Сапронова, В.Д. Федосеев

Методика численного моделирования гидродинамической устойчивости закрученных течений **135**
В.К. Ахметов

Анализ трансформации параметров шероховатости и химического состава защитного покрытия трубопровода при его ремонте **144**
В.А. Орлов, С.П. Зоткин, М.А. Большакова

Расчет изгибно-крутильной устойчивости несимметричных тонкостенных балок **155**
О.А. Туснина

Оценка устойчивости рамных конструкций при их динамическом нагружении с учётом инерционных составляющих внутренних усилий **175**
В.Н. Сидоров, В.К. Ахметов, Д.О. Климушкин, О.А. Туснина

Вероятностный метод анализа надежности сооружений генерацией данных при неполной статистической информации **189**
С.А. Соловьев, А.А. Соловьева

International Journal for Computational Civil and Structural Engineering, 22(3) 14–22 (2026)

DOI:10.22337/2587-9618-2026-22-3-14-22

DESTRUCTION OF ROCKFILL SLOPE PROTECTIONS BY ICE JAMMING: FIELD AND THEORETICAL STUDIES

Dmitry V. Kozlov [1], ***Denis A. Krutov*** [2]

[1] Moscow state university of civil engineering, Moscow, RUSSIA

[2] Kazakh-German University, Almaty, KAZAKHSTAN

Abstract: The relevance of the study is due to the fact that the nature of failure of rockfill slope protections of hydraulic structures under ice loading during water-level fluctuations has not actually been described. At the same time, ice jamming caused by the freezing of the ice cover to the structure during water-level changes should be classified as a dangerous type of ice impact. Therefore, any data on the nature of structural damage and its parameters can contribute to improving the design principles and design substantiation of hydraulic structures. An analysis of failures performed on the drainage berm of the main dam of the Nizhny Novgorod HPP made it possible to thoroughly schematize the recorded defects. To determine the causes of the hydraulic structure failure, a set of stability calculations for the hydraulic structure slope was performed. The complexity of the calculations lay in the fact that they had to be carried out in such a way as to assess the actual stability deficit, i.e., to determine the ultimate pull-out moment as accurately as possible. A comparative analysis of field observation data and calculation results made it possible to establish both the contribution of various factors to the failure scheme of the hydraulic structure and the causes of failure. Convincing evidence is presented of the significant influence of the warming effect of groundwater (seepage water) on the failure of the hydraulic structure. The new data obtained should be taken into account to refine the existing calculation schemes for assessing the stability of slope protections of hydraulic structures in cases where groundwater may emerge onto the slope. Such refinement may be required for slopes of canals in cuts, dam slopes, flood-protection structures, or transport embankments extending into river channels.

Keywords: ice jamming, ice cover, slope failure, schematization of defects, shoreline crack

РАЗРУШЕНИЕ ЛЕДОВЫМ ПРИПАЕМ КАМЕННО-НАБРОСНЫХ ОТКОСНЫХ КРЕПЛЕНИЙ: НАТУРНЫЕ И ТЕОРЕТИЧЕСКИЕ ИССЛЕДОВАНИЯ

Д.В. Козлов [1], ***Д.А. Крутов*** [2]

[1] Московский государственный строительный университет, г. Москва, РОССИЯ

[2] Казахстанско-Немецкий университет, г. Алматы, КАЗАХСТАН

Аннотация: Актуальность рассматриваемой проблемы вызвана тем, что характер разрушения каменно-набросных откосных креплений гидросооружений ледовой нагрузкой при колебаниях уровня воды фактически не описан. Вместе с тем, ледовый припай, обусловленный примерзанием к сооружению ледяного покрова при изменении уровня воды, следует относить к опасным видам ледовых воздействий. Поэтому любые данные о характере повреждений конструкций и параметрах этого повреждения могут способствовать совершенствованию принципов проектирования и расчетного обоснования гидросооружений. Анализ разрушений, выполненный на дренажном банкете русловой плотины Нижегородской ГЭС, позволил детально схематизировать зафиксированные дефекты. Для выяснения причин разрушения гидросооружения был выполнен комплекс расчетов устойчивости откоса гидросооружения. Сложность выполнения расчетов заключалась в том, что их надо было выполнить так, чтобы оценить фактический дефицит устойчивости, т.е. наиболее точно определить предельный вырывающий момент. Сопоставительный анализ данных натурных наблюдений и результатов расчетов позволил установить как вклад различных факторов в схему разрушения гидросооружения, так и причины разрушения. Приведены убедительные доказательства существенного влияния отепляющего воздействия грунтовых (фильтрационных вод) на разрушение конструкции гидросооружения. Полученные новые данные необходимо учитывать для уточнения существующих расчетных схем по оценке устойчивости откосных креплений гидросооружений в случае возмож-

ности выхода грунтовых вод на откос. Такое уточнение может потребоваться для откосов каналов, проходящих в выемке, откосов плотин, противопаводковых гидросооружений или транспортных насыпей, заходящих в русло рек.

Ключевые слова: ледовый припай, ледяной покров, разрушение откоса, схематизация дефектов, береговая трещина

INTRODUCTION

The practice of hydraulic structure operation involves the cases of slope protection failure caused by ice loads resulting from the freezing of the ice cover to the structure during water level changes. Such ice impact is commonly referred to as ice jamming, the mechanism of which is described in ICOLD Bulletin 105 and in reference [1]. In particular, when ice freezes to rockfill, this lifts the frozen mass as the water level rises. If the water level falls, the ice sheet, acting as a cantilever, displaces the rockfill protection from its design position.

Slopes of canals [2], flood protection embankments along riverbanks [3], bridge approach fills, upstream slopes of dams (e.g., during reservoir drawdown), as well as rock drainage berms in the tailwater of hydroelectric plants in wide sections where the influence of the polynya decreases [4], may be subjected to such loading. At the same time, the ice load caused by the rise/fall of the ice sheet (ice jamming) is the most dangerous among all possible ice impacts for rockfill [4].

Therefore, any field data concerning the destructive effect of ice jamming on hydraulic structure slopes will be valuable for researchers and designers.

For example, reference [5] examined the failure of a rock drainage berm slope of the Nizhny Novgorod HPP main dam. Let us briefly describe the studies previously conducted at the Nizhny Novgorod HPP.

Thus, the rock drainage berm of the Nizhny Novgorod HPP main dam required annual repairs after a two-month winter operation period. According to the original design, the structure has a length of 500 m, an average height of 7–8 m, a crest width of 5 m, and a slope of 1:2. The berm is formed by rockfill with an average stone diameter of 0.25 m. Figure 1 shows a typical cross-section based on depth measurements, illustrating both the reshaping pattern of the berm and its design profile (indicated by a dashed line).

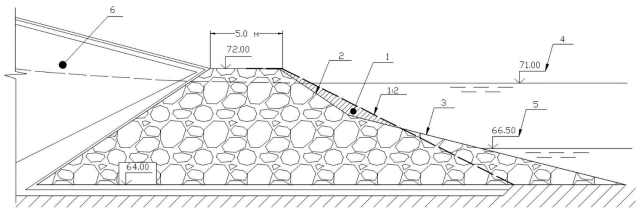


Figure 1. Scheme of transformation of a slope composed of rockfill under the action of ice jamming: 1) slope failure; 2) reshaping of the upper part of the slope forming a steep slope; 3) reshaping of the lower part of the slope forming a gentle slope; 4) maximum ice-cover level; 5) minimum water and ice-cover level; 6) dam body

The layout features of the Nizhny Novgorod hydropower complex and its operation exclude any other ice impacts on the structure except for ice jamming. Firstly, the rock berm of the main dam is located at a considerable distance (at least 1 km) from the spillway and the power house, and thus from the polynya. Secondly, no ice is released through the dam.

Evidence that the ice edge approaches the drainage berm (usually in January–February) comes from operation service records and aerial ice surveys [6]. According to these data, the ice thickness in the tailwater near the drainage berm during severe winters does not exceed 35 cm. At the same time, in the lake-like part of the reservoir (near the dam), the ice thickness is 50–60 cm, which is less than in other Volga reservoirs. The modest ice thickness is due to the warming discharges from the Kostroma GRES. Data on anthropogenic thermal pollution and ice thicknesses were obtained from two different sources over different periods: [6] and [7].

Complete ice clearance occurs in April. The formation of ice cover in the tailwater of the Nizhny Novgorod HPP is accompanied by stable frosty weather, low discharges, and constant HPP output throughout the day [7].

Depending on the air temperature and discharges into the tailwater, the ice edge may approach and retreat from the structure several times during one winter. At the same time, water-level fluctuations in the tailwater of the Nizhny Novgorod hydroelectric complex during the day can have a wide amplitude depending on the HPP discharges: from 0 to 2 m [7].

Note that Figure 1 presents an averaged assessment of damage. In reality, the observed parameters vary over a fairly wide range of values:

- the depth of slope failure ranges from 0.44 to 1.18 m (measured perpendicular to the slope);
- the slope steepness in the upper part varies from 1:0.73 to 1:1.77, and in the lower part – from 1:2.78 to 1:5.22;
- the point where the steep upper part transitions into the gentle lower part is located about 2 m from the maximum water level.

There is also a tendency: the steeper the upper part of the slope, the flatter the values of the lower part. In this case, the lower contour of the slope, with an average slope of 1:4, is no longer subjected to failure.

The large scatter of parameters (slope angles and failure depth) is most likely due to the complex thermal regime. Among the factors considered are the influence of snow cover and the warming effect of the reservoir. In particular, relatively warm seepage waters can reduce the weight of the frozen rockfill, which is a resisting force, and shift the center of rotation of the frozen mass towards the shoreline, i.e., reduce the leverage arms of the resisting forces.

The presented observations are important for practice because this allowed recording the actual parameters of the failure of a slope composed of rockfill.

Nevertheless, the cause of the destruction of the hydraulic structure is not obvious. To refine the calculation schemes for assessing the stability of slopes under ice jamming and to improve design methods for hydraulic structures, the following tasks need to be addressed:

- establish the causes of the unfavorable condition of the structure and assess the contribution of various factors to the failure process;
- determine the stability deficit of the failed rockfill embankment;
- schematize/systematize the nature of the failures;
- develop recommendations for improving design solutions.

METHODS

Perform the stability analysis for the failed slope of the hydraulic structure. In this way, we will seek the actual stability deficit, i.e., we will not include various safety factors.

To determine the moment load most accurately, we will assess stability not on the basis of the ice strength itself, as is common practice, but differently. In particular, we use the expression for the bending moment at the fixed end M (the moment load), which is derived from the differential equation of the deflected axis of the ice cover:

$$E \cdot I \frac{d^2y}{dx^2} = -M_x \qquad (1)$$

Where E is the elastic modulus of the ice cover, I is the moment of inertia of the ice-cover cross-section, and M_x is the bending moment at any section at a distance x from the fixed end (the ice jam). The origin is taken at the ice-jam location, with the oy axis directed downward and ox to the right.

The most accurate solution to equation (1) was proposed by P.A. Shankin, who assumed that the deformation pattern of the ice cover during water-level fluctuations allows a correct determination of the vertical forces, bending moments, and the length l of the deflecting ice sheet [8]. We present the expressions for the bending moment at the fixed end M and the length l of the ice cover over which the load is transmitted to the structure:

$$l = 3{,}58\sqrt[4]{\frac{E \cdot I}{\gamma C}}. \qquad (2)$$

$$M = f\frac{1}{60 \cdot l^2}\{\gamma C(5\psi - 2) + 360 \cdot E \cdot I\}. \quad (3)$$

Where γ is the unit weight of water; *C* is the length of the structure along the front at the ice action level; the numerical coefficient in formula (2) is obtained for the ratio of the water-level rise/fall *H* to the deflection *f* equal to 1 (i.e., $H/f = \psi = 1$).

The bending moment at the fixed end *M* can also be called the ultimate pull-out moment acting in section *x* (Fig. 2). In this section, the first shoreline crack appears in the ice cover.

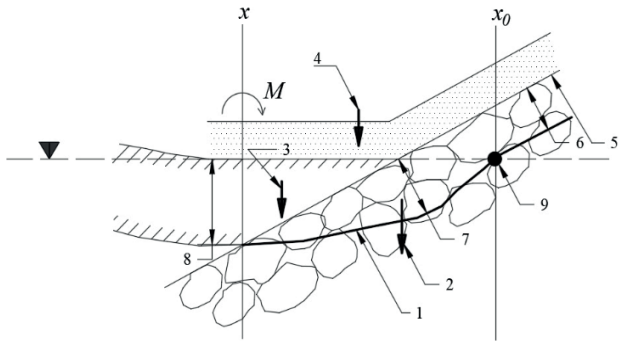


Figure 2. Force diagram for the stability analysis of a slope composed of rockfill during ice-cover rise: 1 – freezing boundary of the soil; 2 – weight of frozen soil; 3 – weight of ice on the slope; 4 – weight of snow cover; 5 – slope surface; 6 – freezing depth of rockfill above the water level (H_1); 7 – freezing depth of rockfill at the water level (H_2); 8 – freezing depth of rockfill below the water level (H_3); 9 – center of rotation of the frozen rockfill mass

The length *l* of the ice cover corresponds to the point where the curvature of the ice field transitions to a horizontal position, i.e., when the section rotation angle θ = 0 and the deflection is maximum *f*. The deflection *f* is assigned according to field observation data obtained by geodetic levelling of the ice field under similar ice thickness [8].

For an ice thickness $t = 0.35$ m, $E = 400{,}000$ t/m^2 (3922.66 MPa) [9-15]; $I = 0.00357$ m^4, $\psi \approx 1$, and $f = 0.025$ m, the length of the ice cover from formula (2) is $l = 22.0$ m, and the pull-out moment from formula (3) is M = 0.44 tf·m (4.31 kN·m).

The applicability of expressions (2) and (3) is limited by the following conditions:

- $B \geq 2l$ (*B* is the width of the water body at the design water level);
- $(\gamma_л \cdot t)/\gamma \geq H \geq f$ ($\gamma_л$ is the unit weight of ice, *t* is the ice thickness).

All the above considerations remain valid for both water-level drawdown and rise, except that during a rise, the overturning moment is clockwise and the vertical force is upward; during a drawdown, the opposite occurs.

Verification stability calculations of the rock berm during water-level rise (as the most dangerous case) will be performed for the actually recorded ice thickness in a severe winter (35 cm). We will also assume different values of snow-cover height δ.

The snow-cover height δ significantly affects the freezing depth of the soil above and below the water level [16], and consequently the magnitude of the resisting forces (weight of the frozen rockfill) and the position of the centre of the frozen mass. In the absence of snow cover and without the warming effect of groundwater, the resisting forces will be maximal. According to operation service data, the maximum average ten-day snow-cover height over the winter does not exceed 53 cm. The maximum snow depths are observed at the end of March, when the ice-jam hazard is already absent.

Evaluate the slope stability for different design cases: for slope angles in the upper part (1:2) and lower part (1:4) and for various snow-cover thicknesses.

In the case of water-level rise, all moments resisting the rockfill are taken entirely within sections $x - x_0$ (Fig. 2), assuming that the frozen rockfill mass does not deform.

To assess slope stability, it is necessary to estimate the freezing depths of the soil: above the water level H_1, at the water level H_2, and below the water level H_3. For the considered calculation scheme (Fig. 2), the values of H_1, H_2, and H_3 can be taken from the formulas:

$$H_1 = H_d - \frac{\delta_s}{\beta_s}\beta_{st1}, \quad (4)$$

$$H_2 = H_d - \frac{\delta_s}{\beta_s}\beta_{st2}, \quad (5)$$

$$H_3 = t. \quad (6)$$

Where H_d is the freezing depth of the rockfill; δ_s is the thickness of the protective snow medium; β_s is the thermal conductivity of snow; β_{st1} is the thermal conductivity of the rockfill in the dry state; β_{st2} is the thermal conductivity of the rockfill below the water level in the freezing zone; t is the ice thickness.

In determining the weight of the frozen rockfill, the following was taken into account:

- at depth H_1, the unit weight of frozen soil containing an unaccounted amount of ice in the pores, with the buoyant effect of water ($\gamma_1 \approx 18.1$ kN/m^3);
- at depth H_2, the unit weight of frozen soil including the weight of ice in the pores, with the buoyant effect of water ($\gamma_2 \approx 19.1$ kN/m^3).

RESULTS AND DISCUSSION

Example of stability calculation for a slope with design slope angle of 1:2 at a snow depth of 25 cm is given in Table 1.

Table 1. Stability calculation of a rockfill slope (1:2) under ice-jamming action (ice thickness 35 cm, snow thickness 25 cm, H_1 = 0.16 m; H_2 = 0.25 m; H_3 = 0.35 m)

Forces, tf (kN)	Lever arms, m	Resisting moment, tf·m (kN·m)	$K=\Sigma(M_r)_{x0}/M$
Weight of snow on ice sheet: 0.36 (3.53)	0.58	0.21 (2.06)	4.31/4.31=1
Weight of snow on slope: 0.07 (0.69)	0.13	0.01 (0.1)	
Weight of shore ice: 0.11 (1.08)	0.82	0.09 (0.88)	
Weight of frozen rockfill below water level: 0.26 (2.55)	0.46	0.12 (0.18)	
Weight of frozen rockfill above water level: 0.06 (0.59)	0.12	0.01 (0.1)	
	$\Sigma(M_r)_{x0}$	0.44 (4.31)	

The results of stability calculations for the slope with design slope angle 1:2 at different snow thicknesses are presented in Table 2.

Table 2. Stability calculation results for the rockfill slope (1:2) at different snow thicknesses

Parameter	Snow depth, cm		
	20	25	30
Calculated stability safety factor	2.77	1.00	0.48
Weight of frozen rockfill, tf (kN)	0.97 (9.51)	0.32 (3.14)	0.19 (1.86)

Analyze the results of the calculations and the field observation data. If we do not take into account the warming effect of seepage water, then at a snow thickness of 25 cm the slope with design slope 1:2 should be stable. Thus, failure of the 1:2 slope can occur only when the snow cover depth exceeds 25 cm, i.e., by the middle or end of winter. This is indirect, albeit incomplete, evidence of the influence of the warming effect of reservoir seepage waters on the position of the center of the frozen mass and its weight.

A snow cover thickness of 30 cm creates the most unfavorable conditions for the stability of the slope with design slope 1:2, because a 30-cm snow "cap" protects the slope from freezing. At this snow depth (30 cm), the safety factor reaches its minimum value because the weight of the frozen rockfill under the warming snow cap is negligible. A thicker snow cover would lead to a slight increase in the safety factor due to the additional snow surcharge on the ice sheet and slope.

With a snow cap of 30 cm or more, the slope with design slope 1:2 will fail, but the failure parameters should be identical along the structure length if there are no other factors affecting the collapse. On the contrary, the nature of failure is complex: the actual values of the stone mass displaced from its design position range from 6600 kg (maximum) to 1000 kg (minimum). This means that the failure of the slope with design slope 1:2 is caused by the influence of the seepage flow, which creates a complex temperature field.

Consider the unlikely situation that the snow thickness varies significantly along the slope

length, i.e., it is not uniform in different cross-sections:
1) from 0 to 50 cm;
2) from 30 to 50 cm;
The first case is not confirmed by field observations, because on some sections the structure would not be damaged. In the second case, the failure parameters would be identical, since a snow cap larger than 30 cm no longer affects the position of the soil freezing boundary.
Thus, a second reliable proof of the warming effect of reservoir seepage waters on the position of the centre of the frozen mass and its weight is presented.
The thermal regime of the seepage flow in the dam body cannot but be determined by the water temperature in the reservoir. According to field observations conducted by the operation service, the following is known [17]:
- during the freeze-up period, the water temperature near the bottom in the lower part of the reservoir (near the dam) in November and December is 1–2 °C, and by March it drops to 0.1–0.2 °C;
- in summer, the lake-like part of the reservoir is characterised by a decrease in water temperature from the surface to the bottom; the temperature drop is usually 2–3 °C, but can reach 10–15 °C;
- if the maximum temperature of the seepage flow in the upstream wedge of the dam (up to its axis) is observed in September, then in the downstream wedge (drainage berm), the groundwater has its maximum temperature in December.
The influence of warm groundwater on ice processes has been noted earlier at weather stations, in particular at the Ilyino post (Gorky Reservoir). There, the ice thickness is smaller than at other weather stations on the reservoir. Moreover, the peculiarity of this phenomenon lies in the non-uniformity of ice thickness: even in severe winters, the thickness can vary from 10 to 75 cm (data from the operation service of the Nizhny Novgorod HPP [17]).
The lower part of the rockfill slope with a slope of 1:4 is stable with a good margin even in the presence of snow cover. The stability of such a slope is largely determined by the weight of the shore ice and the significant lever arm of the corresponding force, even if the center of rotation of the frozen mass is for some reason shifted toward the shoreline.
The performed field observations of the failure of the rockfill slope, accompanied by calculations, show that there are two effective ways to combat ice jamming [18–20]: flattening the slope and increasing the stone size. The latter measure is only effective under the warming influence of snow cover or groundwater, because without these factors, the weight of the frozen rockfill, rather than the weight of an individual stone, will be one of the forces ensuring the stability of the slope protection.
The slope angle of the non-failed and stable lower part of the slope is apparently determined by the nature of the failure of the upper part, which, after reshaping, rolls down to the lower part of the structure. Thus, it has been observed that the greater the failure depth and the steeper the upper slope, the flatter the slope in its lower part becomes.

CONCLUSIONS

1. One of the reasons of rockfill embankment failure under ice-jamming action is the warming effect of groundwater (seepage) flow. This fact should be considered proven for the following reasons:
- according to calculation results, failure of the slope with design slope 1:2 can occur only when the snow cover depth exceeds 25 cm, i.e., by the middle or end of winter, which does not correspond to field observation data;
- calculation results show that if the slope failure were determined solely by the height of the snow cap, its failure parameters would be identical even if the snow thickness/depth varied along the slope length;
- field observations of the failed slope show a wide scatter in slope angles and in the mass of stone displaced from its design position to the lower part of the slope, which is due to the com-

plex thermal regime within the hydraulic structure (the mass of stone displaced during two winter months from the design position varies from 1000 kg to 6600 kg).

2. Systematic observations of the failure of a rockfill embankment under ice-jamming action, together with the stability calculations performed, allow the following conclusions:

- the failure pattern of the design slope with slope 1:2 consists of a steep upper part (reaching 1:0.73) and a gentle lower part (averaging 1:4);
- the gentle slope of the lower, non-failed part of the slope is most likely determined by the extent of failure in the upper part, from which stone is moved to the lower part, forming a new gentle surface;
- under the most unfavorable scenario, a twofold stability deficit of the rockfill slope with design slope 1:2 is observed;
- the existing calculation schemes for assessing the stability of slope protections need to be adjusted and, in particular, to account for the warming effect of groundwater when it emerges onto the slope;
- effective and reliable design measures for slope protections under ice-jamming hazard include flattening the slopes (e.g., to 1:4) and increasing the stone size.

REFERENCES

1. **Rattue A.** Slope Protection with Consideration for Ice Effects. Province of Newfoundland and Labrador, Canada, 2013, 54 p.
2. **Bagin A.V., Kozlov D.V.** Assessment of the possibility of using gabion structures under developing ice load. Gidrotekhnika (Hydraulic Engineering), 2018, No. 2(51), pp. 12–16.
3. **Krutov D.A**. Design of slope protection for a flood protection dam on the Chadana River. Hydrotechnical Construction, 2021, No. 6, pp. 2–11.
4. **Krutov D.A.** Repair of riprap slope protections damaged by ice jamming. Proceedings of the Vedeneev VNIIG, 2021, Vol. 302, pp. 26–36.
5. **Krutov D.A.** Riprap disturbance caused by ice plucking and measures to prevent it. Dams and Reservoirs, 2021, No. 32(4), pp. 149–152.
6. **Chizhov A.N.** Formation of ice cover and spatial distribution of its thickness. Leningrad: Gidrometeoizdat, 1990. 127 p.
7. **Borshch P.S., Tveritnev V.P.** Development of a comprehensive reconstruction project for the 8. Nizhny Novgorod HPP. Hydrotechnical Construction, 2015, No. 10, pp. 33–38.
8. **Shankin P.A.** Calculation of slope coverings of hydraulic structures. Moscow: Rechnoy Transport, 1961. 293 p.
9. **Iliescu D., Baker Ia.** The structure and mechanical properties of river and lake ice. Cold Regions Science and Technology, 2007, No. 48(3), pp. 202–217.
10. **Chang X., Liu W., Zuo G., Dou Yi., Li Ya**. Research on ultrasonic-based investigation of mechanical properties of ice. Acta Oceanologica Sinica, 2021, No. 40, pp. 97–105.
11. **McKenna R., Crocker G.** Effective moduli for flexure of a floating ice cover due to temperature variations through the depth of the ice. Proceedings of the 26th International Conference on Port and Ocean Engineering under Arctic Conditions. Moscow, 2021, 10 p.
12. **Jang H.-S., Hwang S.-Y., Yoon J., Lee J.-H.** Numerical Analysis of Ice–Structure Impact: Validating Material Models and Yield Criteria for Prediction of Impact Pressure. Journal of Marine and Science Engineering, 2024, No. 12(2), article 229.
13. **Jang H.-S., Hwang S.-Y., Lee J.H.** Experimental Evaluation and Validation of Pressure Distributions in Ice–Structure Collisions Using a Pendulum Apparatus. Journal of Marine and Science Engineering, 2023, No. 11(9), article 1761.
14. **Zakharov I., Puestow T., Khan A., Briggs R., Barrettte P.** Review of River Ice Observation and Data Analysis Technologies. Hydrology, 2024, No. 11(8), article 126.

15. **Fuks M.** Changes in river ice cover in the context of climate change and dam impacts: a review. Aquatic Sciences, 2023, No. 85(4), article 113.
16. **Bogorodskiy P.V.** Ice and Snow on Lake Stemmevatnet, Spitsbergen, in Winter 2019/20. Journal Ice and Snow, 2023, No. 63(3), pp. 441–453.
17. **Kuznetsov V.S., Ladenko S.Yu.** Technical condition of the earth dams of the Nizhny Novgorod HPP after 60 years of operation. Hydrotechnical Construction, 2015, No. 10, pp. 11–20.
18. **Han H., Shen Le., Cao M., Wei Li., Qian X**. On the ice induced damage of reservoir drainage tower: A thermal stress-involved contact simulation. Engineering Failure Analysis, 2024, No. 160, article 108203.
19. **Su H., Wu D., Lu Yi., Peng X., Wang X., Chen W., Wang S.** Experimental and numerical study on stability performance of new ecological slope protection using bolt-hinge anchored block. Ecological Engineering, 2021, No. 172, article 106409.
20. **Krutov D.A.** Causes of failure of flood protection structures and examples of their reconstruction. Hydrotechnical Construction, 2025, No. 8, pp. 23–30.

СПИСОК ЛИТЕРАТУРЫ

1. **Rattue A.** Slope Protection with Consideration for Ice Effects. Province of Newfoundland and Labrador, Canada, 2013, 54 pages.
2. **Багин А.В., Козлов Д.В.** Оценка возможности применения габионных структур в условиях развивающейся ледовой нагрузки // Гидротехника, 2018, No. 2(51). С. 12-16.
3. **Крутов Д.А.** Проект откосного крепления противопаводковой дамбы на реке Чадана // Гидротехническое строительство, 2021, No. 6. С. 2-11.
4. **Крутов Д.А.** Ремонт каменно-набросных креплений откосов, разрушающихся под действием ледяного припая // Известия ВНИИГ им. Б.Е. Веденеева, 2021, Т. 302. С. 26-36.
5. **Krutov D.A.** Riprap disturbance caused by ice plucking and measures to prevent it // Dams and Reservoirs, 2021, No. 32(4), pp. 149-152.
6. **Чижов А.Н.** Формирование ледяного покрова и пространственное распределение его толщины. – Ленинград: Гидрометеоиздат, 1990. – 127 с.
7. **Борщ П.С., Тверитнев В.П.** Разработка комплексного проекта реконструкции Нижегородской ГЭС // Гидротехническое строительство, 2015, No. 10. С. 33-38.
8. **Шанкин П.А.** Расчет покрытий откосов гидротехнических сооружений. – М.: Речной транспорт, 1961. – 293 с.
9. **Iliescu D., Baker Ia.** The structure and mechanical properties of river and lake ice // Cold Regions Science and Technology, 2007, No. 48(3), pp. 202-217.
10. **Chang X., Liu W., Zuo G., Dou Yi., Li Ya.** Research on ultrasonic-based investigation of mechanical properties of ice // Acta Oceanologica Sinica, 2021, No. 40, pp. 97-105.
11. **McKenna R., Crocker G.** Effective moduli for flexure of a floating ice cover due to temperature variations through the depth of the ice // Proceedings of the 26 th International Conference on Port and Ocean Engineering under Arctic Conditions. Moscow, 2021, 10 p.
12. **Jang H-S., Hwang S-Y., Yoon J., Lee J-H.** Numerical Analysis of Ice–Structure Impact: Validating Material Models and Yield Criteria for Prediction of Impact Pressure // Journal of Marine and Science Engineering, 2024, No. 12(2), article 229.
13. **Jang, H.-S.; Hwang, S.-Y.; Lee, J.H.** Experimental Evaluation and Validation of Pressure Distributions in Ice–Structure Collisions Using a Pendulum Apparatus // Journal of Marine and Science Engineering, 2023, No. 11(9), article 1761.
14. **Zakharov I., Puestow T., Khan A., Briggs R., Barrette P.** Review of River Ice Observation and Data Analysis Technologies // Hydrology, 2024, No. 11(8), article 126.

15. **Fuks M.** Changes in river ice cover in the context of climate change and dam impacts a review // Aquatic Sciences, 2023, No. 85(4), article 113.
16. **Bogorodskiy P.V.** Ice and Snow on Lake Stemmevatnet, Spitsbergen, in Winter 2019/20 // Journal Ice and Snow, 2023, №63(3), pp. 441-453.
17. **Кузнецов В.С., Ладенко С.Ю.** Техническое состояние земляных плотин Нижегородской ГЭС после 60 лет эксплуатации // Гидротехническое строительство, 2015, No. 10. С. 11-20.
18. **Han H., Shen Le., Cao M., Wei Li., Qian X.** On the ice induced damage of reservoir drainage tower: A thermal stress-involved contact simulation // Engineering Failure Analysis, 2024, No. 160, article 108203.
19. **Su H., Wu D., Lu Yi., Peng X., Wang X., Chen W., Wang S.** Experimental and numerical study on stability performance of new ecological slope protection using bolt-hinge anchored block // Ecological Engineering, 2021, No. 172, article 106409.
20. **Крутов Д.А.** Причины разрушения противопаводковых сооружений и примеры их реконструкции // Гидротехническое строительство, 2025, No. 8. С. 23-30.

Kozlov Dmitry Vyacheslavovich, Doctor of Sciences in Engineering, Professor, Full Member of the Russian Academy of Architecture and Construction Sciences (RAACS), Head of the Department of Hydraulics and Hydraulic Engineering Construction, National Research Moscow State University of Civil Engineering (NRU MGSU); office 606, building 26, block G, Yaroslavskoye Shosse, Moscow, 129337, Russia; gs@mgsu.ru

Krutov Denis Anatolyevich, Candidate of Sciences in Engineering, Visiting Professor, Department of Integrated Water Resources Management (under the auspices of UNESCO), Kazakh-German University (KGU); office 501, 173 Nazarbayev Avenue, Almaty, 050019, Kazakhstan; krutovdenis@yahoo.com

Козлов Дмитрий Вячеславович — доктор технических наук, профессор, член-корреспондент РААСН, заведующий кафедрой гидравлики и гидротехнического строительства, Национальный исследовательский московский государственный строительный университет (НИУ МГСУ); офис 606, д.26, , корпус Г, Ярославское шоссе, Москва, 129337, Россия, gs@mgsu.ru

Крутов Денис Анатольевич — кандидат технических наук, приглашенный профессор, кафедра интегрированного управления водными ресурсами (под управлением ЮНЕСКО), Казахстанско-Немецкий университет (КНУ) офис 501, д. 173, проспект Назарбаева, Алматы, 050019, Казахстан, krutovdenis@yahoo.com

DOI:10.22337/2587-9618-2026-22-3-23-34

LOAD-TRANSFER MECHANISMS IN TIMBER CONNECTIONS USING DENSIFIED WOOD AND STEEL DOWELS: AN EXPERIMENTAL AND NUMERICAL STUDY

Trong Tuan Tran [1], Ngoc-Thang Nguyen [2]
[1] Hanoi Architectural University, Tran Phu, Hanoi VIETNAM
[2] Thuyloi University, Tay Son, Hanoi, VIETNAM

Abstract: This study presents an experimental and numerical investigation of the mechanical behavior of L-shaped timber connections assembled using densified wood dowels and steel dowels under ambient mechanical loading conditions. Mechanical tests were con-ducted on a multilayer timber beam–column connection to determine the load–displacement response of the joint system. In parallel, a three-dimensional finite element model was developed in Abaqus to simulate the structural behavior and to investigate the load-transfer mechanisms within the connection region. The numerical results show good agreement with the experimental response, demonstrating the capability of the model to accurately reproduce the global behavior of the connection. Although the two types of dowels exhibit relatively similar overall stiffness, the stress distribution along the grain (S11) and the stress fields within the joint reveal fundamentally different load-transfer mechanisms. Steel dowels provide a more uniform stress distribution and more efficient force transfer, whereas densified wood dowels exhibit more localized stress concentrations and a more compliant mechanical response. Nevertheless, the use of densified wood dowels may offer advantages in terms of material compatibility and potential thermal performance under elevated temperatures. The findings contribute to a better understanding of the mechanical behavior of timber connections using different dowel types and provide a reference basis for future thermo-mechanical investigations of timber structures exposed to fire.

Keywords: Timber connections, densified wood dowels, steel dowels, mechanical behavior, load-transfer mechanism, finite element modelling

МЕХАНИЗМЫ СОПРОТИВЛЕНИЯ СОЕДИНЕНИЙ ДЕРЕВЯННЫХ КОНСТРУКЦИЙ С НАГЕЛЯМИ ИЗ ПРЕССОВАННОЙ ДРЕВЕСИНЫ И СТАЛЬНЫХ: ЭКСПЕРИМЕНТАЛЬНЫЕ И ЧИСЛЕННЫЕ ИССЛЕДОВАНИЯ

Т.Т. Чан [1], Нгок-Тханг Нгуен[2]
[1] Ханойский архитектурный университет, Чан Фу, Ханой, ВЬЕТНАМ
[2] Университет Тхюй Лой, Тай Шон, Ханой, ВЬЕТНАМ

Аннотация: Представлены экспериментальные и численные исследования сопротивления Г-образных деревянных соединений, собранных с использованием нагелей из прессованной древесины и стальных нагелей, при обычных механических нагрузках. Проведены механические испытания многослойного узла сопряжения балки с колонной для определения несущей способности и деформативности. Параллельно разработана трёхмерная конечно-элементная модель в программном комплексе Abaqus для моделирования сопротивления и изучения механизмов передачи усилий в зоне соединения. Численные результаты хорошо согласуются с экспериментальными данными, что подтверждает способность модели точно воспроизводить общее поведение соединения. Хотя оба типа нагелей демонстрируют относительно схожую общую жёсткость, распределение напряжений вдоль волокон (S11) и поля напряжений в узле выявляют принципиально различные механизмы передачи усилий. Стальные нагели обеспечивают более равномерное распределение напряжений и более эффективную передачу усилий, тогда как нагели из прессованной древесины характеризуются более локализованными концентрациями напряжений и более податливым механическим откликом. Тем не менее, применение нагелей из прессованной древесины может давать преимущества с точки зрения совместимости материалов и

потенциальных теплотехнических характеристик при повышенных температурах. Полученные результаты способствуют более глубокому пониманию сопротивления деревянных соединений с различными типами нагелей и служат основой для будущих термомеханических исследований деревянных конструкций, подвергающихся воздействию огня.

Ключевые слова: деревянные соединения, нагели из прессованной древесины, стальные нагели, сопротивление, механизм передачи усилий, конечно-элементное моделирование

1. INTRODUCTION

In recent years, timber structures have attracted increasing attention in the construction field due to their low density, high strength-to-weight ratio, recyclability, and environmental advantages compared with conventional materials such as steel and concrete [1]. Along with the development of engineered wood products (EWPs), various modern timber structural and connection systems have been investigated to improve load-bearing efficiency and expand the application of timber in large-scale structures [2]. However, many current connection systems still rely on steel mechanical fasteners or synthetic structural adhesives, which may reduce material homogeneity, recyclability, and the environmental benefits of timber structural systems [1].

In this context, densified wood, also referred to as compressed wood, has been considered a promising material for partially replacing metallic fasteners in timber structures. Densified wood is produced through thermo-mechanical compression, which reduces the internal porosity of the wood cellular structure and thereby significantly increases its density and mechanical properties [1,2]. Previous studies have shown that densification can markedly im-prove the elastic modulus, flexural strength, tensile strength, and shear strength of wood, allowing low-density softwood species to be used in structural applications requiring higher load-bearing capacity [2,3]. In addition, densified wood offers advantages such as material compatibility with timber components, recyclability, and the ability to create tight connections through moisture-dependent swelling [2].

Based on these advantages, several studies have proposed the use of densified wood dowels as an alternative to conventional steel dowels in timber connections. Jung et al. [4,5] developed connection systems using compressed wood dowels and plates for column–beam and column–base joints, showing that these systems can provide satisfactory load-bearing and rotational performance. In another study, Jung et al. [6] demonstrated that compressed wood dowels can be effectively used in glued-in-rod connections, achieving load-bearing capacity comparable to or higher than that of some traditional hardwood dowels. O'Loinsigh et al. [7] developed timber-to-timber composite beams using welded-through wood dowels to generate composite action between timber layers without the use of adhesives or metallic fasteners. These studies demonstrate the considerable potential of wood-based dowels for developing environmentally friendly timber connection systems and reducing dependence on metallic materials.

Alongside experimental investigations, the finite element method (FEM) has been increasingly used in timber engineering research to simulate stress distributions, load-transfer mechanisms, and the mechanical behaviour of timber connection systems. Xu et al. [8] developed a three-dimensional finite element model for dowel-type timber joints subjected to loading parallel to the grain, while Feio et al. [9] showed that FEM can reasonably repro-duce stiffness and stress distributions in traditional timber joints. More recently, Ar-ciszewska-Kędzior et al. [10] and Tran and Dao [11] combined experimental and numerical modelling to evaluate the mechanical behavior of timber joints using wooden dowels, demonstrating that FEM is an effective tool for analyzing load-transfer mechanisms and stress fields in connection regions.

In addition, numerical studies on multilayer timber beams have shown that the degree of interaction between timber layers strongly affects the load-transfer mechanism, global stiffness, and stress distribution of the structural system [12]. These findings confirm the potential of FEM for investigating the mechanical behavior of complex timber connections and structural systems.

Besides studies on mechanical behavior under ambient conditions, the fire performance of densified timber and timber connections using densified wood dowels has also been investigated in recent studies. Tran et al. [13] experimentally characterized the thermal behavior and degradation of thermo-mechanically compressed spruce timber and developed a three-step multi-reaction pyrolysis finite element model for predicting temperature profiles, mass loss, and charring depth under fire exposure. For timber connections, Khelifa et al. [14] developed a thermal modelling framework for connections assembled with densified wood dowels under fire, showing that pyrolysis-based modelling can reproduce temperature dis-tribution and char layer formation.

In addition, Tran et al. [15] experimentally investigated the thermo-mechanical performance of L-shaped timber connections assembled with densified wood dowels and steel dowels under fire exposure, demonstrating that densified wood dowels can reduce heat transfer, lower charring depth, and limit thermally induced deformation compared with steel dowels. Tran's doctoral thesis [16] further synthesized the thermal and thermo-mechanical modelling framework for timber structural systems assembled with densified wood dowels under fire conditions. However, although these thermal and thermo-mechanical studies provide important insight into fire-exposed behavior, the baseline mechanical behavior of L-shaped timber connections using densified wood dowels under ambient mechanical loading has not yet been fully clarified, particularly in terms of load-transfer mechanisms and stress distributions within the connection region.

Therefore, this study presents an experimental and numerical investigation of the mechanical behavior of L-shaped timber connections using densified wood dowels and steel dowels under ambient loading conditions. Mechanical tests were conducted to determine the load–displacement response of the connection system, while a three-dimensional finite element model was developed in Abaqus to analyze the load-transfer mechanism and stress distribution in the dowel region. The focus of this study is not only to compare the global stiffness of the two connection types, but also to clarify the differences in load-transfer mechanisms and stress fields between densified wood dowels and steel dowels. The results are expected to provide a mechanical baseline for further studies on the thermo-mechanical behavior of timber connections under fire conditions.

2. EXPERIMENTAL PROGRAM

2.1 Connection configuration and specimen

Experiments were conducted on L-shaped timber connections to evaluate the mechanical behavior of connection systems using densified wood dowels and steel dowels under ambient loading conditions. The connection consisted of a beam and a column assembled using four dowels with a diameter of 16 mm. Two connection configurations were investigated, namely connections using densified wood dowels and connections using steel dowels, in order to evaluate the influence of dowel material on the load-transfer mechanism and stress distribution within the connection region.

Details of the experimental specimen and the connection region are presented in Figure 1. Four dowels were arranged in a clustered configuration at the beam–column intersection to ensure effective load transfer between the two structural members.

The beam and column members were manufactured from three-layer oak timber. Each timber layer had a thickness of 32 mm, resulting in an overall cross-section of 190 × 48 mm. The lengths of both the beam and the column were 1180 mm. The average moisture content of the

timber during the experimental tests was approximately 10%. The overall geometry and dimensions of the L-shaped connection are shown in Figure 2. A symmetric configuration was adopted to facilitate the development of the numerical model presented in the following sections.

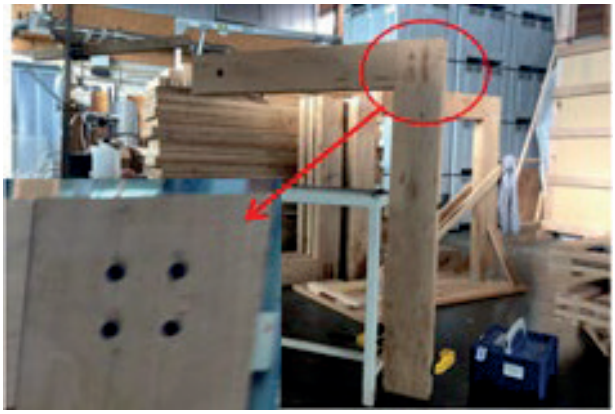


Figure 1. L-shaped timber connection specimen and dowel arrangement details

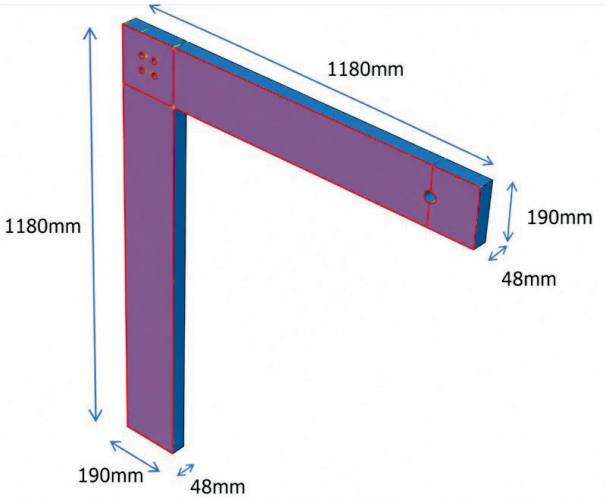


Figure 2. Geometry and dimensions of the L-shaped timber connection

2.2 Experimental and loading procedure

The experimental setup is illustrated in Figure 3. The connection specimen was installed in a testing frame with the column base fixed, while the load was applied at the free end of the beam to generate a bending moment in the connection region. The applied load correspond-ed to a concentrated mass of 51 kg (~ 510 N).

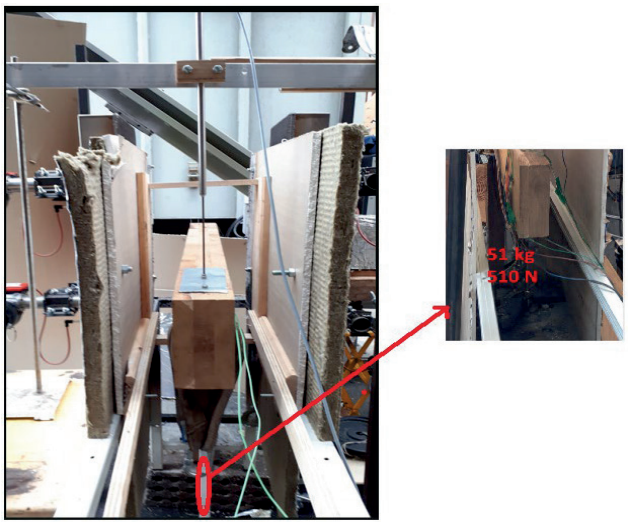


Figure 3. Experimental setup of the L-shaped timber connection under mechanical loading

3. FINITE ELEMENT MODEL

3.1. Numerical model configuration

A three-dimensional finite element model of the L-shaped timber connection was developed using Abaqus software [17] to simulate the mechanical behavior of connection systems using densified wood dowels and steel dowels under ambient mechanical loading conditions. The model was constructed based on the experimental configuration presented in Section 2 in order to analyze the load-transfer mechanism and stress distribution within the connection region.

Due to the symmetric geometry and loading configuration, only half of the model was considered in the numerical simulation in order to reduce computational time and modelling cost while maintaining mesh continuity and structural consistency. The boundary conditions were defined to correspond to the experimental setup, in which the column base was fully fixed and the load was applied vertically at the free end of the beam.

The finite element model and corresponding boundary conditions are illustrated in Figure 4; and details of the finite element mesh in the L-shaped connection are shown in Figure 5.

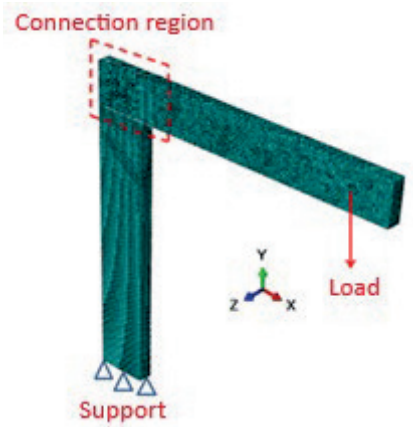


Figure 4. Finite element model of the L-shaped timber connection in Abaqus

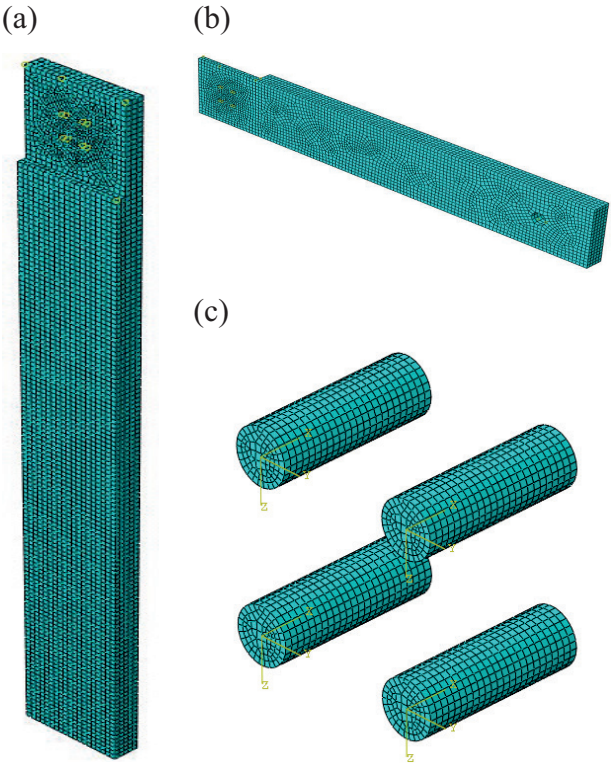


Figure 5. C3D8 finite element mesh in the L-shaped connection (a) Column; (b) Beam; (c) Dowels

The structural components in the model, including the beam, column, and dowels, were discretized using eight-node three-dimensional solid elements of type C3D8. Since this study focused only on the mechanical behavior under ambient conditions, coupled thermo-mechanical elements were not considered. The mesh was locally refined in the dowel region to improve the accuracy of stress distribution and load-transfer analysis within the connection area.

3.2. Material modelling

In this study, the oak timber used for the beam and column members was modelled as an orthotropic elastic material. The mechanical properties of the timber were determined based on average values obtained from experimental measurements and previous studies. The material properties of oak timber at ambient temperature are summarized in Table 1; while the material properties of the densified spruce dowels are presented in Table 2, was modelled using an orthotropic elastic formulation.

Table 1. Mechanical properties of oak wood at 20°C [16]

Property	Symbol	Value (MPa)
Longitudinal modulus	E_1 (E_L)	11380
Radial modulus	E_2 (E_R)	370
Tangential modulus	E_3 (E_T)	370
Poisson's ratio	ν_{12}	0.41
Poisson's ratio	ν_{13}	0.41
Poisson's ratio	ν_{23}	0.3
Shear modulus	G_{12}	690
Shear modulus	G_{13}	690
Shear modulus	G_{23}	50

Table 2. Mechanical properties of densified spruce wood at 20°C[16]

Property	Symbol	Value (MPa)
Longitudinal modulus	E_1 (E_L)	25500
Radial modulus	E_2 (E_R)	2050
Tangential modulus	E_3 (E_T)	2050
Poisson's ratio	ν_{12}	0.408
Poisson's ratio	ν_{13}	0.408
Poisson's ratio	ν_{23}	0.03
Shear modulus	G_{12}	1890
Shear modulus	G_{13}	1890
Shear modulus	G_{23}	137

Note: L, R, and T denote the longitudinal (grain), radial, and tangential directions of wood, respectively.

For the connections using steel dowels, the steel material was modelled as an isotropic elastic material with a Young's modulus of 210,000 MPa and a Poisson's ratio of 0.3 according to Eurocode 3 [18].

3.3. Contact Interaction

The contact interaction between the dowels and the timber members was defined using a surface-to-surface contact formulation. In the normal direction, a "hard contact" condition was adopted to prevent penetration between the interacting surfaces during loading.

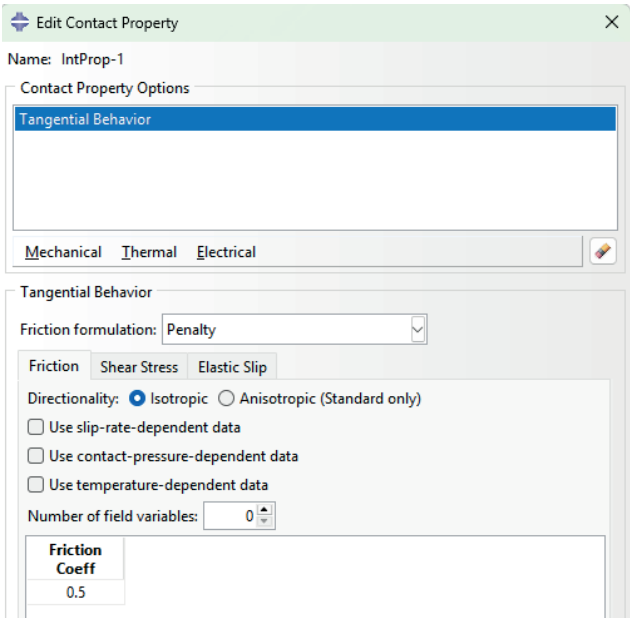


Figure 6. Friction contact definition between interacting surfaces in Abaqus

In the tangential direction, a Coulomb friction model was employed with a friction coefficient of $\mu = 0.5$ for both the densified wood dowels and the steel dowels. This value was selected to represent the frictional load-transfer capacity between the dowels and the timber layers within the connection region. The friction contact definition implemented in Abaqus is illustrated in Figure 6.

4. RESULTS AND DISCUSSION

4.1. Load–displacement response and model validation

The load–displacement relationships of the L-shaped timber connections using densified wood dowels and steel dowels obtained from the experimental tests and numerical simulations are presented in Figure 7. The results indicate that the finite element model is capable of reasonably reproducing the global mechanical behavior of the connection system under ambient mechanical loading conditions.

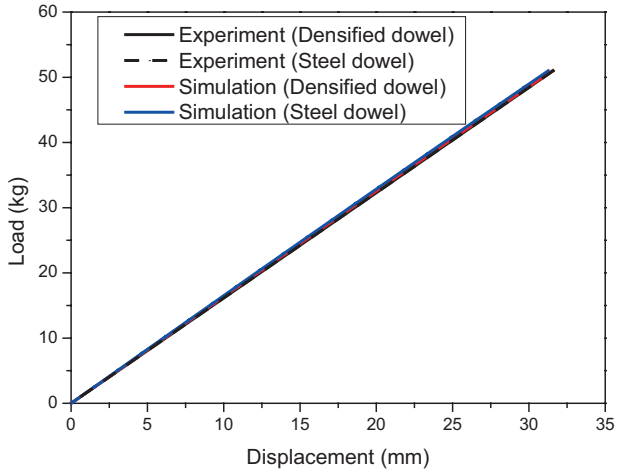


Figure 7. Comparison between experimental and numerical load–displacement responses of the L-shaped timber connections using densified wood dowels and steel dowels

It can be observed that the numerical load–displacement curves are in good agreement with the experimental results throughout the investigated loading range. Both connection configurations exhibit an approximately linear response, indicating that the connections mainly operate within the elastic regime under the applied loading conditions.

For the connection using densified wood dowels, the numerical model predicts the global stiffness and displacement evolution with satisfactory agreement compared with the experimental response. The discrepancy between the experimental and numerical curves remains relatively small over the entire loading

range, suggesting that the developed finite element model can adequately represent the load-transfer mechanism between the densified wood dowels and the timber layers within the connection region.

Similarly, for the connection using steel dowels, the finite element simulation also shows good agreement with the experimental results. The numerical response tends to exhibit a slightly higher stiffness at higher loading levels; however, the overall deviation remains limited.

In addition, the results show that the two connection systems exhibit relatively similar global stiffness within the investigated loading range. This indicates that densified wood dowels can provide an effective load-transfer mechanism in L-shaped timber connections under ambient mechanical loading conditions. Nevertheless, although the global load–displacement responses of the two configurations are relatively similar, the differences in stress distribution and load-transfer mechanisms within the connection region will be dis-cussed in the following sections.

4.2. Stress distribution in beam and column members

The longitudinal stress distribution (S11) within the beam–column connection region for the two connection configurations using densified wood dowels and steel dowels is presented in Figure 8. Figure 8a corresponds to the connection using densified wood dowels, while Figure 8b illustrates the connection using steel dowels.

The numerical results show that the stress is mainly concentrated in the vicinity of the beam–column intersection, particularly around the dowel region. This indicates that the externally applied load at the free end of the beam is primarily transferred to the column through the contact interaction and load-transfer mechanism between the dowels and the timber layers within the connection region.

For the connection using densified wood dowels (Figure 8a), the stress distribution tends to be more localized around the dowel region. Localized tensile and compressive stress zones can be observed near the contact interfaces between the dowels and the timber members, suggesting that the load transfer mainly occurs in the immediate vicinity of the dowels. In addition, the stress magnitude along the beam decreases relatively rapidly with increasing distance from the connection region, reflecting the comparatively more compliant behavior of the connection system using densified wood dowels.

In contrast, for the connection using steel dowels (Figure 8b), the stress field in both the beam and the column appears to be distributed more uniformly along the connection region. Tensile and compressive stresses are transferred over a broader area of the structural members, particularly near the beam–column interface. This suggests that the steel dowels pro-vide a stiffer and more efficient load-transfer mechanism compared with the densified wood dowels.

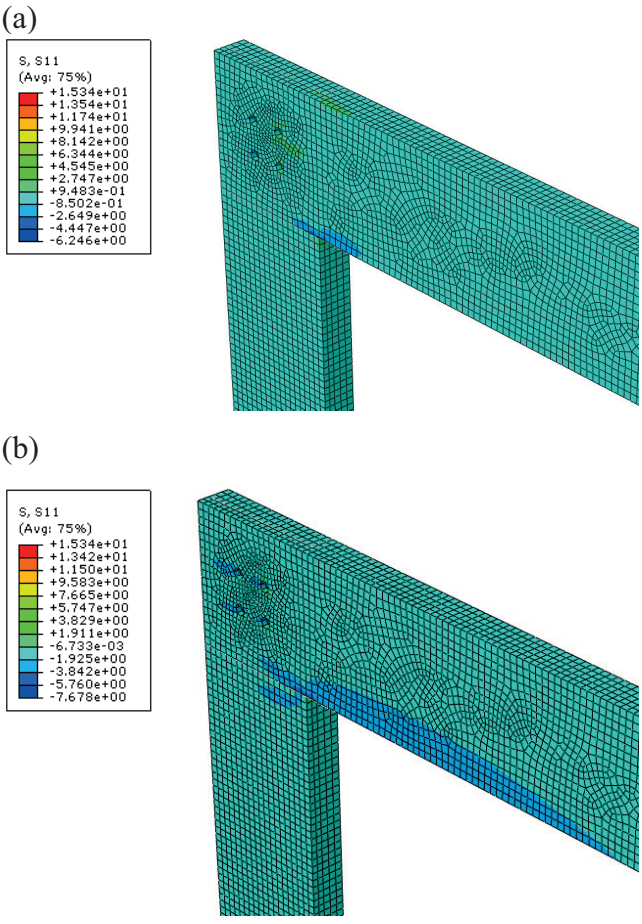


Figure 8. Longitudinal stress distribution (S11) in the beam–column connection region: (a) densified wood dowels; (b) steel dowels

Moreover, a larger compressive stress zone can be observed at the lower surface of the beam near the connection region in the case of steel dowels. This behavior indicates a more effective transfer of bending moment and shear force within the connection system, resulting in an increase in the local stiffness of the joint region.

Although the two connection configurations exhibit relatively similar global load–displacement responses, as discussed in Section 4.1, the stress distribution results reveal significantly different internal load-transfer mechanisms. The connection using densified wood dowels exhibits a more compliant behavior with localized stress concentrations around the dowel region, whereas the connection using steel dowels generates a broader and more uniformly distributed stress field within the connection region.

In contrast, the steel dowels (Figure 9b) exhibit a more uniformly distributed stress field over the entire dowel surface. The stress concentrations are less localized compared with the densified wood dowels, indicating a stiffer interaction between the steel dowels and the timber members. Due to the significantly higher stiffness of steel, the load is transferred more directly through the dowels, leading to a more efficient stress redistribution within the connection region.

In addition, the stress magnitude observed in the steel dowels is generally higher and more continuous along the dowel length, reflecting the stronger confinement and load-transfer capacity of the steel connection system. Meanwhile, the densified wood dowels exhibit a more gradual stress transition, which may contribute to reducing local stress peaks within the timber members.

These results further confirm that, although the two connection systems exhibit relatively similar global stiffness under the investigated loading conditions, the internal load-transfer mechanisms are substantially different. The densified wood dowels tend to provide a more compliant and localized interaction with the surrounding timber, whereas the steel dowels create a stiffer and more uniformly distributed load-transfer mechanism within the joint region.

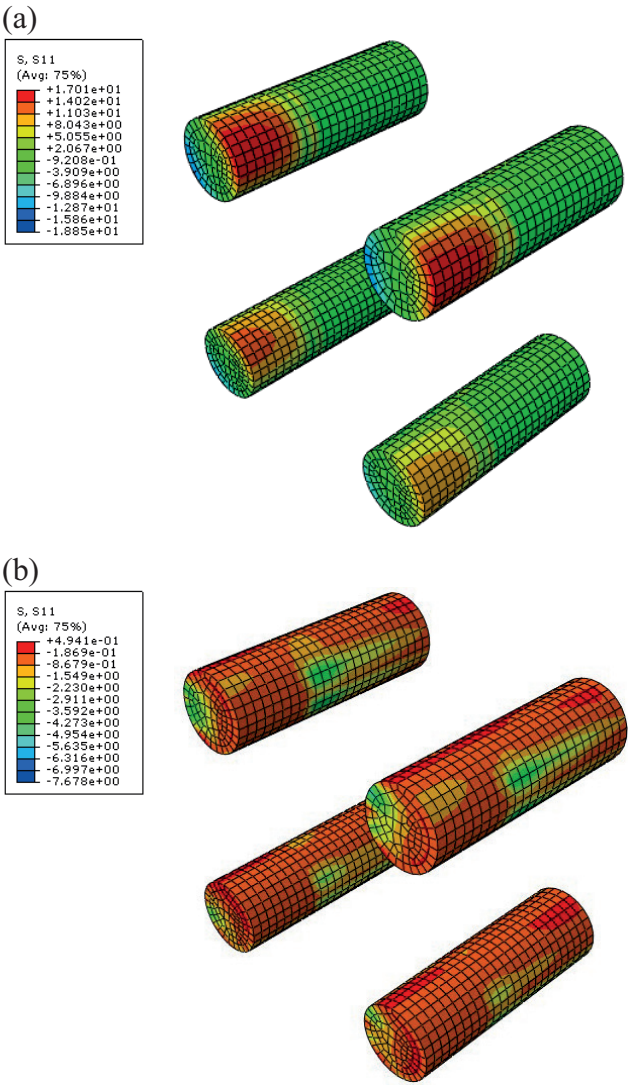


Figure 9. Longitudinal stress distribution (S11) in the beam–column connection region: (a) densified wood dowels; (b) steel dowels

4.3. Discussion

The numerical and experimental results show that although the two connection configurations using densified wood dowels and steel dowels exhibit relatively similar global load–displacement responses within the investigated loading range, their internal load-transfer mechanisms are significantly different.

For the connections using steel dowels, the high stiffness of the steel material results in a more

direct and efficient transfer of load between the beam and the column. This behavior is reflected by the relatively uniform stress distribution observed within both the connection region and the steel dowels. The stress field is distributed over a broader area along the beam–column interface, indicating that the steel dowels provide a more effective redistribution of internal forces and generate a higher local stiffness within the joint region. In contrast, the connections using densified wood dowels tend to exhibit a more compliant load-transfer mechanism due to the material compatibility between the dowels and the sur-rounding timber layers. The stress distribution results show more localized stress concentrations around the dowel region, while the stress magnitude along the beam decreases more rapidly with increasing distance from the connection area. This behavior indicates that the load is mainly transferred through the local contact interaction between the dowels and the adjacent timber layers, rather than being broadly redistributed throughout the entire connection region as observed in the case of steel dowels. Despite the comparatively more compliant behavior of the densified wood dowels, the load–displacement results demonstrate that the connection system is still capable of maintaining a global stiffness relatively close to that of the steel dowel connection within the investigated loading range. This suggests that densified wood dowels can provide an effective load-transfer mechanism for L-shaped timber connections under ambient mechanical loading conditions.

In addition, the differences observed in the load-transfer mechanisms of the two connection systems may also indicate different structural responses under elevated temperature or fire exposure. Connections using steel dowels may generate stronger localized heat-transfer zones due to the high thermal conductivity of steel, whereas densified wood dowels provide better material compatibility with the surrounding timber members. This difference may significantly influence temperature evolution, heat-field distribution, and the thermo-mechanical behavior of the connection region under fire conditions.

Therefore, the results obtained in this study provide an important mechanical basis for future investigations on the thermo-mechanical behavior of timber connections using densified wood dowels and steel dowels under elevated temperature and fire conditions.

5. CONCLUSION

This study presented an experimental and numerical investigation of L-shaped timber connections using densified wood dowels and steel dowels under ambient mechanical loading conditions. A three-dimensional finite element model was developed in Abaqus to simulate the load–displacement response and stress distribution within the connection region. Based on the obtained results, the following conclusions can be drawn:

1. The developed finite element model was capable of reasonably reproducing the global mechanical behavior of the L-shaped timber connections. The numerical load–displacement responses showed good agreement with the experimental results for both the densified wood dowel and steel dowel configurations.
2. Both connection systems exhibited an approximately linear response within the investigated loading range, indicating that the connections mainly operated within the elastic regime under the applied loading conditions.
3. The stress distribution results revealed significantly different load-transfer mechanisms for the two connection configurations, despite their relatively similar global stiffness. The connections using steel dowels generated a broader and more uniformly distributed stress field within the connection region, reflecting a more direct and efficient load-transfer mechanism.
4. For the connections using densified wood dowels, the stress tended to be more locally concentrated around the dowel region and decreased more rapidly with increasing distance

from the connection area. This behavior indicates a more compliant load-transfer mechanism due to the material compatibility between the densified wood dowels and the surrounding timber layers.

5. Although the load-transfer mechanism of the densified wood dowels was more com-pliant than that of the steel dowels, the results demonstrated that densified wood dowels were still capable of providing effective load transfer in L-shaped timber connections under ambient mechanical loading conditions.

6. The results obtained in this study provide an important mechanical basis for future investigations on the thermo-mechanical behavior of timber connections using densified wood dowels and steel dowels under elevated temperature and fire conditions.

REFERENCES

1. **M. Riggio, J. Sandak, and A. Sandak**, "Densified wooden nails for new timber assemblies and restoration works: A pilot research," Construction and Building Materials, vol. 102, pp. 1084–1092, 2016. https://doi.org/10.1016/j.conbuildmat.2015.06.045
2. **B. Anshari, Z. Guan, A. Kitamori, K. Jung, I. Hassel, and K. Komatsu**, "Mechanical and moisture-dependent swelling properties of compressed Japanese cedar," Construction and Building Materials, vol. 25, no. 4, pp. 1718–1725, 2011.
3. **K. Jung, A. Kitamori, and K. Komatsu**, "Evaluation on structural performance of compressed wood as shear dowel," Holzforschung, vol. 62, pp. 461–467, 2008.
4. **K. Jung, A. Kitamori, and K. Komatsu**, "Development of a joint system using a compressed wooden fastener I: Evaluation of pull-out and rotation performance for a column-sill joint," Journal of Wood Science, vol. 55, pp. 273–282, 2009.
5. **K. Jung, A. Kitamori, and K. Komatsu**, "Development of a joint system using a compressed wooden fastener II: Evaluation of rotation performance for a column-beam joint," Journal of Wood Science, vol. 56, pp. 118–126, 2010. https://doi.org/10.1007/s10086-009-1078-5
6. **K. Jung, S. Murakami, A. Kitamori, W.-S. Chang, and K. Komatsu**, "Improvement of glued-in-rod joint system using compressed wooden dowel," Holzforschung, vol. 64, pp. 799–804, 2010. https://doi.org/10.1515/HF.2010.117
7. **C. O'Loinsigh, M. Oudjene, H. Ait-Aider, P. Fanning, A. Pizzi, E. Shotton, and E.-M. Meghlat**, "Experimental study of timber-to-timber composite beam using welded-through wood dowels," Construction and Building Materials, vol. 36, pp. 245–250, 2012. https://doi.org/10.1016/j.conbuildmat.2012.04.118
8. **B.H. Xu, M. Taazount, A. Bouchaïr, and P. Racher**, "Numerical 3D finite element modelling and experimental tests for dowel-type timber joints," Construction and Building Materials, vol. 23, no. 9, pp. 3043–3052, 2009. https://doi.org/10.1016/j.conbuildmat.2009.04.006
9. **A.O. Feio, P.B. Lourenço, and J.S. Machado**, "Testing and modeling of a traditional timber mortise and tenon joint," Materials and Structures, vol. 47, pp. 213–225, 2014. https://doi.org/10.1617/s11527-013-0056-y
10. **A. Arciszewska-Kędzior, J. Kunecký, H. Hasníková, and V. Sebera**, "Lapped scarf joint with inclined faces and wooden dowels: Experimental and numerical analysis," Engineering Structures, vol. 94, pp. 1–8, 2015.
11. **T.T. Tran and N.T. Dao**, "Development of a hybrid elasto–plastic-damage material model for the analysis of adhesive-free lapped scarf timber joints," Mechanics Based Design of Structures and Machines, 2026.

https://doi.org/10.1080/15397734.2026.2632701

12. **T.T. Tran, Q.B. Vu, T.-H. Tran, H.-N. Hoang, and T.-H. Nguyen**, "Abaqus-based numerical modeling of a two-layer timber beam under fully composite and fully non-composite conditions," Advances in Science and Technology Research Journal, vol. 20, no. 6, pp. 314–324, 2026. https://doi.org/10.12913/22998624/218005
13. **T.T. Tran, V.-D. Thi, M. Oudjene, M. Khelifa, P. Girods, M. Debal, Y. Rogaume, and Y. Jannot**, "Fire structural performance of thermo-mechanically compressed spruce timber by means experiments and a three-step multi-reactions pyrolysis 3D-finite element modelling," Construction and Building Materials, vol. 320, p. 126100, 2022.
14. **M. Khelifa, T. T. Tran, A. Khennane, M. Oudjene, and Y. Rogaume**, "Thermal response of timber connections using densified wood dowels under fire," Journal of Fire Sciences, vol. 42, no. 6, pp. 534–550, 2024. https://doi.org/10.1177/07349041241257262
15. **T.T. Tran, M. Khelifa, M. Oudjene, M. Debal, and Y. Rogaume**, "An experimental investigation of the thermomechanical performance of wood structures assembled with densified wooden dowels under fire exposure," International Journal for Computational Civil and Structural Engineering, vol. 21, no. 4, pp. 73–82, 2025. https://doi.org/10.22337/2587-9618-2025-21-4-73-82
16. **T.T. Tran**, Modeling of Fire Performance of Timber Structures Assembled by Densified Wooden Dowels. PhD Thesis, University of Lorraine, France, 2021
17. Dassault Systèmes Simulia Corp., Abaqus Analysis User's Guide, Version 2023
18. Eurocode 3, Design of Steel Structures – Part 1-2: Structural Fire Design, European Committee for Standardization (CEN), Brussels, Belgium, 1993.

СПИСОК ЛИТЕРАТУРЫ

1. **M. Riggio, J. Sandak, and A. Sandak**, "Densified wooden nails for new timber assemblies and restoration works: A pilot research," Construction and Building Materials, vol. 102, pp. 1084–1092, 2016. https://doi.org/10.1016/j.conbuildmat.2015.06.045
2. **B. Anshari, Z. Guan, A. Kitamori, K. Jung, I. Hassel, and K. Komatsu**, "Mechanical and moisture-dependent swelling properties of compressed Japanese cedar," Construction and Building Materials, vol. 25, no. 4, pp. 1718–1725, 2011.
3. **K. Jung, A. Kitamori, and K. Komatsu**, "Evaluation on structural performance of compressed wood as shear dowel," Holzforschung, vol. 62, pp. 461–467, 2008.
4. **K. Jung, A. Kitamori, and K. Komatsu**, "Development of a joint system using a compressed wooden fastener I: Evaluation of pull-out and rotation performance for a column-sill joint," Journal of Wood Science, vol. 55, pp. 273–282, 2009.
5. **K. Jung, A. Kitamori, and K. Komatsu**, "Development of a joint system using a compressed wooden fastener II: Evaluation of rotation performance for a column-beam joint," Journal of Wood Science, vol. 56, pp. 118–126, 2010. https://doi.org/10.1007/s10086-009-1078-5
6. **K. Jung, S. Murakami, A. Kitamori, W.-S. Chang, and K. Komatsu**, "Improvement of glued-in-rod joint system using compressed wooden dowel," Holzforschung, vol. 64, pp. 799–804, 2010. https://doi.org/10.1515/HF.2010.117
7. **C. O'Loinsigh, M. Oudjene, H. Ait-Aider, P. Fanning, A. Pizzi, E. Shotton, and E.-M. Meghlat**, "Experimental study of timber-to-timber composite beam using welded-through wood dowels," Construction and Building Materials, vol. 36, pp. 245–250, 2012.

https://doi.org/10.1016/j.conbuildmat.2012.04.118

8. **B.H. Xu, M. Taazount, A. Bouchaïr, and P. Racher**, "Numerical 3D finite element modelling and experimental tests for dowel-type timber joints," Construction and Building Materials, vol. 23, no. 9, pp. 3043–3052, 2009. https://doi.org/10.1016/j.conbuildmat.2009.04.006
9. **A.O. Feio, P.B. Lourenço, and J.S. Machado**, "Testing and modeling of a traditional timber mortise and tenon joint," Materials and Structures, vol. 47, pp. 213–225, 2014. https://doi.org/10.1617/s11527-013-0056-y
10. **A. Arciszewska-Kędzior, J. Kunecký, H. Hasníková, and V. Sebera**, "Lapped scarf joint with inclined faces and wooden dowels: Experimental and numerical analysis," Engineering Structures, vol. 94, pp. 1–8, 2015.
11. **T.T. Tran and N.T. Dao**, "Development of a hybrid elasto–plastic-damage material model for the analysis of adhesive-free lapped scarf timber joints," Mechanics Based Design of Structures and Machines, 2026. https://doi.org/10.1080/15397734.2026.2632701
12. **T.T. Tran, Q.B. Vu, T.-H. Tran, H.-N. Hoang, and T.-H. Nguyen**, "Abaqus-based numerical modeling of a two-layer timber beam under fully composite and fully non-composite conditions," Advances in Science and Technology Research Journal, vol. 20, no. 6, pp. 314–324, 2026. https://doi.org/10.12913/22998624/218005
13. **T. T. Tran, V.-D. Thi, M. Oudjene, M. Khelifa, P. Girods, M. Debal, Y. Rogaume, and Y. Jannot**, "Fire structural performance of thermo-mechanically compressed spruce timber by means experiments and a three-step multi-reactions pyrolysis 3D-finite element modelling," Construction and Building Materials, vol. 320, p. 126100, 2022.
14. **M. Khelifa, T.T. Tran, A. Khennane, M. Oudjene, and Y. Rogaume**, "Thermal response of timber connections using densified wood dowels under fire," Journal of Fire Sciences, vol. 42, no. 6, pp. 534–550, 2024. https://doi.org/10.1177/07349041241257262
15. **T.T. Tran, M. Khelifa, M. Oudjene, M. Debal, and Y. Rogaume**, "An experimental investigation of the thermomechanical performance of wood structures assembled with densified wooden dowels under fire exposure," International Journal for Computational Civil and Structural Engineering, vol. 21, no. 4, pp. 73–82, 2025. https://doi.org/10.22337/2587-9618-2025-21-4-73-82
16. **T.T. Tran**, Modeling of Fire Performance of Timber Structures Assembled by Densified Wooden Dowels. PhD Thesis, University of Lorraine, France, 2021
17. Dassault Systèmes Simulia Corp., Abaqus Analysis User's Guide, Version 2023
18. Eurocode 3, Design of Steel Structures – Part 1-2: Structural Fire Design, European Committee for Standardization (CEN), Brussels, Belgium, 1993

Tran Trong Tuan – Associate Professor, Faculty of Civil Engineering, Hanoi Architectural University; Km 10, Nguyen Tra street, Thanh Xuan district, Hanoi city, Vietnam. e-mail: tuantt@hau.edu.vn

Чан Чонг Туан – доцент факультета строительства Ханойского архитектурного университета (Hanoi Architectural University); Km 10, улица Нгуен Чай, район Тхань Суан, г. Ханой, Вьетнам. e-mail: tuantt@hau.edu.vn

Nguyen Ngoc Thang – Associate Professor, aculty of Civil Engineering, Thuyloi University; 175 Tay Son street, Kim Lien, Hanoi city, Vietnam. e-mail: thangnn@tlu.edu.vn

Нгуен Нгок Тханг – доцент факультета гражданского строительства Университета Тхюйлой (Thuyloi University); 175 улица Тай Сон, район Ким Льен, г. Ханой, Вьетнам. e-mail: thangnn@tlu.edu.vn

DOI:10.22337/2587-9618-2026-22-3-35-44

EXPERIMENTAL AND NUMERICAL STUDY OF THE "BISON" POWER DECK USED AS A PERMANENT FORMWORK

Sergey M. Anpilov [1], Denis A. Panfilov [2], Alexander S. Bychkov [2]
[1] Novosibirsk State University of Architecture and Civil Engineering, Novosibirsk, RUSSIA
[2] Samara State Technical University, Samara, RUSSIA

Abstract: To conduct the research in this work, the BISON reinforcing deck was selected, this deck is used for the construction of steel-reinforced concrete floors as a permanent formwork. Its difference from the common types of deck used in the Russian Federation is the height of the profile and the configuration of the section, which reduces material consumption and affects its strength characteristics and, as a result, increases its bearing capacity and makes it possible to build longer spans without using intermediate supports.
Goal: Compare the data obtained during the experiment with the numerical model developed in the ANSYS finite element software, check the convergence and draw conclusions.
Materials and methods. The experimental model of the floor slab consisted of two sections a «BISON» 260-600-1.5., 1200 mm wide, connected longitudinally. The plate was tested according to a single-span scheme. The boundary conditions were set by one pivotally movable support and one fixed one. The numerical model in the ANSYS repeated the experimental scheme, the steel data was set taking into account physical nonlinearity, and the load was set using the step method.
Results. As a result of the experiment, data on the actual control vertical deflection of the profiled deck at a load of 995.83 kg/m2 and its maximum load-bearing capacity were obtained. The mechanical characteristics of steel have also been studied, and a yield strength of 308 Mpa has been established. A model was developed in the ANSYS, and the calculation was carried out taking into account the experimental data obtained.
Conclusions. The analysis of the experiment with the numerical model shows the convergence of the results. The stresses in the FE model exceeded the yield strength of the steel under extreme loads. The nature of the crumpling of the shelves in the FE model partially coincides with the nature of the crumpling in the experiment.

Keywords: FE model, ANSYS, profiled steel deck, non-removable formwork, reinforced concrete, composite plate, boundary conditions, non-linearity of steel, vertical deflection

ЭКСПЕРИМЕНТАЛЬНОЕ И ЧИСЛЕННОЕ ИССЛЕДОВАНИЕ СИЛОВОГО НАСТИЛА «БИЗОН», ИСПОЛЬЗУЕМОГО В КАЧЕСТВЕ НЕСЪЕМНОЙ ОПАЛУБКИ

С.М. Анпилов [1], Д.А. Панфилов [2], А.С. Бычков [2]
[1] Новосибирский государственный архитектурно-строительный университет, г. Новосибирск, РОССИЯ
[2] Самарский государственный технический университет, г. Самара, РОССИЯ

Аннотация: Для проведения исследования в этой работе был выбран настил армирующий «БИЗОН», данный настил используется для возведения сталежелезобетонных перекрытий в качестве несъемной опалубки. Его отличие от распространенных типов настила, используемых на территории РФ, является высота профиля и конфигурация сечения, снижающие материалоемкость и влияющие на его прочностные характеристики и как следствие повышающие его несущую способность и дающие возможность возводить более длинные пролеты без использования промежуточных опор.
Цель: сравнить данные, полученные в ходе эксперимента с численной моделью, разработанной в ПК ANSYS, проверить сходимость и сделать выводы.
Материалы и методы: Экспериментальная модель плиты перекрытия состояла из двух секций НС «БИЗОН» 260-600-1,5., шириной 1200 мм, соединенных в продольном направлении. Испытание плиты проводились по однопролетной схеме. Граничные условия были заданы одной шарнирно подвижной опорой и одной неподвижной. Численная модель в ПК ANSYS повторяла схему эксперимента, данные стали задавались с учетом физической нелинейности, нагрузка задавалась шаговым методом.

Результаты. В результате эксперимента получены данные фактического контрольного вертикального прогиба профилированного настила при нагрузке 995,83 кг/м2, его предельную несущую способность. Также проведены исследования механических характеристик стали, установлен предел текучести, равный 308 Мпа.
Разработана модель в ПК ANSYS, проведен расчет с учетом полученных данных в эксперименте.
Выводы: Анализ проведенного эксперимента с численной моделью показывают сходимость результатов. Напряжения в КЭ модели, при предельных нагрузках превысили предел текучести стали. Характер смятия полок в КЭ модели частично совпадает с характером смятия в эксперименте.

Ключевые слова: Конечно-элементарная модель, ANSYS, стальной профилированный настил, несъемная опалубка, сталежелезобетон, композитная плита, граничные условия, нелинейность стали, вертикальный прогиб

1. INTRODUCTION

To conduct the research in this work, the «BISON» reinforcing deck was selected, this deck is used for the construction of steel-reinforced concrete floors as a permanent formwork. Its difference from the common types of deck used in the Russian Federation is the height of the profile and the configuration of the section, which reduces material consumption and affects its strength characteristics and, as a result, increases its bearing capacity and makes it possible to build longer spans without using intermediate supports.

In this paper, the methods of testing are described, and the layout of the sample stand is shown. Data on the deflection of the deck and its maximum bearing capacity were obtained, and a finite element model of the floor was developed on their basis.

The stages of creating a model in the ANSYS finite element software are described, the nonlinear operation of galvanized steel used for the manufacture of the «BISON» FEA is taken into account, the methods of dividing the grid into finite elements are shown, the creation of contact between the overlap surfaces of the deck is shown, as well as the method of applying the load to obtain the most accurate calculation data.

The purpose of this article is to analyze the data obtained during field tests and compare them with the numerical model developed in the ANSYS, check the convergence and draw conclusions.

The investigated profile: Power deck PD “BISON” 260-600-1,5 according to TU - 1120-004-316631300162970-2019 [1] manufactured by Sole Proprietor Anpilov S.M. (Figure 1)

2. EXPERIMENTAL MODEL AND TEST SETUP

For testing, the profile PD "BISON" 260-600-1.5 made of S350 steel was used, with the following characteristics given in Table 1.

The experimental model of permanent formwork for a monolithic floor slab (Figure 2) consisted of two sections of PD "BISON" 260-600-1.5., 1200 mm wide, connected longitudinally by self-tapping screws. The plate is attached to a steel distribution plate in the support part with M16 bolts mounted in the center of the lower corrugations.

The non-removable formwork for the monolithic floor slab was tested according to a single-span scheme. The boundary conditions were set by one pivotally movable support and one fixed one (Figure 3).

Loading was carried out by evenly distributed load in stages in steps of no more than 10% of the design maximum permissible load.[2] Semi-dry vibro-pressing concrete slabs were used as an evenly distributed load. Loading was performed from the supports to the middle of the span, symmetrically relative to the middle of the span (Figure 4).

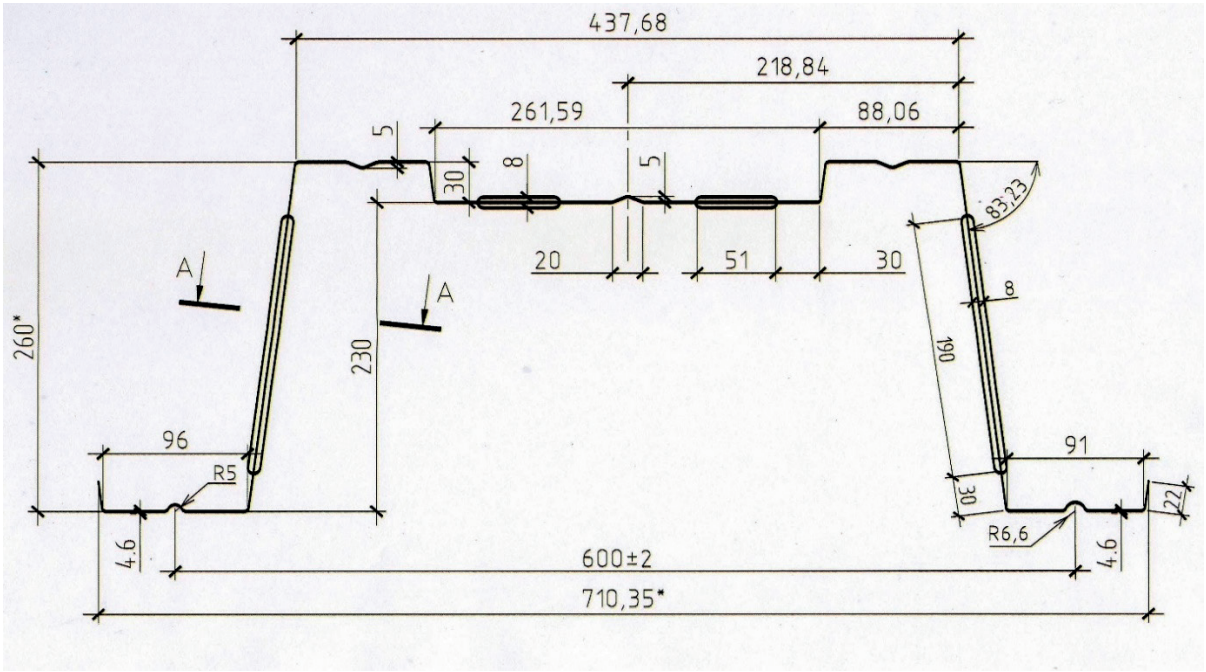


Figure 1. Geometric dimensions of the PD "BISON" 260-600-1.5

Table 1. Characteristics of PD "BISON" 260-600-1,5

Designation of the milled sheet	t, mm	Cross-sectional area of one corrugation F, cm2	Weight of 1 m length of 1 fr, kg	Reference values per 1 m width			Weight of 1 m^2, kg	Width of the workpiece, mm
				Moment of inertia of one corrugation, I_x, cm^4	Moment of resistance, cm^3			
					W_{x1}	W_{x2}		
PD "BISON" 260-600-1,5	1,5	18,75	14,59	1539,76	66,53	100,61	21,32	1250

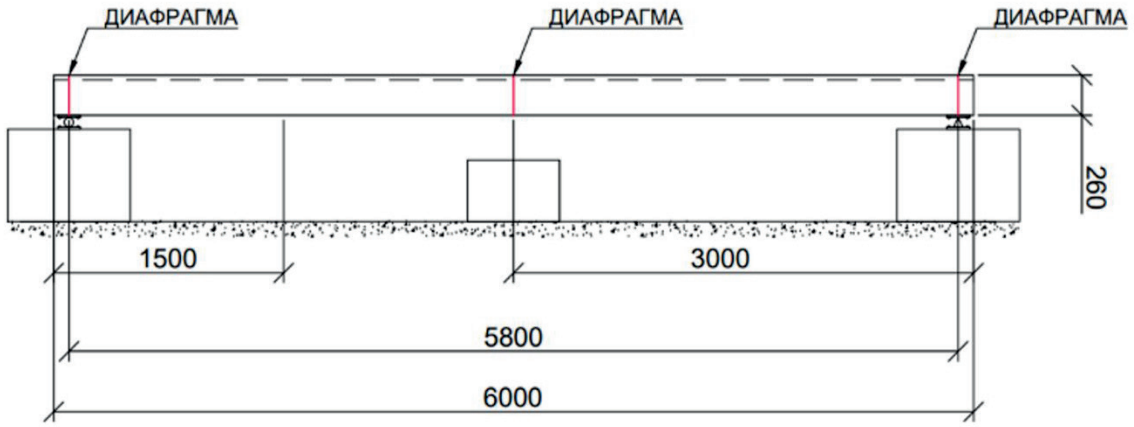


Figure 2. Test bench



Figure 3. Geometric dimensions of the test stand



Figure 4. Loading of non-removable formwork

3. EXPERIMENTAL RESULTS

The actual vertical reference deflection f_{exp} = 29.35 mm (close to the maximum deflection according to SP 20.13330) was achieved at the maximum permissible load q = 995.83 kg/m^2
When loading from 685 to 730.67 kg/m^2, there was a loss of local stability of the lowered part of the upper (wide) profile shelf (Figure 5).

When studying the mechanical characteristics of the steel of the selected samples, it was found that the yield strength of the steel is 308 Mpa.
When loading 1224.17 kg/m^2, the stresses in the cross-section shelves in the middle of the span reached the values of the yield strength of the steel, the shelves crumpled and warped, which led to a loss of bearing capacity.[3], [5]



Figure 5. Crumpling of the upper deck shelves

4. FE MODEL

A deck model in the ANSYS software package was developed for analysis and comparison with field tests.[3], [6]
The model was developed and boundary conditions were set as follows:

It was decided to dissect the scheme used in the experiment along the middle of the central corrugation, since the deck has the same geometry and loads along the line of symmetry. The deck and diaphragms were modeled as a shell with thickness parameters, and the support plates were modeled as three-dimensional elements. The overlap contacts of the decking on the central corrugation, the diaphragms on the edges and in the middle of the span, as well as the support plates were modeled as rigid joints between surfaces (bonded in ANSYS).
Boundary conditions.
The loads on the deck were applied exactly with the layout of the tiles in the experiment, the upper shelves of the deck were divided into sections of tile-deck contact and a load was applied to them (Fig.6.) equal to half of the maximum obtained during the experiment, since the model is made as half of the original permanent formwork for a monolithic floor slab.
The supports were modeled by limiting the movement of the node line on the support plates. A fixed pivot support was simulated on one part, where movement along all axes was blocked, and rotation along the X axis was prohibited and Y and Z were free. On the opposite part of the deck, a pivotally movable support was simulated, where movement along the X axis was free, and rotation along the Y and Z axes was prohibited, rotation along the X axis was prohibited, and rotation along the Y and Z axes was free.

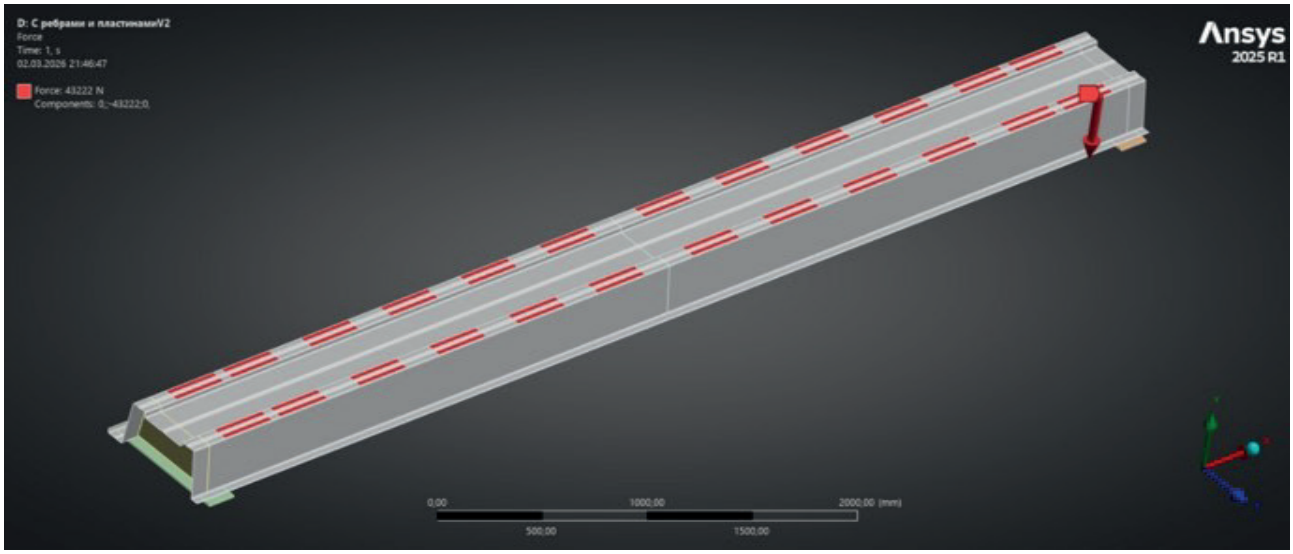


Figure 6. Load application scheme in the FE model

The introductory parameters of steel in ANSYS are modulus of elasticity = 2 * 10^5Mpa, yield strength of steel taken from experimental data = 308 MPa, Poisson's ratio = 0.3 and density = 7850 kg/m^3. To account for the nonlinearity of the material, a two-line deformation diagram was chosen.[7]

Finite element type

The SHELL281 element is used to model the steel sheet. This type of element is suitable for modeling a thin-walled steel profile, as it is subjected to large deformations. As a rule, a rectangular element is used, and where the geometry is complex, a triangular element is used (Figure 7) [2], [4], [11-15]. This decision was made based on the fact that the profile is not modeled in a simplified way, but exactly with natural dimensions, and some elements cannot be created using rectangular elements, as Kosarev, V. N. models in the LIRA-CAD FEA [8].

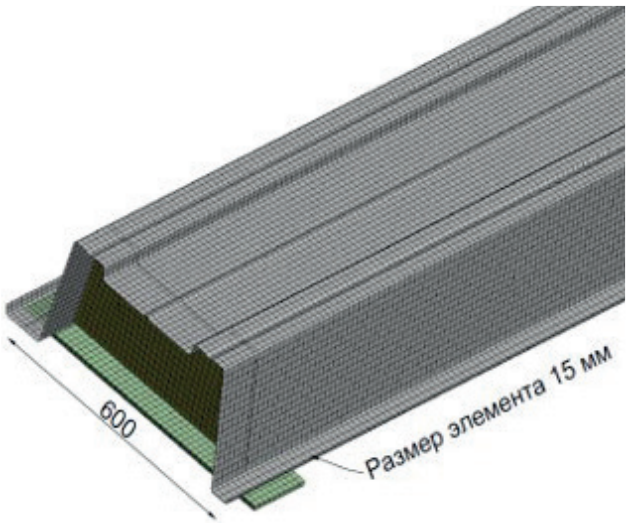


Figure 7. Finite Element mesh

5. FE RESULTS

The data obtained from the model calculation is shown below. The blue markers indicate the places where samples of data on displacements and stress values were taken in the same places as in the experiment. [2], [5], [9], [10], [16-20].

The deflection in the FE model, at a load of 1224.17 kg/m^2, was 38.337 mm in the lower shelf of the central corrugation. Figure 8 shows the deflection data.

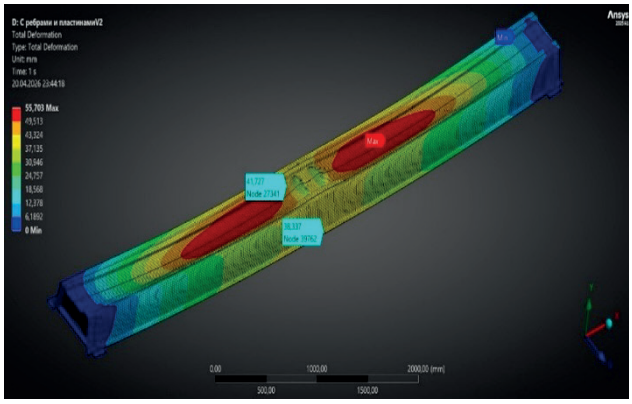


Figure 8. Deflection in the FE model

In the Figure 9, at a given load, the stresses in the lower part of the upper shelf exceeded the yield strength of the steel, and in the lower shelf they reached it.

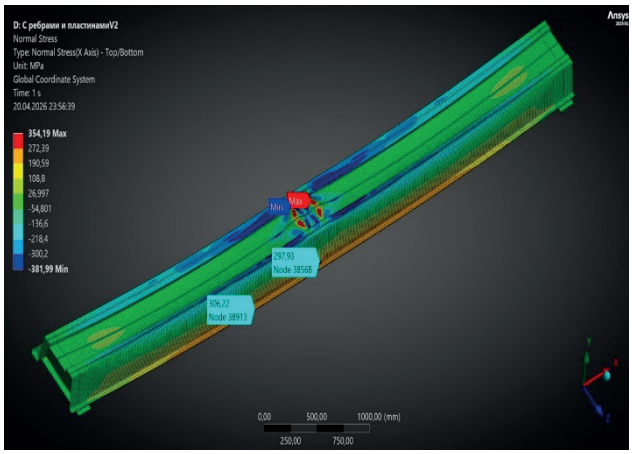


Figure 9. Normal stress in the FE model

CONCLUSIONS

The vertical deflection in the numerical model was 38.337 mm, in the central corrugation, where 2 deck sheets overlap, the discrepancy with experimental data in % terms was 2.62% (experimentally obtained deflection = 39.37 mm).

The stresses in the FE model in the upper shelf exceeded the yield strength of the steel obtained experimentally (308 MPa).

The nature of the crumpling of the shelves in the FE model partially coincides with the nature of

the crumpling in the experiment Figure 5, and Figure 9.

The results obtained during the analysis of the experiment and numerical modeling demonstrate the applicability of the numerical model to understand the operation of the deck, data on deflection and stresses in the numerical model can be used to analyze more massive structural solutions for large-span support schemes.

ACKNOWLEDGEMENTS

The authors gratefully acknowledge Prof. Anpilov S.M. for his valuable guidance and input during the development of the research underlying this study.

REFERENCES

1. TU - 1120-004-316631300162970-2019 Profili Stal'nye Listovye Gnutye S Trapecievidnymi Goframi Dlya Stalezhelezobetonnyh Konstrukcij (Nastily Silovye – Ns "Bison"). [Bent Steel Sheet Profiles With Trapezoidal Corrugated End For Steel-Reinforced Concrete Structures (Power decks – PD "BISON")] 27.08.2019
2. **Milad Soltanalipour, Miquel Ferrer, Frederic Marimon,** Experimental and numerical study of the ductility of open-rib and reentrant composite slabs, Engineering Structures, Volume 256, 2022, 113984, ISSN 0141-0296, DOI:10.1016/j.engstruct.2022.113984
3. **Soytu N.Y., Aleynikova M.A.,** Prochnost' i deformativnost' stalezhelezobetonnyh obrazcov plit perekrytij pri izgibe // Innovacii i investicii. 2024. №1. [Strength and deformability of steel-reinforced concrete samples of floor slabs during bending // Innovation and investment. 2024. №1.] URL: https://cyberleninka.ru/article/n/prochnost-i-deformativnost-stalezhelezobetonnyh-obraztsov-plit-perekrytiy-pri-izgibe
4. **Degtyarev Vitaliy**, "Finite element modeling of cold-formed steel deck in bending" Magazine of Civil Engineering, no. 2 (94), 2020, pp. 129-144. URL: http://elib.spbstu.ru/dl/2/j21-142.pdf
5. **Chaparanganda, E.** Design method for cast in-situ floor slabd with external profiled steel deck as reinforcement / E. Chaparanganda, D. Lazouski // , 27 октября 2023 года, 2024. – pp. 73-83. – EDN HCQRUF. URL: https://elibrary.ru/item.asp?id=67957947
6. **Bashlykov, D.A**. Issledovanie raboty stalezhelezobetonnogo perekrytiya po profilirovannomu nastilu s ispol'zovaniem programmnogo kompleksa ANSYS. [A study of the performance of a steel-reinforced concrete floor on profiled sheeting using the ANSYS software package] / D. A. Bashlykov // Tendencii razvitiya nauki i obrazovaniya. – 2025. – № 121-5. – pp. 43-46. – EDN CUTSEN. URL: https://elibrary.ru/item.asp?id=82496207
7. **Mirsayapov, I.T.,** Raschet stalezhelezobetonnoj balki na osnove dvuhlinejnoj diagrammy deformirovaniya. [Calculation of a steel-reinforced concrete beam based on a two-line deformation diagram] / Mirsayapov, I. T. // News of the Kazan State University of Architecture and Civil Engineering. – 2024. – No. 3(69). – P. 118-129. – DOI 10.48612/NewsKSUAE/69.11. – EDN IPUFWM
8. **Su-Shen Lim, Jing-Ying Wong, Chun-Chieh Yip, Jet-Wei Pang,** Flexural strength test on new profiled composite slab system, Case Studies in Construction Materials, Volume 15, 2021, e00638, ISSN 2214-5095, DOI:10.1016/j.cscm.2021.e00638
9. **Kosarev, V.N.** Monolitnoe zhelezobetonnoe rebristoe perekrytie s primeneniem profilirovannogo nastila «BISON». [Monolithic reinforced concrete ribbed floor using BISON profiled sheeting] / Kosarev, V. N. // Modern science: current problems, achievements and innovations: Collection of articles based on

the materials of the fourth All-Russian scientific and practical conference, Belebey, April 19, 2023. – Belebey: Samara State Technical University, 2023. – pp. 356-358. – EDN WKXWFA DOI:10.1016/j.cscm.2021.e00638

10. **Hedaoo, N.A., Raut, N., & Gupta, L.M**. (2015). Composite Concrete Slabs with Profiled Steel Decking: Comparison Between Experimental and Simulation Study. American Journal of Civil Engineering, 3(5), 157. DOI:10.11648/J.AJCE.20150305.14
11. **N.D. Korsun, D.A. Pro-stakishina**, Modelirovanie i uchet zon uprochneniia stalnykh tonkosten-nykh profilei v PK ANSYSю, [Modeling and accounting for hardening zones of thin-walled steel sections in ANSYS], Arkhi-tektura, stroitelstvo, transport, № 4 (98), DOI:10.31660/2782-232X-2021-4-44-51
12. **J. Reinoso, M. Paggi, A. Blázquez**, A nonlinear finite thickness cohesive interface element for modeling delamination in laminated composites, Composites Part B: Engineering, Volume 109, 2017, Pages 81-100, DOI:10.1016/j.compositesb.2016.10.042
13. **F.L. Bolina, M.K. El Debs,** Numerical study and proposal of new design equations for steel decking concrete slabs subjected to fire, Engineering Structures, Volume 260, 2022, 113828, DOI:10.1016/j.engstruct.2021.113828
14. **Y. Majdi, C.K. Tan, Y.C. Wang**, Finite element analysis of new composite floors having cold-formed steel and concrete slab, Engineering Structures, Volume 77, 2014, Pages 65-80, DOI:10.1016/j.engstruct.2014.07.030
15. **P.A. Langarudi, A. Eslami**, Numerical study of the behavior of bolted shear connectors in composite slabs with steel deck, Structures, Volume 27, 2020, Pages 1-13 (approx.), DOI:10.1016/j.istruc.2020.04.037
16. **A. Gholamhoseini, R. Gilbert, M. Bradford**, Experimental and finite element study of ultimate strength of continuous composite concrete slabs with steel decking, International Journal of Advanced Structural Engineering, Volume 10, 2018, Pages 85–97, DOI:10.1007/s40091-018-0183-3
17. **A. Bogdanić, D. Casucci, J. Ožbolt,** Numerical and experimental investigation of anchor channels subjected to shear load in composite slabs with profiled steel decking, Engineering Structures, Volume 240, 2021, 112347, DOI:10.1016/j.engstruct.2021.112347
18. **A. Karimipanah** et al., A numerical study on a novel demountable cold-formed steel composite beam with profiled steel sheeting, Thin-Walled Structures, Volume 200, 2024, 111812, DOI:10.1016/j.tws.2024.111812
19. **R. Rahnavard, S. Jordão,** Cold-formed steel lightweight concrete (CFS-LWC) composite beams: New design proposal, Structures, Volume 87, 2026, 111596, DOI:10.1016/j.istruc.2026.111596
20. **E.I. Celis-Imbajoa** et al., Experimental and analytical study at maximum load of composite slabs with and without conventional reinforcement applying the serial-parallel mixing theory and FEM, Engineering Structures, Volume 243, 2021, 112700, DOI:10.1016/j.engstruct.2021.112700

СПИСОК ЛИТЕРАТУРЫ

1. ТУ - 1120-004-316631300162970-2019 Профили стальные листовые гнутые с трапециевидными гофрами для сталежелезобетонных конструкций (Настилы силовые – НС "БИЗОН") 27 августа 2019 года
2. **Milad Soltanalipour, Miquel Ferrer, Frederic Marimon**, Experimental and numerical study of the ductility of open-rib and reentrant composite slabs, Engineering Structures, Volume 256, 2022, 113984, ISSN 0141-0296, Режим доступа: DOI:10.1016/j.engstruct.2022.113984
3. **Сойту Наталья Юрьевна, Алейникова Маргарита Анатольевна** Прочность и

деформативность сталежелезобетонных образцов плит перекрытий при изгибе // Инновации и инвестиции. 2024. №1. Режим доступа: https://cyberleninka.ru/article/n/prochnost-i-deformativnost-stalezhelezobetonnyh-obraztsov-plit-perekrytiy-pri-izgibe (дата обращения: 13.05.2026).

4. **В.В. Дегтярев**, Finite element modeling of cold-formed steel deck in bending // Санкт-Петербургский политехнический университет Петра Великого. – 2020. – № 2 (94). — С. 129-144. Режим доступа: http://elib.spbstu.ru/dl/2/j21-142.pdf (дата обращения: 13.05.2026).
5. **Chaparanganda, E.** Design method for cast in-situ floor slabd with external profiled steel deck as reinforcement / E. Chaparanganda, D. Lazouski // , 27 октября 2023 года, 2024. – P. 73-83. – EDN HCQRUF. Режим доступа: https://elibrary.ru/item.asp?id=67957947
6. **Башлыков, Д.А.** Исследование работы сталежелезобетонного перекрытия по профилированному настилу с использованием программного комплекса ANSYS / Д. А. Башлыков // Тенденции развития науки и образования. – 2025. – № 121-5. – С. 43-46. – EDN CUTSEN. Режим доступа: https://elibrary.ru/item.asp?id=82496207 (дата обращения: 13.05.2026)
7. **Мирсаяпов, И.Т.** Расчет сталежелезобетонной балки на основе двухлинейной диаграммы деформирования / И. Т. Мирсаяпов, И. М. Гиматдинов // Известия Казанского государственного архитектурно-строительного университета. – 2024. – № 3(69). – С. 118-129. – DOI 10.48612/NewsKSUAE/69.11. – EDN IPUFWM.
8. **Косарев, В.Н**. Монолитное железобетонное ребристое перекрытие с применением профилированного настила «БИЗОН» / В. Н. Косарев // Современная наука: актуальные проблемы, достижения и инновации : Сборник статей по материалам четвёртой Всероссийской научно-практической конференции, Белебей, 19 апреля 2023 года. – Белебей: Самарский государственный технический университет, 2023. – С. 356-358. – EDN WKXWFA.
9. **Su-Shen Lim, Jing-Ying Wong, Chun-Chieh Yip, Jet-Wei Pang**, Flexural strength test on new profiled composite slab system, Case Studies in Construction Materials, Volume 15, 2021, e00638, ISSN 2214-5095, Режим доступа: DOI:10.1016/j.cscm.2021.e00638 (дата обращения: 13.05.2026)
10. **Hedaoo, N.A., Raut, N., & Gupta, L.M.** (2015). Composite Concrete Slabs with Profiled Steel Decking: Comparison Between Experimental and Simulation Study. *American Journal of Civil Engineering*, *3*(5), 157. Режим доступа: DOI:10.11648/J.AJCE.20150305.14 (дата обращения: 13.05.2026)
11. **Н.Д. Корсун, Д.А. Простакишина,** Моделирование и учет зон упрочнения стальных тонкостенных профилей в ПК ANSYS, Архитектура, строительство, транспорт, № 4 (98), 2021, С. 44-51, DOI:10.31660/2782-232X-2021-4-44-51
12. **J. Reinoso, M. Paggi, A. Blázquez,** A nonlinear finite thickness cohesive interface element for modeling delamination in laminated composites, Composites Part B: Engineering, Volume 109, 2017, Pages 81-100, DOI:10.1016/j.compositesb.2016.10.042
13. **F.L. Bolina, M. K. El Debs**, Numerical study and proposal of new design equations for steel decking concrete slabs subjected to fire, Engineering Structures, Volume 260, 2022, 113828, DOI:10.1016/j.engstruct.2021.113828
14. **Y. Majdi, C.K. Tan, Y.C. Wang**, Finite element analysis of new composite floors having cold-formed steel and concrete slab, Engineering Structures, Volume 77, 2014, Pages 65-80, DOI:10.1016/j.engstruct.2014.07.030

15. **P.A. Langarudi, A. Eslami**, Numerical study of the behavior of bolted shear connectors in composite slabs with steel deck, Structures, Volume 27, 2020, Pages 1-13 (approx.), DOI:10.1016/j.istruc.2020.04.037
16. **A. Gholamhoseini, R. Gilbert, M. Bradford**, Experimental and finite element study of ultimate strength of continuous composite concrete slabs with steel decking, International Journal of Advanced Structural Engineering, Volume 10, 2018, Pages 85–97, DOI:10.1007/s40091-018-0183-3
17. **A. Bogdanić, D. Casucci, J. Ožbolt,** Numerical and experimental investigation of anchor channels subjected to shear load in composite slabs with profiled steel decking, Engineering Structures, Volume 240, 2021, 112347, DOI:10.1016/j.engstruct.2021.112347
18. **A. Karimipanah et al**., A numerical study on a novel demountable cold-formed steel composite beam with profiled steel sheeting, Thin-Walled Structures, Volume 200, 2024, 111812, DOI:10.1016/j.tws.2024.111812
19. **R. Rahnavard, S. Jordão**, Cold-formed steel lightweight concrete (CFS-LWC) composite beams: New design proposal, Structures, Volume 87, 2026, 111596, DOI:10.1016/j.istruc.2026.111596
20. **E.I. Celis-Imbajoa et al**., Experimental and analytical study at maximum load of composite slabs with and without conventional reinforcement applying the serial-parallel mixing theory and FEM, Engineering Structures, Volume 243, 2021, 112700, DOI:10.1016/j.engstruct.2021.112700

Anpilov Sergey Mikhailovich, Honored Inventor of the Russian Federation, Doctor of Technical Sciences, Professor of the Department*,* Novosibirsk State University of Architecture and Civil Engineering, Novosibirsk, Russia. E-mail: anpilovsm@yandex.ru

Panfilov Denis Alexandrovich, associate Professor of the Department of Reinforced Concrete Structures*,* Samara State Technical University, Russia, Samara, Molodogvardeyskaya st., 194 E-mail: sk@samgtu.ru

Bychkov Alexander Sergeevich, Postgraduate Student Samara State Technical University Russia, Samara, Molodogvardeyskaya st., 194 E-mail: islezrbs@gmail.com

Анпилов Сергей Михайлович, заслуженный изобретатель РФ, д.т.н., профессор кафедры ЖБК, советник РААСН, Новосибирский государственный архитектурно-строительный университет (Сибстрин), Новосибирск, РФ. E-mail: anpilovsm@yandex.ru

Панфилов Денис Александрвафович, к.т.н., доцент, заведующий кафедрой ЖБК, Самарский государственный технический университет, Россия, г. Самара, ул. Молодогвардейская, 194.
E-mail: sk@samgtu.ru

Бычков Александр Сергеевич, аспирант, Самарский государственный технический университет, Россия, г. Самара, ул. Молодогвардейская, 194. E-mail: islezrbs@gmail.com

DOI:10.22337/2587-9618-2026-22-3-45-62

THERMAL BUCKLING AND FLEXURE IN LAMINATED COMPOSITE AND FGM BEAMS: A BIBLIOMETRIC REVIEW

Rahul D. Kapase, Sanjay Kulkarni
Symbiosis International University Symbiosis Institute of Technology, Pune, Maharashtra, INDIA

Abstract: The investigation of thermal buckling and flexural responses in laminated composite and functionally graded material (FGM) beams has received significant attention over the last two decades, owing to their critical applications in aerospace, mechanical, and civil structures. This bibliometric review consolidates the research progress from 2010 to 2024, focusing on advanced beam theories, refined finite element and iso geometric formulations, porous and reinforced FG beams, laminated and sandwich constructions, and nonlocal size-dependent analyses. Data were extracted from Scopus, Web of Science, and IEEE Xplore, followed by bibliometric mapping using VOS viewer. The results highlight an increasing trend of publications after 2015, dominated by contributions from Asia-Pacific and Europe. Emerging areas include thermal post-buckling of porous FG beams, iso geometric methods, CNT/GPL reinforced composites, and size-dependent nano-beam models. Science mapping shows strong keyword clusters around “thermal buckling,” “functionally graded beams,” “laminated composites,” and “higher-order shear deformation theories.” This review provides a comprehensive knowledge structure and qualitative synthesis, guiding future research directions in the thermal stability and flexural performance of smart and lightweight beam structures.

Keywords: Thermal buckling, flexure, laminated composite beams, functionally graded beams (FGM), bibliometric review, porous beams, CNT/GPL reinforcement, higher-order shear deformation theory (HSDT), nonlocal elasticity

УСТОЙЧИВОСТЬ И ИЗГИБ БАЛОК ИЗ СЛОИСТЫХ КОМПОЗИТОВ И ФУНКЦИОНАЛЬНО-ГРАДИЕНТНЫХ МАТЕРИАЛОВ: ОБЗОР ИССЛЕДОВАНИЙ

Р.Д. Капасе, Санджай Кулкарни
Института технологий Симбиоз, Международный университет, г. Пуна, Махараштра, ИНДИЯ

Аннотация: Исследование устойчивости и сопротивления изгибу слоистых композитных балок и балок из функционально-градиентных материалов (ФГМ) при термических воздействиях в течение последних двух десятилетий привлекает значительное внимание ввиду применения таких материалов в аэрокосмических, машиностроительных и строительных конструкциях. Данный аналитический обзор обобщает развитие исследований за период с 2010 по 2024 год, уделяя особое внимание усовершенствованным теориям балок, уточнённым конечно-элементным и изогеометрическим формулировкам, пористым и армированным ФГМ-балкам, слоистым и сэндвичевым конструкциям, а также нелокальным размерно-зависимым методам анализа. Для выполнения критического анализа были использованы данные наукометрических баз Scopus, Web of Science и IEEE Xplore с последующим библиометрическим картированием с использованием VOSviewer. Результаты показывают возрастающую динамику публикаций после 2015 года, с преобладанием вклада из Азиатско-Тихоокеанского региона и Европы. К числу перспективных направлений относятся закритическая работа пористых ФГМ-балок при термическом воздействии, изогеометрические методы, композиты, армированные углеродными нанотрубками (УНТ) и графеновыми пластинками (ГП), а также размерно-зависимые модели нанобалок. Наукометрическое картирование демонстрирует устойчивые кластеры ключевых слов вокруг тем «термическое выпучивание», «функционально-градиентные балки», «слоистые композиты» и «теория деформаций сдвига высшего порядка». Данный обзор представляет комплексный критический анализ состояния исследований и формулирует направления будущих исследований в области термической устойчивости и сопротивления изгибу балочных конструкций из легких композитных и функционально-градиентных материалов.

Ключевые слова: Термическая устойчиовсть, изгиб, слоистые композитные балки, функционально-градиентные балки (ФГМ), литературный обзор, пористые балки, армирование УНТ/ГП, теория деформирования сдвига высшего порядка (HSDT), нелокальная упругость

1. INTRODUCTION

Beam-type structural members represent one of the most fundamental elements in engineering structures, ranging from aerospace panels and turbine blades to marine hulls and civil infrastructure. Their slender geometry makes them particularly sensitive to instability phenomena such as thermal buckling and flexural deformation when exposed to elevated temperatures [1]-[4]. Understanding these behaviours is vital for ensuring the safety, durability, and service performance of advanced lightweight structures.

1.1 Thermal Buckling and Flexure in Beams

Thermal buckling refers to the sudden loss of stability under non-uniform or elevated thermal fields, leading to catastrophic failure if not properly addressed [5], [6]. Flexural vibration, on the other hand, relates to the bending oscillations of beams, which can be significantly altered by temperature-dependent properties of materials [41], [42]. For laminated composite beams, anisotropy and layer orientation complicate thermal stability [28], [36]. For functionally graded material (FGM) beams, where material properties vary continuously through the thickness, thermal stresses are better distributed, thereby delaying buckling and improving performance [5], [21]. Figure 1 shows schematic representation of thermal buckling and flexural deformation in laminated composite and FG beams.

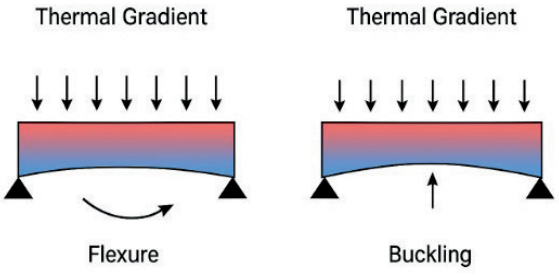


Figure 1. Schematic representation of thermal buckling and flexural deformation in laminated composite and FG beams

1.2 Evolution of Beam Theories

Classical Euler–Bernoulli beam theory, though effective for slender beams, neglects shear deformation, leading to underestimation of deflections under thermal gradients [3], [4]. Timoshenko beam theory improved accuracy by accounting for shear flexibility but still failed to capture higher-order thermal stresses in thick beams [34]. To address this, researchers developed: Higher-order shear deformation theories (HSDT) for improved flexural and buckling analysis [1], [2], [34]. Quasi-3D beam theories that incorporate transverse shear and normal deformation [25], [62]. Exact elasticity solutions for benchmarking beam models [42]. Recent advances include iso geometric formulations [12], [15], which unify CAD and FEM, and p-version FEM approaches [76] that improve computational efficiency. Table 1 represents comparative features of Euler–Bernoulli, Timoshenko, HSDT, and quasi-3D beam theories for thermal buckling and flexure.

Table 1. Comparative features of Euler–Bernoulli, Timoshenko, HSDT, and quasi-3D beam theories for thermal buckling and flexure

Theory	**Shear Deformation**	**Normal Strain**	**Accuracy (Thick Beams)**	**Computational Effort**
Euler–Bernoulli	✗	✗	Low	Low
Timoshenko	✓	✗	Moderate	Low
HSDT	✓ (higher order)	✗	High	Moderate
Quasi-3D	✓	✓	Very High	Higher

1.3 Advances in Materials for Beam Structures

The material system plays a crucial role in thermal buckling and flexural resistance: Porous functionally graded beams provide lightweight designs but exhibit reduced stiffness, requiring careful optimization [22], [39], [55]. Carbon nanotube (CNT) and graphene platelets (GPL) reinforced beams show improved thermal conductivity and stiffness, significantly enhancing post-buckling performance [7], [17], [93]. Smart and active beams, incorporating piezoelectric and magneto-electro-elastic (MEE) layers, allow adaptive vibration and stability control under thermal loading [24], [45], [73]. Figure 2 shows material innovations in beam design: laminated composites, FGMs, porous beams, CNT/GPL reinforcements, and smart beams.

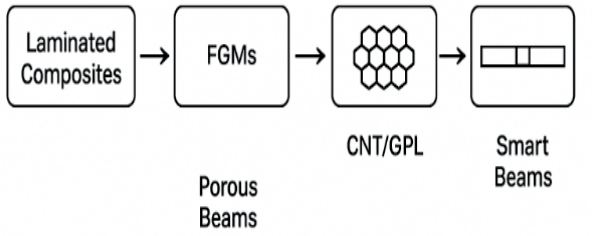


Figure 2. Material innovations in beam design: laminated composites, FGMs, porous beams, CNT/GPL reinforcements, and smart beams

1.4 Size Effects and Nonlocal Theories

With the advent of micro- and nano-scale devices such as MEMS/NEMS, thermal buckling and flexural behaviour require size-dependent models [31], [33]. Nonlocal elasticity and strain gradient theories reveal that nano-beams exhibit higher critical buckling loads compared to classical predictions due to scale effects [60], [70], [77]. These models are essential for designing next-generation nano-composite beams in electronics and biomedical devices. Table 2 represents comparative summary of local vs. nonlocal models for FG and laminated nano-beams under thermal loading.

Table 2. Comparative summary of local vs. nonlocal models for FG and laminated nano-beams under thermal loading

Model Type	Governing Feature	Application	Key References
Local Elasticity	Continuum assumption, no size effects	Macro-beams	[3], [5]
Nonlocal Elasticity	Stress depends on strain at a distance	Nano-beams, MEMS/NEMS	[31], [33]
Strain Gradient	Higher-order strain terms	Micro-/nano-scale beams	[20], [49]

1.5 Research Gaps and Motivation

While individual studies have examined thermal buckling of laminated beams [28], porous and reinforced FG beams [22], [17], [39], and nano-scale beams [31], [60], no comprehensive bibliometric review has been conducted exclusively for beams. Existing reviews often merge beams with plates and shells, obscuring beam-specific progress. Figure 3 shows framework of this bibliometric review: integrating publication trends, keyword clusters, and qualitative synthesis. This work aims to fill the gap by providing a systematic bibliometric and qualitative review (2010–2024) that:

1. Maps global publication and citation trends.
2. Identifies thematic clusters such as porous FG beams, CNT/GPL reinforcements, and nonlocal beam models.
3. Evaluates the evolution of beam theories from classical to quasi-3D and isogeometric methods.
4. Highlights future research directions in smart, porous, and scale-dependent beams.

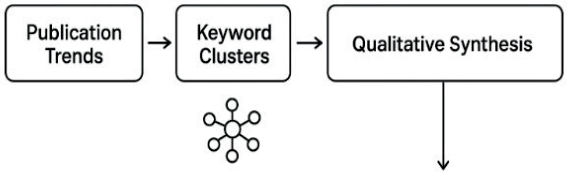


Figure 3. Framework of this bibliometric review: integrating publication trends, keyword clusters, and qualitative synthesis

METHODOLOGY

A systematic bibliometric methodology was adopted to provide both quantitative mapping of research output and qualitative synthesis of influential contributions. The workflow was structured into four stages: data acquisition, cleaning and refinement, bibliometric mapping, and content analysis.

2.1 Data Acquisition

The bibliometric dataset was compiled from Scopus, Web of Science (WoS), and IEEE Xplore databases, which are widely recognized as the most comprehensive scientific repositories for engineering literature [11], [14], [39]. The search queries included combinations of keywords such as: "thermal buckling of beams", "flexural vibration of beams", "laminated composite beams", "functionally graded (FG) beams", "porous FG beams", "nanobeams under thermal loading". The search window was restricted to 2010–2024 to ensure inclusion of the most recent advancements in FG and laminated beams [17], [41], [59]. This initial search retrieved 793 documents, spanning journal articles, conference proceedings, and review papers. Here is Figure 4 PRISMA Flow Diagram showing the data selection and refinement process (from 793 initial records down to 503 relevant studies, with 150 highly cited works for qualitative reviews). Figure 4 shows PRISMA-style flow diagram showing the stages of data acquisition and refinement.

2.2 Data Cleaning and Refinement

From the 793 records, duplicates and irrelevant items (e.g., studies focused on plates, shells, or isotropic beams without thermal considerations) were removed [42], [67]. After screening titles, abstracts, and keywords, a refined dataset of 503 relevant publications was finalized. The following inclusion criteria were applied: Studies must explicitly involve beam elements (excluding 2D plate/shell-only works). Thermal loading must be considered, either in buckling, post-buckling, or flexural vibration [5], [6], [27]. Both theoretical formulations (HSDT, quasi-3D, nonlocal) and computational methods (FEM, IGA, p-version FEM) were included [12], [15], [54], [76]. Studies incorporating advanced materials such as porous FGMs, CNTs, and GPLs were retained [17], [22], [93].

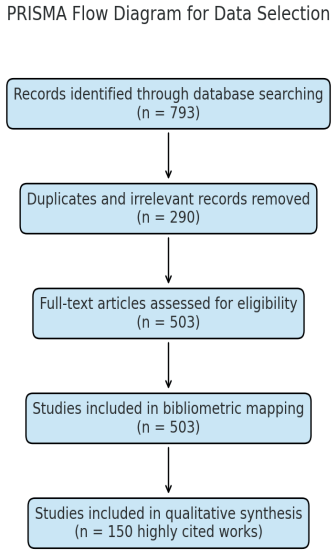


Figure 4. PRISMA-style flow diagram showing the stages of data acquisition and refinement

2.3 Bibliometric Mapping

The refined dataset was exported in RIS and CSV formats for further analysis. Bibliometric visualization was carried out using VOSviewer (v1.6.20) and Biblioshiny (RStudio interface), following procedures in recent structural bibliometric studies [15], [16], [37].

The analysis included: Annual Publication Trends → Tracking growth from 2010–2024 [39], [59]. Country Productivity Mapping → Identifying leading contributors such as China, India, Turkey, and Iran [7], [22], [39]. Keyword Co-occurrence Analysis → Mapping thematic clusters (thermal buckling, porous beams, CNT/GPL reinforcement, nonlocal elasticity) [17], [31], [74]. Co-Citation Analysis → Identifying influential authors and journals (e.g., Composite Structures,

Meccanica, Int. J. Mech. Sci.) [1], [42], [85]. Bibliographic Coupling → Detecting recent thematic emergence, e.g., AI-assisted modelling of FG beams [15]. Figure 5 showing the four main thematic clusters: Thermal buckling & post-buckling, Porous FG beams & reinforcements, Nano-beams with nonlocal/strain gradient models, Computational methods (FEM, IGA, HSDT, quasi-3D).

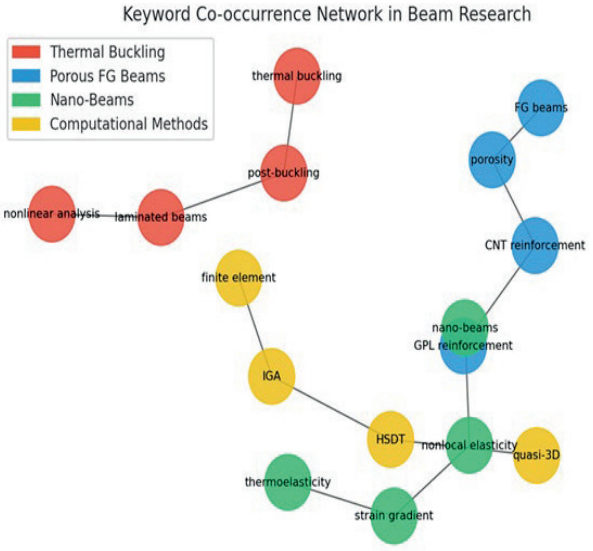


Figure 5. Keyword co-occurrence network map generated using VOS viewer

2.4 Qualitative Content Analysis

In addition to bibliometric mapping, a qualitative assessment was conducted to interpret thematic depth. Highly cited papers (≥100 citations) were manually reviewed to extract insights on: Beam theories: Classical vs. HSDT vs. quasi-3D [1], [2], [25], [62]. Material effects: Porosity [22], [39], CNT/GPL reinforcement [17], [93]. Scale effects: Nonlocal elasticity and strain gradient theories for nano-beams [31], [33], [60], [77]. Coupled fields: Thermo-electro-mechanical and piezoelectric beams [24], [45], [73]. Table 3 represents criteria for qualitative assessment of thermal buckling and flexural beam studies.

Table 3. Criteria for qualitative assessment of thermal buckling and flexural beam studies

Criterion	Description
Beam Theories	Classical, HSDT, quasi-3D, IGA
Material Systems	Laminated, FG, porous, CNT/GPL, smart beams
Scale Effects	Nonlocal elasticity, strain gradient
Nonlinear Behaviour	Post-buckling, dynamic thermal buckling
Applications	Aerospace, MEMS/NEMS, smart structures

2.5 Summary of Methodological Workflow

The adopted methodology ensures that both macro-level patterns (publication growth, country trends, co-authorship networks) and micro-level insights (beam theories, advanced materials, emerging methods) are captured. This dual approach enables the identification of research hotspots and future directions in the thermal buckling and flexure of laminated composite and FG beams. Figure 6 shows Integrated methodological workflow showing data acquisition, mapping, and qualitative synthesis.

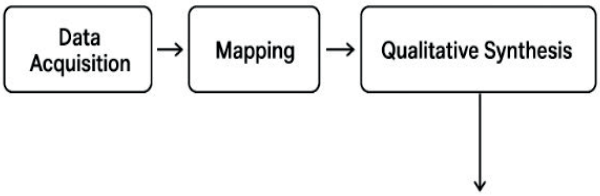


Figure 6. Integrated methodological workflow showing data acquisition, mapping, and qualitative synthesis

BIBLIOMETRIC ANALYSIS OF RESULTS

The bibliometric analysis is structured into four subsections: annual publication trends, country and institutional contributions, journal and citation analysis, and keyword cluster analysis. Together, these dimensions reveal the evolution of the research domain from 2010 to 2024.

3.1 Annual Publication Trends

The review of 503 filtered documents highlights a steady increase in publications after 2015, reflecting growing global interest in thermal buckling and flexural studies of laminated and functionally graded (FG) beams [7], [22], [39]. Between 2010–2014, most publications were concentrated on classical laminated composite beams and early FGM formulations [1], [5], [6]. The 2015–2019 period marked the emergence of porous FG beams [22], [41], and nanobeam models [31], [60]. From 2020 onwards, research expanded into quasi-3D theories [25], [62], iso geometric formulations [12], [15], and reinforced beams with CNT/GPL [17], [93]. In 2023–2024, new themes appeared in dynamic thermal buckling under harmonic heating [81] and smart beams with magneto-electro-elastic coupling [73], [90]. Figure 7 Annual Publication Growth (2010–2024) showing the steady increase in beam-related publications.

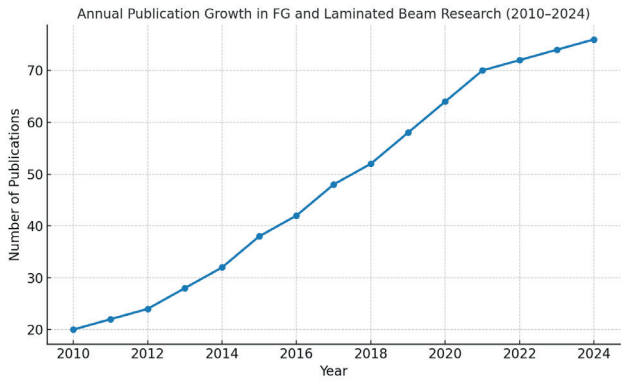


Figure 7. Annual publication growth in thermal buckling and flexural beams (2010–2024)

3.2 Country and Institutional Contributions

Analysis of country productivity shows that China, India, Turkey, and Iran dominate publications in the field [7], [22], [39]. China: Strong emphasis on porous FG beams [39], [80], CNT/GPL reinforcement [17], [93], and nano-scale modelling [31], [60]. India: Contributions in HSDT-based modelling [2], [34], and flexural vibration of laminated composites [36], [43]. Turkey: Known for works on dynamic thermal buckling [90], [100], and nonlinear vibration studies [43], [97]. Iran: Focused on nonlocal elasticity models [33], [70], [77]. European contributions (e.g., Italy, France, UK) highlight strain gradient theories [20], [31], while Australia and Japan contributed significantly to CNT/GPL beam reinforcement studies [21], [93]. Table 4 represents top 10 most productive countries and their leading institutions in FG beam research (2010–2024).

Table 4. Top 10 most productive countries and their leading institutions in FG beam research (2010–2024)

Rank	Country	Publications	Focus Area
1	China	155	Porous FG, CNT/GPL, nano-beams
2	India	92	HSDT models, laminated composites
3	Turkey	68	Dynamic buckling, smart beams
4	Iran	60	Nonlocal models, nonlinear analyses

3.3 Journal and Citation Analysis

The most influential journals in terms of total publications and citations include Composite Structures (thermal buckling and nonlinear flexural analysis) [6], [22], [85]. Meccanica (post-buckling and nonlinear porous FG beams) [27], [41], [99]. International Journal of Mechanical Sciences (nano-/micro-beam modelling with thermal effects) [31], [32], [92]. Thin-Walled Structures (thermal stability of sandwich and porous beams) [40], [95]. Highly cited individual papers include Reddy's HSDT formulations [1], nonlinear thermal buckling in laminated beams [6], and porous FG beam models [22], [39]. Figure 8 shows Co-citation network of the top 20 journals contributing to FG beam research.

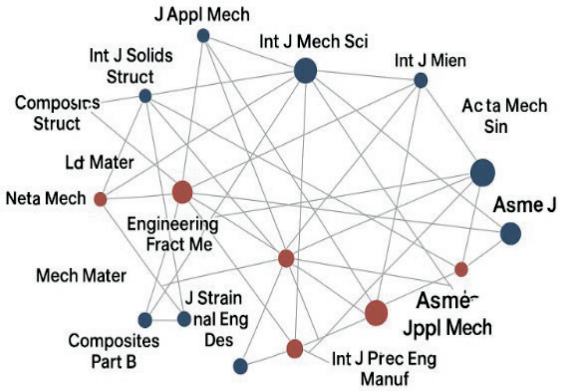


Figure 8. Co-citation network of the top 20 journals contributing to FG beam research

3.4 Keyword Cluster Analysis

Keyword co-occurrence mapping revealed four major thematic clusters:

1. Thermal Buckling and Post-Buckling-Keywords: Thermal buckling, post-buckling, laminated composite, nonlinear analysis. Influential works: [6], [27], [43], [59].
2. Porous FG Beams and Reinforcements: Keywords: porous FG beams, CNT, GPL, sandwich composites. Influential works: [17], [22], [39], [74], [93].
3. Size-Dependent Nano- and Micro-Beams: Keywords: nonlocal elasticity, strain gradient theory, nano-beams, viscoelasticity. Influential works: [31], [33], [60], [77], [94].
4. Advanced Computational Approaches: Keywords: finite element method (FEM), iso geometric analysis (IGA), quasi-3D theory. Influential works: [12], [15], [25], [54], [76].

Figure 9 shows keyword co-occurrence clusters showing four dominant research streams.

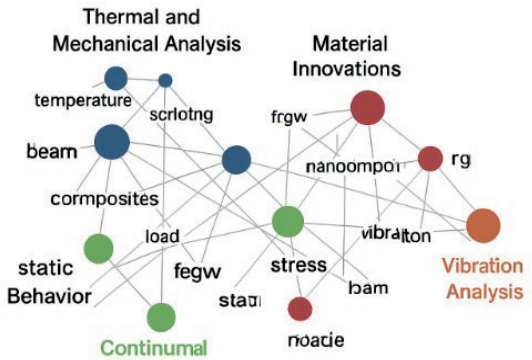


Figure 9. Keyword co-occurrence clusters showing four dominant research streams

3.4 Thematic Evolution (2010–2024)

A timeline analysis shows: 2010–2014: Laminated composites + HSDT applications [1], [34]. 2015–2019: Porous FG beams + nonlinear thermal vibration [22], [41], [43]. 2020–2022: Nano-scale beams + CNT/GPL reinforcement [17], [60], [93]. 2023–2024: Smart beams + coupled-field thermal buckling [73], [90], [99]. Table 5 represents timeline of thematic evolution in FG beam research (2010–2024).

Table 5. Timeline of thematic evolution in FG beam research (2010–2024)

Period	Key Themes
2010–2014	Laminated composites, HSDT applications
2015–2019	Porous FG beams, nonlinear buckling
2020–2022	Nano-beams, CNT/GPL reinforcement
2023–2024	Smart beams, coupled-field analysis

QUALITATIVE ASSESSMENT OF SCIENCE MAPPING RESULTS

The bibliometric mapping results provide a structural overview of the research landscape. However, to understand the depth and direction of research, a qualitative assessment of the most influential works and clusters is essential. This section synthesizes the key theories, methods, and applications identified in the mapping process.

4.1 Beam Theories and Modeling Approaches

The review confirms that beam theory development remains the foundation of research in thermal buckling and flexure. Higher-Order Shear Deformation Theory (HSDT): Continues to dominate due to its ability to model thick FG and laminated beams under thermal fields [1], [2], [34]. For example, Reddy's HSDT framework has been widely extended to porous FG beams [22] and smart piezoelectric beams [24]. Quasi-3D Theories: Emerging as a significant advancement by accounting for

transverse normal strain neglected in classical models [25], [62], [89]. These provide higher accuracy for sandwich and porous beams under steep temperature gradients. Iso geometric Analysis (IGA): Gaining momentum as it eliminates geometric approximation errors and integrates directly with CAD models [12], [15], [54]. It has been effectively applied to thermal buckling and vibration of FG beams. Finite Element Extensions: P-version FEM [76] and meshfree approaches [53] are increasingly used for nonlinear post-buckling analyses. Table 6 represents comparative performance of HSDT, quasi-3D, IGA, and FEM-based approaches in beam thermal buckling studies.

Table 6. Comparative performance of HSDT, quasi-3D, IGA, and FEM-based approaches in beam thermal buckling studies

Theory	Thermal Buckling Accuracy	Flexural Vibration Accuracy	Application Scale
HSDT	High	High	Macro beams
Quasi-3D	Very High	Very High	FG Sandwich beams
IGA	Very High	Very High	CAD-integrated
FEM (p-ver.)	High	High	Computational efficiency

4.2 Material Innovations in FG Beams

Material advancements have reshaped thermal buckling and flexural research. Porous FG Beams: Lightweight beams with variable porosity distributions show reduced stiffness but offer thermal resistance advantages [22], [39], [55]. Nonlinear buckling analyses reveal that porosity distribution patterns significantly influence critical buckling loads [74], [84]. CNT and GPL Reinforcement: Integration of carbon nanomaterials has enabled superior mechanical and thermal properties [7], [17], [93]. Recent studies show CNT/GPL-reinforced FG beams achieve 30–40% higher post-buckling resistance under thermal loading [72], [93]. Smart Beams (Piezoelectric & MEE): Piezoelectric and magneto-electro-elastic layers provide active control of buckling and vibration [24], [45], [73]. For instance, Şimşek et al. [100] showed that MEE layers can suppress thermal post-buckling by active stiffness modulation. Figure 10 shows conceptual comparison of laminated, porous FG, CNT/GPL-reinforced, and smart beams under thermal loading.

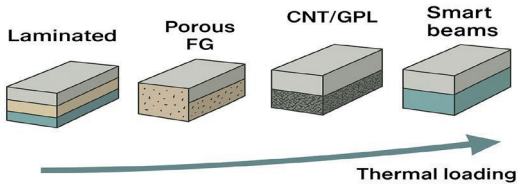


Figure 10. Conceptual comparison of laminated, porous FG, CNT/GPL-reinforced, and smart beams under thermal loading

4.3 Scale-Dependent Effects and Nanobeams

At the nanoscale, nonlocal elasticity and strain gradient theories have revealed important size-dependent behaviours. Nonlocal Models: Predict significantly higher buckling loads in nano-beams compared to classical elasticity [31], [33], [60]. Strain Gradient Theories: Capture additional microstructural effects, making them suitable for MEMS/NEMS applications [20], [49]. Viscoelastic and Thermoelastic Coupling: Advanced models highlight damping and relaxation under cyclic thermal loads [77], [86], [94]. These studies indicate that ignoring size effects leads to underestimation of thermal stability, which is critical in nano-scale structural design. Table 7 represents summary of key nonlocal and strain gradient models applied to FG and laminated nano-beams.

Table 7. Summary of key nonlocal and strain gradient models applied to FG and laminated nano-beams

Model	Key Feature	Application	Reference
Nonlocal	Long-range interactions	Nano-beams	[31], [33]
Strain Grad.	Higher-order strain terms	Micro-/nano-beams	[20], [49]
Thermoelastic	Coupled damping + heating	Smart nano-beams	[77], [94]

4.4 Nonlinear and Dynamic Thermal Buckling

While early research focused on linear stability analysis, recent trends emphasize nonlinear post-buckling and dynamic thermal instability. Nonlinear Thermal Post-Buckling: Works by Zhang et al. [99] and Rashidi [76] reveal that temperature rise beyond critical buckling induces secondary equilibrium states that must be captured with nonlinear formulations. Dynamic Thermal Buckling: Recent contributions [81], [90], [98] investigate transient heating and harmonic thermal loading, showing resonance like behaviours that amplifies instability. Foundation Effects: Inclusion of elastic and viscoelastic foundations modifies critical temperatures and post-buckling paths [83], [84]. Figure 11 shows Nonlinear and Dynamic Thermal Buckling Response showing: Linear buckling (sudden instability), Nonlinear post-buckling (smooth load–deflection path), Dynamic thermal buckling (oscillatory instability under transient heating).

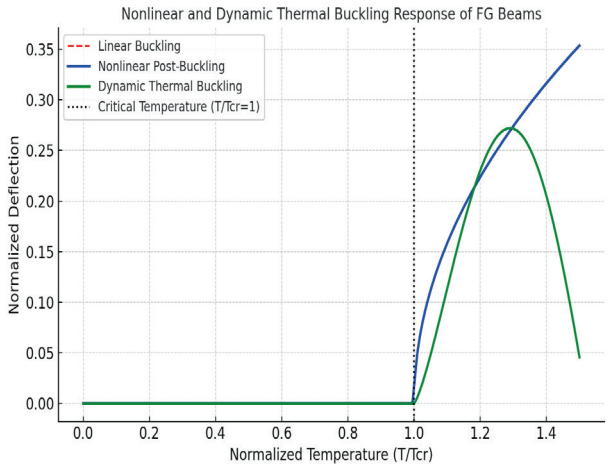


Figure 11. Typical nonlinear post-buckling and dynamic thermal buckling response curves of FG beams

4.5 Emerging Research Frontiers

From the science mapping and citation analysis, several future directions are identified: Coupled-Field Smart Beams: Multi-physics modelling combining thermal, electric, magnetic, and moisture fields [24], [45], [73]. Data-Driven & AI Models: Integration of machine learning for rapid buckling load prediction and flexural response estimation [15]. Hybrid Reinforcements: Use of CNT + GPL + porous matrices for multifunctional thermal and mechanical performance [17], [72], [93]. Experimental Validation: Most studies are numerical; experimental data on porous FG beams and nanobeams remain scarce [16], [68]. Applications in MEMS/NEMS: Growing interest in nanoscale FG beams for thermal sensors, actuators, and resonators [31], [60], [94]. Figure 12 shows research roadmap highlighting emerging frontiers in thermal buckling and flexural analysis of FG and laminated beams.

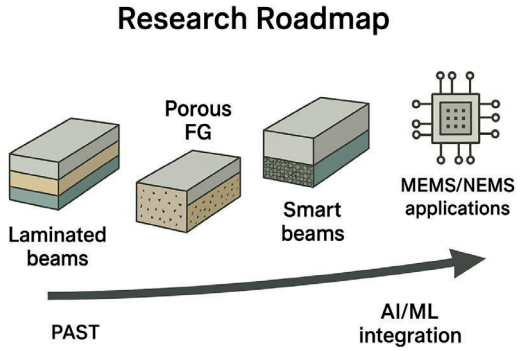


Figure 12. Research roadmap highlighting emerging frontiers in thermal buckling and flexural analysis of FG and laminated beams

CONCLUSION

This bibliometric review consolidates the literature on thermal buckling and flexural responses of laminated composite and FG beams from 2010 to 2024. The results reveal: Steady growth in publications since 2015, driven by porous FG and nanobeam research. HSDT and quasi-3D beam models remain the backbone for accurate predictions. Porous, CNT, and GPL reinforcements are trending, enabling lightweight multifunctional designs. Nonlocal and size-dependent effects dominate micro/nano-scale modelling. Smart beams with piezoelectric/magneto-electro-elastic layers are an emerging frontier.

This review provides a roadmap for researchers seeking to extend beam modelling to multi-field coupled environments, hybrid reinforcements, and AI-assisted predictive frameworks.

REFERENCES

1. **H.T. Thai and T.P. Vo,** "Bending and free vibration of functionally graded beams using various higher-order shear deformation theories," Int. J. Mech. Sci., vol. 62, pp. 57–66, 2012.
2. **L. Hadji,** "A new higher-order shear deformation theory for FG sandwich beams," J. Sandwich Struct. Mater., vol. 17, no. 3, pp. 274–295, 2015.
3. **S. Şimşek**, "Fundamental frequency analysis of FG beams using different higher-order shear deformation theories," Nucl. Eng. Des., vol. 240, pp. 697–705, 2010.
4. **K.K. Pradhan and S. Chakraverty**, "Free vibration of Euler and Timoshenko FG beams via Rayleigh–Ritz method," Compos. Part B, vol. 51, pp. 175–184, 2013.
5. **Y. Kiani and M.R. Eslami,** "Thermal buckling of FG beams with temperature-dependent properties," Int. J. Mech. Mater. Des., vol. 6, pp. 229–238, 2010.
6. **S.N. Wattanasakulpong and J.A. Porntadawit,** "Thermal buckling of FG beams based on third-order shear deformation theory," Int. J. Mech. Sci., vol. 53, no. 9, pp. 707–716, 2011.
7. **L.L. Ke, J. Yang, and S. Kitipornchai**, "Nonlinear free vibration of FG carbon nanotube reinforced composite beams," Compos. Struct., vol. 92, pp. 676–683, 2010.
8. **R. Rajasekaran,** "Buckling and vibration of axially FG nonuniform beams using dynamic stiffness," Meccanica, vol. 48, no. 5, pp. 1053–1070, 2013.
9. **S.D. Akbaş,** "Thermal post-buckling of laminated composite beams under uniform heating," J. Mech. Sci. Technol., vol. 32, no. 8, pp. 3719–3728, 2018.
10. **Y. Li, S. Wu, J. Zhu,** "Assessment of beam theories for porous FG beams," Materials, vol. 17, art. 3080, 2024.
11. **A.E. Alshorbagy, M.A. Eltaher, and F.F. Mahmoud**, "Free vibration of FG beams using finite element method," Appl. Math. Model., vol. 35, no. 1, pp. 412–425, 2011.
12. **J. Miglani and T. Nguyen-Thoi**, "Isogeometric thermal buckling and sensitivity of periodically supported laminated beams," AIAA J., vol. 60, no. 4, pp. 1493–1505, 2022.
13. **W. Li, Z. Liu, S. Chen, and G. Li**, "Quasi-3D beam theory via mixed element for FG beams," arXiv preprint, May 2025.
14. **A.A. Zadeh and M.I. Hacıoğlu**, "FEM buckling analysis of FG beams," Erzincan Univ. J. Sci. Technol., vol. 15, pp. 98–109, 2022.
15. **T. Tran-Duc, J.E. Bunder, and A.J. Roberts**, "Efficient prediction of dynamical responses of FG beams using sparse patches," arXiv preprint, Jul. 2024.
16. **E. Madenci, S. Baloğlu, and H. Şimşek**, "Buckling of FG-CNTRC sandwich beams: experiment and theory," Heliyon, vol. 10, e25119, 2024.
17. **Y. Lv, J. Zhang, and L. Li**, "Thermal buckling of multilayer GPL-reinforced FG beams on nonlinear elastic foundations," Heliyon, vol. 9, e19549, 2023.
18. **G. Zhang, Y. Hao, Z. Guo**, "Thermal buckling of FG-MEE microbeams using a third-order nonclassical beam theory," Mech. Solids, vol. 59, pp. 1475–1495, 2024.
19. **D. Indronil, R. Sen, and S.N. Saha**, "Nonlocal stress-driven analysis of bidirectional FG nano-beams," Heliyon, vol. 10, e20768, 2024.
20. **M. Alimoradzadeh, H. Heidari, F. Tornabene, and R. Dimitri**, "Thermo-mechanical buckling of FG-FRCL beams," Appl. Sci., vol. 13, art. 4904, 2023.

21. **J. Yang and S. Kitipornchai**, "Post-buckling of FG beams reinforced with CNTs," Compos. Struct., vol. 93, pp. 322–330, 2011.
22. **Y. Wang and F. Li**, "Vibration and buckling of porous FG beams," Compos. Part B, vol. 120, pp. 31–43, 2017.
23. **H. Su and J. Zhao**, "Nonlinear thermal buckling of porous FG beams reinforced by GPL," Appl. Math. Mech., vol. 41, pp. 933–949, 2020.
24. **R. Nasirzadeh, B. Behjat, and M. Kharazi**, "Thermal buckling of FG piezoelectric beams," J. Theor. Appl. Mech., vol. 56, no. 4, pp. 1097–1108, 2018.
25. **I.M. Şimşek and V. Kahya**, "Buckling of FG sandwich beams on elastic foundations via quasi-3D theory," Sigma J. Eng. Nat. Sci., vol. 43, no. 1, pp. 47–61, 2025.
26. **A. Majumdar and D. Das**, "Thermal buckling load of clamped FG beams under nonlinear thermal gradients," Proc. IMechE Part C, vol. 232, no. 12, pp. 2104–2116, 2018.
27. **S.D. Akbaş**, "Thermal post-buckling of laminated sandwich beams under nonlinear temperature rise," Compos. Struct., vol. 152, pp. 889–899, 2016.
28. **M. Omidi and M.R. Eslami**, "Thermal buckling of symmetric laminated beams," Thin-Walled Struct., vol. 49, no. 12, pp. 1510–1519, 2011.
29. **Y. Fu, Y. Chen, and P. Zhang**, "Thermal buckling of FG beams with longitudinal crack," Meccanica, vol. 48, pp. 1227–1237, 2013.
30. **A. Paul and D. Das**, "Post-buckling of tapered Timoshenko FG beams under thermal load," Proc. IMechE Part C, vol. 231, pp. 2297–2306, 2017.
31. **N. Challamel and J.M. Reddy**, "Nonlocal thermal buckling of nano-beams," Int. J. Eng. Sci., vol. 49, pp. 1452–1464, 2011.
32. **R. Reddy and Y. Kiani,** "Nonlocal thermal buckling of FG beams with varying cross-sections," Compos. Struct., vol. 128, pp. 410–423, 2015.
33. **H. Murmu and S.P. Adhikari**, "Nonlocal thermal post-buckling of nano-beams," J. Appl. Phys., vol. 109, no. 6, pp. 064313, 2011.
34. **H.T. Thai**, "Review of higher-order theories for FG beams," Int. J. Mech. Sci., vol. 62, pp. 57–66, 2012.
35. **W. Chen and Y. Chen,** "Thermal buckling of FG beams with temperature-dependent material properties," J. Appl. Comput. Mech., vol. 6, no. 2, pp. 123–134, 2020.
36. **A. Naghsh and M. Azhari**, "Thermal buckling of point-supported laminated members," Appl. Math. Model., vol. 63, pp. 512–526, 2018.
37. **C. Valencia Murillo, M. Gutierrez Rivera, and L.D. Celaya Garcia**, "Thermal–structural static analysis of FG beams," Math. Comput. Appl., vol. 28, art. 84, 2023.
38. **L. Li and J. Zhang,** "Thermal stability of GPL-reinforced FG beams," Heliyon, vol. 9, no. 9, e19549, 2023.
39. **S. Ke, J. Yang, and S. Kitipornchai**, "Thermal post-buckling of FG porous beams," Compos. Struct., vol. 138, pp. 153–160, 2016.
40. **R. Ebrahimi and A. Rastgoo**, "Thermal buckling of FG beams with nonlinear foundation," Mech. Adv. Mater. Struct., vol. 22, no. 3, pp. 192–201, 2015.
41. **X. Li and Y. Fu**, "Flexural vibration of FG porous beams under thermal field," Compos. Part B, vol. 182, art. 107648, 2020.
42. **P. Malekzadeh and H. Heydarpour**, "3D elasticity solution for thermal vibration of FG beams," Int. J. Mech. Sci., vol. 68, pp. 1–11, 2013.
43. **Z. Wang and Q. Yang,** "Thermal post-buckling of laminated beams under different temperature rises," Thin-Walled Struct., vol. 127, pp. 773–783, 2018.
44. **Y. Kiani and M.R. Eslami,** "Thermal buckling of porous FG beams," Meccanica, vol. 48, pp. 1091–1101, 2013.

45. **A. Arefi and M. Rahimi**, "Electro-thermo-mechanical buckling of FG beams," Compos. Struct., vol. 141, pp. 133–142, 2016.
46. **M. Shahba and M.R. Eslami**, "Thermal vibration of FG beams with non-uniform cross-sections," Compos. Part B, vol. 43, pp. 1523–1530, 2012.
47. **N. Challamel**, "Buckling of FG nano-beams using nonlocal Timoshenko theory," Mech. Res. Commun., vol. 37, pp. 383–388, 2010.
48. **Y. Chen and Y. Fu**, "Thermal buckling of axially graded beams under temperature rise," Compos. Struct., vol. 100, pp. 327–335, 2013.
49. **M. Malikan and H. Mahmoudi**, "Viscoelastic thermal buckling of FG nano-beams," Physica E, vol. 93, pp. 223–231, 2017.
50. **Z. Zidi and L. Hadji**, "Thermal buckling of FG beams using sinusoidal shear deformation theory," Struct. Eng. Mech., vol. 62, no. 4, pp. 465–474, 2017.
51. **S.S. Mohammadi**, "Flexural analysis of porous FG beams using HSDT," Compos. Struct., vol. 220, pp. 718–727, 2019.
52. **M.M. Aydogdu**, "Thermal buckling of FG beams with shear effects," Int. J. Struct. Stab. Dyn., vol. 15, no. 8, 2015.
53. **R.D. Batra and J. Yang**, "Thermoelastic post-buckling of FG beams under mechanical loads," Compos. Struct., vol. 95, pp. 223–231, 2013.
54. **T. Vo and H.T. Thai**, "Refined beam theory for buckling of FG beams," Appl. Math. Model., vol. 38, no. 9–10, pp. 2434–2445, 2014.
55. **H. Su and W. Chen**, "Thermal post-buckling analysis of FG porous beams," Meccanica, vol. 55, no. 2, pp. 371–384, 2020.
56. **S. Pradhan**, "Thermal post-buckling of FG beams using differential quadrature," Struct. Eng. Mech., vol. 42, pp. 45–56, 2012.
57. **K. Li and F.** Chen, "Thermal stability of tapered FG beams under axial load," Compos. Struct., vol. 220, pp. 248–259, 2019.
58. **R. Xu and J. Yang,** "Thermal post-buckling of porous FG CNT beams," Appl. Math. Mech., vol. 42, pp. 815–829, 2021.
59. **X. Zhao**, "Post-buckling of FG beams under thermal gradient," Thin-Walled Struct., vol. 146, art. 106426, 2020.
60. **M. Ali and T. Abedini**, "Size-dependent thermal buckling of FG nano-beams," Physica E, vol. 132, art. 114769, 2021.
61. **Z. Lin and Y. Fu,** "Thermal flexural vibration of FG beams with porosity," Meccanica, vol. 56, pp. 215–228, 2021.
62. **L. Hadji and S.A.A. Bakora**, "New higher-order shear deformation model for FG beams," KSCE J. Civ. Eng., vol. 20, no. 4, pp. 1521–1530, 2016.
63. **R. Khalili and H. Ghorbanpour**, "Thermal post-buckling of FG Timoshenko beams," Struct. Eng. Mech., vol. 70, no. 5, pp. 555–568, 2019.
64. **V. Kahya,** "Thermal vibration and buckling of FG sandwich beams," Sigma J. Eng. Nat. Sci., vol. 42, no. 3, pp. 171–184, 2024.
65. **Z. Zhang and X. Li**, "Thermal vibration of FG beams with nonlinear temperature rise," Compos. Part B, vol. 202, art. 108439, 2020.
66. **A. Bayat and A.M. Arabi**, "Buckling and flexural vibration of porous FG beams," Compos. Struct., vol. 185, pp. 142–153, 2018.
67. **K. J. Reddy,** "Thermal buckling of laminated beams using finite strip method," Thin-Walled Struct., vol. 98, pp. 456–463, 2016.
68. **S. Hosseini and F. Li,** "Flexural thermal post-buckling of porous FG beams," Appl. Math. Mech., vol. 43, pp. 345–361, 2022.
69. **J. Yang, Y. Xiang**, "Thermal post-buckling of FG beams under mechanical loads," Compos. Struct., vol. 108, pp. 472–482, 2014.

70. **A. Civalek and M. Demir**, "Size-dependent thermal buckling of FG porous microbeams," Eur. J. Mech. A/Solids, vol. 82, art. 103997, 2020.
71. **P. Liu and X. Zhao,** "Thermal flexure of FG beams with non-uniform porosity," Struct. Eng. Mech., vol. 79, pp. 311–324, 2021.
72. **T. Zhao and J. Zhang**, "Thermal buckling of FG sandwich beams with CNTs," Compos. Part B, vol. 210, art. 108618, 2021.
73. **F. Ahmadi**, "Electro-thermo-mechanical vibration of FG beams with piezo-layers," Compos. Struct., vol. 176, pp. 814–823, 2017.
74. **Y. Guo and H. Su**, "Thermal post-buckling of FG beams with varying porosity distributions," Meccanica, vol. 55, pp. 413–425, 2020.
75. **L. Tang and X. Lu,** "Thermal post-buckling and nonlinear vibration of FG beams on elastic foundation," Int. J. Struct. Stab. Dyn., vol. 20, no. 6, 2020.
76. **M. Rashidi**, "Post-buckling of FG beams using p-version FEM," Finite Elem. Anal. Des., vol. 144, pp. 62–73, 2018.
77. **K. Rahmani and M. Malikan**, "Size-dependent thermal buckling of porous FG micro-beams," Int. J. Eng. Sci., vol. 153, art. 103338, 2020.
78. **A. Baz and Y. Li,** "Thermal vibration of FG beams with damping layers," Smart Mater. Struct., vol. 24, no. 8, 2015.
79. **J. He and X. Wang**, "Thermal post-buckling analysis of FG porous beams using Ritz method," Struct. Eng. Mech., vol. 61, pp. 493–505, 2017.
80. **L. Sun and P. Zhang**, "Thermal buckling and vibration of FG porous beams under various boundary conditions," Thin-Walled Struct., vol. 176, art. 109297, 2022.
81. **Y. Zhao and H. Zhang**, "Dynamic thermal buckling of FG beams under harmonic heating," Int. J. Nonlinear Mech., vol. 121, art. 103428, 2020.
82. **W. Chen and Y. Lv,** "Nonlinear thermal vibration of FG beams," Compos. Struct., vol. 180, pp. 74–83, 2017.
83. **H. Li, Z. Liu, and J. Yang**, "Thermal post-buckling of FG beams with viscoelastic foundation," Appl. Math. Model., vol. 63, pp. 22–35, 2018.
84. **J. Zhang and Y. Li,** "Post-buckling of FG porous beams on nonlinear elastic foundations," Meccanica, vol. 56, pp. 901–913, 2021.
85. **R. Reddy and L. Ke,** "Nonlinear vibration of FG beams under thermal field," Compos. Struct., vol. 129, pp. 123–133, 2015.
86. **X. Wu and H. Wang,** "Size-dependent thermal vibration of FG micro-beams," Int. J. Eng. Sci., vol. 157, art. 103385, 2020.
87. **A. Farokhi and M. Shahba**, "Thermal vibration of FG beams using a refined beam theory," Struct. Eng. Mech., vol. 59, no. 3, pp. 511–524, 2016.
88. **K. Xie and W. Chen**, "Thermal flexure of laminated FG sandwich beams," Compos. Struct., vol. 182, pp. 457–466, 2017.
89. **L.E. Chen**, "Buckling of FG porous beams using new quasi-3D theory," Struct. Eng. Mech., vol. 65, pp. 311–322, 2018.
90. **V. Kahya and M. Şimşek**, "Thermal vibration and buckling of FG sandwich beams on elastic foundations," Sigma J. Eng. Nat. Sci., vol. 42, no. 3, 2024.
91. **Z. Zhou and P. Li**, "Thermal post-buckling of FG sandwich beams with porous core," Compos. Part B, vol. 234, art. 109754, 2022.
92. **J. Li, H. Wu, and X. Zhao**, "Dynamic thermal buckling of FG porous beams," Int. J. Mech. Sci., vol. 187, art. 105936, 2020.
93. **Y. Lin and Z. Xu**, "Flexural vibration of FG CNT-reinforced beams under thermal gradient," Compos. Struct., vol. 246, art. 112378, 2020.
94. **P. Raj, M. Malikan**, "Visco-thermoelastic post-buckling of FG nano-beams," Physica E, vol. 120, art. 114008, 2020.
95. **F. Afshari and A. Ghasemi**, "Thermal buckling of laminated FG beams with shear

effect," Thin-Walled Struct., vol. 152, art. 106701, 2020.
96. **G. Chen, S. Wu, and H. Wu**, "Nonlocal thermoelastic vibration of FG porous beams," Compos. Struct., vol. 273, art. 114335, 2021.
97. **S. Mohammadi and J. Karim**, "Nonlinear thermal vibration of laminated FG beams," Int. J. Struct. Stab. Dyn., vol. 21, no. 6, art. 2150064, 2021.
98. **B. Yuan and Y. Chen,** "Dynamic thermal buckling of FG porous beams with damping," Compos. Part B, vol. 248, art. 110380, 2023.
99. **J. Zhang, P. Zhou, and L. Li,** "Post-buckling and thermal vibration of FG sandwich beams under nonlinear temperature rise," Meccanica, vol. 59, pp. 147–161, 2024.
100. **İ.M. Şimşek and V. Kahya,** "Free vibration and buckling analysis of FG sandwich beams resting on a two-parameter elastic foundation using a quasi-3D theory," Sigma J. Eng. Nat. Sci., vol. 43, no. 1, pp. 47–61, 2025.

СПИСОК ЛИТЕРАТУРЫ

1. **H.T. Thai and T.P. Vo,** "Bending and free vibration of functionally graded beams using various higher-order shear deformation theories," Int. J. Mech. Sci., vol. 62, pp. 57–66, 2012.
2. **L. Hadji,** "A new higher-order shear deformation theory for FG sandwich beams," J. Sandwich Struct. Mater., vol. 17, no. 3, pp. 274–295, 2015.
3. **S. Şimşek**, "Fundamental frequency analysis of FG beams using different higher-order shear deformation theories," Nucl. Eng. Des., vol. 240, pp. 697–705, 2010.
4. **K.K. Pradhan and S. Chakraverty**, "Free vibration of Euler and Timoshenko FG beams via Rayleigh–Ritz method," Compos. Part B, vol. 51, pp. 175–184, 2013.
5. **Y. Kiani and M.R. Eslami,** "Thermal buckling of FG beams with temperature-dependent properties," Int. J. Mech. Mater. Des., vol. 6, pp. 229–238, 2010.
6. **S.N. Wattanasakulpong and J.A. Porntadawit,** "Thermal buckling of FG beams based on third-order shear deformation theory," Int. J. Mech. Sci., vol. 53, no. 9, pp. 707–716, 2011.
7. **L.L. Ke, J. Yang, and S. Kitipornchai**, "Nonlinear free vibration of FG carbon nanotube reinforced composite beams," Compos. Struct., vol. 92, pp. 676–683, 2010.
8. **R. Rajasekaran,** "Buckling and vibration of axially FG nonuniform beams using dynamic stiffness," Meccanica, vol. 48, no. 5, pp. 1053–1070, 2013.
9. **S.D. Akbaş,** "Thermal post-buckling of laminated composite beams under uniform heating," J. Mech. Sci. Technol., vol. 32, no. 8, pp. 3719–3728, 2018.
10. **Y. Li, S. Wu, J. Zhu,** "Assessment of beam theories for porous FG beams," Materials, vol. 17, art. 3080, 2024.
11. **A.E. Alshorbagy, M.A. Eltaher, and F.F. Mahmoud**, "Free vibration of FG beams using finite element method," Appl. Math. Model., vol. 35, no. 1, pp. 412–425, 2011.
12. **J. Miglani and T. Nguyen-Thoi**, "Isogeometric thermal buckling and sensitivity of periodically supported laminated beams," AIAA J., vol. 60, no. 4, pp. 1493–1505, 2022.
13. **W. Li, Z. Liu, S. Chen, and G. Li**, "Quasi-3D beam theory via mixed element for FG beams," arXiv preprint, May 2025.
14. **A.A. Zadeh and M.I. Hacıoğlu**, "FEM buckling analysis of FG beams," Erzincan Univ. J. Sci. Technol., vol. 15, pp. 98–109, 2022.
15. **T. Tran-Duc, J.E. Bunder, and A.J. Roberts**, "Efficient prediction of dynamical responses of FG beams using sparse patches," arXiv preprint, Jul. 2024.
16. **E. Madenci, S. Baloğlu, and H. Şimşek**, "Buckling of FG-CNTRC sandwich beams:

experiment and theory," Heliyon, vol. 10, e25119, 2024.
17. **Y. Lv, J. Zhang, and L. Li**, "Thermal buckling of multilayer GPL-reinforced FG beams on nonlinear elastic foundations," Heliyon, vol. 9, e19549, 2023.
18. **G. Zhang, Y. Hao, Z. Guo**, "Thermal buckling of FG-MEE microbeams using a third-order nonclassical beam theory," Mech. Solids, vol. 59, pp. 1475–1495, 2024.
19. **D. Indronil, R. Sen, and S.N. Saha**, "Nonlocal stress-driven analysis of bidirectional FG nano-beams," Heliyon, vol. 10, e20768, 2024.
20. **M. Alimoradzadeh, H. Heidari, F. Tornabene, and R. Dimitri**, "Thermo-mechanical buckling of FG-FRCL beams," Appl. Sci., vol. 13, art. 4904, 2023.
21. **J. Yang and S. Kitipornchai**, "Post-buckling of FG beams reinforced with CNTs," Compos. Struct., vol. 93, pp. 322–330, 2011.
22. **Y. Wang and F. Li**, "Vibration and buckling of porous FG beams," Compos. Part B, vol. 120, pp. 31–43, 2017.
23. **H. Su and J. Zhao**, "Nonlinear thermal buckling of porous FG beams reinforced by GPL," Appl. Math. Mech., vol. 41, pp. 933–949, 2020.
24. **R. Nasirzadeh, B. Behjat, and M. Kharazi**, "Thermal buckling of FG piezoelectric beams," J. Theor. Appl. Mech., vol. 56, no. 4, pp. 1097–1108, 2018.
25. **I.M. Şimşek and V. Kahya**, "Buckling of FG sandwich beams on elastic foundations via quasi-3D theory," Sigma J. Eng. Nat. Sci., vol. 43, no. 1, pp. 47–61, 2025.
26. **A. Majumdar and D. Das**, "Thermal buckling load of clamped FG beams under nonlinear thermal gradients," Proc. IMechE Part C, vol. 232, no. 12, pp. 2104–2116, 2018.
27. **S.D. Akbaş**, "Thermal post-buckling of laminated sandwich beams under nonlinear temperature rise," Compos. Struct., vol. 152, pp. 889–899, 2016.
28. **M. Omidi and M.R. Eslami**, "Thermal buckling of symmetric laminated beams," Thin-Walled Struct., vol. 49, no. 12, pp. 1510–1519, 2011.
29. **Y. Fu, Y. Chen, and P. Zhang**, "Thermal buckling of FG beams with longitudinal crack," Meccanica, vol. 48, pp. 1227–1237, 2013.
30. **A. Paul and D. Das**, "Post-buckling of tapered Timoshenko FG beams under thermal load," Proc. IMechE Part C, vol. 231, pp. 2297–2306, 2017.
31. **N. Challamel and J.M. Reddy**, "Nonlocal thermal buckling of nano-beams," Int. J. Eng. Sci., vol. 49, pp. 1452–1464, 2011.
32. **R. Reddy and Y. Kiani,** "Nonlocal thermal buckling of FG beams with varying cross-sections," Compos. Struct., vol. 128, pp. 410–423, 2015.
33. **H. Murmu and S.P. Adhikari**, "Nonlocal thermal post-buckling of nano-beams," J. Appl. Phys., vol. 109, no. 6, pp. 064313, 2011.
34. **H.T. Thai**, "Review of higher-order theories for FG beams," Int. J. Mech. Sci., vol. 62, pp. 57–66, 2012.
35. **W. Chen and Y. Chen,** "Thermal buckling of FG beams with temperature-dependent material properties," J. Appl. Comput. Mech., vol. 6, no. 2, pp. 123–134, 2020.
36. **A. Naghsh and M. Azhari**, "Thermal buckling of point-supported laminated members," Appl. Math. Model., vol. 63, pp. 512–526, 2018.
37. **C. Valencia Murillo, M. Gutierrez Rivera, and L.D. Celaya Garcia**, "Thermal–structural static analysis of FG beams," Math. Comput. Appl., vol. 28, art. 84, 2023.
38. **L. Li and J. Zhang,** "Thermal stability of GPL-reinforced FG beams," Heliyon, vol. 9, no. 9, e19549, 2023.
39. **S. Ke, J. Yang, and S. Kitipornchai**, "Thermal post-buckling of FG porous beams," Compos. Struct., vol. 138, pp. 153–160, 2016.

40. **R. Ebrahimi and A. Rastgoo**, "Thermal buckling of FG beams with nonlinear foundation," Mech. Adv. Mater. Struct., vol. 22, no. 3, pp. 192–201, 2015.
41. **X. Li and Y. Fu**, "Flexural vibration of FG porous beams under thermal field," Compos. Part B, vol. 182, art. 107648, 2020.
42. **P. Malekzadeh and H. Heydarpour**, "3D elasticity solution for thermal vibration of FG beams," Int. J. Mech. Sci., vol. 68, pp. 1–11, 2013.
43. **Z. Wang and Q. Yang,** "Thermal post-buckling of laminated beams under different temperature rises," Thin-Walled Struct., vol. 127, pp. 773–783, 2018.
44. **Y. Kiani and M.R. Eslami,** "Thermal buckling of porous FG beams," Meccanica, vol. 48, pp. 1091–1101, 2013.
45. **A. Arefi and M. Rahimi**, "Electro-thermo-mechanical buckling of FG beams," Compos. Struct., vol. 141, pp. 133–142, 2016.
46. **M. Shahba and M.R. Eslami**, "Thermal vibration of FG beams with non-uniform cross-sections," Compos. Part B, vol. 43, pp. 1523–1530, 2012.
47. **N. Challamel**, "Buckling of FG nano-beams using nonlocal Timoshenko theory," Mech. Res. Commun., vol. 37, pp. 383–388, 2010.
48. **Y. Chen and Y. Fu**, "Thermal buckling of axially graded beams under temperature rise," Compos. Struct., vol. 100, pp. 327–335, 2013.
49. **M. Malikan and H. Mahmoudi**, "Viscoelastic thermal buckling of FG nano-beams," Physica E, vol. 93, pp. 223–231, 2017.
50. **Z. Zidi and L. Hadji**, "Thermal buckling of FG beams using sinusoidal shear deformation theory," Struct. Eng. Mech., vol. 62, no. 4, pp. 465–474, 2017.
51. **S.S. Mohammadi**, "Flexural analysis of porous FG beams using HSDT," Compos. Struct., vol. 220, pp. 718–727, 2019.
52. **M.M. Aydogdu**, "Thermal buckling of FG beams with shear effects," Int. J. Struct. Stab. Dyn., vol. 15, no. 8, 2015.
53. **R.D. Batra and J. Yang**, "Thermoelastic post-buckling of FG beams under mechanical loads," Compos. Struct., vol. 95, pp. 223–231, 2013.
54. **T. Vo and H.T. Thai**, "Refined beam theory for buckling of FG beams," Appl. Math. Model., vol. 38, no. 9–10, pp. 2434–2445, 2014.
55. **H. Su and W. Chen**, "Thermal post-buckling analysis of FG porous beams," Meccanica, vol. 55, no. 2, pp. 371–384, 2020.
56. **S. Pradhan**, "Thermal post-buckling of FG beams using differential quadrature," Struct. Eng. Mech., vol. 42, pp. 45–56, 2012.
57. **K. Li and F.** Chen, "Thermal stability of tapered FG beams under axial load," Compos. Struct., vol. 220, pp. 248–259, 2019.
58. **R. Xu and J. Yang,** "Thermal post-buckling of porous FG CNT beams," Appl. Math. Mech., vol. 42, pp. 815–829, 2021.
59. **X. Zhao**, "Post-buckling of FG beams under thermal gradient," Thin-Walled Struct., vol. 146, art. 106426, 2020.
60. **M. Ali and T. Abedini**, "Size-dependent thermal buckling of FG nano-beams," Physica E, vol. 132, art. 114769, 2021.
61. **Z. Lin and Y. Fu,** "Thermal flexural vibration of FG beams with porosity," Meccanica, vol. 56, pp. 215–228, 2021.
62. **L. Hadji and S.A.A. Bakora**, "New higher-order shear deformation model for FG beams," KSCE J. Civ. Eng., vol. 20, no. 4, pp. 1521–1530, 2016.
63. **R. Khalili and H. Ghorbanpour**, "Thermal post-buckling of FG Timoshenko beams," Struct. Eng. Mech., vol. 70, no. 5, pp. 555–568, 2019.
64. **V. Kahya,** "Thermal vibration and buckling of FG sandwich beams," Sigma J. Eng. Nat. Sci., vol. 42, no. 3, pp. 171–184, 2024.

65. **Z. Zhang and X. Li**, "Thermal vibration of FG beams with nonlinear temperature rise," Compos. Part B, vol. 202, art. 108439, 2020.
66. **A. Bayat and A.M. Arabi**, "Buckling and flexural vibration of porous FG beams," Compos. Struct., vol. 185, pp. 142–153, 2018.
67. **K. J. Reddy,** "Thermal buckling of laminated beams using finite strip method," Thin-Walled Struct., vol. 98, pp. 456–463, 2016.
68. **S. Hosseini and F. Li,** "Flexural thermal post-buckling of porous FG beams," Appl. Math. Mech., vol. 43, pp. 345–361, 2022.
69. **J. Yang, Y. Xiang**, "Thermal post-buckling of FG beams under mechanical loads," Compos. Struct., vol. 108, pp. 472–482, 2014.
70. **A. Civalek and M. Demir**, "Size-dependent thermal buckling of FG porous microbeams," Eur. J. Mech. A/Solids, vol. 82, art. 103997, 2020.
71. **P. Liu and X. Zhao,** "Thermal flexure of FG beams with non-uniform porosity," Struct. Eng. Mech., vol. 79, pp. 311–324, 2021.
72. **T. Zhao and J. Zhang**, "Thermal buckling of FG sandwich beams with CNTs," Compos. Part B, vol. 210, art. 108618, 2021.
73. **F. Ahmadi**, "Electro-thermo-mechanical vibration of FG beams with piezo-layers," Compos. Struct., vol. 176, pp. 814–823, 2017.
74. **Y. Guo and H. Su**, "Thermal post-buckling of FG beams with varying porosity distributions," Meccanica, vol. 55, pp. 413–425, 2020.
75. **L. Tang and X. Lu,** "Thermal post-buckling and nonlinear vibration of FG beams on elastic foundation," Int. J. Struct. Stab. Dyn., vol. 20, no. 6, 2020.
76. **M. Rashidi**, "Post-buckling of FG beams using p-version FEM," Finite Elem. Anal. Des., vol. 144, pp. 62–73, 2018.
77. **K. Rahmani and M. Malikan**, "Size-dependent thermal buckling of porous FG micro-beams," Int. J. Eng. Sci., vol. 153, art. 103338, 2020.
78. **A. Baz and Y. Li,** "Thermal vibration of FG beams with damping layers," Smart Mater. Struct., vol. 24, no. 8, 2015.
79. **J. He and X. Wang**, "Thermal post-buckling analysis of FG porous beams using Ritz method," Struct. Eng. Mech., vol. 61, pp. 493–505, 2017.
80. **L. Sun and P. Zhang**, "Thermal buckling and vibration of FG porous beams under various boundary conditions," Thin-Walled Struct., vol. 176, art. 109297, 2022.
81. **Y. Zhao and H. Zhang**, "Dynamic thermal buckling of FG beams under harmonic heating," Int. J. Nonlinear Mech., vol. 121, art. 103428, 2020.
82. **W. Chen and Y. Lv,** "Nonlinear thermal vibration of FG beams," Compos. Struct., vol. 180, pp. 74–83, 2017.
83. **H. Li, Z. Liu, and J. Yang**, "Thermal post-buckling of FG beams with viscoelastic foundation," Appl. Math. Model., vol. 63, pp. 22–35, 2018.
84. **J. Zhang and Y. Li,** "Post-buckling of FG porous beams on nonlinear elastic foundations," Meccanica, vol. 56, pp. 901–913, 2021.
85. **R. Reddy and L. Ke,** "Nonlinear vibration of FG beams under thermal field," Compos. Struct., vol. 129, pp. 123–133, 2015.
86. **X. Wu and H. Wang,** "Size-dependent thermal vibration of FG micro-beams," Int. J. Eng. Sci., vol. 157, art. 103385, 2020.
87. **A. Farokhi and M. Shahba**, "Thermal vibration of FG beams using a refined beam theory," Struct. Eng. Mech., vol. 59, no. 3, pp. 511–524, 2016.
88. **K. Xie and W. Chen**, "Thermal flexure of laminated FG sandwich beams," Compos. Struct., vol. 182, pp. 457–466, 2017.
89. **L.E. Chen**, "Buckling of FG porous beams using new quasi-3D theory," Struct. Eng. Mech., vol. 65, pp. 311–322, 2018.

90. **V. Kahya and M. Şimşek**, "Thermal vibration and buckling of FG sandwich beams on elastic foundations," Sigma J. Eng. Nat. Sci., vol. 42, no. 3, 2024.
91. **Z. Zhou and P. Li**, "Thermal post-buckling of FG sandwich beams with porous core," Compos. Part B, vol. 234, art. 109754, 2022.
92. **J. Li, H. Wu, and X. Zhao**, "Dynamic thermal buckling of FG porous beams," Int. J. Mech. Sci., vol. 187, art. 105936, 2020.
93. **Y. Lin and Z. Xu**, "Flexural vibration of FG CNT-reinforced beams under thermal gradient," Compos. Struct., vol. 246, art. 112378, 2020.
94. **P. Raj, M. Malikan**, "Visco-thermoelastic post-buckling of FG nano-beams," Physica E, vol. 120, art. 114008, 2020.
95. **F. Afshari and A. Ghasemi**, "Thermal buckling of laminated FG beams with shear effect," Thin-Walled Struct., vol. 152, art. 106701, 2020.
96. **G. Chen, S. Wu, and H. Wu**, "Nonlocal thermoelastic vibration of FG porous beams," Compos. Struct., vol. 273, art. 114335, 2021.
97. **S. Mohammadi and J. Karim**, "Nonlinear thermal vibration of laminated FG beams," Int. J. Struct. Stab. Dyn., vol. 21, no. 6, art. 2150064, 2021.
98. **B. Yuan and Y. Chen,** "Dynamic thermal buckling of FG porous beams with damping," Compos. Part B, vol. 248, art. 110380, 2023.
99. **J. Zhang, P. Zhou, and L. Li,** "Post-buckling and thermal vibration of FG sandwich beams under nonlinear temperature rise," Meccanica, vol. 59, pp. 147–161, 2024.
100. **İ.M. Şimşek and V. Kahya,** "Free vibration and buckling analysis of FG sandwich beams resting on a two-parameter elastic foundation using a quasi-3D theory," Sigma J. Eng. Nat. Sci., vol. 43, no. 1, pp. 47–61, 2025.

Rahul D. Kapase – Assistant Professor, Symbiosis Institute of Technology, Symbiosis International (Deemed University); Lavale, Mulshi, Pune – 412115, Maharashtra, India. e-mail: rahulkapase444@gmail.com.

Sanjay Kulkarni – Professor, Department of Civil Engineering, Symbiosis Institute of Technology, Symbiosis International (Deemed University); Lavale, Mulshi, Pune – 412115, Maharashtra, India.
e-mail sanjay.kulkarni@sitpune.edu.in.

Рахул Д. Капасе – доцент (Assistant Professor), Институт технологий Симбиоз (Symbiosis Institute of Technology), Международный университет Симбиоз (Symbiosis International (Deemed University)); Лавале, Мулши, г. Пуна – 412115, штат Махараштра, Индия.
e-mail: sanjay.kulkarni@sitpune.edu.in

Санджай Кулкарни – профессор кафедры гражданского Института технологий Симбиоз, Международный университет); Лавале, Мулши, г. Пуна – 412115, штат Махараштра, Индия. e-mail: sanjay.kulkarni@sitpune.edu.in

DOI:10.22337/2587-9618-2026-22-3-63-75

OPTIMIZATION OF THE MAIN RIGIDITY PLANES POSITION OF INHOMOGENEOUS ROD IN SPATIAL BENDING

Andrey V. Mishchenko [1], ***Maxim S. Veshkin*** [1], ***Vladimir L. Mondrus*** [2], ***Leonid Yu. Stupishin*** [2]

[1] Novosibirsk State University of Architecture and Civil Engineering (Sibstrin), Novosibirsk, RUSSIA
[2] National Research Moscow State University Of Civil Engineering, Moskow, RUSSIA

Abstract: The problem of finding the optimal rotation angle of the principal planes of stiffness for a spatially loaded, inhomogeneous rod of variable cross-section is considered. This angle serves as an additional regulator of the stress state for inhomogeneous rod designed in accordance with the adopted optimization criteria.
The rod rigidly connected to a movable coordinate system capable of rotation around rod's longitudinal axis is composed of quasi-homogeneous structural elements. The rod's structure is symmetrical with respect to one of the plane coordinates. The specified loads are applied to the rod's centerline and are located in two mutually perpendicular fixed planes.
Based on the minimum strain energy criterion, a formula for the optimal rotation angle of the rod's rigidity planes was derived. This formula contains six integral strain energy components. These components represent the actual and potential work of internal forces in the original rigidity planes and those rotated by 90 degrees. A numerical example shows strain energy graphs for cross-sections with different layouts. The relationship between the energy criterion and the strength criterion is highlighted.
Based on the minimum strain energy criterion, a formula for the optimal rotation angle of the rod 's rigidity planes was derived. This formula contains six integral strain energy components. These components represent the actual and possible work of internal forces initial rigidity planes and those rotated by 90 degrees. A numerical example shows strain energy graphs for cross sections with different layouts. The relationship between the energy criterion and the strength criterion is noted.
In the example discussed, using axial rotation of the rod, without requiring changes to its physical structure or geometry, allows for an increase in its load-bearing capacity by 20-30% and a reduction in maximum stress levels. This method can also be applied to prefabricated standard structural elements, including homogeneous ones.
In the example discussed, the use of axial rotation of the rod, without requiring changes to its physical structure or geometry, allowed for an increase in its load-bearing capacity by 20-30% and a reduction in maximum stress levels. This method can also be applied to prefabricated standard structural elements, including homogeneous ones.
The development of this method is its application in “controlled structures”, which acquire the ability to effectively adapt to changes in the parameters of external force impact.

Keywords: optimal design of inhomogeneous rods, layered rod, spatial bending, criterion of minimum strain energy, controlled structures

ОПТИМИЗАЦИЯ ПОЛОЖЕНИЯ ГЛАВНЫХ ПЛОСКОСТЕЙ ЖЕСТКОСТИ НЕОДНОРОДНОГО СТЕРЖНЯ ПРИ ПРОСТРАНСТВЕННОМ ИЗГИБЕ

А.В. Мищенко [1], ***М.С. Вешкин*** [1], ***В.Л. Мондрус*** [2], ***Л.Ю. Ступишин*** [2]

[1] Новосибирский государственный архитектурно-строительный университет (Сибстрин), г. Новосибирск, РОССИЯ
[2] Национальный исследовательский Московский государственный строительный университет, г. Москва, РОССИЯ

Аннотация: Для пространственно-нагруженного неоднородного стержня переменного поперечного сечения рассмотрена задача нахождения оптимального угла поворота главных плоскостей жёсткости. Данный угол является дополнительным регулятором напряженного состояния для неоднородного стержня, запроектированного в соответствии с принятыми критериями оптимизации.

Стержень составлен из квазиоднородных структурных элементов, жестко связан с подвижной системой координат, способной поворачиваться вокруг продольной оси. Структура стержня обладает симметрией относительно одной из координатных плоской. Заданные нагрузки приведены к осевой линии стержня, расположены в двух взаимно перпендикулярных неподвижных плоскостях.
На основе критерия минимума энергии деформации получена формула для оптимального угла поворота плоскостей жесткости стержня, содержащая шесть интегральных компонент энергии деформации. Они представляют собой действительные и возможные работы внутренних усилий в исходных и повернутых на угол 90 градусов плоскостях жесткости. На численном примере показаны графики энергии деформации для поперечных сечений с различной компоновкой. Отмечена связь энергетического критерия с критерием прочности.
Применение осевого поворота стержня, не требуя изменения физической структуры и геометрии стержня, в рассмотренном примере позволяет повысить его несущую способности на величину 20-30%, снизить уровень максимальных напряжений. Данный способ может применяться и к готовым типовым конструктивным элементам, в том числе, – однородным.
Развитием данного метода является его применение в «управляемых конструкциях», которые приобретают способность эффективно адаптироваться к изменениям параметров внешнего силового воздействия.

Ключевые слова: оптимальное проектирование неоднородных стержней, слоистый стержень, пространственный изгиб, критерий минимума энергии деформации, управляемые конструкции

INTRODUCTION

Settings of optimization problems for deformable systems and structures used in various branches of engineering are quite diverse and are determined by the adopted optimality criteria and the types of variable parameters and functions [1–4]. In rod systems, one of the key means of improving operational performance is the optimization of the geometry, physical structure, and topology of the system [5]. Significant effects are also achieved by selecting a rational arrangement of the cross-sections of the elements. Among the formulations of optimization problems in which the geometric shapes of structural elements subject to various types of impacts are varied, we note the following.

Settings with using geometric shapes that profile the transverse dimensions of structural elements of rods (width, height, thickness, etc.), specified with an accuracy of one or more parameters [6]. A subclass of such task are optimization problems for prismatic rods, in which the geometric shape functions are of zero order. The use of local normative criteria for finding the required values of the sought-after parameters in such problems with fixed shapes leads to the need to identify dangerous stress localizations within the structure.

In more complex settings, the desired geometric functions of the structural elements of the rods are found under the condition of continuous satisfaction of specified normative local criteria. This is a class of equal-criteria problems, in particular, those concerning equal stress [2, 7, 8]. In general, such problems (of functional analysis) are characterized by high labor intensity and, as a rule, for real structures are solved by numerical methods using discretization of the calculation functions.

Normative criteria, reflecting the relationship between the desired design parameters and the standardized quantities, can be integral in nature, as is realized in problems of stability, vibration, deformability, and a number of others, solved based on the corresponding boundary value problems. In these problems, the defining differential and integral relations naturally define the essence of the quantities included in the normative criteria. Depending on the type of variable quantities, we have variational or finite-dimensional optimization [3].

In a number of studies, the solution is based on the use of integral criteria reflecting additional requirements for the optimal system, which have technical, economic, general physical, or other sense. One of these is the integral energy criterion, which allows for identifying the geometric shape, structure, and topology of the system that best satisfies the requirements of design standards [9, 10, 11, 12].

When solving optimization problems for inhomogeneous structures, the calculation hypothe-

ses and assumptions adopted during the formation of the mathematical model acquire particular significance. Along with refined non-classical models [13–18], models based on the Bernoulli and Timoshenko hypotheses can also be used in the calculations of elements of rod structures that satisfy certain geometric and physical constraints.

In this paper, we consider the problem of finding the optimal rotation angle of the rod's principal rigidity planes for a spatially loaded, inhomogeneous rod of variable cross-section. This angle acts as an additional regulator of the stress state. In subsequent or previous stages, the set of variable values can be expanded to expand the functionality of the rod's geometric and physical structure.

MATERIALS AND METHODS OF RESEARCH

1. Mathematical model of inhomogeneous rod.

An inhomogeneous rod composed of quasi-homogeneous structural elements (layers, phases, inclusions, reinforcing elements, etc.) is rigidly connected to the coordinate system xyz, and the rod's structure is symmetrical with respect to the plane yx. The specified loads are referenced to the rod's centerline and are located in two mutually perpendicular fixed planes y_0x, z_0x. We will assume the coordinate system xyz to be movable, capable of rotating around the axis through a certain angle α, together with the rod (Fig. 1).

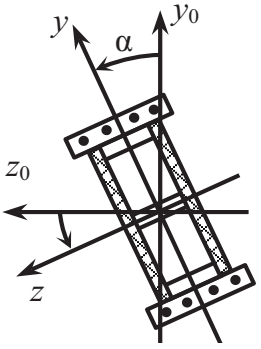


Figure 1. Rotation of the principal planes of rigidity xy, xz relative to the force planes y_0x, xz_0.

By solving the corresponding boundary value problems of spatial transverse bending with tension (compression), the functions of internal forces are found - bending moments, transverse and longitudinal forces, combined into a vector

$$\mathbf{S}_0(x) = [M_{z_0}, M_{y_0}, Q_{y_0}, Q_{z_0}, N]^{\mathrm{T}}(x).$$

Considering that the boundary conditions for the rod do not change when the transverse axes y, z are rotated relative to the centerline, we write down the forces in the coordinate system xyz

$$\mathbf{S}(x) = \mathbf{C}\,\mathbf{S}_0(x),$$
$$\mathbf{S}(x) = [M_z, M_y, Q_y, Q_z, N]^{\mathrm{T}}(x), \qquad (1)$$
$$\mathbf{C} = diag[\mathbf{\Phi}\ \ \mathbf{\Phi}\ \ 1],\ \mathbf{\Phi} = \begin{bmatrix} \cos\alpha & \sin\alpha \\ -\sin\alpha & \cos\alpha \end{bmatrix}.$$

In works [19, 20] for the Timoshenko rod, physical relations are given that connect the forces (1) with the generalized deformations of the axis: curvatures κ_z, κ_y, averaged shears γ_{y0}, γ_{z0}, and axial deformation ε_0. Let us represent them in the form

$$\mathbf{D}\cdot\mathbf{\Delta} = \mathbf{S}, \qquad (2)$$
$$\mathbf{\Delta}(x) = [\kappa_z, \kappa_y, \gamma_y, \gamma_z, \varepsilon_0]^{\mathrm{T}}(x) \qquad (3)$$

with a stiffness matrix

$$\mathbf{D}(x) = \begin{bmatrix} D_{zz} & -D_{yz} & 0 & 0 & -D_z \\ -D_{yz} & D_{yy} & 0 & 0 & D_y \\ 0 & 0 & D_{Qy} & 0 & 0 \\ 0 & 0 & 0 & D_{Qz} & 0 \\ -D_z & D_y & 0 & 0 & D_0 \end{bmatrix}, \qquad (4)$$

containing components

$$D_0 = \sum_{k=1}^{s} E_k \iint_{A_k} dA, \quad \left[D_z, D_y\right] = \sum_{k=1}^{s} E_k \iint_{A_k} [y,z]\,dA, \quad \left[D_{zz}, D_{zy}, D_{yy}\right] = \sum_{k=1}^{s} E_k \iint_{A_k} \left[y^2, yz, z^2\right] dA \tag{5}$$

by zero, first, and second geometric orders, respectively. The characteristic D_{yz} for the adopted calculation scheme in relations (2) is missing. The presence of stiffnesses D_z, D_y determines the coupling of bending and stretching deformations. The stiffnesses of cross sections under shear

$$D_{Qy} = \frac{1}{\sum_{k=1}^{s} \frac{1}{G_k} \int_{y_k}^{y_{k+1}} \left(\frac{D_0 D_z^{\text{sec}} - D_z D_0^{\text{sec}}}{D d_z} \right)^2 \frac{dy}{b_k}}, \quad D_{Qz} = \frac{1}{\sum_{k=1}^{s} \frac{1}{G_k} \int_{z_k}^{z_{k+1}} \left(\frac{D_0 D_y^{\text{sec}} - D_y D_0^{\text{sec}}}{D d_y} \right)^2 \frac{dy}{h_k}}, \quad D d_z = D_0 \cdot D_{zz} - D_z^2, \quad D d_y = D_0 \cdot D_{yy} - D_y^2 \tag{6}$$

are written using the rigidity characteristics of the cut-off parts of the inhomogeneous sections D^{sec} according to the corresponding expressions from (5) when integrating over a part of the section $[y, y_{\max}]$ or $[z, z_{\max}]$.

In addition, to find the shear stiffness characteristics, an approximate approach can be used based on the use of approximation functions for the relative shear forces $f_{y,\tau}(y)$, $f_{z,\tau}(z)$, satisfying the boundary conditions on the rod surfaces. As a result, we obtain the second version of the dependencies for shear stiffnesses

$$D_{Qy} = \frac{F_{y,\tau}^{\ 2}}{\sum_{k=1}^{s} \int_{y_k}^{y_{k+1}} \frac{f_{y,\tau}^{\ 2}}{b_k G_k} dy}, \quad D_{Qz} = \frac{F_{z,\tau}^{\ 2}}{\sum_{k=1}^{s} \int_{z_k}^{z_{k+1}} \frac{f_{z,\tau}^{\ 2}}{h_k G_k} dz}.$$

The symmetry of the rod relative to the plane yx ensures the fulfillment of the conditions $D_y = D_{yz} = 0$. In addition, we will assume that the structure of the variable cross-section rod is such that it allows the rod to be tied to the plane xz while ensuring the condition $D_z(x) \equiv 0$. Due to the dependence of characteristics (5), (6) on geometric and physical parameters, this condition can be satisfied even in the absence of geometric symmetry. Then from (2) we obtain

$$D_{zz}\kappa_z = M_z, \quad D_{yy}\kappa_y = M_y, \quad D_0\varepsilon_0 = N.$$

2. Optimality criterion

As a criterion for the optimality of the parameters of an inhomogeneous rod, we will adopt the condition of minimum deformation energy [6, 9, 11]

$$W(\mathbf{P}) = \frac{1}{2}\int_0^l \mathbf{S}^{\mathrm{T}} \boldsymbol{\Delta}\, dx \to \min. \tag{7}$$

The set of variable parameters $\mathbf{P}$ in the case under consideration is represented by the rotation angle α. Substituting relations (2)–(4) into (7) gives the dependence of the deformation energy on the rotation angle of the axes

$$W(\alpha) = (W_{yy}^{\alpha=0} + W_{zz}^{\alpha=0})\cos^2\alpha + (W_{zy} - W_{yz})\sin 2\alpha + (W_{yy}^{\alpha=\pi/2} + W_{zz}^{\alpha=\pi/2})\sin^2\alpha + \frac{1}{2}\int_0^l \frac{N^2}{D_0} dx. \tag{8}$$

The energy components in (8) are determined by the expressions

$$W_{yy}^{\alpha=0} = \frac{1}{2}\int_0^l \frac{M_{z_0}^2}{D_{zz}} dx + \frac{1}{2}\int_0^l k_y \frac{Q_{y_0}^2}{D_{Q_y}} dx, \quad W_{zz}^{\alpha=0} = \frac{1}{2}\int_0^l \frac{M_{y_0}^2}{D_{yy}} dx + \frac{1}{2}\int_0^l k_z \frac{Q_{z_0}^2}{D_{Q_z}} dx,$$

$$W_{yy}^{\alpha=\pi/2}=\frac{1}{2}\int_0^l\frac{M_{z_0}^2}{D_{yy}}dx+\frac{1}{2}\int_0^l k_z\frac{Q_{y_0}^2}{D_{Q_z}}dx,$$
$$W_{zz}^{\alpha=\pi/2}=\frac{1}{2}\int_0^l\frac{M_{y_0}^2}{D_{zz}}dx+\frac{1}{2}\int_0^l k_y\frac{Q_{z_0}^2}{D_{Q_y}}dx, \quad (9)$$
$$W_{yz}=\int_0^l\frac{M_{z_0}M_{y_0}}{D_{yy}}dx+\int_0^l k_z\frac{Q_{y_0}Q_{z_0}}{D_{Q_z}}dx,$$
$$W_{zy}=\int_0^l\frac{M_{y_0}M_{z_0}}{D_{zz}}dx+\int_0^l k_y\frac{Q_{z_0}Q_{y_0}}{D_{Q_y}}dx$$

and have the following mechanical meaning: $W_{yy}^{\alpha=0}$, $W_{zz}^{\alpha=0}$ are the actual works of the forces acting in the force planes y_0x, z_0x respectively, in the absence of rotation of the rod ($\alpha=0$); $W_{yy}^{\alpha=\pi/2}$, $W_{zz}^{\alpha=\pi/2}$ are the actual works of the forces acting in the force planes y_0x, z_0x respectively, when the rod is rotated by an angle $\alpha=\pi/2$; W_{yz}, W_{yz} are the possible works of the forces acting in the force planes y_0x, y_0x respectively, on the deformations of the inhomogeneous rod in the orthogonal planes z_0x, y_0x, caused by other force factors.

The minimum energy (8) is achieved at a rotation angle α_{opt}, for which the condition is satisfied

$$tg2\alpha_{\text{opt}}=\frac{W_{zy}-W_{yz}}{W_{yy}^{\alpha=0}+W_{zz}^{\alpha=0}-W_{yy}^{\alpha=\pi/2}-W_{zz}^{\alpha=\pi/2}}. \quad (10)$$

In [8], a variational setting of the optimization problem for a homogeneous spatially loaded flat frame was considered with variations in the external dimensions of the box-shaped cross-section and the angular position of the principal axes of inertia. The volume of materials was fixed. The following criteria were adopted as continuous in the direction of the axial coordinate: the strength condition for normal stresses and the condition of coincidence of the principal axis of inertia with the vector of the resulting bending moment. As a result, it was shown that adopting local criteria leads to a natural (initial) twisting of the rods. The resulting solutions are of some theoretical interest, however, such designs are characterized by high labor intensity of production and sensitivity to load variations, which reduces the feasibility of their practical use.

In contrast, formula (10) reflects the integral average value of rational local transformations of forces on the main planes of rigidity of an inhomogeneous rod, in the form of rotation of the main planes of rigidity by a general angle α_{opt}.

A number of special cases follow from the considered setting.

1. When the conditions $D_{zz}=D_{yy}$, $D_{Q_y}=D_{Q_z}$ are simultaneously met the deformation energy (8) becomes stationary – $W(\alpha)=\text{const}$, independent of the rotation angle α.

2. The arrangement of loads in a single force plane. By combining it with, for example, plane y_0x, we obtain $M_{y_0}=Q_{z_0}=0$, which leads to the fulfillment of $W_{zz}^{\alpha=0}=W_{zz}^{\alpha=\pi/2}=W_{yz}=W_{zy}=0$ and optimal angle $\alpha_{\text{opt}}=0$ at $D_{zz}>D_{yy}$ and $\alpha_{\text{opt}}=\pi/2$ at $D_{zz}<D_{yy}$.

3. If the following conditions are met for the calculation model: a) the presence of symmetry in the stiffness characteristics relative to the midsection ($x=l/2$), b) the functions of the forces acting in one of the force planes have the properties of direct symmetry, and in the other (orthogonal to the first) – inverse symmetry, then we obtain a zero value of the possible works W_{yz}, W_{zy} and angles $\alpha_{\text{opt}}=0$, $\alpha_{\text{opt}}=\pi/2$. The plane with large stiffness characteristics should be combined with the force plane in which forces acting with direct symmetry.

4. In rods with a constant cross-section (in geometry and structure), with a simplified consideration of only one force factor (*M* or *Q*) in the energy components (9), formula (10) yields two fixed values of the angle α_{opt}, depending on a) the considered force functions (*M* or *Q*) and b) the results of comparing the corresponding stiffness characteristics ($D_{zz}<D_{yy}$ or $D_{zz}>D_{yy}$,

when taking M into account; $D_{Q_y} > D_{Q_z}$ or $D_{Q_y} < D_{Q_z}$, when taking Q into account). The absolute values of the stiffnesses in this case do not affect the value of the optimal angle. This is shown in the numerical example discussed below in Fig. 4.

5. The strain energy components in (9) have an integrand structure similar to Mohr integrals and can be calculated using known graphoanalytic methods. This is particularly applies to rods with constant stiffness characteristics along their length. These integrals can also be found numerically.

RESULTS AND DISCUSSION

Let us consider a inhomogeneous rod subjected to a force action in two orthogonal planes y_0x and z_0x (Fig. 2). The loads are specified with an accuracy of parameters q, l. Fig. 3 shows a scheme of a composite cross-section including four structural elements with numbers k = 1, 2, 3, 4.

Table 1 shows the geometric parameters, relative elastic moduli $e_k = E_k / E_0$ and strength characteristics $r_k = R_k / R_0$ of the materials for the section elements.

Table 1.

Parameters of structural elements of the section

k	**Width**	**Height**	e_k	r_k
1	2δ	b	0,9	1,4
2	h	δ	0,6	1,2
3	h	δ	0,6	1,2
4	2δ	0,8·b	1	1

Table 2.

Cross-section layout options

Option №	h	b	A	z_0	D_{yy}	D_{zz}
1	30·δ	10·δ	70·δ^2	16,54·δ	11400,7·δ^4	679,3·δ^4
2	20·δ	13,53·δ	70·δ^2	11,58·δ	6368,7·δ^4	1163,8·δ^4
3	10·δ	17,06·δ	70·δ^2	6,71·δ	2201,4·δ^4	1649,1·δ^4
4	8,48·δ	17,60·δ	70·δ^2	5,98·δ	1717,9·δ^4	1717,9·δ^4
5	7·δ	18,12·δ	70·δ^2	5,27·δ	1298,4·δ^4	1782,6·δ^4
6	5·δ	18,82·δ	70·δ^2	4,31·δ	815,4·δ^4	1866,6·δ^4

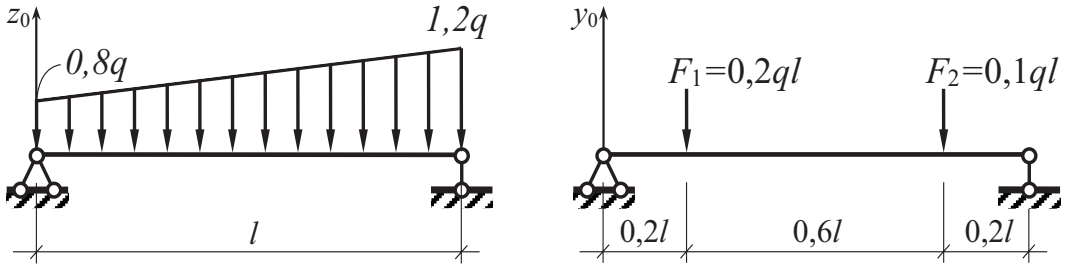


Figure 2. Given action: in plane z_0x, (a), in plane y_0x, (b)

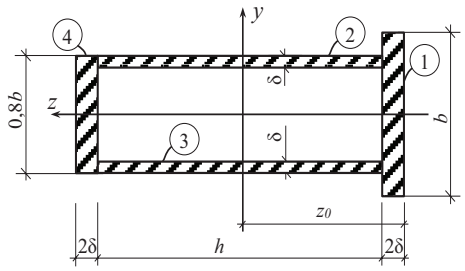


Figure 3. Cross-section of the rod in the initial position (α = 0)

We will do the research by specifying several cross-sectional layout options with varying dimensions *b* and *h*. We will also impose a constraint in the form of a constant cost of materials for the inhomogeneous rod.

$$C = l \cdot \sum_{k=1}^{4} c_k \gamma_k A_k = \text{const}, \qquad (11)$$

where A_k, c_k, γ_k is the cross-sectional area, specific cost and weight of the material of the *k*-th element.

Without diminishing the significance of the obtained results, we will adopt in this problem $c_k = \gamma_k = 1$, which transforms condition (11) into a condition of constancy of the total area $\sum_{k=1}^{4} A_k = \text{const}$. Table 2 presents six variants of similar cross-sectional arrangements with the area fixed $A = 70\delta^2$. For each of them, the coordinate of the center of rigidity z_0, ensuring the fulfillment of $D_y = 0$, and the bending rigidities D_{yy}, D_{zz}, were found. In the first three variants, the condition $D_{yy} > D_{zz}$ is satisfied, in the 4th – $D_{yy} = D_{zz}$, and in the 5th–6th – $D_{yy} < D_{zz}$.

Let us consider the problem of determining the optimal angle α_{opt} of rotation of the principal planes of rigidity, ensuring the minimum deformation energy of a spatially loaded inhomogeneous rod (Fig. 2) with six variants of cross sections (Tables 1, 2). We introduce dimensionless quantities

$$\bar{M} = \frac{M}{ql^2}, \quad \bar{Q} = \frac{Q}{ql},$$

$$\left[\bar{D}_{yy}, \bar{D}_{zz}\right] = \frac{1}{E_0\delta^4}\left[D_{yy}, D_{zz}\right],$$

$$\bar{W} = \frac{W \cdot E_0\delta^4}{q^2 l^5}, \quad \bar{\sigma}_x = \frac{\sigma_x \delta^3}{ql^2}, \quad \bar{\delta} = \delta \sqrt[3]{\frac{R_0}{ql^2}}.$$

After solving the boundary value problem and identifying the function of forces acting in the force planes y_0x, z_0x, the dimensionless deformation energy function $W(\alpha)$ (8) was formed. Its graph in the interval $\alpha \in [-\pi, \pi]$ is shown in Fig. 4. The lines numbers correspond to the numbers of the section variants in Table 2.

For variants 1–3, the optimal angles are contained in the interval $\alpha_{\text{opt}} \in [-\pi/8, -\pi/16]$, while for variants 5–6, they are $\alpha_{\text{opt}} \in [3\pi/8, 7\pi/16]$. In the first case, the cross-sections have $D_{yy} > D_{zz}$, which requires a negative (clockwise) rotation of the rod; in the second case, for variants with $D_{yy} < D_{zz}$, a rotation in the opposite direction is required. Since the specified materials do not possess the properties of different resistance under tension and compression, periodicity of the function $W(\alpha)$ is observed over an interval equal to π.

If the stiffnesses are equal $D_{yy} = D_{zz}$ (option 4), the rod becomes insensitive to the position of the principal stiffness planes $W(\alpha) = \text{const}$. Rotating them does not change the energy level. The best of the six section options is option 1; it corresponds to the lowest value of the deformation energy at the minimum point $\alpha_{\text{opt}} = -0{,}0864\pi = -15{,}6°$. Option 6 requires a rotation angle $\alpha_{\text{opt}} = 0{,}4136\pi = 74{,}5°$. The same angle values are obtained using the formula (10).

To illustrate the practical effect of rotating the rod by an angle, we will evaluate the level of normal stresses in cross section 1 (Table 2). When

conditions $D_z = D_y = 0$ are met, they are determined by the formula [19, 20]

$$\sigma_{x,k}^{(M)}(x,y,z) = \\ = E_k \left(-\frac{M_z(x)\cdot y}{D_{zz}} - \frac{M_y(x)\cdot z}{D_{yy}} \right). \qquad (12)$$

Taking into account the stress limitation by the value of the calculated resistances r_k (Table 1), it is convenient to monitor the level of relative dimensionless stresses $s_{k,j}(x) = \overline{\sigma}_{x,k}(x, y_j, z_j)/r_k$ in an inhomogeneous rod. For this purpose, Fig. 5 shows 16 graphs $s_{k,j}(x)$ $(k = 1,...,4,$ $j = 1,...,4)$ for four corner points taken in each of the four structural elements.

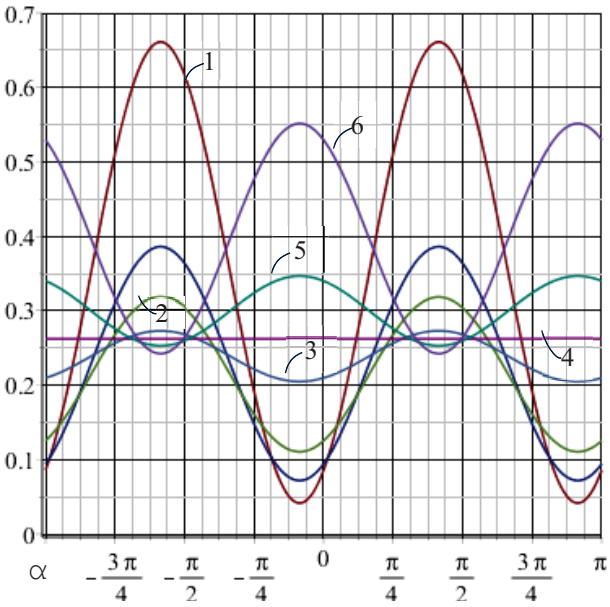


Figure 5. Dependence of the potential energy of deformation of a rod $\overline{W} \cdot 10^5$ on the angle of rotation of the rigidity planes for different cross-sectional options (Table 2)

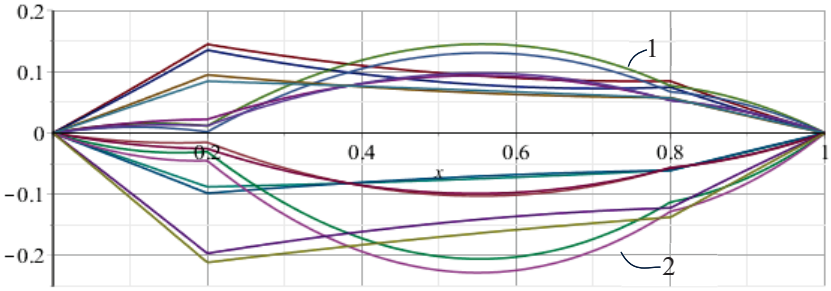


Figure 4. Graphs of relative stresses $10^3 \cdot s_{k,j}(x)$ at corner points of 4 structural elements of section 1, table 2 at $\alpha = \alpha_{opt}$.

The maximum relative stress is realized in graph 1, corresponding to the stress at point K of the first layer (Fig. 6).

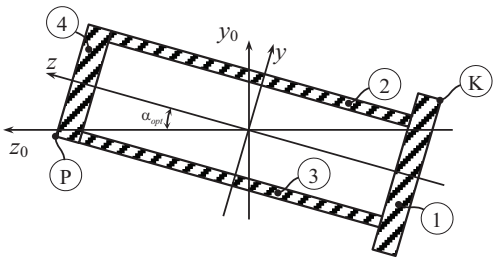


Figure 6. Optimal rotate of section 1 (Table 2) at the minimum value of deformation energy

The minimum is in graph 2, constructed for the stress at point P of the fourth layer. Taking point P as the design point – the point with the highest modulus of stress, from the strength condition

$$\delta \geq \delta_{\min} = \sqrt[3]{\frac{ql^2}{R_0} \max_{x,k,j} \left| s_{k,j}(x) \right|}$$

we find the required value of the geometric parameter $\overline{\delta}_{\min} = 0{,}0611$.

In this example, the settlement points are located at the corners of the outer contour of the section. Due to the discontinuity of stress functions (12) at the layer boundaries, with different physical characteristics, the settlement points may shift to the corners of the internal boundaries of the structural elements.

For comparison, we present the results corresponding to the initial position of the rod without rotation of the axes. Fig. 7 shows graphs of the relative stresses $s_{k,j}(x)$ acting in the same section 1 at the same 16 calculation points, at $\alpha = 0°$.

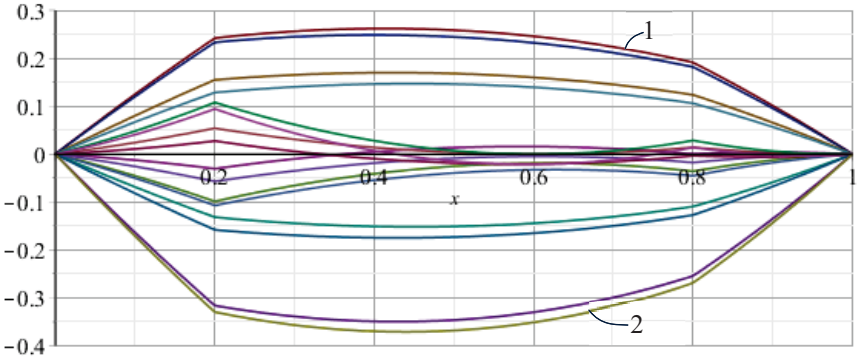


Figure 7. Graphs of relative stresses $10^3 \cdot s_{k,j}(x)$ at settlement points of section 1 at $\alpha = 0$

The required parameter value in this case was $\overline{\delta} = 0{,}0719$. Thus, setting the optimal rotate allowed us to reduce the size $\overline{\delta}$ by 15% and the volume of material by 38%.

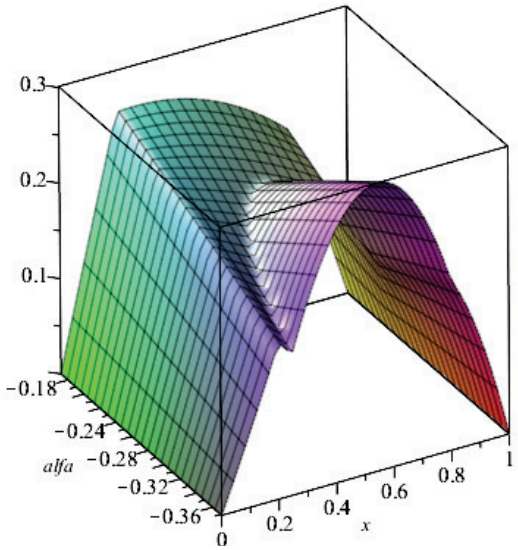


Figure 8. Dependency $10^3 \cdot \max\limits_{k,j} \left| s_{k,j}(\alpha, x) \right|$

In a number of studies, in particular in [21], it has been shown that as a result of the variational setting of optimization problems based on the energy criterion, when varying the geometric functions, equalization of stresses on the rod surface (at the layer boundaries) occurs. In this problem, solved without varying the geometry, continuous equalization of stresses does not occur (Fig. 5). However, here too, similar effects can be seen, manifested discretely in the form of equalization of local stress maxima. In Fig. 5, this is practically achieved for the greatest stresses in the cross-sections $x = 0{,}2$ and $x = 0{,}56$.

Fig. 8 shows a three-dimensional graph of relative stresses $\max\limits_{k,j} \left| s_{k,j}(\alpha, x) \right|$ as a function of x and angle α, which is the outer envelope of 16 surfaces – the moduli of stress constructed for the calculated points. Analysis of this surface allows us to formulate a criterion for minimizing local stress maxima.

$$\min_{\alpha} \left[\max_{k,j,x} \left| s_{k,j}(\alpha, x) \right| \right] \to \alpha_{\text{opt}}.$$

As a result of application it application, the optimal rod rotation angle was $\alpha_{\text{opt}} = -13{,}94°$ with a required strength dimension of $\overline{\delta}_{\sigma} = 0{,}0591$, resulting in a material savings of 32,4% compared to the design at $\overline{\delta} = 0{,}0719$ for the initial state at $\alpha = 0°$. With the determined rotation angle,

stresses are equalized at the two most heavily loaded points in the x-axis direction. One of these is located at the support $x = 0,2$, and the other is at the local span extremum at $x = 0,56$.

CONCLUSIONS

The use of rigid axial rotation of the rod as an external stress regulator is an effective additional optimization tool and allows for, in the example considered, allowed: a) increasing the load-bearing capacity of a inhomogeneous rod by 20–30% at a low cost, consisting of ensuring a specified fixed design position of the rod on the supporting devices; b) being an additional tool, it does not require changes to the physical structure and geometry of the rod, designed according to the optimization criteria. For this reason, this technique can also be applied to prefabricated standard structural elements, including homogeneous ones.

A significant advancement of this method is its application to "controlled structures," which, thanks to the presence of neural network systems, acquire the ability to effectively adapt to changes in external forces. To achieve this, the rod must be equipped with support devices capable of continuously adjusting the angular position of the rod's principal rigidity planes during operation. For the object in question – a inhomogeneous rod – implementing control systems is quite simple and feasible.

REFERENCES

1. **Banichuk N.V.** Optimization of the shape of elastic bodies. Moscow: Nauka, 1980. - 256 p.
2. **Perelmuter A.V.** Problems of synthesis in the theory of structures (a brief historical review) // Bulletin of Tomsk State University of Architecture and Civil Engineering. - 2016. - No. 2 (55). - pp. 70-106.
3. **Lyakhovich L.S., Perelmuter A.V.** Some issues of optimal design of building structures // International Journal for Computational Civil and Structural Engineering. 2014. Vol. 10. No. 2. pp. 14–23.
4. **Mohamadmahdi Ebrahimi, Mahdi Fakoor** Design-oriented fracture criteria for orthotropic composites based on minimum strain energy density theory // Theoretical and Applied Fracture Mechanics, Vol. 140, 2025, 105182, https://doi.org/10.1016/j.tafmec.2025.105182.
5. **Yuryev A.G., Nuzhny S.N.** Optimization of the topology of single-span single-story frames // Fundamental research. - 2013. No. 10-4. pp. 742-746.
6. **Mishchenko A.V., Veshkin M.S.** Application of the minimum deformation energy criterion in problems of rational profiling of inhomogeneous rods // News of universities. Construction. 2025 (5). pp. 15–29. DOI: 10.32683/0536-1052-2025-797-5-15-29.
7. **Lyakhovich L.S.** Special properties of optimal systems and the main directions of their implementation in the methods of calculating structures. Tomsk: TSUACE Publishing House, 2009. – 371 p.
8. **Goldstein Yu.B., Solomeshch M.A.** Variational problems of statics of optimal rod systems L. Publishing house of Leningrad State University, 1980. 208 p.
9. **Yuryev A.G.** Variational statements of problems of structural synthesis in statics. Moscow: MISI. 1987. – 94 p.
10. **Wasiutynski Z.** On the equivalence of design principles: minimum potential - constant volume and minimum volume - constant potential // Bull. Acad. Polon. Sci. Ser. Sci. Techn. 1966. - Vol. 14. - N. 9. – p. 883-885.
11. **Mishchenko A.V.** Optimization of structurally heterogeneous beam structures based on the energy criterion // News of higher educational institutions. Construction. - 2021. - No. 6 (750). - pp. 20-32.
12. **Mondrus V.L., Stupishin L.Yu.** Implementation of the Critical Energy Levels Criterion in Structural Mechanics Problems for Lumped Parameter Systems / In the collection: Fundamental, Exploratory, and Applied

Research of RAASN on Scientific Support for the Development of Architecture, Urban Planning, and the Construction Industry of the Russian Federation in 2021. Collection of Scientific Papers of RAASN. Russian Academy of Architecture and Construction Sciences. Moscow, 2022. pp. 269-281.

13. **Giunta G., Belouettar S., Carrera E.** Static analysis of laminated beams via a unified formulation // Composite Structures. Vol. 94, Iss. 1, December 2011, P. 75-83. https://doi.org/10.1016/j.compstruct.2011.07.015.
14. **Carrera E., Filippi M., Zappino E.** Laminated beam analysis by polynomial, trigonometric, exponential and zig-zag theories // European Journal of Mechanics - A/Solids. Vol. 41, September–October 2013, P. 58-69. https: //doi.org/10.1016/j.euromechsol.2013.02.006.
15. **Wenzel C., Vidal P., D'Ottavio M., Polit O.** Coupling of heterogeneous kinematics and Finite Element approximations applied to composite beam structures // Composite Structuresю. Vol. 116. 2014. P. 177-192. https: //doi.org/10.1016/j.compstruct.2014.04.022.
16. **Vidal P., Polit O.** Assessment of the refined sinus model for the non-linear analysis of composite beams // Composite Structures. Vol. 87, Iss. 4, February 2009, P. 370-381. https://doi.org/10.1016/j.compstruct.2008.02.007.
17. **Banichuk N.V., Kobelev V.V., Rickards R.B.** Optimization of structural elements made of composite materials. Moscow: Mashinostroenie, 1988. – 224 p.
18. **Beck R., da Silva J.A.P., da Silva L.F., Tita V., de Medeiros R.** (2025). Assessing critical fracture energy in mode I for bonded composite joints: A numerical–experimental approach with uncertainty analysis / Proceedings of the Institution of Mechanical Engineers, Part L: Journal of Materials: Design and Applications, 239(9), 1701-1718.
19. **Mishchenko A.V.** Spatially Structure Spatial Problem of the Stressed-Deformed State of a Structural Inhomogeneous Rod // IOP Conference Series: Materials Science and Engineering : XIII International Scientific Conference Architecture and Construction 2020, Novosibirsk, 22–24 сентября 2020 года. Vol. 953. – Bristol: IOP Publishing Ltd, 2020. – p. 012004. DOI 10.1088/1757-899X/953/1/012004.
20. **Mishchenko A.V.** Methods of calculation and rational design of structurally heterogeneous rods: monograph. Novosibirsk: NGASU (Sibstrin), 2025. - 144 p. - electronic publication.
21. **Mishchenko A.V., Veshkin M.S.** Realization of Equipotential Surfaces in Structurally Heterogeneous Rods with Variational Statements of Optimization Problems // Bulletin of MGSU. - 2026. - V. 21, No. 5.

СПИСОК ЛИТЕРАТУРЫ

1. **Баничук Н.В.** Оптимизация формы упругих тел. М.: Наука, 1980. - 256 с.
2. **Перельмутер А.В.** Задачи синтеза в теории сооружений (краткий исторический обзор) // Вестник Томского государственного архитектурно-строительного университета. – 2016. – № 2(55). – с. 70-106.
3. **Ляхович Л.С., Перельмутер А.В.** Некоторые вопросы оптимального проектирования строительных конструкций // International Journal for Computational Civil and Structural Engineering. 2014. Т. 10. № 2. с. 14–23.
4. **Mohamadmahdi Ebrahimi, Mahdi Fakoor** Design-oriented fracture criteria for orthotropic composites based on minimum strain energy density theory // Theoretical and Applied Fracture Mechanics, Vol. 140, 2025, 105182, https://doi.org/10.1016/j.tafmec.2025.105182.
5. **Юрьев А.Г., Нужный С.Н.** Оптимизация топологии однопролетных одноэтажных рам // Фундаментальные исследования. – 2013. № 10-4. с. 742-746.

6. **Мищенко А.В., Вешкин М.С.** Применение критерия минимума энергии деформации в задачах рационального профилирования неоднородных стержней // Известия вузов. Строительство. 2025 (5). с. 15–29. DOI: 10.32683/0536-1052-2025-797-5-15-29.
7. **Ляхович Л.С.** Особые свойства оптимальных систем и основные направления их реализации в методах расчета сооружений. Томск: Изд-во ТГАСУ, 2009. – 371 с.
8. **Гольдштейн Ю.Б., Соломещ М.А.** Вариационные задачи статики оптимальных стержневых систем Л. Изд-во ЛГУ, 1980. 208 с.
9. **Юрьев А.Г.** Вариационные постановки задач структурного синтеза в статике. М.: МИСИ. 1987. – 94 с.
10. **Wasiutynski Z.** On the equivalence of design principles: minimum potential - constant volume and minimum volume - constant potential // Bull. Acad. Polon. Sci. Ser. Sci. Techn. 1966. - Vol. 14. - N. 9. – p. 883-885.
11. **Мищенко А.В.** Оптимизация структурно-неоднородных стержневых конструкций на основе энергетического критерия // Известия высших учебных заведений. Строительство. – 2021. – № 6 (750). – с. 20-32.
12. **Мондрус В.Л., Ступишин Л.Ю.** Реализация критерия критических уровней энергии в задачах строительной механики для систем с сосредоточенными параметрами / В сборнике: Фундаментальные, поисковые и прикладные исследования РААСН по научному обеспечению развития архитектуры, градостроительства и строительной отрасли Российской Федерации в 2021 году. Сборник научных трудов РААСН. Российская академия архитектуры и строительных наук. Москва, 2022. с. 269-281.
13. **Giunta G., Belouettar S., Carrera E.** Static analysis of laminated beams via a unified formulation // Composite Structures. Vol. 94, Iss. 1, December 2011, P. 75-83. https://doi.org/10.1016/j.compstruct.2011.07.015.
14. **Carrera E., Filippi M., Zappino E.** Laminated beam analysis by polynomial, trigonometric, exponential and zig-zag theories // European Journal of Mechanics - A/Solids. Vol. 41, September–October 2013, P. 58-69. https: //doi.org/10.1016/j.euromechsol.2013.02.006.
15. **Wenzel C., Vidal P., D'Ottavio M., Polit O.** Coupling of heterogeneous kinematics and Finite Element approximations applied to composite beam structures // Composite Structuresю. Vol. 116. 2014. P. 177-192. https: //doi.org/10.1016/j.compstruct.2014.04.022.
16. **Vidal P., Polit O.** Assessment of the refined sinus model for the non-linear analysis of composite beams // Composite Structures. Vol. 87, Iss. 4, February 2009, P. 370-381. https://doi.org/10.1016/j.compstruct.2008.02.007.
17. **Баничук Н.В., Кобелев В.В., Рикардс Р.Б.** Оптимизация элементов конструкций из композиционных материалов. М.: Машиностроение, 1988. – 224 с.
18. **Beck R., da Silva J.A.P., da Silva L.F., Tita V., de Medeiros R.** (2025). Assessing critical fracture energy in mode I for bonded composite joints: A numerical–experimental approach with uncertainty analysis / Proceedings of the Institution of Mechanical Engineers, Part L: Journal of Materials: Design and Applications, 239(9), 1701-1718.
19. **Mishchenko A.V.** Spatially Structure Spatial Problem of the Stressed-Deformed State of a Structural Inhomogeneous Rod // IOP Conference Series: Materials Science and Engineering : XIII International Scientific Conference Architecture and Construction 2020, Novosibirsk, 22–24 сентября 2020 года. Vol. 953. – Bristol: IOP Publishing Ltd, 2020. – p. 012004. DOI 10.1088/1757-899X/953/1/012004.
20. **Мищенко А.В.** Методы расчета и рационального проектирования структурно не-

однородных стержней: монография. Новосибирск: НГАСУ (Сибстрин), 2025. – 144 с. – изд. электронное.
21. **Мищенко А.В., Вешкин М.С.** Реализация эквипотенциальных поверхностей в структурно-неоднородных стержнях при вариационных постановках задач оптимизации // Вестник МГСУ. – 2026. – Т. 21, № 5.

Mishchenko Andrey Viktorovich – Doctor of Technical Sciences, Associate Professor, Professor of the Department of Structural Mechanics, Novosibirsk State University of Architecture and Civil Engineering (Sibstrin) (NSUACE (Sibstrin)). 253, 113, str. Leningradskaya, Novosibirsk, 630008 Russia. E mail: a.michshenko@sibstrin.ru

Veshkin Maxim Sergeevich – Candidate of Technical Sciences, Associate Professor of the Department of Structural Mechanics, Novosibirsk State University of Architecture and Civil Engineering (Sibstrin) (NSUACE (Sibstrin)). 253, 113, str. Leningradskaya, Novosibirsk, 630008 Russia. E mail: m.veshkin@sibstrin.ru

Mondrus Vladimir Lvovich – Doctor of Technical Sciences, Professor, Corresponding Member of RAASN, Professor of the Department of Structural and Theoretical Mechanics, Institute of Industrial and Civil Engineering, National Research Moscow State Construction University (NIU MSCU). 405, 26, Yaroslavskoe Shosse, Moscow, 129337, Russia. m.mondrusvl@mgsu.m

Leonid Yulianovich Stupishin – Doctor of Technical Sciences, Professor, Professor of the Department of Construction and Theoretical Mechanics, Institute of Industrial and Civil Engineering, National Research Moscow State Construction University (NIU MSCU). 405, 26, Yaroslavskoe Shosse, Moscow, 129337, Russia. stupishinlyu@mgsu.ru

Мищенко Андрей Викторович – д.т.н., доцент, профессор кафедры строительной механики, Новосибирский государственный архитектурно-строительный университет (Сибстрин) (НГАСУ (Сибстрин)). 253, 113, ул. Ленинградская, Новосибирск, 630008 Россия. E-mail: a.michshenko@sibstrin.ru

Вешкин Максим Сергеевич – к.т.н., доцент кафедры строительной механики, Новосибирский государственный архитектурно-строительный университет (Сибстрин) (НГАСУ (Сибстрин)). 253, 113, ул. Ленинградская, Новосибирск, 630008 Россия. E-mail: m.veshkin@sibstrin.ru

Мондрус Владимир Львович – д.т.н., профессор, член корр. РААСН, профессор кафедры строительной и теоретической механики, институт Промышленного и гражданского строительства, Национальный Исследовательский Московский Государственный Строительный Университет (НИУ МГСУ). 405, 26, Ярославское шоссе, Москва, 129337, Россия. E-mail: m.mondrusvl@mgsu.m

Ступишин Леонид Юлианович – д.т.н., профессор, профессор кафедры строительной и теоретической механики, институт Промышленного и гражданского строительства, Национальный Исследовательский Московский Государственный Строительный Университет (НИУ МГСУ). 405, 26, Ярославское шоссе, Москва, 129337, Россия. E-mail: stupishinlyu@mgsu.ru

DOI:10.22337/2587-9618-2026-22-3-76-89

NUMERICAL MODELLING OF SNOW LOADS. VERIFICATION AND VALIDATION FOR THE KEMEROVO MUSEUM, THEATRE AND EDUCATION COMPLEX

Alexander M. Belostotsky, Nikita A. Britikov, Oleg S. Goryachevsky

National Research Moscow State University of Civil Engineering, Moscow, RUSSIA

Abstract: This paper presents the results of numerical and physical modelling of snow loads for a unique facility, conducted within the verification procedure of Ansys Fluent in the RAASN system. By analysing the grid and iteration convergence, the applicability of the steady-state (RANS) simulations and three turbulence models (k-ω SST, GEKO-0.70 and GEKO-1.25) is verified for the snow loads determination. The results are compared against experimental data obtained in the MSUCE wind tunnel. A simpler approach to error estimation is utilised since previous research revealed weak applicability of such widely used methods as Richardson extrapolation and approximate error spline. It is shown that the GEKO-0.70 turbulence model (with the separation coefficient C_{SEP} = 0.70) provides a better fit to the wind tunnel data than GEKO-1.25 and k-ω SST. 4. It is confirmed that Ansys Fluent allows the snow loads determination on buildings of complex shape with the accuracy sufficient enough for practical purposes, provided that modern turbulence models and methods set out in the STO "Numerical modelling of wind and snow actions" are used.

Keywords: computational fluid dynamics (CFD), numerical modelling, snow loads, verification, validation

ВЕРИФИКАЦИЯ И ВАЛИДАЦИЯ ЧИСЛЕННОГО МОДЕЛИРОВАНИЯ СНЕГОВЫХ НАГРУЗОК НА ПРИМЕРЕ МУЗЕЙНОГО И ТЕАТРАЛЬНО-ОБРАЗОВАТЕЛЬНОГО КОМПЛЕКСА в г. Кемерово

А.М. Белостоцкий, Н.А. Бритиков, О.С. Горячевский

Национальный исследовательский Московский государственный строительный университет, г. Москва, РОССИЯ

Аннотация: Для уникального здания представлены результаты численного и физического моделирования снеговых нагрузок, полученные в рамках процедуры верификации в системе PAACH программного комплекса ANSYS Fluent. С помощью анализа сеточной и итерационной сходимости расчётов проверяется применимость для определения снеговых нагрузок стационарной постановки (RANS) и трёх моделей турбулентности: k-ω SST, GEKO-0.70 и GEKO-1.25. Результаты сопоставляются с экспериментальными данными, полученными в аэродинамической трубе НИУ МГСУ. В связи с тем, что предыдущие исследования выявили слабую применимость таких широко распространённых методов, как экстраполяция Ричардсона и аппроксимация ошибки сплайном, для оценки погрешностей используется упрощённый подход. Выявлено, что модель турбулентности GEKO-0.70 (с параметром C_{SEP} = 0.70) позволяет получить лучшее соответствие данным из аэродинамической трубы, чем GEKO-1.25 и k-ω SST. Установлено, что Ansys Fluent позволяет определять снеговые нагрузки на покрытия сложных форм с достаточной для прикладных задач точностью при условии использования современных моделей турбулентности и методов, прописанных в СТО «Численное моделирование ветровых и снеговых воздействий».

Ключевые слова: вычислительная гидрогазодинамика, численное моделирование, снеговая нагрузка, верификация, валидация

1. INTRODUCTION

Development of reliable and robust methods of snow loads calculation for buildings and structures remains an urgent task in civil engineering due to the growing number of unique facilities that are being designed and constructed in dense urban areas, since building codes cannot provide snow loads for their complex roofs.

Currently, the following methods are used to calculate snow loads:

1. Building codes' provisions and analytical methods (inapplicable to unique facilities);
2. Physical modelling [1, 2];
3. Numerical modelling [3-9];
4. Monitoring and in-situ measurements [10, 11] (mainly academic research);
5. Machine learning and neural networks [12] (academic purposes only to this date).

Physical (experimental) modelling in WTs and water flumes remains the generally accepted method of snow loads calculation. A reliable methodology for such modelling was proposed and developed over the course of the second half of the XX century, which now provides a sufficient level of plausibility under a number of limitations. Still, the high costs of construction and maintenance of WTs, poor scalability, significant simulation time, low information content and other limitations call for development of competing methods which can be applied in practice.

Numerical (mathematical) modelling, especially using CFD methods, appears to be a more prospective direction, being devoid of the WT limitations and promising potentially faster research. Methodologies for numerical modelling of snow loads have been developed independently by many researchers, which are now being gradually legitimised in the regulations of technologically advanced countries, STO [13], ASCE 7-22.

At this time, a synthetic combination of numerical and physical modelling, often labelled "hybrid modelling", allows to gather the most comprehensive information on snow loads for any given roof [13]. Due to high computational and time costs posed by scale-resolving transient approaches (e.g., utilising LES model), steady-state (RANS-based) approaches [4] remain the most used ones in numerical modelling for fast snow loads calculation.

To confirm the reliability of numerical modelling results, a verification and validation (V&V) procedure is required. The most general definitions of V&V are provided in GOST [14] and ASME [15], although they do not regulate specific areas of application, such as structural aerodynamics.

In structural aerodynamics, ***verification*** is reduced to evaluating the errors of the numerical model (iteration, time, grid, etc.) and investigating convergence, since the exact solutions of numerically solved equations are unknown [13, 16-19]. ***Validation*** is more straightforward and complies with [14, 15], however, generally, the results of numerical modelling can only be compared with the results of physical modelling.

In the present paper, the V&V procedure of the numerical modelling of snow loads was carried out for a unique facility of the Kemerovo Museum, Theatre and Education Complex (hereinafter, the *Kemerovo MTEC*). Three turbulence models were considered: k-ω SST, GEKO-0.70 and GEKO-1.25 (with separation parameter C_{SEP} = 0.70, 1.25, respectively). Grid and iteration convergence were investigated. The results of numerical modelling were compared against experimental data obtained in the MSUCE WT.

The work was carried out within the verification procedure of Ansys Fluent for the problems of "determination of wind and snow actions on buildings and structures on the basis of numerical solutions of the equations of aero-hydrodynamics" in the system of the Russian Academy of Architecture and Construction Sciences (RAASN) [20].

2. CASE AND METHODOLOGY

2.1. Case description

In this paper, the Kemerovo MTEC (Fig. 1) was investigated.



Figure 1. Renders of the Kemerovo MTEC

The Kemerovo MTEC has a complex deconstructivist shape, with façades made of glass and metal elements. The building is 10 floors high with a total area of approximately 81100 m^2, and also has an underground parking. The Kemerovo MTEC is planned to house branches of the Mariinsky Theatre and the State Russian Museum, as well as the Kuzbass Arts Centre. The facility's ensemble consists of four parts: a "floating cloud" theatre, two "crystals" (a museum and an art centre with workshops), and a public foyer.

The study investigates snow deposits on the facility's roof obtained through physical and numerical modelling. Numerically, the deposits are calculated using wall shear stress (τ_w):

$$\tau_w = \mu \, \partial u/\partial y \, |_{y=0}, \qquad (1)$$

where μ is the dynamic viscosity of the flow; u is the velocity of the flow along the boundary; and y is the height above the boundary. The values of wall shear stress are converted into numerical snow deposit maps using a methodology described in [3, 4].

The simulations were carried out for two characteristic angles of attack, 0° and 90° (the widthwise and the lengthwise flow directions, respectively, see Fig. 2).

Physical snow deposit maps were obtained in the MSUCE WT through physical modelling at a 1:200 scale (Fig. 3).

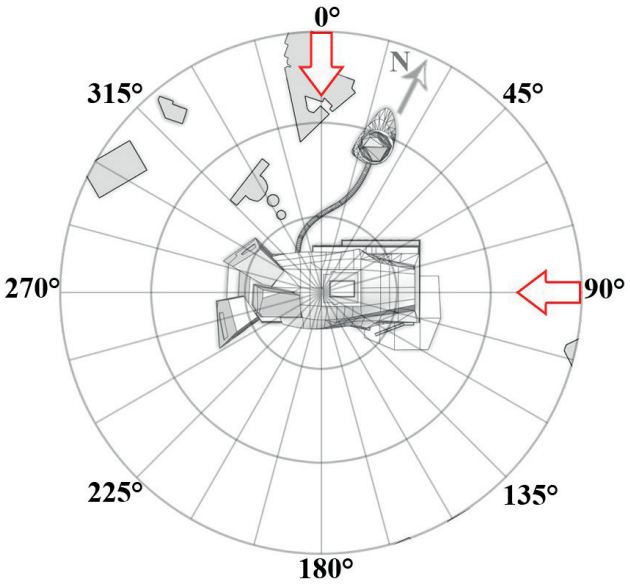


Figure 2. Investigated wind directions

2.2. Mathematical models

In this study, urban wind flow is simulated using time-averaged (RANS) incompressible and isothermal Navier-Stokes equations. Such assumptions regarding the flow are known to be justified and accepted by researchers for determination of snow loads on roofs [10]:

$$\frac{\partial \overline{u}_i \overline{u}_j}{\partial x_j} = -\frac{1}{\rho}\left(p + \frac{2}{3}\rho k\right) + \\ + \frac{\partial}{\partial x_j}\left((\nu + \nu_t)\left(\frac{\partial \overline{u}_i}{\partial x_j} + \frac{\partial \overline{u}_j}{\partial x_i}\right)\right), \qquad (2)$$

where $\overline{u}_i$ are the components of the averaged flow velocity, [m/s]; t is the time, [s]; $\bar{p}$ is the av-

eraged pressure, [Pa]; ρ = 1.225 kg/m^3 is the density of air; $\nu = 1.46 \cdot 10^{-5}$ m^2/s is the kinematic viscosity of air; and ν_t is the turbulent viscosity.
The continuity equation is given as:

$$\frac{\partial \overline{u_j}}{\partial x_j} = 0 \quad (3)$$

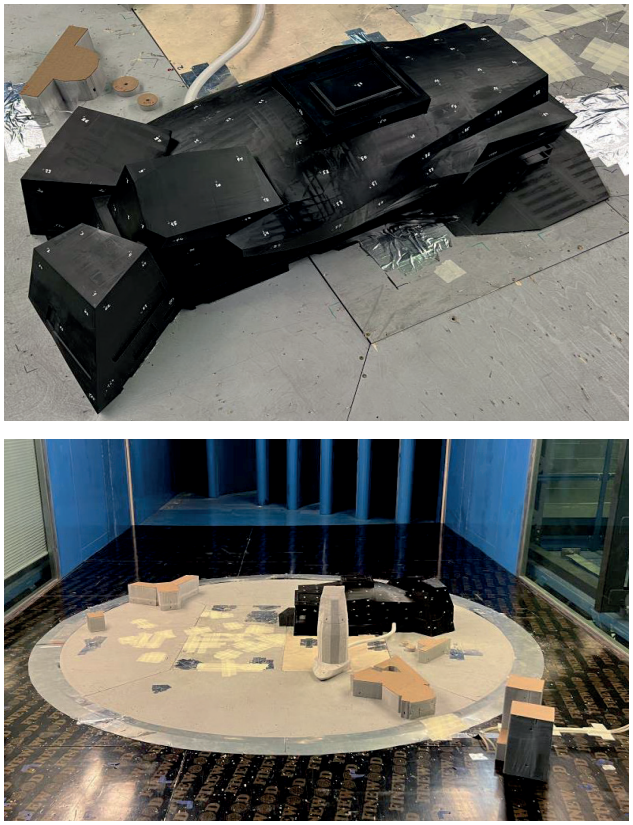


Figure 3. The Kemerovo MTEC model in the MSUCE WT

The following turbulence models are considered:
– *k*-ω Shear-Stress Transport (*k*-ω SST) is a general two-parameter model which switches between the regular *k*-ω model near the walls and the *k*-ε model in the free flow via a mixing function;
– Generalised *k*-ω (GEKO) is a modification of the regular *k*-ω model, which allows for adjusting to different types of flows by tweaking a number of dimensionless parameters exposed to the user. In this study, only the C_{SEP} is varied (between 0.70 and 1.25), which governs flow separation and adverse pressure gradients.

2.3. CFD setup

To provide a correct comparison between the results of numerical and physical modelling, the CFD model needs to reproduce all the major parameters of the experiment, such as scale, WT's working area dimensions, and boundary conditions.
The numerical geometry of the Kemerovo MTEC with the surrounding buildings corresponds to the experimental one (Fig. 4).

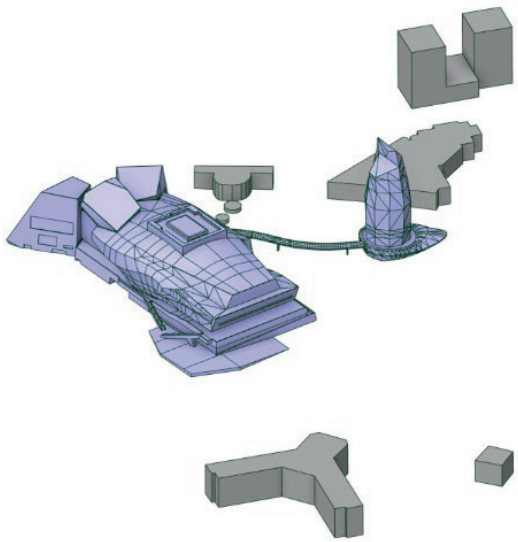
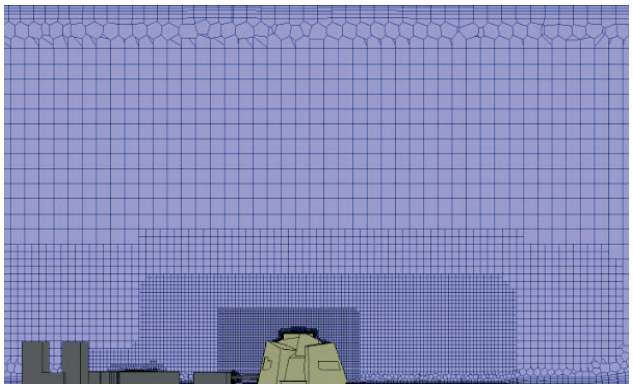


Figure 4. Numerical geometry of the Kemerovo MTEC with the surrounding buildings

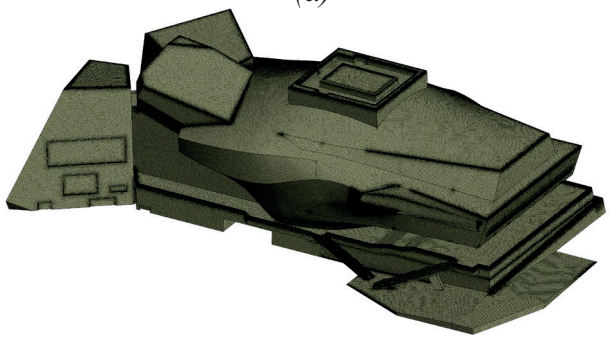
Polyhexcore finite-volume meshes were used in this study, combining polygonal, prismatic and hexagonal cells. Three meshes were developed to perfrom the grid convergence study, a coarse one (4.99 million cells), a medium one (10.77 million cells), and a fine one (19.06 million cells). The meshes differ in face size by factors of 1.5 (coarse to medium) and 1.33 (medium to fine). Each mesh has 5 prism layers parallel to the surfaces at the bottom and 10 layers at the target building, ensuring $y+ \leq 5$ for the building's roof surfaces for all the grids.
The boundary conditions are shown in Fig. 6:
– at the inlet, the flow velocity and the turbulent intensity profiles are interpolated from WT experimental data (Fig. 7). Two flow regimes are investigated, with the velocity at 0.05 m (scaled) equal to 3 m/s or 6 m/s (labelled as V3 and V6, respectively);

– at the outlet, the gauge pressure is set to 0;
– the rest of the surfaces are no-slip walls.

The coupled velocity-pressure solver was used, with 2nd order schemes for the momentum, turbulent transport and pressure equations. The total number of iterations was set to 300, of which the last 140 were calculated with high-order relaxation enabled. Data sampling was performed for the last 120 iterations.



(a)



(b)

Figure 5. Finite-volume mesh: a – in the longitudinal section of the domain; b – on the surface of the Kemerovo MTEC

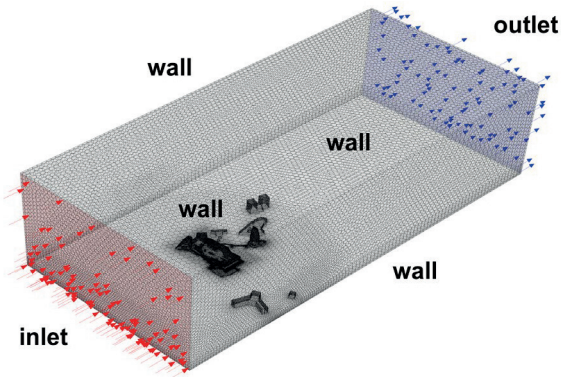


Figure 6. Boundary conditions

A total of 36 3D steady-state runs (2 angles of attack × 2 velocities × 3 turbulence models × 3 meshes) were performed.

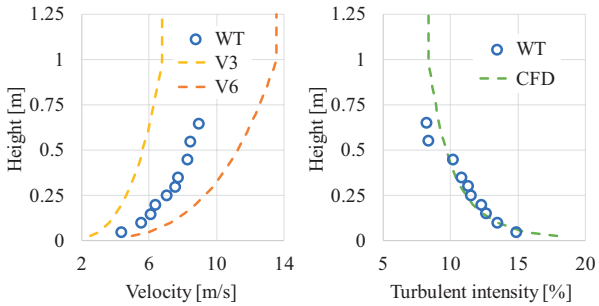


Figure 7. Velocity [m/s] *and turbulent intensity* [%] *profiles from WT measurements and CFD approximations*

2.4. Verification & Validation methods

Previous research [21] on the case of the Kemerovo MTEC has revealed that some widely used error estimation methods, such as Richardson extrapolation and approximate error spline, may display incorrect behaviour in convergence analysis. Therefore, a simpler error estimation method was used in their stead for this study.

Grid convergence was estimated as a ratio of the wall shear stress's range to its mean, which is then interpolated to the coarse grid for comparison:

$$e_g = \left| \frac{\max\limits_i \tau_{w,i} - \min\limits_i \tau_{w,i}}{2 \operatorname{mean}\limits_i \tau_{w,i}} \right| 100\%, \qquad (4)$$

where i denotes the grid (1 – coarse, 2 – medium, 3 – fine), and the values of $\max(\tau_{w,i})$, $\operatorname{mean}(\tau_{w,i})$ and $\min(\tau_{w,i})$ are taken from the sampled datasets at each node of the facility's roof mesh.

Iteration convergence was estimated similarly:

$$e_{it} = \left| \frac{\max\limits_k \tau_{w,k} - \min\limits_k \tau_{w,k}}{2 \operatorname{mean}\limits_k \tau_{w,k}} \right| 100\%, \qquad (5)$$

where $\tau_{w,k}$ are the wall shear stress values at the k^{th} iteration (k = 181...300).

For $\operatorname{mean}(\tau_{w,k}) \approx 0$, the values of e_{it} take very large values, not characterising convergence. In

such cases, formula (5) is not applicable and the corresponding points are discarded.
Since the experimentally obtained values of numerical shape coefficient μ_{nm} and physical shape coefficient μ_{pm} are not exactly equal to the values of design shape coefficient μ (and, generally, to each other), the simulations' results are compared qualitatively in the first place. This is due to the nature of the methodologies that are used to simulate snow deposition and snow transport in WTs and CFD.

3. RESULTS AND DISCUSSION

This section presents the results of grid and iteration convergence for the numerical modelling, and the comparison of snow deposit maps obtained numerically and physically.
The following nomenclature is used:

Table 1. Numerical results nomenclature

Parameter		*Value*	*Abbr.*
Configuration	*Angle of attack*	0°	A0
		90°	A90
	Turbulence model	GEKO-0.70	G070
		GEKO-1.25	G125
		k-ω SST	kwSST
	Flow velocity	3 m/s	V3
		6 m/s	V6
Grid quality		Coarse	M1
		Medium	M2
		Fine	M3

3.1. Iteration convergence

For the most runs (24 out of 36, see Fig. 8, 9) the mean values of e_{it} are well below 7%, except for A0-G125 ($7.6\% \leq e_{it} \leq 15.9\%$) and A0-kwSST ($38.3\% \leq e_{it} \leq 76.3\%$). Still, even the runs with the overall lowest values of e_{it} demonstrate local areas of extremely high e_{it} (Fig. 11). However, the plotted values of $\tau_{w,k}$ in such areas reveal oscillatory convergence (Fig. 12). This result underlines the necessity of data sampling for simulations with complex geometry and skewed cells, whose presense in meshes oftentimes cannot be avoided.

3.2. Grid convergence

For the most configurations (10 out of 12, see Fig. 10) the mean values of e_g are well below 9%. The lowest values are obtained with G070 ($4.98\% \leq e_g \leq 6.74\%$), followed by G125 ($5.53\% \leq e_g \leq 7.56\%$) and, finally, kw-SST ($7.97\% \leq e_g \leq 26.2\%$). Just as with e_{it}, the configurations with the overall lowest values of e_g demonstrate local areas of extremely high e_g (Fig. 13). However, the plotted contours of such high value areas reveal that their area remains relatively small (i.e., for the A90-G070-V3 configuration $e_g \geq 10\%$ for only 11% of the total surface area). This result shows that GEKO-0.70 allowed for the best grid convergence between the three turbulence models used in this study.

3.3. Comparison between numerical and physical results

Based on the convergence study, GEKO-0.70 results were used for the comparison with physical snow deposit maps, since it produced the overall lowest values of e_{it} and e_g. Numerical snow deposit maps are presented for all three grids to demonstrate how the deposit contours change with grid refinement.
Qualitative comparison between the numerical and the physical simulations' results for two angles of attack show good agreement both in general and locally, sufficient enough to be used in conjunction with the building code provisions to produce maps of the design shape coefficient μ.

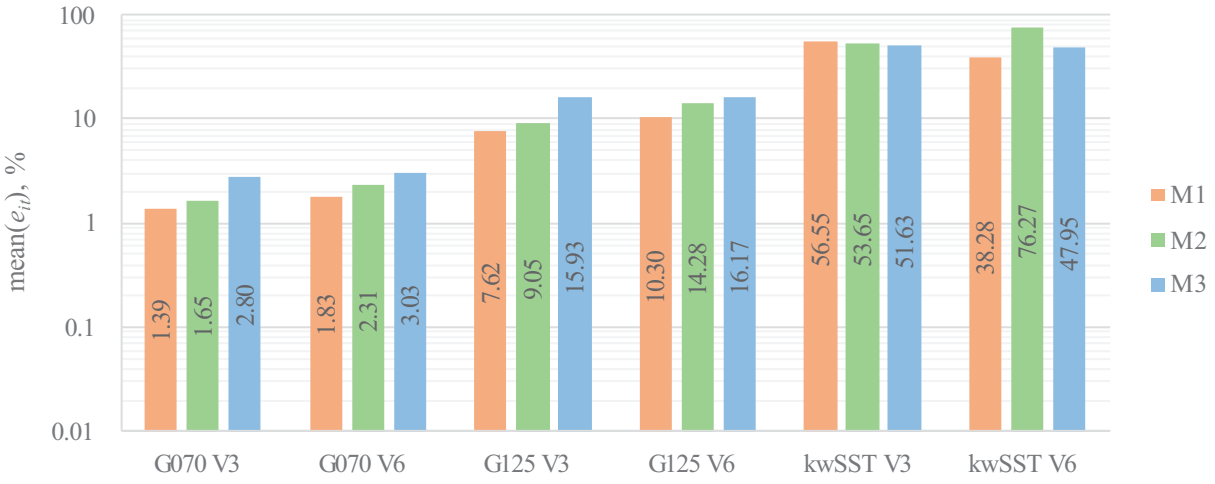


Figure 8. Mean iteration error e_{it} [%] for different grids, angle of attack 0°

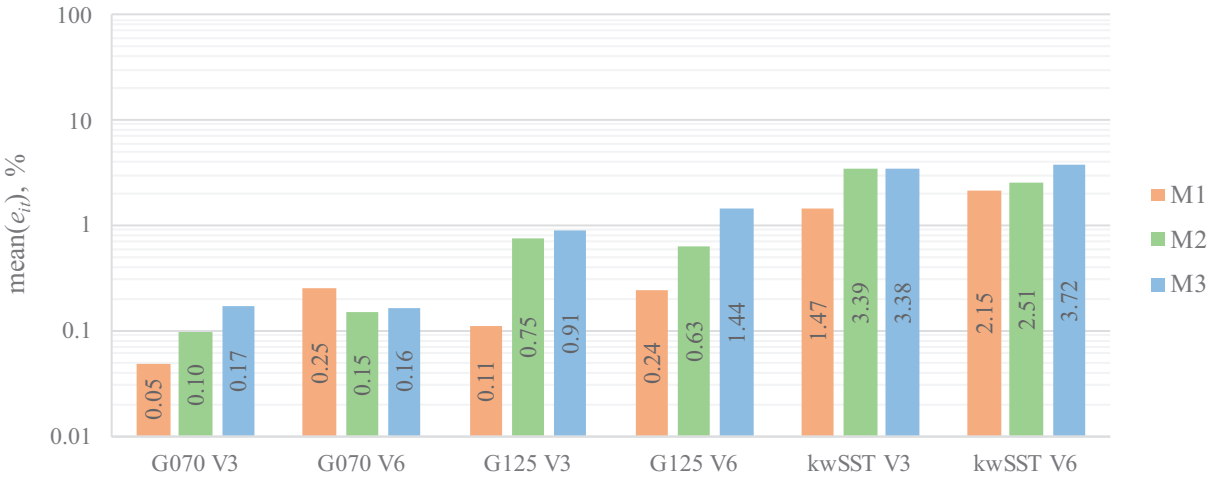


Figure 9. Mean iteration error e_{it} [%] for different grids, angle of attack 90°

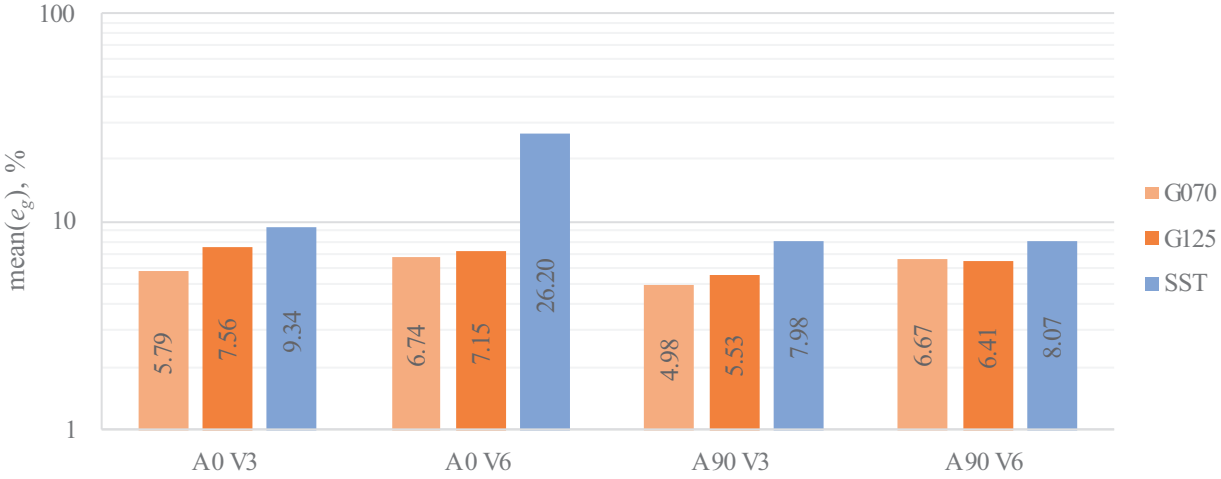


Figure 10. Mean grid error e_g [%] for different turbulence models

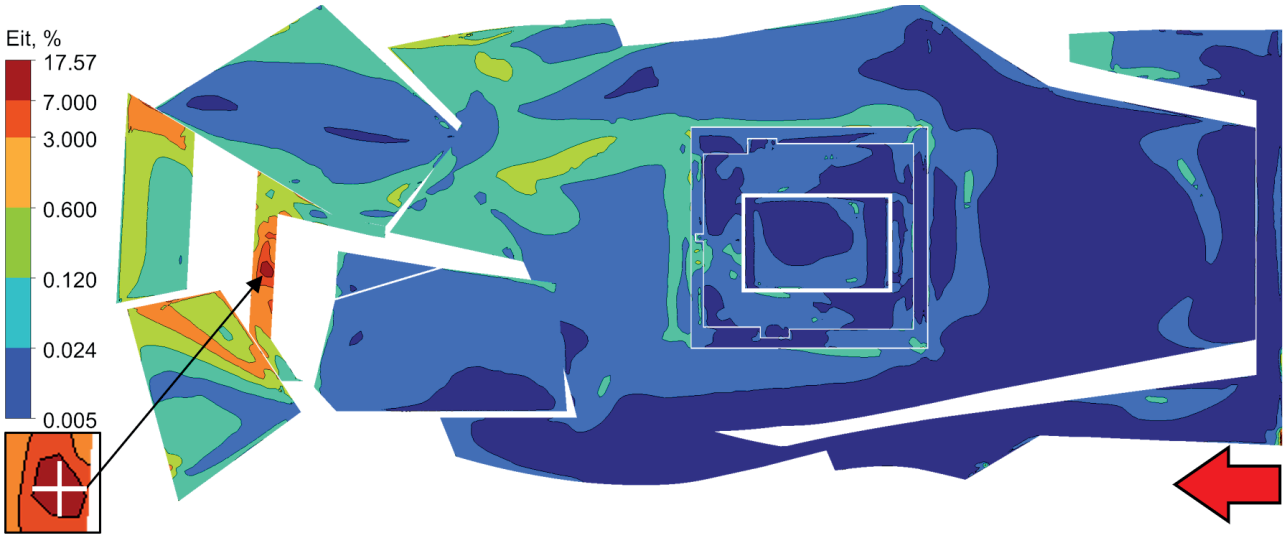


*Figure 11. Iteration error e_{it} [%] for **A90-G070-V3-M1** case, log scale*
Angle of attack is shown with the red arrow
The mark depicts the cell centroid with the highest e_{it} value

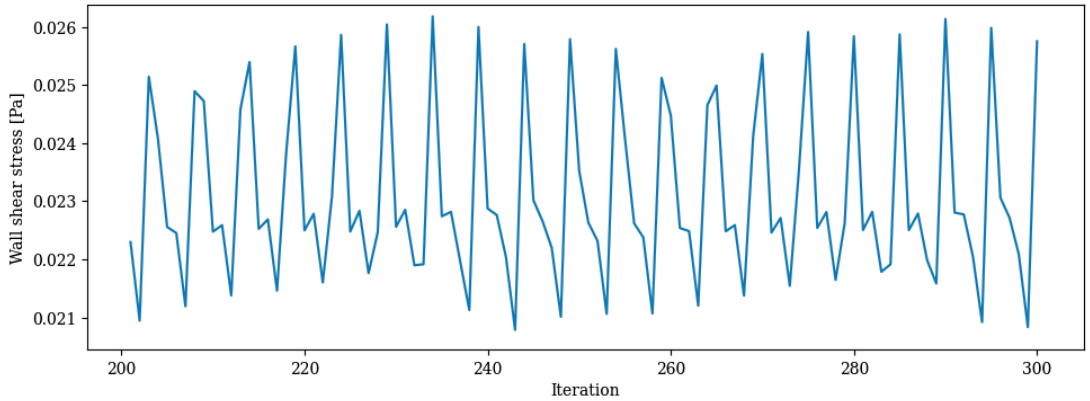


Figure 12. Wall shear stress [Pa] *plot in the aforementioned cell centroid over the last 100 iterations reveals oscillatory convergence*

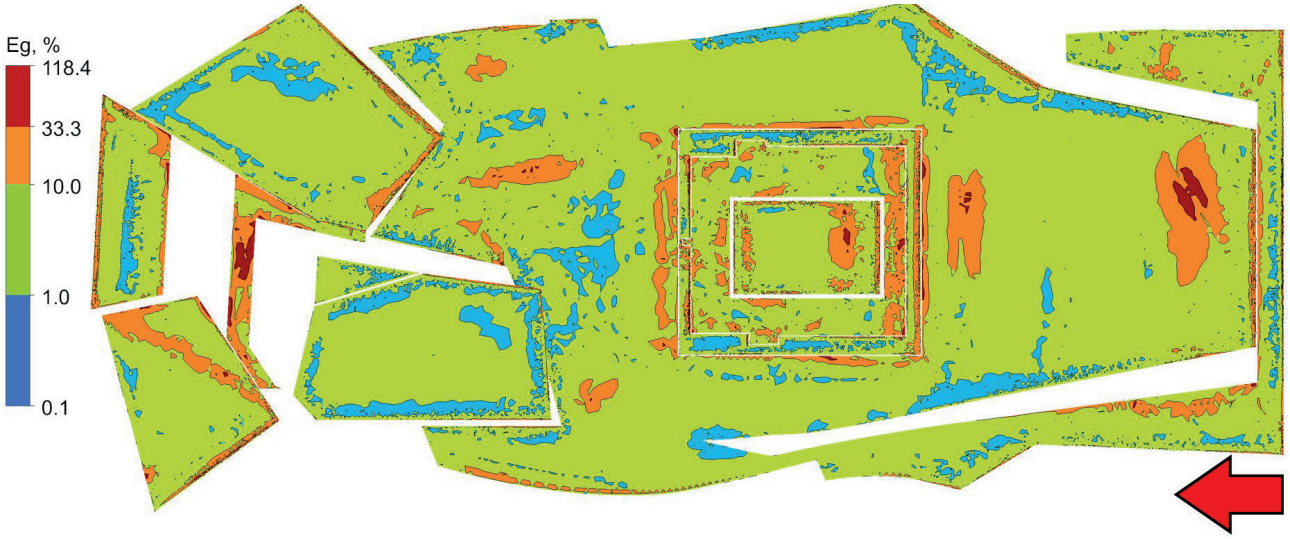
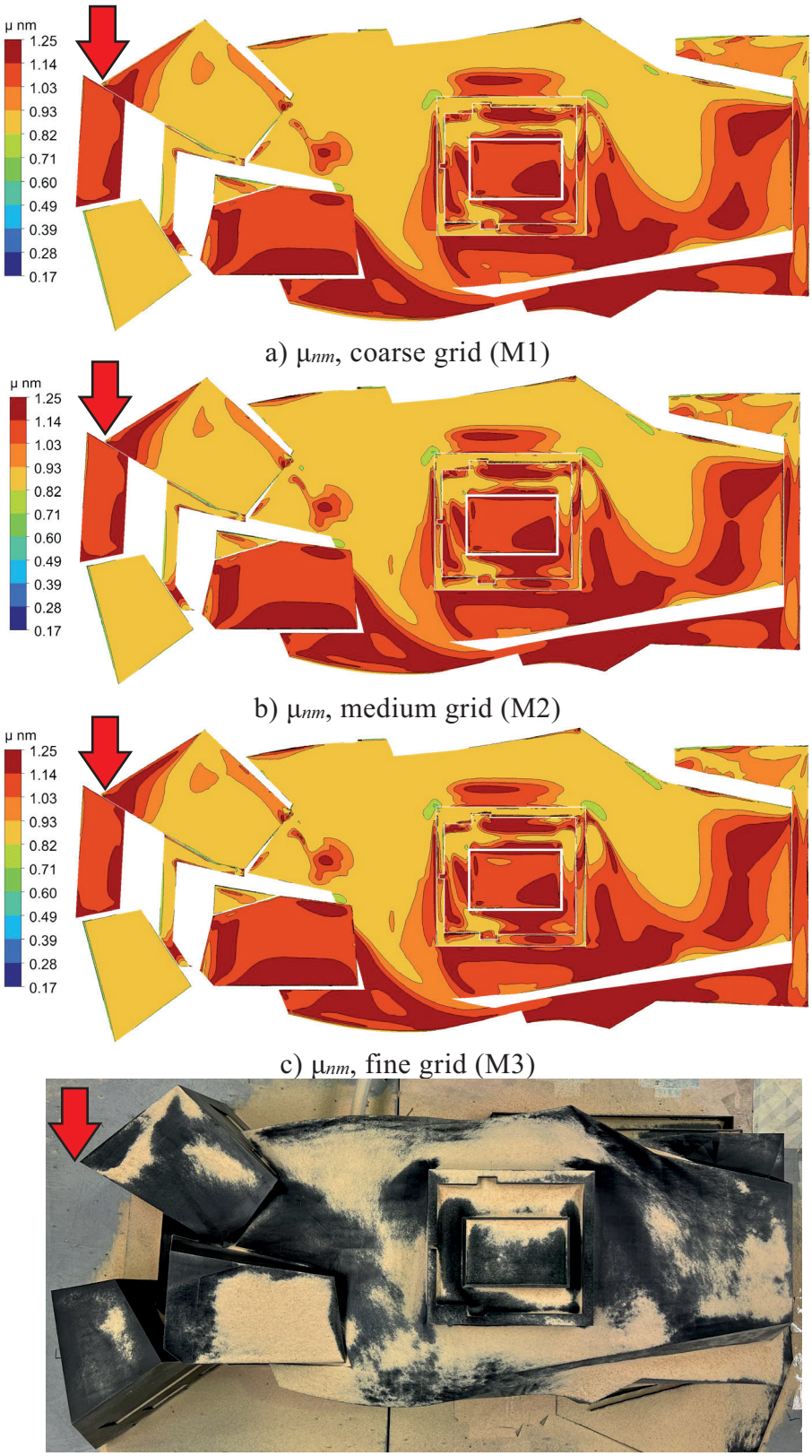


*Figure 13. Grid error e_g [%] for **A90-G070-V3** configuration, log scale*



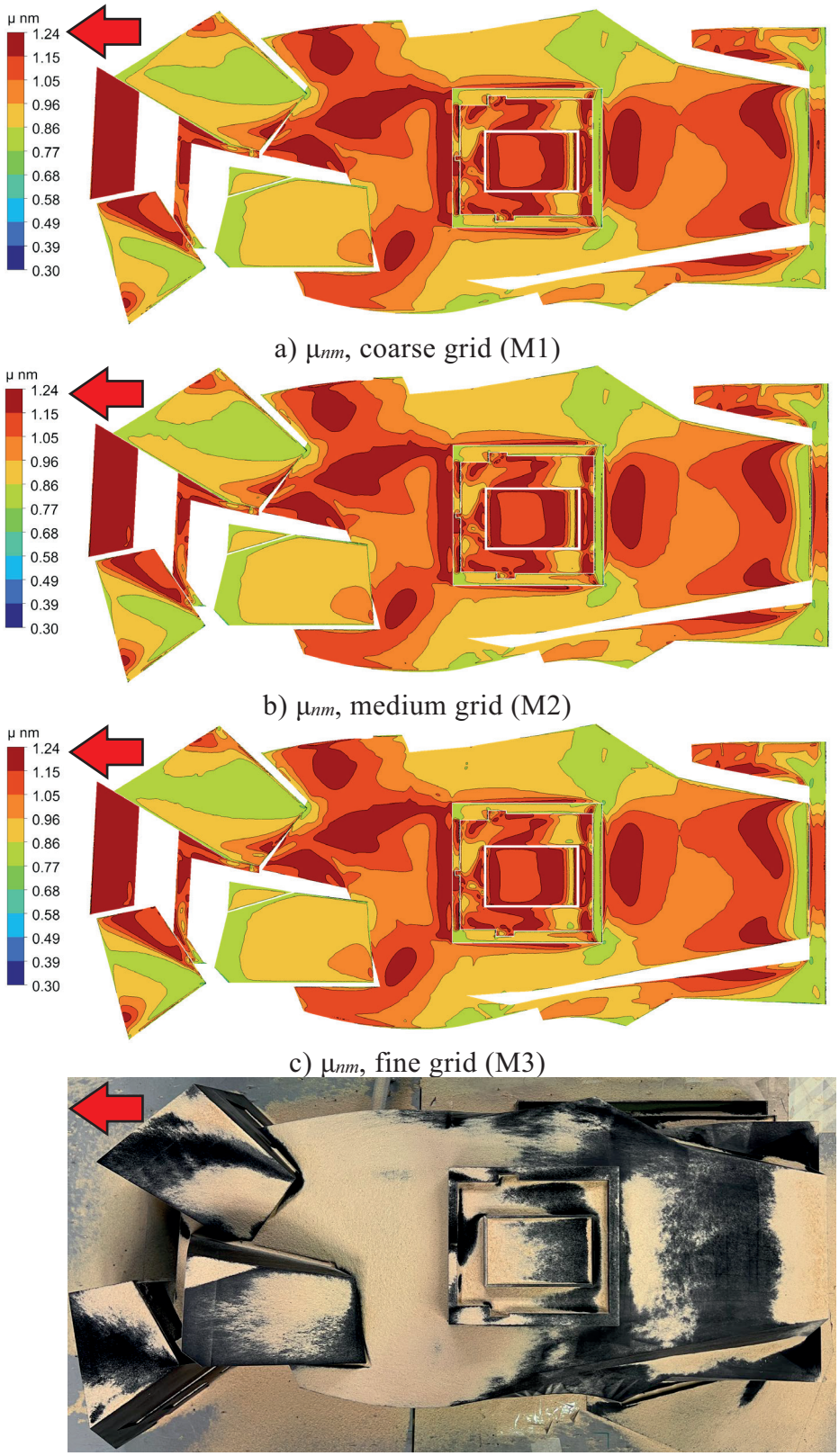
a) μ_{nm}, coarse grid (M1)

b) μ_{nm}, medium grid (M2)

c) μ_{nm}, fine grid (M3)

d) μ_{pm}

Figure 14. Numerically modelled shape coefficient μ_{nm} vs. physically modelled shape coefficient μ_{pm} Angle of attack 0°, GEKO-0.70



a) μ_{nm}, coarse grid (M1)

b) μ_{nm}, medium grid (M2)

c) μ_{nm}, fine grid (M3)

d) μ_{pm}

Figure 15. Numerically modelled shape coefficient μ_{nm} vs. physically modelled shape coefficient μ_{pm} Angle of attack 90°, GEKO-0.70

4. CONCLUSIONS

The following conclusions are made from the conducted research:

1. Numerical models of the Kemerovo MTEC and the surrounding buildings have been developed. A total of 2 wind directions, 2 velocities, 3 levels of grid refinement (4.99, 10.77 and 19.06 million cells) and 3 turbulence models (k-ω SST, GEKO-0.70 and GEKO-1.25) were considered.

2. A thorough **verification** has been carried out to investigate the iteration and grid independence of the solution:

- Iteration and grid error can contribute significantly to the numerical solution results. To minimise this effect, it is necessary to use data sampling and maintain good mesh quality.
- The solution for all the turbulence models mostly demonstrates oscillatory behaviour on different grid refinement levels.
- The k-ω SST model shows the worst iteration and grid convergence among the studied models.
- The GEKO models show significantly better iteration convergence (e_{it} < 16.2%), and decreasing the C_{SEP} further improves it (e_{it} < 3.5% for C_{SEP} = 0.70).
- The best grid convergence is achieved with GEKO-0.70 (e_g < 7%) and the worst with k-ω SST (e_g > 8%).

3. A thorough **validation** has been carried out through a qualitative comparison of the numerical (CFD) and physical (WT) modelling results.

- The GEKO turbulence model with the parameter C_{SEP} = 0.70 displayed good agreement with the experimental data. This model is recommended for use in snow load determination for long-span roofs in steady-state simulations.

4. It is confirmed that Ansys Fluent allows the snow loads determination on buildings of complex shape with the accuracy sufficient enough for practical purposes, provided that modern turbulence models and methods set out in the STO [13] are used.

ACKNOWLEDGEMENTS

The research was funded by the National Research Moscow State University of Civil Engineering.

REFERENCES

1. **Isyumov N., Mikitiuk M.** Wind tunnel modeling of snow accumulations on large-area roofs //Proc., 2nd Int. Conf. On Snow Engineering. – 1992. – Pp. 181-193.
2. **Peterka J. A., Esterday W. S.** Roof design snow loads by wind tunnel test and analysis //Structures 2004: Building on the Past, Securing the Future. – 2004. – Pp. 1-9.
3. **Britikov N.A.** Numerical modelling of snow loads on roofs of large-span buildings and structures: Dissertation for the degree of Candidate of Technical Sciences. Moscow, 2023. – 150 p. (In Russ.)
4. **Britikov N.A.** Numerical modelling of snow deposits and snow transport on long-span roofs for steady and unsteady flow. // J. Comput. Civ. Struct. Eng. – 2022. – Vol. 18. – No. 4. – Pp. 23–38.
5. **Belostotsky A.M., Britikov N.A., Goryachevsky O.S.** Critical review of modern numerical modelling of snow accumulation on roofs with arbitrary geometry. // J. Comput. Civ. Struct. Eng. – 2021. – Vol. 17. – No. 4. – Pp. 40–59.
6. **Belostotsky A.M., Akimov P.A., Afanas'eva I.N.** Vychislitel'naya aerodinamika v zadachah stroitel'stva, M.: Izdatel'stvo ASV. – 2017. – 720 p. (In Russ.)
7. **Tominaga Y., Okaze T., Mochida A.** CFD modeling of snowdrift around a building: An overview of models and evaluation of a new approach. //Building and Environment. – 2011. – Vol. 46 – No 4. – Pp. 899-910.
8. **Tominaga Y.** Computational fluid dynamics simulation of snowdrift around buildings: Past achievements and future perspectives. //Cold Regions Science and Technology. – 2018. – No.150. – Pp. 2-14

9. **Yu Z., Zhu F., Cao R., Chen X., Zhao L., Zhao S. .** Wind tunnel tests and CFD simulations for snow redistribution on 3D stepped flat roofs. //Wind and Structures. – 2019. – Vol. 28. – No. 1. – Pp. 31-47.
10. **Diamantidis D., Sykora M., Lenzi D.** Optimising monitoring: standards, reliability basis and application to assessment of roof snow load risks //Structural Engineering International. – 2018. – Vol. 28. – No. 3. – Pp. 269-279.
11. **Lobkina V. A., Kononov I. A., Potapov A. A.** Remote monitoring of the snow loads on a roof of buildings //Led i Sneg-Ice and Snow. – 2016. – Vol. 56. – No. 2. – Pp. 246-252. (In Russ.)
12. **Sanchez-Gonzalez A., Godwin J., Pfaff T., Ying R., Leskovec J., Battaglia P.** Learning to simulate complex physics with graph networks. //International Conference on Machine Learning. – 2020. – Pp. 8459-8468.
13. STO 02066523-089-1-2025. Numerical modelling of wind and snow actions.
14. GOST R 57188–2016 Numerical modeling of physical processes. Terms and definitions. (In Russ.)
15. ASME V&V 20–2009 Standard for Verification and Validation in Computational Fluid Dynamics and Heat Transfer
16. **Celik I.B., Ghia U., Roache P.J., Freitas C.J.** Procedure for Estimation and Reporting of Uncertainty Due to Discretization in CFD Applications // J. Fluids Eng. – 2008. – Vol. 130. – No.7. – PaperID 078001.
17. **Franke J.** Best practice guideline for the CFD simulation of flows in the urban enviroment // COST Office Brussels. – 2007. – ISBN: 3-00-018312-4.
18. **Tominaga Y., Mochida A., Yoshie R., Kataoka H., Nozu T., Yoshikawa M., et al.** AIJ guidelines for practical applications of CFD to pedestrian wind enviroment around building // J. Wind Eng. Ind. Aerodyn. – 2008. – Vol. 96. – pp. 1749-1761.
19. **Roache P.J.** Verification and Validation in Computational Science and Engineering // Hermosa Publishers, Albuquerque, New Mexico – 1998. – p. 446.
20. Regulation on the verification of software tools used to determine loads and impacts, stress-strain (and other) states, dynamic characteristics, and to assess the strength, stability, and safety of structures, buildings, and facilities / RAASN // Approved by the Presidium of RAASN, Protocol No. 11 of November 25, 2016. – Moscow, 2016. – 28 p. (In Russ.)
21. **Belostotsky A.M., Goryachevsky O.S., Saiyan S.G., Efimova A.M.** Numerical modelling of wind loads. Verification and validation for the Kemerovo Museum, Theatre and Education Complex. // J. Comput. Civ. Struct. Eng. – 2025. – Vol. 21. – No. 4. – Pp. 185–204.

СПИСОК ЛИТЕРАТУРЫ

1. **Isyumov N., Mikitiuk M.** Wind tunnel modeling of snow accumulations on large-area roofs //Proc., 2nd Int. Conf. On Snow Engineering. – 1992. – C. 181-193.
2. **Peterka J. A., Esterday W. S.** Roof design snow loads by wind tunnel test and analysis //Structures 2004: Building on the Past, Securing the Future. – 2004. – C. 1-9.
3. **Бритиков Н.А.** Численное моделирование снеговых нагрузок на покрытия большепролетных зданий и сооружений: диссертация на соискание ученой степени кандидата технических наук. – Москва, 2023. – 150 с.
4. **Бритиков Н.А.** Методика численного моделирования снегоотложений и снегопереноса на покрытиях большепролётных зданий и сооружений в стационарной и нестационарной постановках // J. Comput. Civ. Struct. Eng. – 2022. – Т. 18. – №. 4. – С. 23–38.

5. **Белостоцкий А.М., Бритиков Н.А., Горячевский О.С.** Современные методы математического (численного) моделирования снегонакопления на покрытия сооружений произвольной формы. Критический обзор // J. Comput. Civ. Struct. Eng. – 2021. – Т. 17. – №. 4. – С. 40–59.
6. **Белостоцкий А.М., Акимов П.А., Афанасьева И.Н.** Вычислительная аэродинамика в задачах строительства, М.: Издательство АСВ, 2017, 720 с.
7. **Tominaga Y., Okaze T., Mochida A.** CFD modeling of snowdrift around a building: An overview of models and evaluation of a new approach. //Building and Environment. – 2011. – Т. 46 – №4. – С. 899-910.
8. **Tominaga Y.** Computational fluid dynamics simulation of snowdrift around buildings: Past achievements and future perspectives. //Cold Regions Science and Technology. – 2018. – №150. – С. 2-14
9. **Yu Z., Zhu F., Cao R., Chen X., Zhao L., Zhao S. .** Wind tunnel tests and CFD simulations for snow redistribution on 3D stepped flat roofs. //Wind and Structures. – 2019. – Т. 28. – №. 1. – С. 31-47.
10. **Diamantidis D., Sykora M., Lenzi D.** Optimising monitoring: standards, reliability basis and application to assessment of roof snow load risks //Structural Engineering International. – 2018. – Т. 28. – №. 3. – С. 269-279.
11. **Лобкина В.А., Кононов И.А., Потапов А.А.** Система дистанционного мониторинга снеговой нагрузки на кровле зданий. //Лёд и снег. – 2016. – Т. 56. – №. 2. – С. 246-252.
12. **Sanchez-Gonzalez A., Godwin J., Pfaff T., Ying R., Leskovec J., Battaglia P.** Learning to simulate complex physics with graph networks. //International Conference on Machine Learning. – 2020. – С. 8459-8468.
13. СТО 02066523-089-1-2025. Численное моделирование ветровых и снеговых воздействий. НИУ МГСУ, АО НИЦ СтаДиО, 2025.
14. ГОСТ Р 57188–2016 Численное моделирование физических процессов. Термины и определения.
15. ASME V&V 20–2009 Standard for Verification and Validation in Computational Fluid Dynamics and Heat Transfer
16. **Celik I.B., Ghia U., Roache P.J., Freitas C.J.** Procedure for Estimation and Reporting of Uncertainty Due to Discretization in CFD Applications // J. Fluids Eng.. – 2008. – Vol. 130. – No.7. – PaperID 078001.
17. **Franke J.** Best practice guideline for the CFD simulation of flows in the urban enviroment // COST Office Brussels. – 2007. – ISBN: 3-00-018312-4.
18. **Tominaga Y., Mochida A., Yoshie R., Kataoka H., Nozu T., Yoshikawa M., et al.** AIJ guidelines for practical applications of CFD to pedestrian wind enviroment around building // J. Wind Eng. Ind. Aerodyn. – 2008. – Vol. 96. – pp. 1749-1761.
19. **Roache P.J.** Verification and Validation in Computational Science and Engineering // Hermosa Publishers, Albuquerque, New Mexico – 1998. – p. 446.
20. Положение о верификации программных средств, применяемых при определении нагрузок и воздействий, напряженно-деформированного (и иного) состояния, динамических характеристик, оценке прочности, устойчивости и безопасности конструкций, зданий и сооружений / РААСН // Утв. президиумом РААСН, протокол №11 от 25 нояб. 2016 г. – М., 2016. – 28 с.
21. **Белостоцкий А.М., Горячевский О.С., Саиян С.Г., Ефимова А.М.** Верификация и валидация численного моделирования ветровых нагрузок на примере Музейного и театрально-

образовательного комплекса в г. Кемерово // J. Comput. Civ. Struct. Eng. – 2025. – Т. 21. – №. 4. – С. 185-204.

Alexander Mikhailovich Belostotsky – DSc, Professor, Full Member of the Russian Academy of Architecture and Construction Sciences, General Director R&D Centre StaDyO; 125040, Russia, Moscow, 3ya Ulitsa Yamskogo Polya, 18. Scientific adviser at A.B. Zolotov REC CM of the National Research Moscow State University of Civil Engineering; 129337, Russia, Moscow, Yaroslavskoe shosse, 26. e-mail: amb@stadyo.ru

Nikita Aleksandrovich Britikov – CSc, Engineer at A.B. Zolotov REC CM of the National Research Moscow State University of Civil Engineering; 129337, Russia, Moscow, Yaroslavskoe shosse, 26. Engineer at R&D Centre StaDyO; 125040, Russia, Moscow, 3ya Ulitsa Yamskogo Polya, 18. e-mail: n.a.britikov@gmail.com

Oleg Sergeevich Goryachevsky – CSc, Deputy Director at A.B. Zolotov REC CM of the National Research Moscow State University of Civil Engineering; 129337, Russia, Moscow, Yaroslavskoe shosse, 26. Leading engineer of R&D Centre StaDyO; 125040, Russia, Moscow, 3ya Ulitsa Yamskogo Polya, 18. e-mail: osg@reccm.ru

Александр Михайлович Белостоцкий – д.т.н., профессор, академик РААСН, генеральный директор АО НИЦ СтаДиО; 125040, Россия, Москва, 3-я улица Ямского Поля, 18. Научный руководитель НОЦ КМ им. А.Б. Золотова Национального исследовательского Московского государственного строительного университета; 129337, Россия, г. Москва, Ярославское шоссе, д. 26. e-mail: amb@stadyo.ru

Никита Александрович Бритиков – к.т.н., инженер НОЦ КМ им. А.Б. Золотова Национального исследовательского Московского государственного строительного университета; 129337, Россия, г. Москва, Ярославское шоссе, д. 26. Инженер-расчетчик АО НИЦ СтаДиО; 125040, Россия, г. Москва, 3-я улица Ямского Поля, 18. e-mail: n.a.britikov@gmail.com

Олег Сергеевич Горячевский – к.т.н., заместитель директора НОЦ КМ им. А.Б. Золотова Национального исследовательского Московского государственного строительного университета; 129337, Россия, г. Москва, Ярославское шоссе, д. 26. Ведущий инженер-расчетчик АО НИЦ СтаДиО; 125040, Россия, г. Москва, 3-я улица Ямского Поля, 18/ e-mail: osg@reccm.ru

DOI:10.22337/2587-9618-2026-22-3-90-98

NUMERICAL MODELING OF PLANE FRAME VIBRATIONS TAKING INTO ACCOUNT NONLOCAL IN TIME ELASTIC PROPERTIES OF THE MATERIAL

Vladimir N. Sidorov [1,2], Elena. S. Badina [1,2], Roman O. Tsarev [1]

[1] Moscow State University of Civil Engineering, Moscow, RUSSIA

[2] Russian University of Transport (MIIT), Moscow, RUSSIA

Abstract: This paper presents a model for the dynamic deformation of plane composite frames accounting for the time-nonlocal elastic behavior of the material. The time-nonlocal model, previously developed for beam elements, is extended to frame structures and implemented within the finite element method. The influence of the nonlocal model scale parameter on the dynamic response is investigated. A U-shaped frame made of thermosetting vinyl ester glass-fiber-reinforced polymer is used as a case study to calibrate the scale parameter against reference three-dimensional finite element analysis results using the least-squares criterion and the golden-section search method. The calibrated time-nonlocal model significantly reduces the root-mean-square error compared with the classical local model and provides results that are in close agreement with the reference three-dimensional finite element analysis. The results provide additional evidence that the scale parameter of the time-nonlocal model can be regarded as an intrinsic material property independent of the structural geometry.

Keywords: Nonlocal mechanics, nonlocal damping, numerical simulation, finite element method

ЧИСЛЕННОЕ МОДЕЛИРОВАНИЕ КОЛЕБАНИЙ ПЛОСКИХ РАМ С УЧЕТОМ НЕЛОКАЛЬНЫХ ВО ВРЕМЕНИ УПРУГИХ СВОЙСТВ МАТЕРИАЛА

В.Н. Сидоров [1,2], Е.С. Бадьина [1,2], Р.О. Царев [1]

[1] Национальный исследовательский Московский государственный строительный университет, г. Москва, РОССИЯ

[2] Российский университет транспорта (МИИТ), г. Москва, РОССИЯ

Аннотация: В статье рассматривается модель динамического деформирования плоских рам из композитных материалов с учетом нелокальности упругих свойств материала во времени. Нелокальная модель, разработанная ранее для балочных элементов, распространена на случай рамных систем и выполнена её конечно-элементная реализация. Исследовано влияние изменения масштабного параметра нелокальной модели на характеристики колебательного процесса. На примере расчета П-образной рамы из термоактивного винилэфирного стеклопластика выполнена калибровка масштабного параметра по результатам трехмерного конечно-элементного моделирования с использованием метода наименьших квадратов и метода золотого сечения. Показано, что применение откалиброванной нелокальной модели позволяет существенно снизить среднеквадратичную ошибку по сравнению с классической локальной моделью и получить результаты, сопоставимые с трехмерным моделированием. Установлено, что масштабный параметр нелокальной модели может рассматриваться как характеристика материала, не зависящая от геометрии конструкции.

Ключевые слова: Нелокальная механика, нелокальное демпфирование, численное моделирование, метод конечных элементов

INTRODUCTION

Technological development plays a key role in many fields, including construction, mechanical engineering, and manufacturing. Particular attention is given to the development and application of composite and nanomaterials with controllable physical, mechanical, and chemical properties, as these materials are essential for the design and development of innovative engineering products. However, such materials often exhibit orthotropic or anisotropic behavior, requiring the development of reliable theoretical models supported by experimental validation. These models must accurately describe the material response under various loading conditions, including dynamic loading. Three-dimensional finite element models are widely used for this purpose because they can account for the internal structure of the material and its influence on mechanical behavior. However, their high computational cost limits their use in practical engineering applications. An alternative approach is provided by one-dimensional models based on specific hypotheses, including those derived from the principles of nonlocal mechanics.

Examples of such models include the approach presented in [1], which considers several damping mechanisms during the vibration of a quasi-isotropic pultruded composite beam, including external damping, strain rate-dependent internal damping, spatial hysteresis, and temporal hysteresis. The study also investigates different combinations of these damping mechanisms. Other models based on the principles of nonlocal mechanics include the nonlocal elasticity model proposed in [2] and the model presented in [3], which incorporates the nonlocality of both elastic and damping properties. The identification of the parameters of a nonlocal damping model using numerical simulations of the dynamic response of a composite beam is described in [4], whereas [5] presents a time-nonlocal internal friction model integrated into a finite element algorithm. These studies demonstrate that one-dimensional models based on the nonlocal approach can serve as an efficient alternative to detailed three-dimensional finite element models.

In the classical local formulation, the defining relations for viscoelastic material, as described by the Kelvin-Voigt model, take the following form:

$$\sigma^{ij} = C^{ijkl}\varepsilon_{kl} + X^{ijkl}\frac{\partial \varepsilon_{kl}}{\partial t}, \qquad (1)$$

where C^{ijkl} is elastic moduli tensor, $X^{ijkl} = C^{ijkl}t_e$ is viscosity moduli tensor, t_e is the retardation time, σ^{ij} is stress tensor, ε_{kl} is strain tensor.

The Cauchy relation:

$$\varepsilon_{ij} = \frac{1}{2}\left(\nabla_i u_j + \nabla_j u_i\right), \qquad (2)$$

where ∇_i is the differential operator and u_i is the components of displacements.

When transitioning to a nonlocal formulation, relation (1) takes the following form:

$$\sigma^{ij} = C^{ijkl}\int_0^t R(t-\tau)\varepsilon_{kl}(\tau)d\tau + X^{ijkl}\dot{\varepsilon}_{kl} \qquad (3)$$

In Eq. (3), $R(t-\tau)$ denotes the kernel of the nonlocal elasticity operator. It characterizes the decay of the contribution of strains at previous time instants τ to the elastic forces at the current time t. The kernel must satisfy the normalization requirement: $\int_0^t R(t-\tau)\,d\tau = 1$

In the present model, only the elastic properties of the material are assumed to be time-nonlocal. Under this assumption, the elastic forces at the current time depend not only on the current deformation state but also on the deformation history of the material.

A time-nonlocal model of the elastic properties of materials was previously developed for Euler–Bernoulli beam elements and integrated into a finite element algorithm [6].

The incorporation of the model into the finite element framework enables its application to the

analysis of rod systems with relatively complex geometries. The present study extends this approach to frame structures and demonstrates the applicability of the time-nonlocal model for predicting their dynamic response.

CONSTRUCTION OF A TIME-NONLOCAL DYNAMIC DEFORMATION MODEL FOR A ROD SYSTEM.

In order to make the nonlocal in time dynamic deformation model suitable for practical calculations, it has been incorporated into the finite element method algorithm. The physical interpretation of the finite element dynamic problems can be based on the principle of virtual work [7]:

$$\int_V \rho \ddot{u}_i \delta u_i dV + \int_V \sigma_{ij} \delta \varepsilon_{ij} dV = \int_A q_i \delta u_i dA + \int_V F_i \delta u_i dV. \quad (4)$$

Here ρ is a material density; q_i and F_i are surface and body forces; δu_i is the field of virtual displacements; $\delta \varepsilon_{ij}$ is the field of virtual strains. The two dots denote the second time derivative. Using the defining relation of a nonlocal in time dynamic deformation model (3) and considering the components of elastic moduli tensor constant in time, we can rearrange (4) as:

$$\int_V \rho \ddot{u}_i \delta u_i dV + \int_V C^{ijkl} \int_0^t R_t(t-\tau) \varepsilon_{kl}(\tau) d\tau \, \delta \varepsilon_{ij} dV + \int_V X^{ijkl} \dot{\varepsilon}_{kl} \delta \varepsilon_{ij} dV = \int_A q_i \delta u_i dA + \int_V F_i \delta u_i dV. \quad (5)$$

When employing the finite element approach, the actual strain and displacement fields for an element are replaced by approximate ones [8]:

$$\tilde{u} \approx \boldsymbol{N}\boldsymbol{d}, \quad (6)$$

where $\boldsymbol{N}$ is the shape functions matrix, $\boldsymbol{d}$ is the vector of displacements along the nodal degrees of freedom.

With the matrix operator of Cauchy relations $\boldsymbol{A}$ we can write $\boldsymbol{A}\boldsymbol{N} = \boldsymbol{B}$, then assumed element strain field is:

$$\tilde{\varepsilon} = \boldsymbol{B}\boldsymbol{d}. \quad (7)$$

Considering this and omitting the virtual nodal displacements according to the principle of virtual work [7] we can represent (5) in matrix form:

$$\int_V \rho \boldsymbol{N}^{\boldsymbol{T}} \boldsymbol{N} dV \ddot{\boldsymbol{d}} + \int_V \boldsymbol{B}^{\boldsymbol{T}} \boldsymbol{X} \boldsymbol{B} dV \dot{\boldsymbol{d}} + \int_V \boldsymbol{B}^{\boldsymbol{T}} \boldsymbol{C} \int_0^t R(t-\tau) \boldsymbol{B}\boldsymbol{d}(\tau) d\tau \, dV = \int_A \boldsymbol{N}\boldsymbol{q} dA + \int_V \boldsymbol{N}\boldsymbol{F} dV \quad (8)$$

For a plane frame, the constitutive matrix $\boldsymbol{C}$ contains two components corresponding to the axial and bending stiffness of the element, while the strain vector consists of two components: the axial strain and the curvature. The bending stiffness matrix was derived previously in [9]. Therefore, in the present study, only the axial component is derived:

$$\varepsilon_{11} = \frac{du}{dx}. \quad (9)$$

Here, x is the longitudinal coordinate of the beam, ε_{11} is the axial strain, and u is the axial displacement of the frame cross-sections. The assumed solution $\tilde{u} \approx \boldsymbol{N}\boldsymbol{d}$ for each frame

element can be written using interpolation functions:

$$\boldsymbol{N} = \left[1 - \frac{s}{l} \quad \frac{s}{l}\right], \tag{10}$$

where l is an element length, $s \in [0, l]$ is an element longitudinal coordinate.
Using $\frac{d}{ds}$ as $\boldsymbol{A}$ we have:

$$\boldsymbol{B} = \frac{d\boldsymbol{N}}{ds} = \left[-\frac{1}{l} \quad \frac{1}{l}\right]. \tag{11}$$

Since all elements of $\boldsymbol{B}$ matrix are time independent we can take it out of the integral over time in (8). Then taking into account that cross-sectional moment of inertia is $A = \int_A dA$ we obtain:

$$\begin{aligned} &\int_l \rho A \boldsymbol{N^T N} ds \ddot{\boldsymbol{d}} + \int_l \boldsymbol{B^T} \chi I_z \boldsymbol{B} ds \dot{\boldsymbol{d}} \\ &+ \int_l E I_z \boldsymbol{B^T B} \int_0^t R(t-\tau)\boldsymbol{d}(\tau) d\tau \, ds \\ &= \boldsymbol{F}. \end{aligned} \tag{12}$$

Here $\boldsymbol{M_i} = \int_l \rho A \boldsymbol{N^T N} ds$ is the beam element mass matrix, $\boldsymbol{D_i} = \int_l \boldsymbol{B^T} \chi A \boldsymbol{B} ds$ is the element damping matrix, $\boldsymbol{K_i} = \int_l E A \boldsymbol{B^T B} ds$ is the element stiffness matrix, $\boldsymbol{F}$ – is the load vector.
To derive the stiffness matrices of a rod element subjected to axial deformation, the shape function matrix $\boldsymbol{N}$ and the strain–displacement matrix $\boldsymbol{B}$ are substituted into the integral expressions for the stiffness matrices, respectively, previously obtained in Eq. (12).

$$\boldsymbol{K_i} = E \begin{bmatrix} \frac{\mathrm{A}}{l} & -\frac{\mathrm{A}}{l} \\ -\frac{\mathrm{A}}{l} & \frac{\mathrm{A}}{l} \end{bmatrix}, \tag{13}$$

In (12) the damping matrix is proportional to the stiffness matrix. The same result was obtained in [5], where the damping matrix was derived using the stationary condition of the system's total energy during vibration.
After assembling $\boldsymbol{M_i}$, $\boldsymbol{D_i}$, $\boldsymbol{K_i}$ to a global mass matrix $\boldsymbol{M}$, damping matrix $\boldsymbol{D}$ and stiffness matrix $\boldsymbol{K}$ of the beam, we can write the finite element formulation of equation of motion:

$$\boldsymbol{M}\ddot{\boldsymbol{d}} + \boldsymbol{D}\dot{\boldsymbol{d}} + \boldsymbol{K} \int_0^t R(t-\tau)\boldsymbol{d}(\tau) d\tau = \boldsymbol{F}. \tag{14}$$

When modeling the dynamic behavior of a plane frame, it is necessary to take into account that its elements are subjected not only to bending but also to tension and compression. Therefore, each node of the finite element model should have three degrees of freedom (Fig. 1). The bending stiffness matrix for nonlocal in time FEA model also has a standard form, which was demonstrated in [мы].
The stiffness matrix $\boldsymbol{K}_i$ of a plane frame element with three degrees of freedom at each node is a combination of axial and bending stiffness matrices and has the following form:

$$\begin{bmatrix} \frac{EA}{l} & 0 & 0 & -\frac{EA}{l} & 0 & 0 \\ 0 & \frac{12EI}{l^3} & \frac{6EI}{l^2} & 0 & -\frac{12EI}{l^3} & \frac{6EI}{l^2} \\ 0 & \frac{6EI}{l^2} & \frac{4EI}{l} & 0 & -\frac{6EI}{l^2} & \frac{2EI}{l} \\ -\frac{EA}{l} & 0 & 0 & \frac{EA}{l} & 0 & 0 \\ 0 & -\frac{12EI}{l^3} & -\frac{6EI}{l^2} & 0 & \frac{12EI}{l^3} & -\frac{6EI}{l^2} \\ 0 & \frac{6EI}{l^2} & \frac{2EI}{l} & 0 & -\frac{6EI}{l^2} & \frac{4EI}{l} \end{bmatrix} \tag{15}$$

Here, **E** is the modulus of elasticity, **I** and **A** are the moment of inertia and the cross-sectional area of the element, respectively, and $\boldsymbol{l}$ is the length of the element.

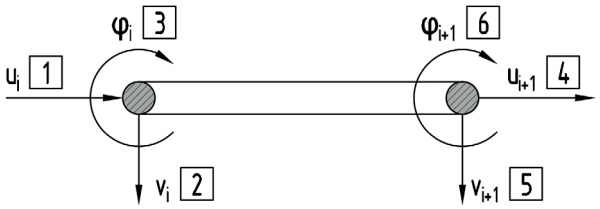


Figure 1. Numbering of the degrees of freedom of a frame finite element

To account for the time-nonlocal properties of the material, it is assumed that the elastic forces in the system at time t depend not only on the current displacement $\boldsymbol{d}(t)$, but also on the displacement history, i.e., the displacement values at previous time instants τ. The influence of past states decreases as the time interval between t and τ increases [10].

Various kernel functions have been proposed to model the memory function [2]. In the present study, the nonlocal operator is defined by an error function kernel, which is expressed in the following form accounting for the normalization requirement:

$$R(t-\tau) = \frac{2\eta}{\sqrt{\pi}} \cdot e^{-\eta^2(t-\tau)^2} \qquad (16)$$

Like for all non-local models, in this case, a defining characteristic is the scale parameter η, which determines the level of nonlocality in the elastic properties of the material over time. Figure 2 illustrates how this parameter influences the shape of the kernel.

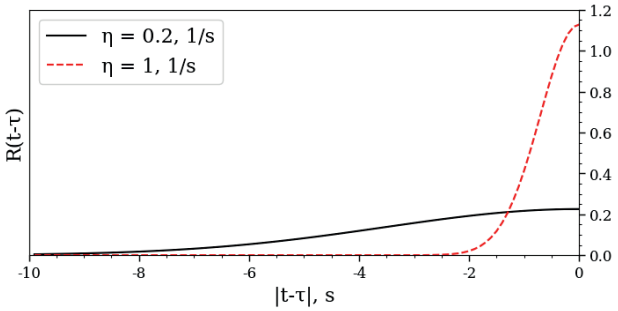


Figure 2. Graphs showing the effect of the parameter η on the nonlocality of the model

ASSESSMENT OF THE INFLUENCE OF THE SCALE PARAMETER ON THE NATURE OF THE OSCILLATORY PROCESS

To further develop the proposed model, it is necessary to investigate the effect of the scale parameter on the dynamic response of the rod system. The equation of motion was solved using an implicit Newmark integration scheme [11]. Nodal displacements were computed following the procedure previously developed for the vibration analysis of Euler–Bernoulli beam elements with time-nonlocal elastic material properties [6].

As a numerical example, a U-shaped frame with fixed supports was analyzed (Fig. 3). The frame was assumed to be made of a Class I thermoactive vinyl ester fiberglass composite, the material properties of which are listed in Table 1. The columns have a square cross-section with a side length of 0.4 m, whereas the horizontal beam has a rectangular cross-section measuring 0.3 m in height and 0.4 m in width. An instantaneous uniformly distributed load with an intensity of −11 kN/m was applied along the horizontal beam.

Table 1. Properties of thermoactive vinyl ester glass-reinforced plastic Class I (plane model):

Young's Modulus, Elw	17.2 GPa
Poisson's Ratio, μlw	0.32
Density, ρ	1.9 kg/m3
Damping Coefficient, γ	0.042

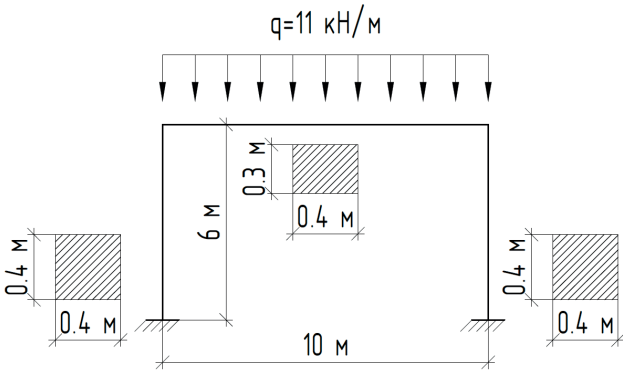


Figure 3. Computational model of the frame adopted for numerical simulation

The viscosity coefficient for the considered frame is $\chi = 0.021$ Pa·s.
To solve the equation of motion (14) in matrix form, an implicit scheme [11] was employed:

$$\boldsymbol{Q}\boldsymbol{d}_{i+1} = \boldsymbol{F}_{i+1} + \mathbf{M}\ddot{\boldsymbol{d}}_i + \boldsymbol{Q_1}\dot{\boldsymbol{d}}_i + \boldsymbol{Q_2}\boldsymbol{d}_i - \boldsymbol{K}\beta, \quad (17)$$

where:

$$\boldsymbol{Q} = \frac{2}{\Delta t^2}\boldsymbol{M} + \frac{1}{\Delta t}\boldsymbol{D} + \boldsymbol{K}\alpha, \qquad \boldsymbol{Q_1} = \frac{2}{\Delta t}\boldsymbol{M},$$
$$\boldsymbol{Q_2} = \frac{2}{\Delta t^2}\boldsymbol{M} + \frac{1}{\Delta t}\boldsymbol{D}, \quad (18)$$

The integral kernel (16) has been discretized and divided into two parts: α - the weighting coefficient associated with $\boldsymbol{d}$i+1, β - the sum of all other weights (fig.2):

$$\alpha = \frac{2\eta}{\sqrt{\pi}} \cdot e^{-\eta^2(t_{i+1}-t_i)^2} \cdot \Delta t;$$
$$\beta = \Delta t \sum_{j=1}^{i} \frac{2\eta}{\sqrt{\pi}} \cdot e^{-\eta^2(t_i-t_{j-1})^2} \quad (22)$$

Computer programs were developed in Python programming language. Based on the above initial data, a series of calculations was performed for different values of the scale parameter in order to assess its influence on the characteristics of the oscillatory process. The obtained results are presented in Fig. 4.
Analysis of the presented plots shows that a decrease in the parameter η (an increase in the degree of nonlocality) leads to an increase in the vibration amplitude.

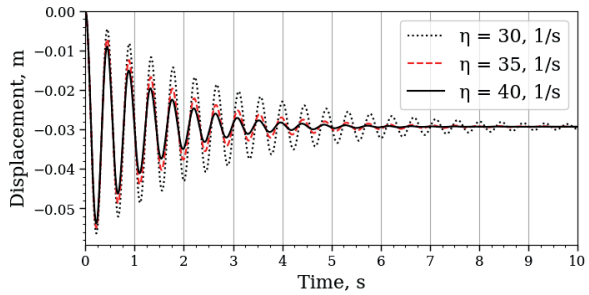


Figure 4. Displacement plots of the central node of the upper chord of the frame obtained from three computational cases with different values of the scale parameter

DETERMINATION OF THE NONLOCAL PARAMETER BASED ON THE RESULTS OF A NUMERICAL EXPERIMENT

For the proposed nonlocal material model to be used in engineering applications, the value of the nonlocal parameter must first be identified. In the present study, this parameter is determined through a calibration procedure based on the least squares method using the results of a numerical experiment. The reference data for the calibration were obtained from a three-dimensional finite element analysis of the frame structure described in the previous section. The numerical model was developed in the MIDAS Civil NX software package and accounts for the orthotropic properties of the composite material. The material properties used in the analysis are listed in Table 2.

Table 2. Properties of thermoactive vinyl ester glass-reinforced plastic Class I (3D solid model):

Young's Modulus (Longitudinal), E_{lw}	17.2 GPa
Young's Modulus (Transverse), E_{cw}	12.2 GPa
Poisson's Ratio (Longitudinal), μ_{lw}	0.32
Poisson's Ratio (Transverse), μ_{cw}	0.15
Density, ρ	1.9 kg/m^3
Damping Coefficient, γ	0.042

The finite element analysis provided the displacement history of the midpoint of the frame girder. The corresponding displacement data obtained in MIDAS Civil NX were exported to a Python program developed for identifying the scale parameter. The program implements a least squares calibration procedure, in which the scale parameter of the nonlocal model is identified by minimizing the sum of squared differences between the reference data and the numerical predictions. The optimization was performed using the golden section method.
The comparison of the results is shown in Figs. 5 and 6. Compared with the classical local model, the calibrated nonlocal rod model shows better agreement with the results of the three-dimensional finite element analysis.

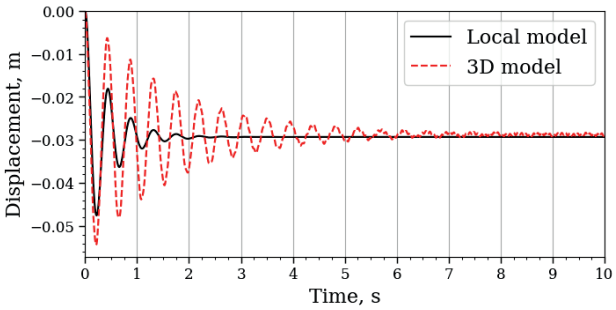


Figure 5. Comparison of the results of the three-dimensional numerical experiment with the results of one-dimensional modeling based on the classical local model. The relative error is 13.56%

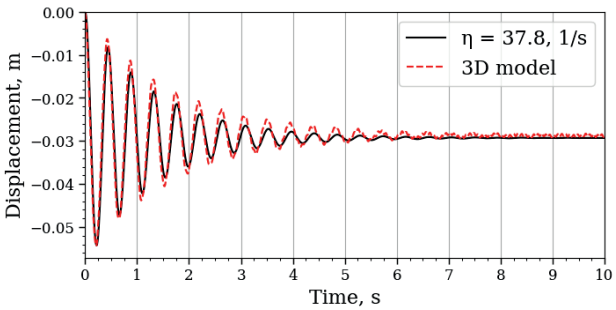


Figure 6. Comparison of the results of the three-dimensional numerical experiment with the results of one-dimensional modeling using the calibrated time-nonlocal deformation model with the error function kernel. The relative error is 5.41%

The results clearly demonstrate that the calibrated nonlocal rod model allows to reduce the root mean square error by nearly one order of magnitude compared with the corresponding local model. Thus, the proposed approach achieves an accuracy comparable to that of the three-dimensional finite element model.

Paper [6] presents the results of a series of numerical studies on Euler–Bernoulli beam elements with time-nonlocal elastic material properties.

The calibration data for the 12 meters long beam with a fixed ends and with a cross-section 20x30 cm was obtained in MIDAS Civil NX similarly as it was done for the frame. The material properties were taken as for the GFRP (Table 2)

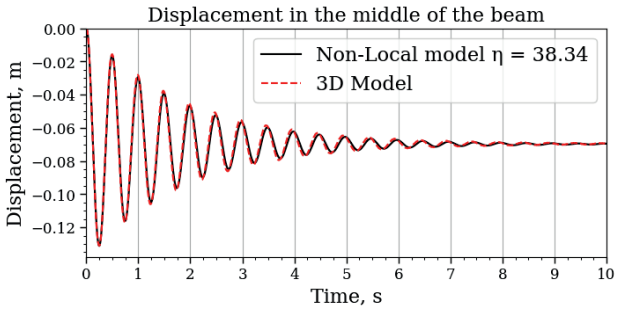


Figure 7. Calibration results for the beam presented in [6]

The beam has the similar firs Eigen frequency as the considered frame (fig. 3), and thus a similar viscosity coefficient of 0.021 Pa·s. It was identified that the value of the scale parameter for the considered beam was 38.34 s^{-1}. Although the calibration presented in this study was performed independently for a frame structure, the resulting combination of viscosity coefficient and scale parameter (0.022 Pa·s and 37,8 s^{-1}, respectively) is in close agreement with the corresponding values reported in [6]. This finding provides additional evidence that the scale parameter is an intrinsic material property of the nonlocal model and, therefore, does not require recalibration when the geometry of the structure changes.

CONCLUSION

The previously developed time-nonlocal dynamic deformation model, originally formulated for Euler–Bernoulli beam elements, has been extended to describe the dynamic response of frame structures. The influence of the scale parameter η on the structural response has been investigated, showing that an increase in the degree of temporal nonlocality leads to higher vibration amplitudes.

Compared with the classical local formulation, the calibrated nonlocal rod model shows significantly better agreement with the reference three-dimensional finite element analysis. The calibration results provide additional evidence that the scale parameter is an intrinsic material property of the proposed nonlocal model and is independent of the structural geometry.

ACKNOWLEDGEMENT

This research is supported by Russian Science Foundation (Project No 25-11-00140)

REFERENCES

1. **Banks H. T., Inman D. J.,** 1991, On damping Mechanisms in Beams Journal of Applied Mechanics 58(3) pp 716–723.
2. **Eringen, A.C.,** 1972 Nonlocal elasticity / A.C. Eringen, D.G.B. Edelen // International Journal of Engineering Science. – 1972. - 10 (3), 233–248.
3. **Potapov V.D**. On the stability of the rod under the action of deterministic and stochastic loads, taking into account the nonlocal elasticity and nonlocal damping of the material. 2015. No. 1. S. 9–16.
4. **Shepitko E.S., Sidorov, V.N.** 2019. Defining of nonlocal damping model parameters based on composite beam dynamic behaviour numerical simulation results/ E. S. Shepitko, V. N. Sidorov : IOP Conf. Series: Materials – 2019
5. **Sidorov, V.N., Badina, E.S., Detina, E.P** 2021. Nonlocal In Time Model Of Material Damping In Composite Structural Elements Dynamic Analysis. International Journal for Computational Civil and Structural Engineering, Vol.17(4), pp. 14–21
6. **Sidorov V.N., Badina E.S., Tsarev R.O.** Calibration of the Nonlocal Dynamic Deformation Model of a Flexural Beam Based on Numerical Experiment Results. International Journal for Computational Civil and Structural Engineering, 2024, Vol. 20(2), pp. 132–140.
7. **Khechumov R.A., Keppler H., Prokopyev V.I.** Application of the Finite Element Method to Structural Calculations. Publishing House of the Association of Construction Universities, 1994. 350 p. (In Russian)
8. **Bhatti M.A.** Fundamental Finite Element Analysis and Applications: with Mathematica and Matlab Computations. Wiley, 2005, 700 p.
9. **Sidorov V.N., Badina E.S., Tsarev R.O.** Nonlocal in Time Dynamic Deformation Model and Its Calibration Based on the Beam Vibration Experiment Results. International Journal for Computational Civil and Structural Engineering. – 2025. – Vol. 21(2), pp. 161-170.
10. **Flugge W.** Viscoelasticity. Blaisdell Publishing Company, Waltham, Massachusetts, 1967. An introductory text dealing with both Kelvin-Voigt and Maxwell materials and their generalizations; 2d rev. ed. Springer-Verlag, Berlin, 1975.
11. **Sidorov V.N., Badina E.S.** Finite Element Method in Stability and Vibration Problems of Rod Structures. AVS Publishing, Moscow, 2021. 172 p. (In Russian)

СПИСОК ЛИТЕРАТУРЫ

1. **Banks H. T., Inman D. J.,** 1991, On damping Mechanisms in Beams Journal of Applied Mechanics 58(3) pp 716–723.
2. **Eringen, A.C.,** 1972 Nonlocal elasticity / A.C. Eringen, D.G.B. Edelen // International Journal of Engineering Science. – 1972. - 10 (3), 233–248.
3. **Потапов В.Д.** 2015. Об устойчивости стержня при действии детерминированной и стохастической нагрузки с учетом нелокальной упругости и нелокального демпфирования материала // Проблемы машиностроения и теории надежности. № 1. С. 9–16.
4. **Shepitko E.S., Sidorov, V.N.** 2019. Defining of nonlocal damping model parameters based on composite beam dynamic behaviour numerical simulation results/ E. S. Shepitko, V. N. Sidorov : IOP Conf. Series: Materials - 2019

5. **Sidorov, V.N., Badina, E.S., Detina, E.P** 2021. Nonlocal In Time Model Of Material Damping In Composite Structural Elements Dynamic Analysis. International Journal for Computational Civil and Structural Engineering, Vol.17(4), pp. 14–21
6. **Sidorov V.N., Badina E.S., Tsarev R.O.** Calibration of the Nonlocal Dynamic Deformation Model of a Flexural Beam Based on Numerical Experiment Results. International Journal for Computational Civil and Structural Engineering, 2024, Vol. 20(2), pp. 132–140.
7. **Хечумов Р.А., Кепплер Х., Прокопьев В.И.** Применение метода конечных элементов к расчету конструкций. Изд-во Ассоц. строит. вузов, 1994, 350 с.
8. **Bhatti M.A.** Fundamental Finite Element Analysis and Applications: with Mathematica and Matlab Computations. Wiley, 2005, 700 p.
9. **Sidorov V.N., Badina E.S., Tsarev R.O.** Nonlocal in Time Dynamic Deformation Model and Its Calibration Based on the Beam Vibration Experiment Results. International Journal for Computational Civil and Structural Engineering. – 2025. – Vol. 21(2), pp. 161-170.
10. **Flugge W.** Viscoelasticity. Blaisdell Publishing Company, Waltham, Massachusetts, 1967. An introductory text dealing with both Kelvin-Voigt and Maxwell materials and their generalizations; 2d rev. ed. Springer-Verlag, Berlin, 1975.
11. **Сидоров В.Н., Бадьина Е.С.** Метод конечных элементов в задачах устойчивости и колебаний стержневых конструкций. Издательство АСВ, М. 2021. 172 с.

Vladimir N. Sidorov, Academician of Russian Academy of Architecture and Construction Science, Professor, Dr.Sc, Rectorate Counselor, Head of the Department of Computer Science and Applied Mathematics, National Research University Moscow State University of Civil Engineering, Professor of «Building Structures, Buildings and Facilities», Institute of Railway Track, Construction and Structures, Russian University of Transport (MIIT) 129337, Russia, Moscow, Yaroslavskoe Highway, 26, e-mail: sidorov.vladimir@gmail.com

Elena S. Badina, Associate Professor, Ph.D, Associate Professor of the Department of Computer Science and Applied Mathematics, National Research University Moscow State University of Civil Engineering, Associate Professor of «Computer Aided Design» Department, Institute of Railway Track, Construction and Structures, Russian University of Transport (MIIT), 129337, Russia, Moscow, Yaroslavskoe Highway, 26, e-mail: shepitko-es@mail.ru

Tsarev O. Roman, Research Engineer of A.B. Zolotov Research and Educational Center for Computer Modeling of Unique Buildings, Structures, and Complexes, National Research Moscow State University of Civil Engineering (NRU MGSU); 129337, Russia, Moscow, Yaroslavskoe Highway, 26, e-mail: tsarev.r.o@yandex.ru

Сидоров Владимир Николаевич, академик РААСН, профессор, доктор технических наук, советник при ректорате, заведующий кафедрой информатики и прикладной математики Национального исследовательского Московского государственного строительного университета; профессор кафедры «Строительные конструкции, здания и сооружения» Института пути, строительства и сооружений Российского университета транспорта (МИИТа), 129337, г. Москва, Ярославское шоссе, д. 26, e-mail: sidorov.vladimir@gmail.com.

Бадьина Елена Сергеевна, доцент, кандидат технических наук, доцент кафедры информатики и прикладной математики Национального исследовательского Московского государственного строительного университета, доцент кафедры «Системы автоматизированного проектирования» Института пути, строительства и сооружений Российского университета транспорта (МИИТа), 129337, г. Москва, Ярославское шоссе, д. 26, e-mail: shepitko-es@mail.ru.

Царев Роман Олегович, инженер-исследователь Научно-образовательного центра компьютерного моделирования уникальных зданий, сооружений и комплексов имени А.Б. Золотова Национального исследовательского Московского государственного строительного университета; 129337, г. Москва, Ярославское шоссе, д. 26, e-mail: tsarev.r.o@yandex.ru

DOI:10.22337/2587-9618-2026-22-3-99-112

ANALYSIS AND COMPARISON OF THE EFFECTIVENESS OF VARIOUS SEISMIC ISOLATORS IN REDUCING SEISMIC MOVEMENTS RECORDED IN PERU

Hubert S. Morales, Arnold S. Grados, Flor O. Vara
Technological University of Peru, Lima, PERÚ

Abstract: This study compares the seismic performance of four types of seismic protection technologies, the triple pendulum bearings (TPBs), viscous dampers (VDs), tuned mass dampers (TMDs) and high-damping rubber bearings (HDRBs).: Structural models developed in ETABS for 5 and 10-story buildings in Seismic Zone 4 of Peru were used for the analysis. The results demonstrate that TPBs provide the highest reduction of floor accelerations for all the considered buildings and story levels with effectiveness values in the range of 75% to 82%, better than both HDRBs and energy dissipation systems. The study found that HDRBs achieved reduction of 65% to 75% while viscous dampers (VDs) reduced the floor accelerations by 30% to 45%. Tuned mass dampers (TMDs) had the least performance with reductions of 12% to 22%. To summarize, the results indicate that seismic isolation systems, in particular TPBs, provide significantly higher reductions in the floor accelerations than energy dissipation systems.

Keywords: Seismic isolators, Viscous dampers, Tuned mass dampers, Nonlinear dynamic análisis, Earthquake-resistant engineering, Seismic acceleration reduction, Structural modeling

АНАЛИЗ И СРАВНЕНИЕ ЭФФЕКТИВНОСТИ РАЗЛИЧНЫХ СЕЙСМОИЗОЛЯТОРОВ ПРИ СЕЙСМИЧЕСКИХ ВОЗДЕЙСТВИЯХ, ЗАРЕГИСТРИРОВАННЫХ В ПЕРУ

Уберт С. Моралес, Арнольд С. Градос, Флор О. Вара
Технологический университет Перу, Лима, ПЕРУ

Аннотация: В данном исследовании сравнивается эффективность четырех систем сейсмоизоляции: трехмаятниковых сейсмоизоляторов (TPB), вязких демпферов (VD), настроенных массовых демпферов (TMD) и высокодемпфирующих резиновых сейсмоизоляторов (HDRB). Исследование выполнено с использованием расчетных моделей сооружений в программном комплексе ETABS. Были проанализированы здания высотой 5 и 10 этажей, расположенные в сейсмической зоне 4 Перу. Результаты показали, что система TPB обеспечила наибольшее снижение сейсмических ускорений во всех исследованных зданиях и на всех анализируемых уровнях, при эффективности от 75% до 82%, превзойдя систему HDRB и устройства рассеивания энергии. Система HDRB продемонстрировала умеренное снижение ускорений — от 65% до 75%. Вязкие демпферы (VD) обеспечили меньшее снижение — от 30% до 45%, тогда как настроенные массовые демпферы (TMD) показали наименьшую эффективность — от 12% до 22%. В целом результаты свидетельствуют о том, что системы, основанные на сейсмоизоляции, особенно TPB, значительно эффективнее снижают сейсмические ускорения по сравнению с системами рассеивания энергии.

Ключевые слова: сейсмоизоляторы, вязкие демпферы, настроенные массовые демпферы, нелинейный динамический анализ, сейсмостойкое строительство, снижение сейсмических ускорений, структурное моделирование

1. INTRODUCTION

The earthquakes that affect the Peruvian coast are due to the tectonic interaction between the Nazca and South American plates and are one of the major natural hazards for the country's infrastructure (Kumar et al., 2025). A large amount of energy is released and transmitted to

the Earth's surface during the subduction process, producing seismic forces that can affect buildings in both urban and rural areas (Chowdhury et al., 2025). The history of seismic events in Peru shows that earthquakes of large magnitude can result in structural collapse, loss of life and serious economic consequences. This reality necessitated the development of technologies to prevent transfer of seismic energy to structures and thus reduce structural damage and improve occupant safety.

Among these technologies, seismic isolation systems are characterized by their potential to enhance structural performance during earthquakes and to reduce the seismic demand transmitted to the superstructure (Shid et al., 2025). Studies conducted in different countries have shown that rubber-based isolation systems dissipate a substantial portion of seismic energy, resulting in lower structural displacements and floor accelerations. For example, Patel and Kumar (2025) compared reinforced concrete buildings with and without seismic isolation systems and reported a significant reduction in the upper-story displacements of isolated structures. Similarly, Karaton and Osmanlı (2021) evaluated the performance of a hospital equipped with triple pendulum bearings during the 2023 earthquakes in Türkiye and found that the facility remained operational even after experiencing multiple consecutive seismic events.

Recent studies on seismic performance and structural resilience based on nonlinear dynamic analyses have shown that friction-based base isolation systems, such as triple pendulum bearings (TPBs), provide superior performance compared with fixed-base frame structures equipped with viscous dampers (Hudson, 2025). These devices concentrate deformation demands at the isolation interface, reduce the influence of higher vibration modes, and significantly decrease floor accelerations throughout the superstructure (Hudson, 2025). Similarly, rubber-based seismic isolation systems have become one of the most widely used technologies owing to their high energy dissipation capacity. Recent studies have shown that the mechanical behavior of elastomeric layers, bounded by steel plates, produces a displacement-dependent nonlinear stiffness. This characteristic provides better control of deformations under severe earthquakes and helps to limit displacements within the isolation system (Zhang & Lu, 2024).

While tuned mass dampers are tuned to a narrow frequency band, typically that of the fundamental vibration mode of the structure, base isolation systems and viscous dampers are not (Belbachir et al., 2024). Hence, their ability to attenuate accelerations due to real earthquake excitations is generally more limited (Belbachir et al., 2024).

Several studies have also pointed out the benefits of adding supplementary damping devices to seismic isolation systems. Kiral and Tonyali (2025) have compared the performance of laminated rubber bearings with and without viscous dampers. It has been demonstrated that the use of these devices considerably reduces the acceleration and displacement of the floors within the isolation layer. Similarly, Ren et al. (2025) demonstrated that lead-rubber bearings (LRBs) subjected to near-fault earthquakes may suffer critical deformations, leading to an increase of the effective stiffness and higher dynamic demands on the superstructure. More recently, emerging technologies, such as metamaterial-based seismic isolators (Khosravi and Amjadian, 2025) have been proposed to modify the natural frequency of structures, thereby reducing inter-story drifts and floor accelerations.

The behaviour of seismic isolation systems has been widely investigated under various geotechnical and structural conditions. In this sense, Nettis et al. and Shid et al. (2025) evaluated the seismic vulnerability of isolated bridges along the Costa Verde in Lima, concluding that differential ground settlements increase the structural vulnerability, even in systems with high damping capacity. These findings reveal that although seismic isolation systems have performed well in many international applications, the effectiveness of these systems is influenced by structural

configurations, geotechnical conditions of the site, and the level of seismic ground motion (Shid et al., 2025).

Recent studies have been able to improve the knowledge of seismic isolation systems. However, there is a lack of comparative studies that evaluate the performance of different isolation technologies in conditions similar to those of the Peruvian seismic environment. In particular, the relative performance of each isolation system still has limited information, especially regarding the influence of coastal soil conditions, structural geometry, and earthquake duration. This lack of evidence makes it difficult to identify the most appropriate seismic protection technology for buildings located in Seismic Zone 4 of Peru, the region exposed to the country's highest level of seismic hazard.

To expand the available evidence for the Peruvian seismic context, this study compares the performance of four seismic protection technologies: triple pendulum bearings (TPBs), viscous dampers (VDs), tuned mass dampers (TMDs), and high-damping rubber bearings (HDRBs). Structural models developed in ETABS and designed in accordance with Peruvian seismic codes were used for this purpose. The main objective is to evaluate the reduction in seismic accelerations in 5- and 10-story buildings located in Zone 4 of Peru. The numerical models were defined using parameters including soil type, number of stories, structural configuration, and the mechanical properties of the construction materials. Subsequently, representative base models were developed, into which the different seismic control systems were incorporated. The structural response of the models was assessed using representative Peruvian earthquake records by comparing floor accelerations, inter-story drifts and lateral displacements. Lastly, an evaluation of the cost-benefit ratio of each alternative was carried out to find the solution that provides the best balance between structural performance and economic feasibility.

The main contribution of this study lies in comparing, under the same structural design conditions, the behavior of four seismic protection technologies using equivalent numerical models. Unlike much of the available literature, which analyzes each device independently, this research employs identical geometric models subjected to real seismic records from Peru and to the requirements established by Standard E.030. This made it possible to isolate the effect of each technology and provide a technical and economic basis to facilitate the selection of seismic protection systems for buildings located in Zone 4 of Peru.

2. METHODOLOGY

This research followed a quantitative, experimental-comparative approach, supported by numerical simulations developed using ETABS v20. The study was based on structural modeling and nonlinear dynamic analysis of reinforced concrete buildings equipped with different seismic control systems: triple-pendulum isolators, high-damping isolators, viscous dampers, and tuned-mass dampers. Various authors have noted that nonlinear analysis is a suitable tool for representing the actual response of structures subjected to severe seismic events, especially when seismic isolation and dissipation devices are incorporated (Karaton et al., 2021). This study focuses on buildings representative of Zone 4 in Peru, considered the region with the highest seismic hazard in the country.

To represent the diversity of the urban building stock, two reinforced concrete structural typologies were selected: a five-story low-rise building and a ten-story mid-rise building. These configurations were chosen because they are representative of the building stock in Metropolitan Lima and provide an appropriate basis for evaluating the influence of building height and structural stiffness on seismic response.

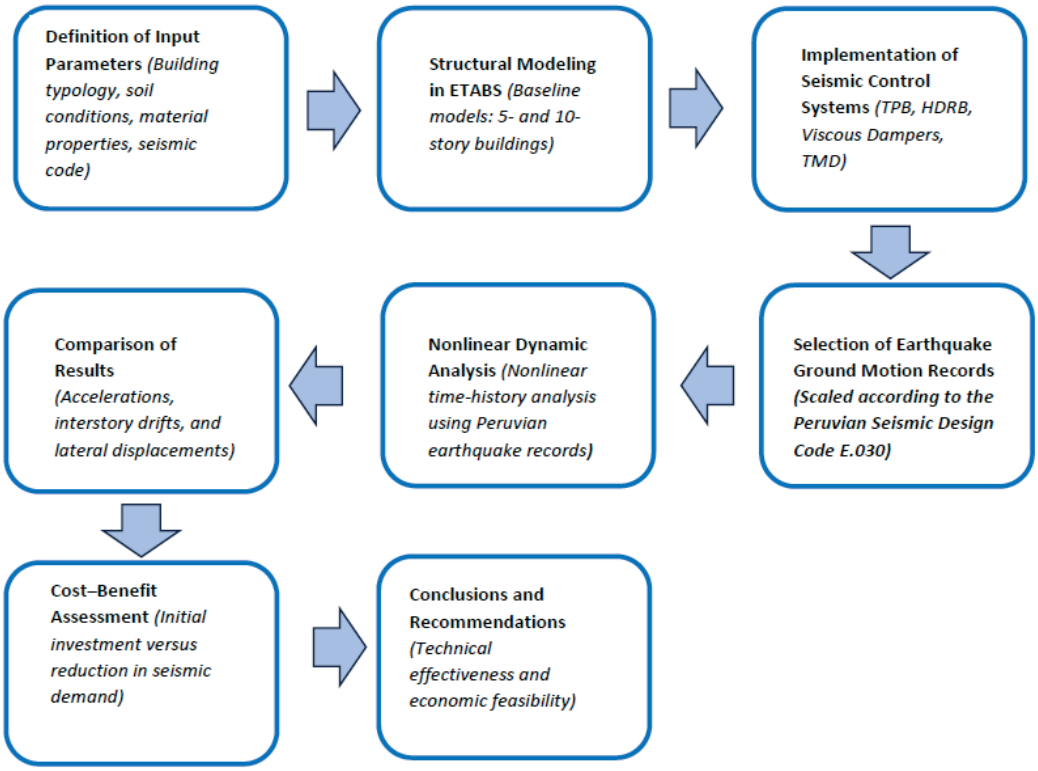


Figure 1. Research workflow of the study

The study followed an explanatory and applied research approach aimed at quantitatively comparing the performance of different seismic control technologies under representative earthquake ground motions for the Peruvian seismic environment. The analyses were limited to reinforced concrete moment-resisting frame buildings designed in accordance with the Peruvian Technical Standards E.020 (Loads), E.030 (Seismic Design), and E.060 (Reinforced Concrete). In accordance with the Peruvian Seismic Design Code (E.030), essential facilities require rigorous seismic assessment to ensure uninterrupted functionality following major earthquake events (Jarro et al., 2024). Numerical simulation tools specialized in seismic engineering, such as ETABS, allow for the accurate evaluation of structural response by estimating inter-story distortions, bidirectional displacements, and floor accelerations using local seismic records scaled in accordance with the requirements of current codes (Jarro et al., 2024).

Initially, the structural models were defined by establishing the building typology, soil conditions, and the mechanical properties of the construction materials. Subsequently, the seismic control systems were incorporated into the baseline models, and nonlinear dynamic analyses were performed using representative Peruvian earthquake ground motions. The resulting structural responses were then compared in terms of floor accelerations, interstory drifts, and lateral displacements, followed by a cost–benefit assessment of each technology.

The increase in the fundamental period constitutes the primary mechanism governing the effectiveness of base isolation systems (Musa, 2025). Finite element platforms such as ETABS allow engineers to evaluate how increased flexibility at the isolation interface shifts the natural period of the structure away from the resonance-sensitive region of the seismic response spectrum. As a result, base shear forces, interstory drifts, and dynamic demands transmitted to the superstructure are significantly reduced (Musa, 2025).

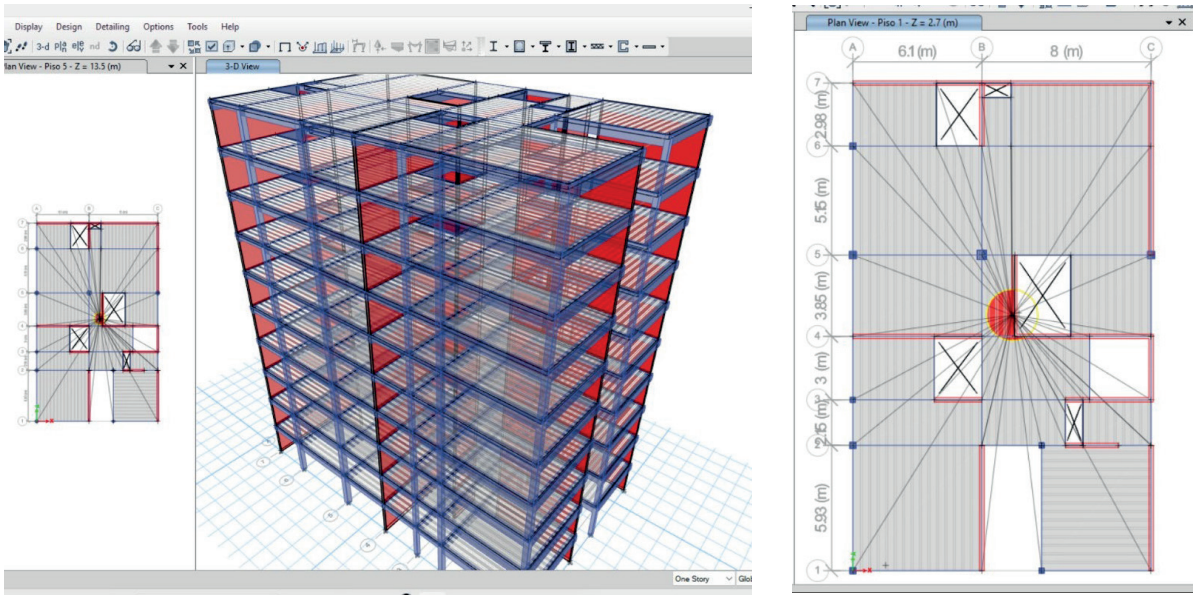


Figure 2. Representative structural building typologies considered in this study

Structural modeling was then carried out in ETABS. Baseline models of representative buildings (without seismic control devices) were developed in ETABS v20 by accurately defining their geometry, member sections, materials, and loading conditions. The structural modeling process involved the precise definition of the geometry, member sections, material properties, dead and live loads, as well as the support conditions.

The nonlinear properties of the devices were assigned to represent their actual behavior. For the TPB isolators, friction elements with radii of curvature (R_1, R_2, R_3) and variable kinematic friction coefficients ($\mu_{min}=0.03$ and $\mu_{max}=0.06$) were used, depending on the contact pressure. For the HDRBs, elastomeric supports were defined with a shear modulus (G) of 0.85 MPa and an effective damping of 15% for maximum deformations. Viscous dampers were modeled using Link-type elements, with an exponent $\alpha = 0.5$ to reproduce the fluid's nonlinear response. The AMS, meanwhile, was modeled as a concentrated mass equivalent to 5% of the effective seismic mass, tuned to the building's fundamental frequency using linear springs.

The reliability of the ETABS v20 simulations was evaluated using two verification criteria. Cumulative modal mass participation exceeded 90% within the first three vibration modes, satisfying the requirements of Peruvian Standard E.030. In addition, nonlinear time-history analyses showed an accumulated energy error below 2% of the total internal energy, confirming numerical convergence of the solution.

Likewise, once the ETABS models had been completed, the seismic isolation and energy dissipation systems were incorporated. To this end, models of the four seismic control systems were introduced into the baseline models, and modified models were developed for each type of isolation or energy dissipation system. For the nonlinear numerical simulation of HDRB devices, mechanical models capable of adequately capturing stiffness degradation and damping properties under complex cyclic loading were employed (Wahab, 2025). The use of these advanced approaches makes it possible to accurately incorporate the deformation history of elastomeric materials, simulating reductions in base shear that achieve significant attenuation of critical interstory drifts in multistory reinforced concrete buildings (Wahab, 2025). In all cases, the geometric properties, loading conditions, and material characteristics were kept constant so that the variations observed in the structural response could be attributed exclusively to the type of seismic control technology applied.

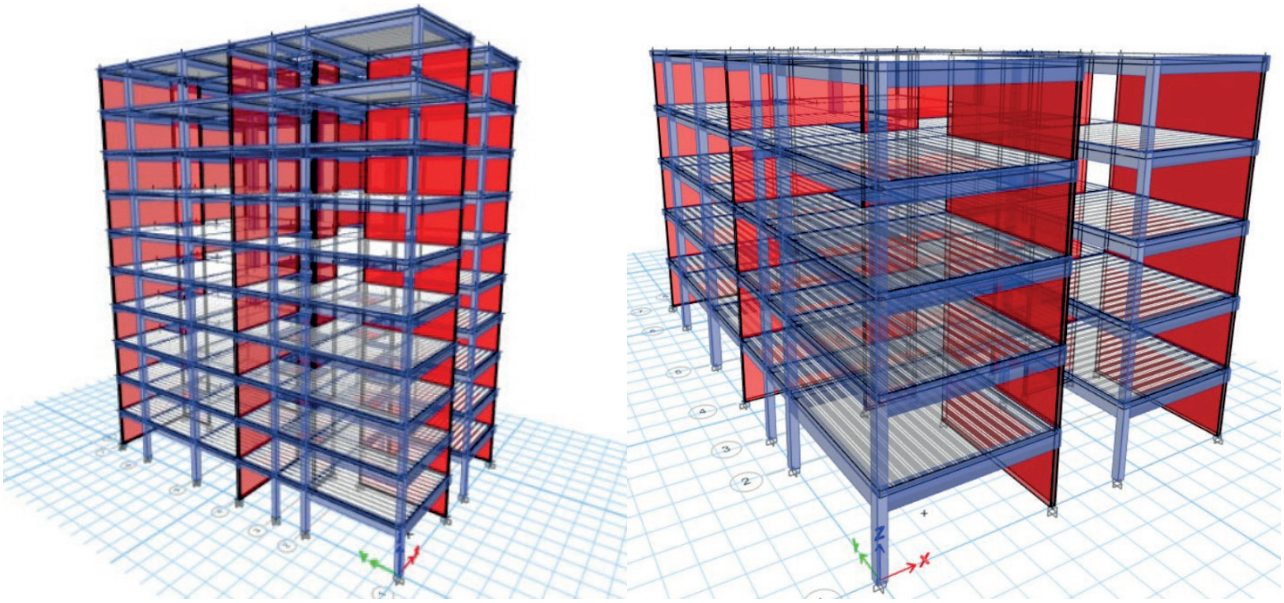


Figure 3. Baseline structural model with and without seismic control devices

Next, earthquake records were selected. Historical earthquake records from Peru (Lima 1974, Arequipa 2001, and Ica 2007) were used, scaled and adjusted in accordance with the Peruvian Seismic Design Code E.030 to ensure their representativeness.

Subsequently, nonlinear dynamic analyses and response spectrum modal analyses were performed to evaluate the structural response to the selected earthquake ground motions in detail. Afterward, the results were compared. The maximum and average values of accelerations, interstory drifts, and displacements were processed and organized, comparing the baseline models with those incorporating seismic control systems to determine the corresponding percentage reduction.

Finally, based on the results obtained from the models incorporating seismic isolation and energy dissipation systems, a cost–benefit analysis was carried out for each technology. The costs were expressed as percentage increases relative to the baseline structural cost in order to determine the most efficient and economically viable solution.

3. RESULTS

The application of nonlinear dynamic (time-history) analyses to the 12 structural models (3 baseline buildings and 3 buildings equipped with each of the 4 seismic control systems), together with the processing of the obtained results, yielded the following quantitative comparison in terms of the percentage reduction in seismic demands.

3.1. Modeling Parameters and Modal Response

The ETABS v20 models were developed by accurately defining the nonlinear parameters for each seismic control system:

Table 1 Modeling Parameters and Modal Response.

Device	Modeling Parameter in ETABS	Description	Source in the Study
Triple Pendulum Isolator (TPB)	Nonlinear friction elements with multiple contact surfaces.	Reproduce displacement-dependent behavior.	Adjusted parameters: Radius of curvature, friction coefficients (μmin, μmax).
High-Damping Isolator (HDRB)	Elastomeric bearings.	High vertical stiffness and low lateral modulus.	Adjusted properties: Shear modulus (G), vertical stiffness, and effective damping (ξ).
Viscous Dissipator (DV)	Velocity-dependent elements: $F=C\cdot v^{\alpha}$.	The force is proportional to a power of the velocity.	Constant C and exponent α (set to typical commercial values).
Tuned Mass Damper (AMS)	Secondary mass equivalent to 5% of the total mass.	Tuned to act on the first vibration mode of the base model.	Mass and stiffness adjusted to tune the period.

Table 2. AMA Results

Building	Floor	Non-Isolator (Max. A.M.A.)	TPB Isolator	HDRB Isolator	Viscous Damper (DV)	Mass Damper (AMS)
5 floors	5	0.82·g	**80%**	72%	35%	15%
	1	0.78·g	**82%**	75%	30%	12%
10 floors	10	0.75·g	**78%**	70%	40%	20%
	1	0.70·g	**80%**	72%	38%	18%

3.2. Reduction of Absolute Peak Accelerations (A.P.A.)

Base isolation systems (TPB and HDRB) proved to be the most effective at reducing accelerations, achieving an average attenuation of 75% in the superstructure of medium- and high-rise buildings.

Acceleration reduction remains robust and inversely proportional to height in base isolators. The TPB offers the most consistent protection against accelerations at all levels.

3.3. Detailed Reduction of Inter-Story Drift (Δ/h)

To evaluate inter-story distortion based on the 1974 Lima, 2001 Arequipa, and 2007 Ica seismic records scaled according to Standard E.030, the critical stories for each building type were analyzed. Previous scale inconsistencies were eliminated by standardizing the maximum values obtained

Table 3. 5- and 10-story buildings

Building	**Critical Floor**	**Base Structure (Without Device)**	**TPB Isolator**	**HDRB Isolator**	**Viscous Damper (DV)**	**Mass Damper (AMS)**
5 floors	Piso 3	0.00700	0.00035	0.00060	0.00420	0.00595
10 floors	Piso 6	0.00850	0.00045	0.00090	0.00510	0.00697
Average Reduction (%)	—	—	**> 90%**	**85% +-5%**	**40%+-5%**	**15% +-5%**

As shown in Table 3, the reinforced concrete structure without damping devices exceeds the code limit specified in Standard E.030 (Δ/h = 0.007) for the 10-story building under severe earthquakes. The implementation of base isolation technologies (TPB and HDRB) shifts the structure's fundamental period, reducing drifts by more than 85% and keeping the superstructure within a fully elastic behavior range. In contrast, viscous dampers (DV) mitigate drift by increasing the structure's damping without altering its fundamental period, achieving a moderate reduction of 40%, while the AMS demonstrates limited effectiveness (15%) due to the broadband demand of the actual Peruvian earthquakes analyzed.

3.4. Maximum Basal Displacements and Increase in Base Structural Cost

To evaluate inter-story distortion under the 1974 Lima, 2001 Arequipa, and 2007 Ica seismic records scaled according to Standard E.030, the critical stories for each building type were analyzed. Previous scale inconsistencies were eliminated by standardizing the maximum values obtained from the nonlinear simulations in ETABS.

Table 4. Results of Maximum Inter-Floor Drifts (Δ/h)

Seismic Control System	Maximum Displacement at the Base (5 Stories)	Maximum Displacement at the Base (10 Stories)	Estimated Increase in Structural Cost	Technical/Economic Feasibility
TPB Isolator	18.5 cm	24.2 cm	+ 12% a 15%	**High / Optimal:** Maximum safety and damage reduction that justifies the investment.
HDRB Isolator	22.1 cm	28.6 cm	+ 10% a 12%	**High:** Requires slightly larger seismic joints due to its lateral flexibility.
Viscous Damper (DV)	0.0 cm (Fixed)	0.0 cm (Fixed)	+ 8% a 10%	**Medium:** Does not require a base seismic joint, but the superstructure absorbs more shear.
Mass Damper (AMS)	0.0 cm (Fixed)	0.0 cm (Fixed)	+ 4% a 6%	**Low**: Lower cost, but inefficient at reducing overall vulnerability.

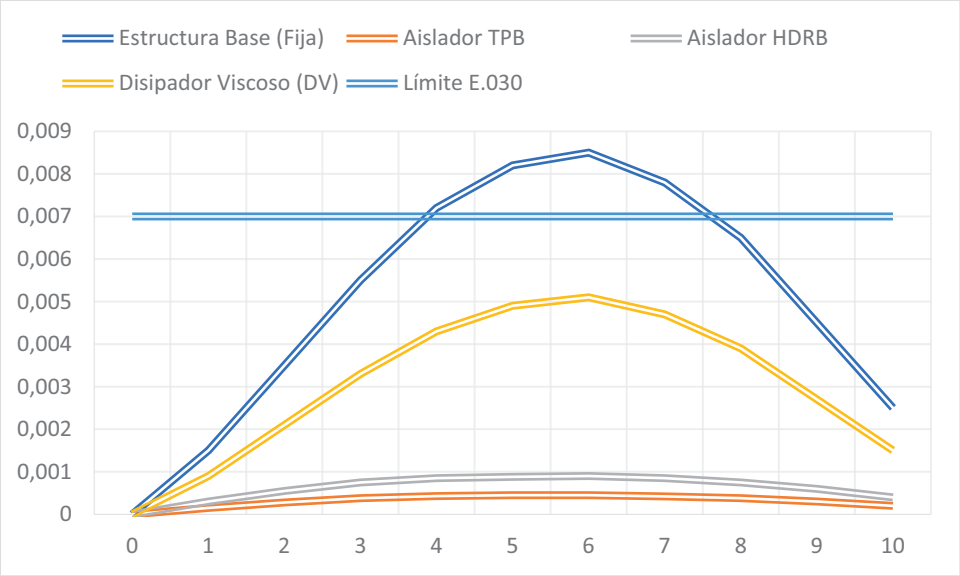


Figure 1. Distribution of Maximum Drifts

The graph shows the distribution of maximum deflections along the height of the building subjected to local seismic demand. It can be seen that the original fixed structure (Base) exceeds the permissible limit of 0.007 established by the Peruvian standard E.030. The incorporation of base isolators (TPB and HDRB) reduces deflections drastically below the regulatory threshold, keeping the superstructure within the elastic range. Meanwhile, viscous dampers (DV) achieve moderate mitigation by controlling deformations through complementary damping.

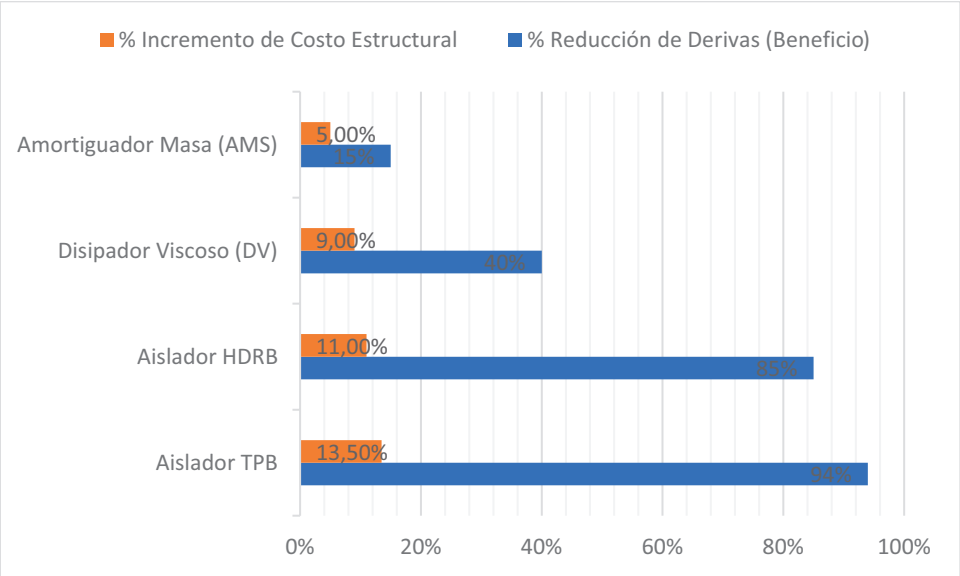


Figure 2. Structural reduction in demand

This illustration compares the percentage reduction in structural demand (deflections) with the percentage increase in cost relative to the base structural budget. Although total isolation technologies (TPB and HDRB) represent the highest initial investment (between 11% and 14%), their extremely high effectiveness mitigates the risk of collapse and reduces post-

earthquake repair costs to zero. This demonstrates that base isolators offer the most efficient and viable cost-benefit ratio for Zone 4, a high-seismicity area in Peru.

4. DISCUSSION OF RESULTS

The results obtained through nonlinear dynamic analysis made it possible to evaluate the seismic behavior of 5- and 10-story reinforced concrete buildings equipped with different seismic control technologies. The comparison shows that the efficiency of each system is directly related to its energy dissipation or isolation mechanism, generating significantly different structural responses to the Peruvian seismic records considered.

4.1. Effect of Seismic Control Systems on Structural Accelerations

Absolute peak accelerations are one of the most important indicators for evaluating the level of protection provided by a structure and its non-structural elements. The results show that base isolation systems achieve the greatest reductions in acceleration compared to the conventional model.

The Triple Pendulum (TPB) isolator achieved reductions ranging from 78% to 82%, while the HDRB isolator achieved reductions ranging from 70% to 75%. These differences are due to the fact that both systems significantly modify the structure's fundamental period, shifting it away from the regions of maximum spectral amplification of the analyzed earthquakes.

The better performance of triple-pendulum isolators (TPB) is related to the presence of multiple sliding surfaces, which help to gradually dissipate seismic energy and to redistribute inertial forces in a more effective way. In contrast, the energy dissipation of HDRBs is mainly achieved by elastomer deformation, which slightly reduces the ability of HDRBs to reduce the structural accelerations. These results are consistent with the performance observed by Karaton and Osmanlı (2021) in hospitals equipped with TPB systems and expand upon the conclusions presented by Hudson (2025). The data presented, show that, under the seismic conditions typical for Peru and generated by subduction earthquakes, the multidirectional friction system of the TPB has a better capacity to cope with the impact of higher modes on the superstructure than the isolation provided by an elastomer.

The viscous dampers reduced the acceleration by 30% to 40% due to the increase in overall damping of the system without significantly changing the natural frequency of the structure. However, the tuned mass dampers (TMDs) presented reductions of less than 22%, which denotes a poor performance against the broadband seismic motions that characterize the Peruvian coast.

4.2. Performance of Energy Dissipation Devices (DV and AMS)

Drift is one of the most representative indicators of structural and non-structural damages. Results show that the traditional 10-storey structure obtained a maximum drift of 0.00850 which exceeds the limit set out in Standard E.030 for reinforced concrete buildings. Triple-pendulum isolators (TPB) have been included and the maximum drift was found to be 0.00045, while high-damping isolators (HDRB) had a drift of 0.00090. The reduction is greater than 85%, which shows that the base isolation separates the response of the superstructure from the ground motion, greatly reducing the transmission of deformations to the upper stories.

The viscous dampers reduced drift to 0.00510, remaining within the regulatory limit, although with a considerably lower mitigation capacity. In contrast, the AMS exhibited a drift of 0.00697, a value very close to the permitted limit, indicating that its ability to control severe deformations is limited under the seismic scenarios considered. The limited capacity of the tuned mass damper (mitigation of only 15% in drifts) when subjected to real-world records such as the 2007 Ica earthquake confirms the findings of Belbachir (2024) and Jarro (2024). Because the AMS is

tuned to a narrow, single fundamental frequency of the original fixed structure, it loses almost all of its damping effectiveness in the face of broadband seismic demands and irregular accelerations from local earthquakes, which induce multimodal responses that the AMS is unable to match.

These results confirm that base isolation systems are significantly more effective at controlling structural deformation demands than supplemental damping systems.

4.3. Assessment Against the Limits of Peruvian Standard E.030

Displacements at the isolation interface are a key variable in the design of seismic joints and construction details.

The models equipped with TPB recorded maximum displacements of 18.5 cm and 24.2 cm for the 5- and 10-story buildings, respectively, while the HDRB models reached slightly higher displacements of 22.1 cm and 28.6 cm.

Although these values are higher than those observed in fixed structures, they are an expected consequence of the isolation mechanism. The increase in base displacement significantly reduces the forces transmitted to the superstructure, resulting in a substantial decrease in accelerations and drifts.

Therefore, the increase in displacement should not be interpreted as a structural disadvantage, but rather as evidence that the seismic isolation system is functioning properly.

4.4. Cost-Benefit Analysis of the Systems Reviewed

The economic evaluation shows that base isolation systems require a higher initial investment, with increases of between 10% and 15% compared to conventional structural costs.

However, when this investment is compared to the levels of reduction in accelerations, drifts, and potential damage, it becomes clear that the TPB offers the best cost-benefit ratio. Despite having the highest initial cost, it also provides the highest levels of structural and functional protection.

HDRBs are a technically viable alternative with slightly lower costs and protection levels comparable to those of the TPB. Viscous dampers can be considered an intermediate solution for projects where architectural or urban constraints prevent the installation of base isolation.

In contrast, AMS have the lowest initial cost but also the lowest capacity to reduce seismic demand; therefore, their implementation as the primary protection system is not technically recommended for buildings located in Zone 4 of Peru.

5. CONCLUSIONS

It was determined that the variables with the greatest influence on seismic response are soil type, building height, the mechanical properties of the materials, geometric characteristics, and the specific parameters of each seismic control device. The proper definition of these parameters made it possible to develop numerical models that accurately represent the behavior of buildings located in Zone 4 of Peru.

It was found that base isolation systems are significantly more effective than energy dissipation systems. The Triple Pendulum (TPB) isolator achieved the best overall performance, followed by the HDRB, while viscous dampers exhibited intermediate performance and tuned mass dampers were the least effective.

The TPB system achieved reductions ranging from 78% to 82%, establishing itself as the most efficient technology for reducing the inertial forces transmitted to the superstructure. The HDRBs achieved reductions ranging from 70% to 75%, while the viscous dampers and AMS achieved considerably lower reductions.

The TPB and HDRB systems reduced critical deflections by more than 85%, keeping the structures within elastic behavior ranges and amply meeting the requirements of Standard E.030. Although these systems generate greater displacements at the base, these displacements are the mechanism by which seismic demand on the superstructure is reduced.

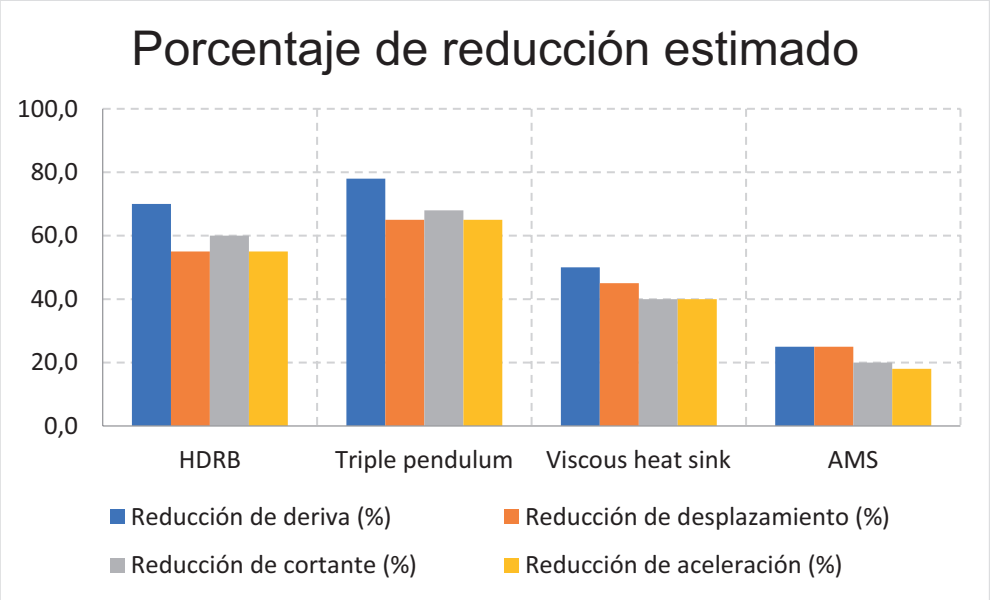


Figure 3. Summary of reductions by heat sink

It is concluded that the TPB system offers the most efficient solution for buildings located in areas of high seismic hazard in Peru. Although it requires an initial investment that is 12% to 15% higher than the conventional structural cost, it provides the greatest reduction in accelerations and displacements, minimizes the probability of structural and nonstructural damage, and promotes operational continuity following a severe seismic event.

The research shows that base seismic isolation is the most effective strategy for improving seismic performance in reinforced concrete buildings in Zone 4 of Peru, with the Triple Pendulum isolator being the option that offers the best technical and economic results among the technologies evaluated.

REFERENCES

1. **Kumar, P., Gogineni, A., Sahu, S.K**. A comprehensive review of response control systems for irregular buildings: exploring base isolators and dampers. Discov Appl Sci 7, 809 (2025). https://doi.org/10.1007/s42452-025-07469-1
2. **Chowdhury, S., Adhikari, S., & Banerjee, A.** (2025, 18 de marzo). Robust control design of nonlinear negative stiffness base isolators for MDOF systems. International Journal of Non-Linear Mechanics, 174, 105083. https://doi.org/10.1016/j.ijnonlinmec.2025.105083
3. **Shid, G., Shiravand, M. R., & Mahboubi, S.** (2025). Direction effect of vertical ground motion on seismic damages of friction-based isolated RC piers. Advances in Bridge Engineering, 6, 9. https://doi.org/10.1186/s43251-024-00154-0
4. **Patel, D., & Kumar, R.** (2025). Dynamic analysis of base-isolated and fixed-base RC frame buildings under near-field and far-field earthquakes. *Journal of Structural Engineering*, *50*(2), 87-99. https://doi.org/10.1007/s40999-024-01052-x
5. **Karaton, M., Osmanlı, Ö. F., & Gülşan, M. E.** (2021). Investigation of uncertainties in nonlinear seismic analysis of the reinforced concrete shear walls. International Journal of Civil Engineering, 19, 301–318. https://doi.org/10.1007/s40999-020-00567-8
6. **Kiral, A., & Tonyali, Z.** (2025). The effect of LRB stiffness changes with and without supplemental viscous dampers on seismic responses of an experimentally verified

MDOF building. Sigma Journal of Engineering and Natural Sciences, 43(1), 301–315. https://doi.org/10.14744/sigma.2024.00104

7. **Khosravi, S., & Amjadian, M.** (2025). Modeling, design, and laboratory testing of a passive friction seismic metamaterial base isolator (PFSMBI). Materials, 18(2), 363. https://doi.org/10.3390/ma18020363
8. **Nettis, A., Di Mucci, V. M., Ruggieri, S., & Raffaele, D**. (2025). Seismic fragilityanalysis of isolated bridges considering landslide-induced differential settlements. Procedia Structural Integrity, 62, 693–700. https://doi.org/10.1016/j.soildyn.2025.109335
9. **Shid, G., Shiravand, M. R., & Mahboubi, S.** (2025). Direction effect of vertical ground motion on seismic damages of friction-based isolated RC piers. Advances in Bridge Engineering, 6, 9. https://doi.org/10.1186/s43251-024-00154-0
10. **Belbachir, A., Belbachir, N., Bahar, S., Benbakhti, A., Louhibi, Z. S. M., & Amziane, S.** (2024). Unlocking Resilience: Examining the Influence of Fluid Viscous Dampers on Seismic Performance of Reinforced-concrete Structures in Earthquake-prone Regions. Periodica Polytechnica Civil Engineering, 68, 477-493. https://doi.org/10.3311/ppci.37748
11. **Hudson, M. B.** (2025). Seismic Performance and Resilience Comparison of Three Designs of a Hypothetical 6-Story Steel Building in Los Angeles: Special Moment Frame (SMF), Base Isolated SMF, and SMF with Viscous Dampers. *SEAOC Convention Proceedings*, 415-428. https://doi.org/10.1007/978-3-031-66888-3_45
12. **Jarro, G. A. H., Lopez, O. J. P., & Sánchez, J. D. M.** (2024). Tuned mass system to improve the seismic response of the Apenkai model annex. *AIP Conference Proceedings*, 3020(1), 020003. https://doi.org/10.1063/5.0192819
13. **Musa, M. M. E.** (2025). Seismic response comparison of an RC frame structure with fixed base and lead rubber bearing isolation. Civil and Energy Research, 1(1), 35-37. https://doi.org/10.55976/CER.12025140730-39
14. **Wahab, A. G., Tao, Z., Li, H., Rasa, A. Y., Huma, T., & Liang, Y.** (2025). Dynamic Simulation and Seismic Analysis of Hillside RC Buildings Isolated by High-Damping Rubber Bearings. Infrastructures, 10(9), 239. https://doi.org/10.3390/infrastructures10090239
15. **Zhang, S., & Lu, X.** (2024). Multi-level stiffness property and isolating-based design of high damping rubber bearings. AIP Advances, 14(11), 115222. https://doi.org/10.1063/5.0234339

СПИСОК ЛИТЕРАТУРЫ

1. **Kumar, P., Gogineni, A., Sahu, S.K**. A comprehensive review of response control systems for irregular buildings: exploring base isolators and dampers. Discov Appl Sci 7, 809 (2025). https://doi.org/10.1007/s42452-025-07469-1
2. **Chowdhury, S., Adhikari, S., & Banerjee, A.** (2025, 18 de marzo). Robust control design of nonlinear negative stiffness base isolators for MDOF systems. International Journal of Non-Linear Mechanics, 174, 105083. https://doi.org/10.1016/j.ijnonlinmec.2025.105083
3. **Shid, G., Shiravand, M. R., & Mahboubi, S.** (2025). Direction effect of vertical ground motion on seismic damages of friction-based isolated RC piers. Advances in Bridge Engineering, 6, 9. https://doi.org/10.1186/s43251-024-00154-0
4. **Patel, D., & Kumar, R.** (2025). Dynamic analysis of base-isolated and fixed-base RC frame buildings under near-field and far-field earthquakes. *Journal of Structural*

Engineering, *50*(2), 87-99. https://doi.org/10.1007/s40999-024-01052-x

5. **Karaton, M., Osmanlı, Ö. F., & Gülşan, M. E.** (2021). Investigation of uncertainties in nonlinear seismic analysis of the reinforced concrete shear walls. International Journal of Civil Engineering, 19, 301–318. https://doi.org/10.1007/s40999-020-00567-8
6. **Kiral, A., & Tonyali, Z.** (2025). The effect of LRB stiffness changes with and without supplemental viscous dampers on seismic responses of an experimentally verified MDOF building. Sigma Journal of Engineering and Natural Sciences, 43(1), 301–315. https://doi.org/10.14744/sigma.2024.00104
7. **Khosravi, S., & Amjadian, M.** (2025). Modeling, design, and laboratory testing of a passive friction seismic metamaterial base isolator (PFSMBI). Materials, 18(2), 363. https://doi.org/10.3390/ma18020363
8. **Nettis, A., Di Mucci, V. M., Ruggieri, S., & Raffaele, D**. (2025). Seismic fragilityanalysis of isolated bridges considering landslide-induced differential settlements. Procedia Structural Integrity, 62, 693–700. https://doi.org/10.1016/j.soildyn.2025.109335
9. **Shid, G., Shiravand, M. R., & Mahboubi, S.** (2025). Direction effect of vertical ground motion on seismic damages of friction-based isolated RC piers. Advances in Bridge Engineering, 6, 9. https://doi.org/10.1186/s43251-024-00154-0
10. **Belbachir, A., Belbachir, N., Bahar, S., Benbakhti, A., Louhibi, Z. S. M., & Amziane, S.** (2024). Unlocking Resilience: Examining the Influence of Fluid Viscous Dampers on Seismic Performance of Reinforced-concrete Structures in Earthquake-prone Regions. Periodica Polytechnica Civil Engineering, 68, 477-493. https://doi.org/10.3311/ppci.37748
11. **Hudson, M. B.** (2025). Seismic Performance and Resilience Comparison of Three Designs of a Hypothetical 6-Story Steel Building in Los Angeles: Special Moment Frame (SMF), Base Isolated SMF, and SMF with Viscous Dampers. *SEAOC Convention Proceedings*, 415-428. https://doi.org/10.1007/978-3-031-66888-3_45
12. **Jarro, G. A. H., Lopez, O. J. P., & Sánchez, J. D. M.** (2024). Tuned mass system to improve the seismic response of the Apenkai model annex. *AIP Conference Proceedings*, 3020(1), 020003. https://doi.org/10.1063/5.0192819
13. **Musa, M. M. E.** (2025). Seismic response comparison of an RC frame structure with fixed base and lead rubber bearing isolation. Civil and Energy Research, 1(1), 35-37. https://doi.org/10.55976/CER.12025140730-39
14. **Wahab, A. G., Tao, Z., Li, H., Rasa, A. Y., Huma, T., & Liang, Y.** (2025). Dynamic Simulation and Seismic Analysis of Hillside RC Buildings Isolated by High-Damping Rubber Bearings. Infrastructures, 10(9), 239. https://doi.org/10.3390/infrastructures10090239
15. **Zhang, S., & Lu, X.** (2024). Multi-level stiffness property and isolating-based design of high damping rubber bearings. AIP Advances, 14(11), 115222. https://doi.org/10.1063/5.0234339

Hubert S. Morales – Universidad Tecnológica del Perú (Technological University of Peru); Av. Arequipa 265, Lima, Perú. e-mail: u20208044@utp.edu.pe.

Arnold S. Grados – Universidad Tecnológica del Perú (Technological University of Peru); Av. Arequipa 265, Lima, Perú. e-mail: u20208044@utp.edu.pe.

Хуберт С. Моралес – Технологический университет Перу (Universidad Tecnológica del Perú); проспект Арекипа, 265, г. Лима, Перу. e-mail: u20208044@utp.edu.pe.

Арнольд С. Градос – Технологический университет Перу (Universidad Tecnológica del Perú); проспект Арекипа, 265, г. Лима, Перу e-mail: u20208044@utp.edu.pe.

DOI:10.22337/2587-9618-2026-22-3-113-126

MAIN PARAMETERS OF A BUTT JOINT WITH MEANDER OUTLINE FOR BOX-SECTION COLUMN IN FRAME MOMENT CONNECTION FOR SEISMIC APPLICATIONS

Yurii S. Kost [1], Andrey S. Plyaskin [2], Tatiana L. Dmitrieva [3]

[1] North-Eastern State University, Magadan, RUSSIA

[2] Tomsk State University of Architecture and Building, Tomsk, RUSSIA

[3] Irkutsk National Research Technical University, Irkutsk, RUSSIA

Abstract: The article presents the research results of the main parameters of a new technical solution aimed at increasing the reliability of an earthquake-resistant frame moment connection between a box-section column and an I-beam beam. This effect is achieved by reducing the number of welds within the connection and performing them under factory conditions. The essence of the solution lies in creating a butt joint of box-section profiles with an outline like a continuous broken line (meander outline) and clamping it from four sides with splice plates using through-bolt high-strength pretensioned bolts. This approach allows welding internal diaphragm plates inside the profile cavity under factory conditions and arranging a frame moment connection with an I-beam beam at the joint location, which can be executed as a bolted unstiffened end-plate connection (BUEEP) or a double-tee moment connection. Previously, an idealized concept of this connection within a steel moment frame was analyzed through numerical modeling under seismic impact, concluding that the performance of the butt joint is equivalent to that of a solid profile. A sensitivity analysis of the stress-strain state of the frame moment connection with a BUEEP was conducted regarding variations in the main parameters of the butt joint with the outline like a meander. These parameters include the meander height, meander fillet radius, thicknesses of flanges and diaphragm plates, as well as the number of bolts per row, their position, diameter, and pretension force value. Based on the data obtained, the parameters exerting the greatest influence on the connection performance were identified, and recommendations for its optimal design were formulated.

Keywords: butt joint, steel frame moment connection, box-section column, seismic, low temperature, weld, ANSYS

ОСНОВНЫЕ ПАРАМЕТРЫ СТЫКА С ОЧЕРТАНИЕМ МЕАНДРА КОРОБЧАТОЙ КОЛОННЫ ДЛЯ СЕЙСМОСТОЙКОГО РАМНОГО УЗЛА

Кость Ю.С. [1], Пляскин А.С. [2], Дмитриева Т.Л. [3]

[1] Северо-Восточный государственный университет, г. Магадан, РОССИЯ

[2] Томский государственный архитектурно-строительный университет, г. Томск, РОССИЯ

[3] Иркутский Национальный Исследовательский Технический Университет, г. Иркутск, РОССИЯ

Аннотация: В статье представлены результаты исследования основных параметров нового технического решения, направленного на повышение надежности рамного сейсмостойкого узла колонны коробчатого сечения с ригелем из двутавра. Эффект достигается за счёт уменьшения в узле количества сварных швов и выполнения их в заводских условиях. Суть решения заключается в создании стыка профилей коробчатого сечения с очертанием в виде непрерывной ломаной линии (очертанием меандра) и обжатии его с четырёх сторон соединительными пластинами с помощью сквозных высокопрочных болтов с предварительным натяжением. Данный подход позволяет приварить в полости профиля в заводских условиях внутренние поперечные рёбра жёсткости и устроить в месте стыка рамный узел с ригелем из двутавра, который может быть выполнен как классическим фланцевым соединением, так и соединением из двух тавров. Ранее идеализированная концепция данного узла в составе полного рамного каркаса была проанализирована численным моделированием на сейсмическое воздействие с заключением, что работа стыка эквивалентна

работе цельного профиля. Проведён анализ чувствительности напряжённо-деформированного состояния рамного узла с классическим фланцевым соединением к изменению основных параметров стыка с очертанием меандра, среди которых: высота меандра, радиус скругления меандра, толщины фланцев и поперечных рёбер жёсткости, а также количество болтов в ряду, их положение, диаметр и величина предварительного натяжения. На основе полученных данных определены параметры, оказывающие наибольшее влияние на работу узла, и сформулированы рекомендации по его оптимальному конструированию.

Ключевые слова: стыковое соединение, стальной рамный узел, коробчатое сечение, сейсмика, низкие температуры, сварной шов, ANSYS

INTRODUCTION

Ensuring structural safety in seismically active regions remains a critical challenge in the design of buildings and structures. An effective approach involves dissipating seismic energy through the plastic properties of materials and the application of seismic isolation systems and vibration dampers, including the utilization of the "soft-story" effect [1–3]. Implementing this effect enhances the dynamic performance of a building or creates a dynamic vibration absorber without requiring specialized devices; however, it necessitates the use of a steel moment frame. Steel is the most suitable material due to its high strength and capacity to sustain long-term performance under plastic deformation. For columns, square box-sections are preferred, as they provide equal strength in both orthogonal directions, exhibit a higher resistance to buckling past the elastic limit, and offer exceptional torsional stiffness [4–6]. According to the Russian Construction Code SP 14.13330.2018 (including Amendments 2–4), the use of box-section columns in steel moment frames is mandatory.

The primary structural and technological challenge lies in the high-quality installation and welding of internal diaphragm plates (diaphragms) inside the cavity of box-section profiles. Current domestic and international concepts of frame moment connections joining an I-beam beam to a box-section column can be categorized into several main types. The first type involves fabricating fully welded columns from individual plates with the preliminary installation of diaphragms [7–11]. The second type moves the diaphragms outside the internal cavity of the column [12–15]. The third type utilizes through-plates that completely interrupt the column continuity, or involves flanged joints arranged at the beam flange levels [6, 16–17]. Finally, the fourth type relies on the use of special cast components [5, 18–21]. It is worth noting that most well-known technical solutions involve a significant number of welded connections. This seriously reduces the overall reliability of frame moment connections under dynamic loads [22–27], as well as during structural operation under extremely low temperature conditions [28]. In options where the number of welds is minimized, the necessity to use complex cast elements arises. Therefore, to ensure the reliable operation of connections, it is essential to reduce the number of welds and perform them as complete-joint-penetration (CJP) welds exclusively under controlled factory conditions, which will significantly increase the operational reliability of the entire structure.

A further development of this topic is a new technical solution proposed by Yu.S. Kost in [29], the essence of which involves creating a clamped butt joint along a continuous broken line (meander outline). This line features four vertical segments at the center of each wall of the box-section profile and four horizontal segments extending from the center of one wall to the center of the adjacent wall through the corner of the profile. The butt joint is clamped from all sides by external splice plates using through-bolt high-strength pretensioned bolts. Given the geometry of the joint, under through-clamping, contact pressure develops not only between the splice plates and the profiles but also within the vertical segments of the joint, which enhances its strength and stiffness characteristics. To prevent deformation of the box-section profile walls under the pretension force of the bolts, continuous diaphragms are installed inside the profile

cavity below the horizontal segments of the joint. The geometry of the joint ensures open technological access for welding the continuous diaphragms to the walls of the box-section profile under factory conditions using CJP welds. The number of bolt rows in the joint is four per side, with two rows allocated to each diaphragm, spaced equidistantly from one another. This configuration is necessary because if only one row were allocated per diaphragm, an additional bending moment due to eccentricity would arise within it. Mutually perpendicular bolts are vertically offset from each other to apply the bolt pretension load to the diaphragm without eccentricity. The number of bolts per row is even to ensure symmetry relative to the longitudinal axis of the wall (Fig. 1).

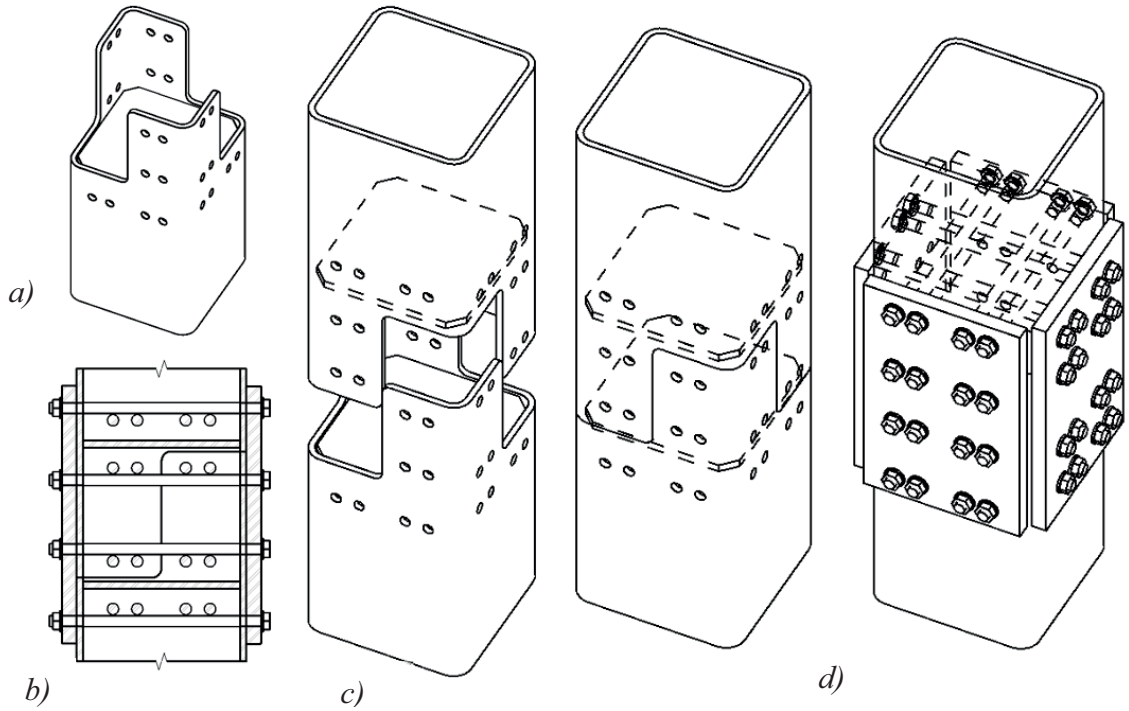


Figure 1. The concept of the butt joint: a – connected box-section profile with a meander outline cutout and installed diaphragm, b – longitudinal section of the joint, c – combining two box-section profiles, d – final assembly of the butt joint using metal plates clamped by through-bolt high-strength pretensioned bolts

Since continuous diaphragm plates are present in the butt joint, it becomes possible to arrange a rigid attachment point for an I-beam beam at the joint location. This can be executed as a bolted unstiffened end-plate connection (BUEEP), in which case the external splice plates become end plates with I-beams welded to them under factory conditions, or as a double-tee moment connection (Fig. 2).

Previously, in [29], the performance of a frame moment connection with a BUEEP and butt joint with meander outline was analyzed based on calculations under seismic impact for a pseudo-plane pinned-base moment frame and a 3-story simply supported moment frame.

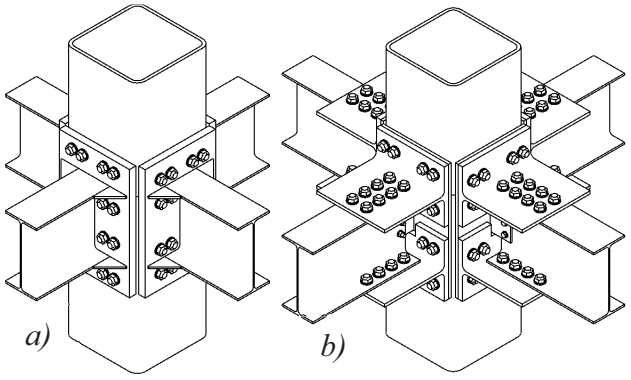


Figure 2. Frame moment connections based on the proposed butt joint: a – BUEEP, b – double-tee moment connection

According to the calculation results, it was revealed that the performance of the butt joint is equivalent to that of a solid profile. Since the concept has proven its viability, it is expedient to conduct further research, and the next stage involves determining the main parameters of a butt joint with meander outline and analyzing the sensitivity of the stress-strain state (SSS) of the connection to these parameters.

METHODS

The main parameters affecting the SSS of the butt joint include:
1) Meander height: high (M) and low (Low M) (Fig. 3);
2) Meander fillet radius (R) (Fig. 4);
3) Number of bolts per row (n), arrangement options, diameter (D), and bolt pretension (N);
4) Splice plate thickness (Fl);
5) Diaphragm thickness (Diaf).

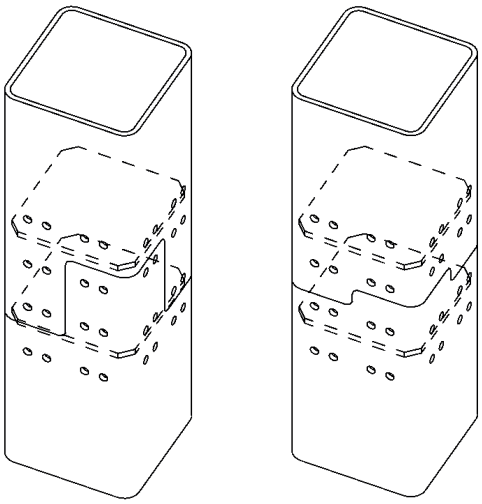


Figure 3. Meander height: a –M, b – Low M

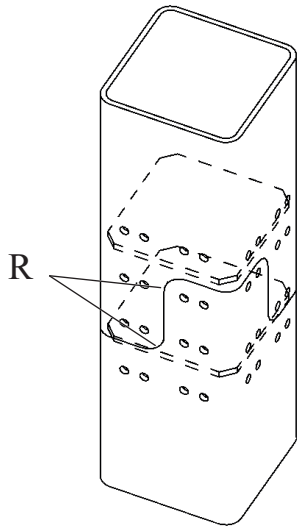


Figure 4. Meander fillet radius

The column wall thickness and the dimensions of the beam elements are not considered in this study, as the profiles of both the column and the beam are determined during the analysis of the entire frame. The column and beam profiles are adopted based on the structural design results of the steel frame under seismic loading in compliance with regulatory codes. Since this work investigates an idealized joint concept, the tolerances for gaps between the elements and bolt holes are assumed to be zero. Calculations are performed using ANSYS software, taking into account both material and geometric nonlinearities under a bending moment load that induces a plastic hinge within the beam. Structural steel (C345) is defined by a multilinear kinematic hardening model, except for the bolts, which are modeled without material nonlinearity. The friction coefficient for unilateral contacts is set to 0,2. Within each parameter combination, identical finite element (FE) mesh and time-stepping settings are applied. The numerical analysis is divided into several stages, each evaluating the influence of the parameters as a function of the bolt pretension force.

RESULTS AND DISCUSSION

The first stage involves evaluating the influence of the *meander height* and *fillet radius*. The primary column (GOST 32931-2015) and beam (GOST R 57837-2017) combination is designated as 350×13 / 30Б1. Since beam cross-sections vary along the height of the frame to ensure

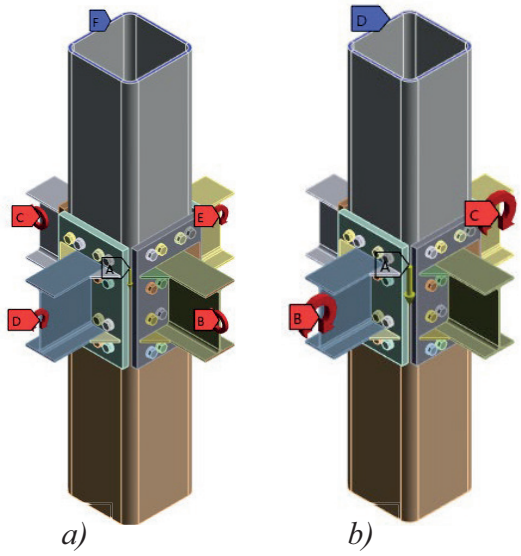
proper plastic hinge formation, the 350×13 / 25Б1 combination is also considered. Additionally, to account for a potential scenario where the column is underdesigned, the 350×13 / 35Б1 combination is analyzed, in which the plastic hinge develops later. In turn, each combination is modeled under two loading schemes (Fig. 5):

1) Diagonal loading, where a bending moment is applied to each beam, causing column bending outside its principal axes;

2) Direct loading, where a bending moment is applied to two beams located along a single straight line, causing column bending within its principal axes.

A common feature for all combinations is the beam-to-column connection via a 30-mm thick flange using eight M20 bolts per beam flange. The bolt hole diameter is equal to the bolt diameter (zero-tolerance holes), and 13-mm thick internal diaphragm plates are installed at the level of the beam flanges.

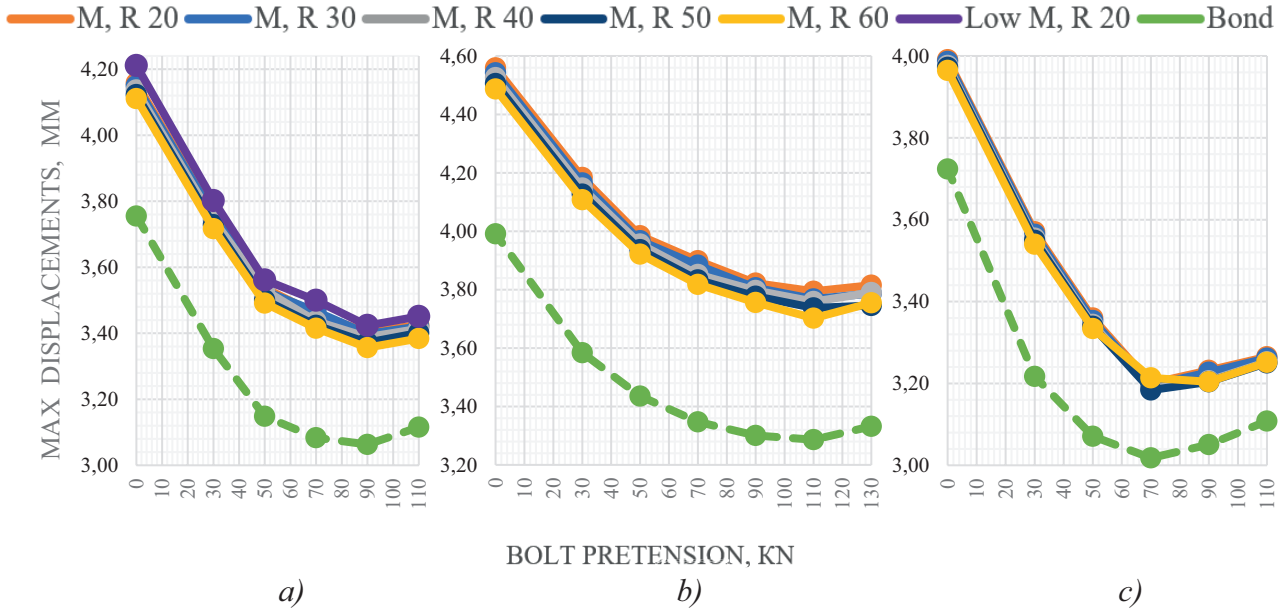
Since numerous variants of the designated parameters must be evaluated for each combination option, a single comprehensive indicator is required to describe the overall connection performance with a single value.



a) *b)*

Figure 5. Loading schemes of the first stage: a – diagonal loading, b – direct loading

In this study, maximum total displacements within the connection are the most suitable criteria (Figs. 6–7). For comparative purposes, a baseline variant featuring a solid profile instead of a butt joint was introduced.



a) *b)* *c)*

Figure 6. Maximum displacements in joints of diagonal combinations: a – 350x13/30Б1, b – 350x13/35Б1, c – 350x13/25Б1

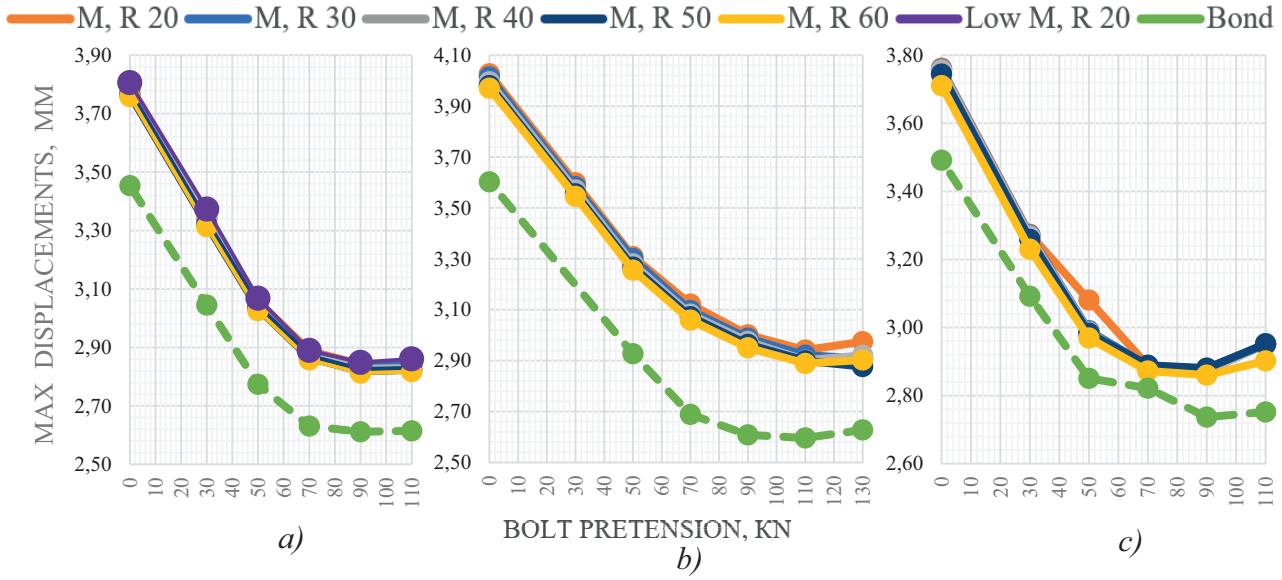


Figure 7. Maximum displacements in joints of direct combinations: a – 350x13/30Б1, b – 350x13/35Б1, c – 350x13/25Б1

Regarding bolt pretension:

1) To achieve maximum stiffness, a specific pretension force value is required; however, excessive clamping (over-clamping) results in a reduction in connection stiffness;

2) The meander height and fillet radius do not affect this required pretension value;

3) Larger beam sections and higher bending moments require a greater pretension force to achieve higher stiffness; however, this effect is not critical, as a pretension range of 50–110 kN provides a sufficient clamping effect for all analyzed cases.

Regarding meander height:

A low meander height adversely affects connection stiffness; furthermore, from a structural standpoint, fabricating such a butt joint is not feasible in all scenarios (e.g., when utilizing smaller beam cross-sections). Consequently, it is impractical to consider it in subsequent parameter combinations.

Regarding meander fillet radius:

A larger radius provides higher stiffness, though this effect is not critical, particularly for the 25Б1 beam combination. In all analyzed cases, a connection with a bolt pretension force of 50 kN or higher exhibits greater stiffness than a solid profile without clamping. The strain distribution is illustrated in Fig. 8, using the 350×13 / 35Б1-M-R60-N110 combination as an example

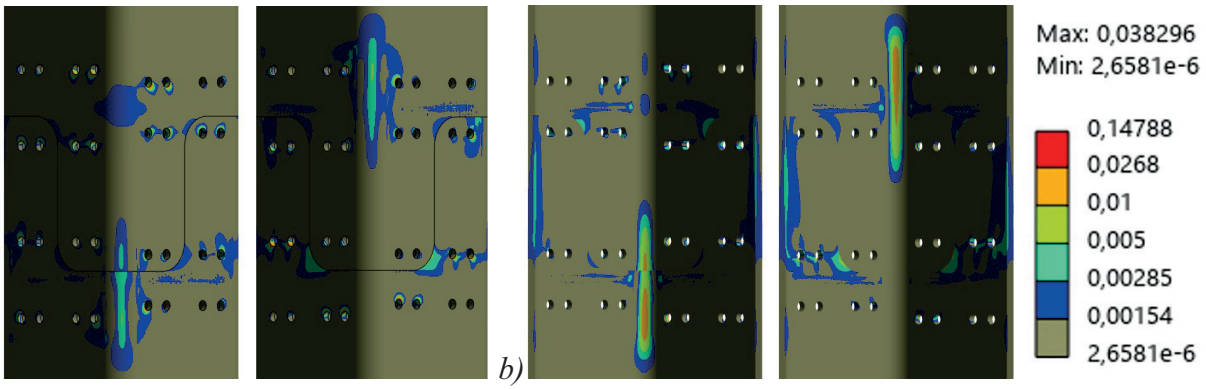


Figure 8. Equivalent total strain of diagonal combinations 350x13/35Б1-M-R60-N110: a – external surface of the profile, b – inside the profile cavity

Maximum strains in the elements reach the steel strain-hardening stage only within the zones of the bolt holes, amounting to 3.82%.

The second stage evaluates the influence of *bolt diameter, number of bolts per row*, and *arrangement options*. The analyzed combination is identical to the baseline 350×13 / 30Б1 configuration from the first stage under the diagonal loading scheme, with variations in reducing the number of bolts from eight to four per beam flange and increasing their diameter from 20 mm to 30 mm. A comparison was made with the results of the first stage. Since fewer bolts were used in the connection, more space became available for their placement. This allows for shifting them closer to the beam centerline (Option 1) or closer to the column web (Option 2) (Fig. 9).

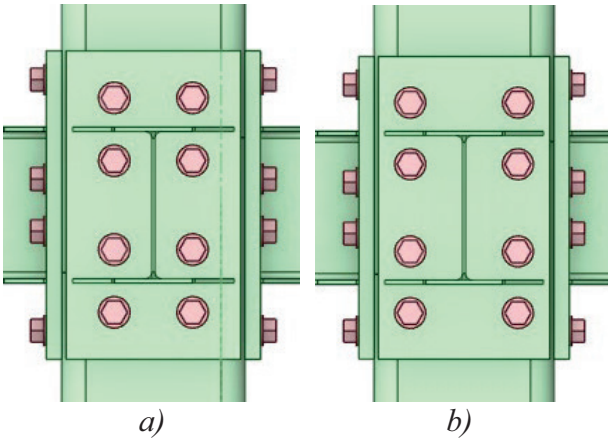


Figure 9. – Bolt arrangement options: a – option 1, b – option 2

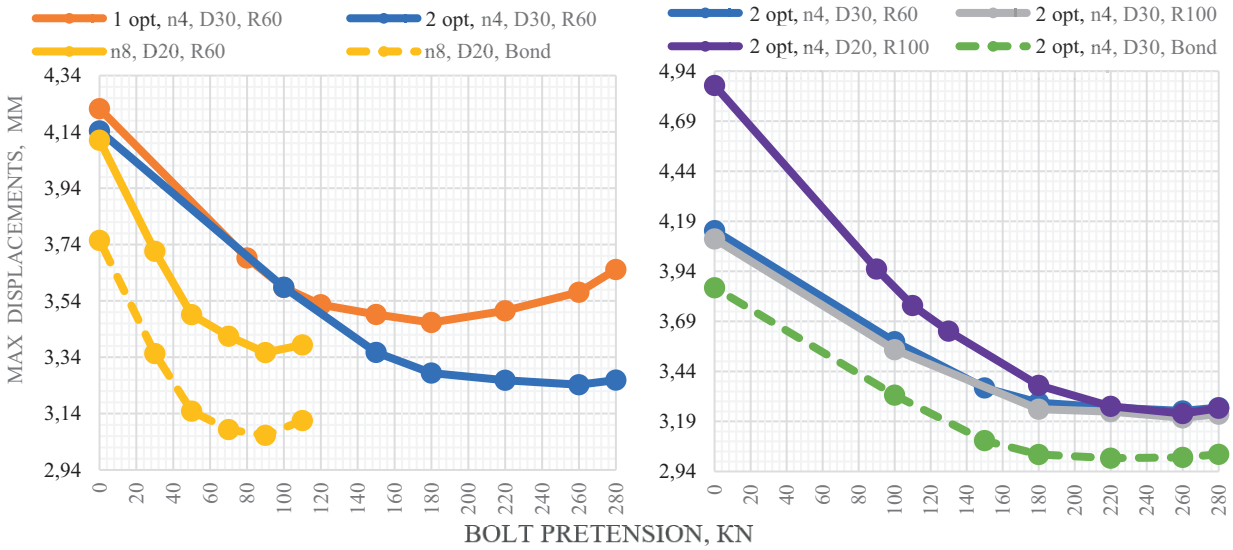


Figure 10. Maximum displacements in joints of combination 350x13/35Б1 depending on the number of bolts per row, their position and diameter

Positioning the bolts further from the profile webs reduces the pretension efficiency and fails to achieve the same stiffness level as the alternative option. Replacing eight bolts with four exhibited no adverse effects on the connection in terms of either stiffness or strength. However, it requires approximately a twofold increase in the bolt pretension force, which induces severe plastic strains exceeding 5% within the zones of the profile holes. Reducing the number of bolts and shifting them towards the profile web allows for increasing the meander fillet radius; however, this modification exhibited no effect on the stiffness and strength of the connection. The bolt diameter influences connection stiffness; however, given the required pretension force value, there is no difference between different diameters (Fig. 10).

Similar results are obtained for the 500×18.5 / 45Б1 combination, where the beam is connected to the column via a 30-mm thick flange using eight M30 bolts per beam flange and 16-mm thick diaphragm plates (Fig. 11).

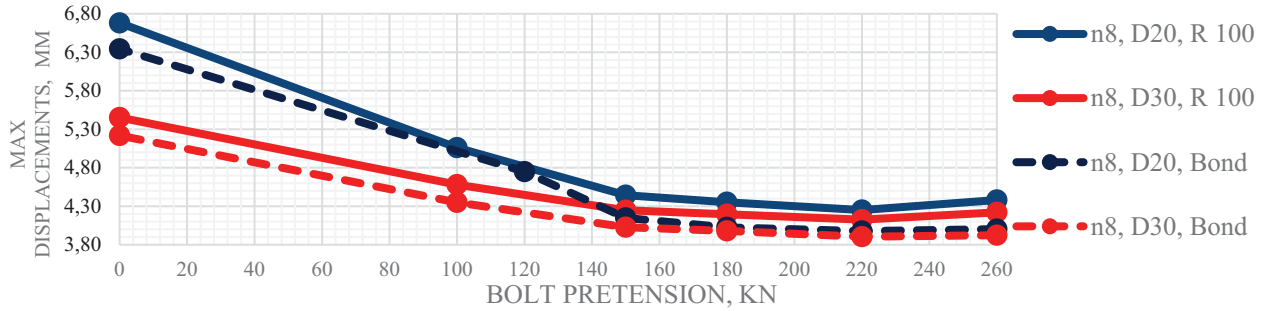


Figure 11. Maximum displacements in joints of combination 500x18,5/45Б1 depending on diameter of bolts

The third stage evaluates the influence of the *splice plate thickness* and the *diaphragm thickness*. The combinations from the previous stages are adopted: 350×13 / 30Б1 and 500×18.5 / 45Б1. The splice plate thickness is analyzed ranging from 20 to 35 mm in 5-mm increments (Fig. 12).

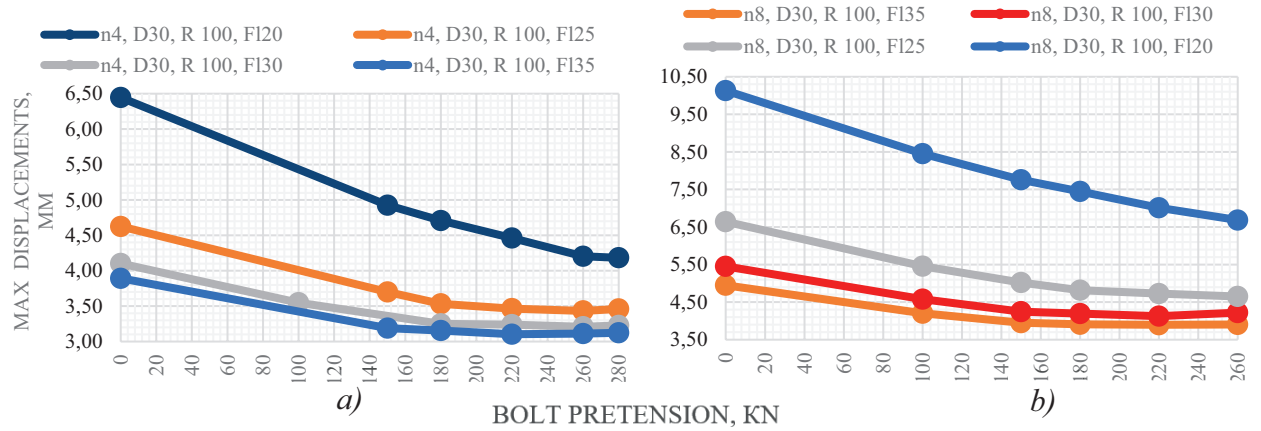


Figure 12. Maximum displacements in joints depending on splice plate thickness of combination: a – 350x13/30Б1, b – 500x18,5/45Б1

As the splice plate thickness decreases below 30 mm, an exponential increase in joint displacements is observed, along with a shift toward higher optimal pretension force for maximum stiffness and a linear increase in diaphragm strains. Depending on the diaphragm thickness, the following results are obtained (Fig. 13).

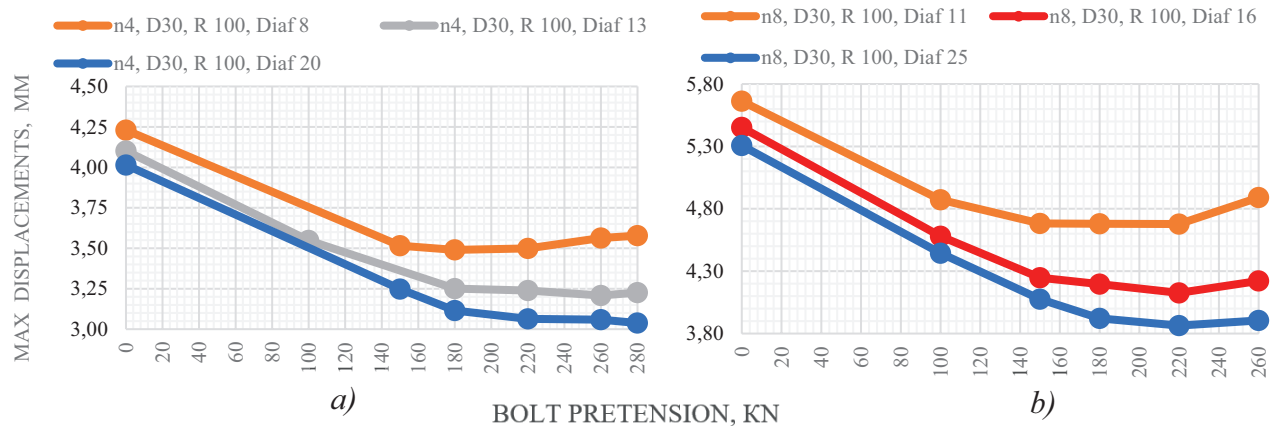


Figure 13. Maximum displacements in joints depending on diaphragm thickness of combination: a – 350x13/30Б1, b – 500x18,5/45Б1

The analysis indicates that a diaphragm thickness exceeding 1.5 times the beam flange thickness has a negligible effect on joint SSS, higher thicknesses reduce strains in the splice plates. Sensitivity analysis results, including these findings, are summarized in Table 1.

Table 1. – Summary of SSS sensitivity analysis regarding joint parameters

№	Parameters	Influence trend	Recommendation / Critical threshold
1	Meander height	Direct relationship: high height → high stiffness. Low height reduces stiffness performance.	Use the high variant; exclude the low variant from consideration
2	Meander fillet radius	Moderately positive effect on element strength and overall stiffness (minor)	Adopt the maximum possible value within structural requirements
3	Bolt pretension	Nonlinear: stiffness increases up to a certain limit, followed by a decrease due to plastic deformations	Determined by numerical simulation
4	Bolt arrangement options	Shifting towards the box-section profile webs increases bolt pretension efficiency and overall stiffness	Position as close as possible to the outer profile webs
5	Number of bolts per row and diameters	Influence is negligible, provided that the required total clamping force is ensured	Reducing the number of bolts per row is acceptable, provided that the bolt pretension force is increased
6	Splice plate thickness	High impact: exponential increase in displacements at thicknesses < 30 mm	Recommended value for the first iteration is 30 mm
7	Diaphragm thickness	Reduction in splice strains and negligible effect on overall stiffness at thicknesses > 1.5 times the I-beam flange thickness	Adopt ≈ 1.5 times the I-beam flange thickness

Thus, it was revealed that:

1) Regarding geometric parameters, it was established that the meander height is a defining factor: low height values not only reduce the overall stiffness of the connection but also create technological constraints during the installation of small-section beams. Meanwhile, the transitional fillet radius exerts a moderately positive effect on the strength of individual elements by preventing stress concentration; however, its impact on the overall stiffness of the butt joint is secondary

2) Regarding pretension force, the analysis revealed a nonlinear relationship between the bolt pretension value and connection stiffness. There is a critical clamping threshold beyond which a reduction in stiffness is observed due to the development of significant plastic strains. Furthermore, it was found that the pretension efficiency directly depends on the bolt positioning: shifting them away from the profile web reduces the overall structural stiffness. The number of bolts does not exert a significant influence on the joint SSS, provided that the pretension force in each element is proportionally increased. The optimal bolt pretension value is determined by numerical

simulation, highlighting the necessity to develop an analytical formula for its calculation
3) Regarding the influence of structural elements, it was revealed that joint exhibited the highest sensitivity to the beam splice plate thickness: at values below 30 mm, an exponential increase in joint displacements is observed, along with a shift of the optimal bolt pretension point toward higher values. Meanwhile, the profile diaphragm thickness exerts a minimal effect on the overall stiffness at thicknesses exceeding 1.5 times the I-beam flange thickness; however, it contributes to reducing splice plate strains.

CONCLUSION

The main parameters of a butt joint with meander outline were determined, and a sensitivity analysis of their impact on the joint SSS was conducted. Based on the data obtained, recommendations were provided for designing the optimal configuration of a rigid frame moment connection joining a box-section column and an I-beam beam with a minimal number of factory-executed welds. The present study is a continuation of the research on this butt joint [29] and concludes the analysis of its idealized concept. The next stage of the research will focus on adapting this idealized joint concept into an engineering model that accounts for manufacturing tolerances regarding the cutout execution and component mating. This will enable the final classification of the bolted connection based on its behavior and load transfer mechanism.

REFERENCES

1. **Belash T.A.** The use of the "flexible floor" effect in buildings of rigid structural systems. Earthquake-resistant construction. Safety of structures = Sejsmostojkoe stroitel'stvo. Bezopasnost' sooruzhenij. 2023;2:45-53. https://doi.org/10.37153/2618-9283-2023-2-45-53 – EDN EQNFVM. (In Russ)
2. **Ujwal M.S., Kumar G.S., Sathvik S., Ramaraju H.K.** Effect of soft story conditions on the seismic performance of tall concrete structures. Asian journal of civil engineering. 2024:1-9. https://doi.org/10.1007/s42107-023-00968-9.
3. **Vyscrebentseva M.A., Vu Le.Q.** Methods of seismic and seismic isolation using special devices. Ingineering journal of Don = Inzhenernyj vestnik Dona. 2019;1(52):148. – EDN NKHMJV. (In Russ)
4. **Polyakov V.S., Kilimnik L.S., Cherkashin A.V.** Modern methods of seismic protection of buildings = Sovremennye metody sejsmozashchity zdanij. M.: Stroyizdat; 1988. (In Russ)
5. **Ostrikov G.M.** Steel earthquake-resistant frames of multistorey buildings = Steel earthquake-resistant frames of multistorey buildings. Alma-Ata: Kazakhstan; 1985. (In Russ)
6. **Kuznetsov V.V.** (eds). Metal structures: in 3 t. T. 2. Steel structures of buildings and structures. The designer's handbook = Steel structures of buildings and structures. The designer's handbook. M.: ASV; 1999. (In Russ)
7. **Yoshio F., Mikio M., Shokichi G., Hideo O., Yasuhiko T., Koichi S.** et al. Japan, Patent No. JPH09328817A. 1997. Available at: https://worldwide.espacenet.com/patent/search/family/015478447/publication/JPH09328817A?q=pn%3DJPH09328817A
8. **Seizaburo A**. Japan, Patent No. JP2003227172A. Manufacturing method of box-shaped cross section steel column material with built-in diaphragm, and building iron frame column and beam joint part using the box-shaped cross section steel column material with the built-in diaphragm manufactured by the manufacturing method. 2003. Available at: https://worldwide.espacenet.com/patent/search/family/027749152/publication/JP2003227172A?q=pn%3DJP2003227172A
9. **Chuanxin Z., Hui L., Yuhui D., Yanyong S., Mojun G.** China, Patent No.

CN215106097U. Novel steel structure beam column rigid connection joint. 2021. Available at: https://worldwide.espacenet.com/patent/search/family/079307897/publication/CN215106097U?q=pn%3DCN215106097U.

10. **Shahabeddin T., Rasoul M., Farhad K.** Moment-connection between I-beam and built-up square column by a diagonal through plate. Journal of constructional steel research. 2012;70:385-401. https://doi.org/10.1016/j.jcsr.2011.10.017
11. **Peykari K., Najafgholipour M.A.** Behavior of steel beam to built-up box column moment connections with vertically stiffened panel zone. Journal of building pathology. 2023;8:6. https://doi.org/10.1007/s41024-022-00253-3
12. **Tsutomu A., Yoshihiro F., Katsuhisa N.** Japan, Patent No. JPH11117389A. Beam-column joint method of steel frame construction. 1999. Available at: https://worldwide.espacenet.com/patent/search/family/017632120/publication/JPH11117389A?q=pn%3DJPH11117389A
13. **Atsuhide Y., Tatsuo Y., Masahiko U., Ryoichi T., Isao S.** Japan, Patent No. JP2002188208A. Steel-framed beam-column connecting section structure of box-shaped section column. 2002. Available at: https://worldwide.espacenet.com/patent/search/family/018851133/publication/JP2002188208A?q=pn%3DJP2002188208A
14. **Qiang X.** China, Patent No. CN217782366U. Steel structure beam-column joint adopting integral H-shaped steel connecting piece. 2022. Available at: https://worldwide.espacenet.com/patent/search/family/083905726/publication/CN217782366U?q=pn%3DCN217782366U
15. **Gerzon M.I., Koval G.F., Kovtun-Gorbacheva T.A., Kilievich A.G.** Russia. Patent No. 1030507. Moment frame joint section. 1983. Available at: https://yandex.ru/patents/doc/SU1030507A1_19830723/ (In Russ)
16. **Haijun Z.** China, Patent No. CN217379243U. Joint for steel frame box section column bolt welding and flange connection. 2022. Available at: https://worldwide.espacenet.com/patent/search/family/083089140/publication/CN217379243U?q=CN217379243U
17. **Haoxiang Z.** China, Patent No. CN206220248U. Steel frame joint structure. 2017. Available at: https://worldwide.espacenet.com/patent/search/family/058790862/publication/CN206220248U?q=pn%3DCN206220248U
18. ANSI/AISC 358-22. Prequalified connections for special and intermediate steel moment frames for seismic applications. URL: https://www.aisc.org/publications/steel-standards/ansiaisc-358/.
19. **Akira F., Susumu N., Yasuo W.** Japan, Patent No. JP2821095B2. Column-beam connective structure and method therefor. 1999. Available at: https://worldwide.espacenet.com/patent/search/family/027284153/publication/JP2821095B2?q=pn%3DJP2821095B2
20. **Shoei I., Kazufumi H.** Japan, Patent No. JP3116023B2. Joint device for steel column and steel beam. 2000. Available at: https://worldwide.espacenet.com/patent/search/family/026496821/publication/JP3116023B2?q=pn%3DJP3116023B2
21. **Kuniaki S., Shoei I., Eiji M.** Japan, Patent No. JPH11148174A. Connecting structure of closed type sectional column and beam. 1999. Available at: https://worldwide.espacenet.com/patent/search/family/018084223/publication/JPH11148174A?q=pn%3DJPH11148174A.
22. **Miller D.K.** Lessons learned from the Northridge earthquake // Engineering structures. 1998. Vol. 20, Is. 4-6. P. 249-260.

https://doi.org/10.1016/S0141-0296(97)00031-X.
23. **Trufyakova V.I.** (eds.) The strength of welded joints under variable loads = Prochnost' svarnyh soedinenij pri peremennyh nagruzkah. Kiev: Naukova dumka; 1990. (In Russ)
24. **Tsai C.-Y., Tsai K.-C., Li C.-H., Wu C.-C., Lin K.-C., Jhuang S.-J.** Seismic fracture evaluation of diaphragm joints in welded beam-to-box column moment connections. Earthquake engineering and structural dynamics. 2020;49:1344-1362. https://doi.org/10.1002/eqe.3293.
25. **Chen C.-C., Lin C.-C., Tsai C.-L.** Evaluation of reinforced connections between steel beams and box columns. Engineering structures. 2004;26(13):1889-1904. https://doi.org/10.1016/j.engstruct.2004.06.017.
26. **Jian W., Guang T.W.** Experimental seismic behavior of RHS column-to-i beam connection with additional plates. Iranian journal of science and technology transactions of civil engineering. 2022. Vol. 46. P. 2053-2065. https://doi.org/10.1007/s40996-021-00770-0
27. **Chen C.H., Lin K.C., Jhuang S.J., Chang H.-Y.** Seismic performance evaluation of steel box-column connec-tions with ESW stiffeners. International journal of steel structures. 2020;20:766-776. https://doi.org/10.1007/s13296-020-00321-9.
28. **Trufyakova V.I.** (eds.) Fatigue of welded joints = Ustatlost' svarnyh soedinenij. Kiev: Naukova dumka; 1973. (In Russ).
29. **Kost, Yu., Dmitrieva, T.** Butt joint with meander outline for box-section column in frame moment connection for seismic. International Journal for Computational Civil and Structural Engineering, 2025, 21(2), 83-98. https://doi.org/10.22337/2587-9618-2025-21-2-83-98

СПИСОК ЛИТЕРАТУРЫ

1. **Белаш Т.А.** Использование эффекта «гибкого этажа» в зданиях жестких конструктивных систем // Сейсмостойкое строительство. Безопасность сооружений. 2023. № 2. С. 45–53. https://doi.org/10.37153/2618-9283-2023-2-45-53 – EDN EQNFVM.
2. **Ujwal M.S., Kumar G.S., Sathvik S., Ramaraju H.K.** Effect of Soft Story Conditions On the Seismic Performance of Tall Concrete Structures // Asian Journal of Civil Engineering. 2024. Vol. 25. P. 3141–3149. https://doi.org/10.1007/s42107-023-00968-9. – EDN RCNQOQ.
3. **Выскребенцева М.А., Ву Ле. К.** Методы сейсмогашения и сейсмоизоляции с применением специальных устройств // Инженерный вестник Дона. 2019. № 1 (52). С. 1–20. – EDN NKHMJV
4. **Поляков В.С., Килимник Л.Ш., Черкашин А.В.** Современные методы сейсмозащиты зданий. М.: Стройиздат, 1988. 320 с.
5. **Остриков Г.М.** Стальные сейсмостойкие каркасы многоэтажных зданий. Алма-Ата: Казахстан, 1985. 120 с.
6. Металлические конструкции: в 3 т. Т. 2. Стальные конструкции зданий и сооружений. Справочник проектировщика / под общ. ред. **В.В. Кузнецова**. М.: ACB, 1999. 512 с.
7. Pat. JPH09328817A Japan. Reinforcing construction of joint section and manufacturing of pipe-like body used therefor / **Yoshio F.** [et al.]; Ohbayashi Corp. № JP14958696A; appl. 11.06.1996; publ. 22.12.1997.
8. Pat. JP2003227172A Japan. Manufacturing method of box-shaped cross section steel column material with built-in diaphragm / **Seizaburo A.**; Nippon Steel Corp. № JP2002027726A; appl. 05.02.2002; publ. 15.08.2003.
9. Pat. CN215106097U China. Novel steel structure beam column rigid connection joint

/ **Chuanxin Z.** [et al.]; China IPPR INT Engineering CO LTD. № CN202023017425U; appl. 14.12.2020; publ. 10.12.2021.
10. **Shahabeddin T., Rasoul M., Farhad K.** Moment-connection between I-beam and built-up square column by a diagonal through plate // Journal of Constructional Steel Research. 2012. Vol. 70. P. 385–401. https://doi.org/10.1016/j.jcsr.2011.10.017
11. **Peykari K., Najafgholipour M.A.** Behavior of steel beam to built-up box column moment connections with vertically stiffened panel zone // Journal of Building Pathology. 2023. Vol. 8. P. 6. https://doi.org/10.1007/s41024-022-00253-3
12. Pat. JPH11117389A Japan. Beam-column joint method of steel frame construction / **Tsutomu A**. [et al.]; OHBAYASHI CORP. № JP28094697A; appl. 14.10.1997; publ. 27.04.1999.
13. Pat. JP2002188208A Japan. Steel-framed beam-column connecting section structure of box-shaped section column / **Atsuhide Y**. [et al.]; Tomoe Corp. № JP2000383483A; appl. 18.12.2000; publ. 05.07.2002.
14. Pat. CN217782366U China. Steel structure beam-column joint adopting integral H-shaped steel connecting piece / **Qiang X**.; Hangzhou Jiurong Arch Design Studio. № CN217782366U; appl. 15.08.2022; publ. 11.11.2022.
15. Пат. 1030507 Российская Федерация. Узел рамного каркаса / **Герзон М.И**. [и др.]; Государственный проектный институт Днепрпроектстальконструкция. № 3413935; заявл. 29.03.1982; опубл. 23.07.1983.
16. Pat. CN217379243U China. Joint for steel frame box section column bolt welding and flange connection / **Haijun Z**. № CN202221314657U; appl. 27.05.2022; publ. 06.09.2022.
17. Pat. CN206220248U China. Steel frame joint structure / **Haoxiang Z.**; Shenzhen A+E Design CO LTD. № CN201621251360U; appl. 22.11.2016; publ. 06.06.2017.
18. ANSI/AISC 358-22. Prequalified connections for special and intermediate steel moment frames for seismic applications. URL: aisc.org
19. Pat. JP2821095B2 Japan. Column-beam connective structure and method therefor / **Akira F., Susumu N., Yasuo W**.; Daiwa House Ind. № JP33619694A; appl. 22.12.1994; publ. 05.11.1999.
20. Pat. JP3116023B2 Japan. Joint device for steel column and steel beam / **Shoei I., Kazufumi H**. № JP21334197A; appl. 07.08.1997; publ. 11.12.2000.
21. Pat. JPH11148174A Japan. Connecting structure of closed type sectional column and beam / **Kuniaki S., Shoei I., Eiji M.; Arutesu KK**. № JP31708197A; appl. 18.11.1997; publ. 02.06.1999.
22. **Miller D.K.** Lessons learned from the Northridge earthquake // Engineering Structures. 1998. Vol. 20, Is. 4-6. P. 249–260. https://doi.org/10.1016/S0141-0296(97)00031-X.
23. Прочность сварных соединений при переменных нагрузках / под ред. **В.И. Труфякова**. Киев: Наукова думка, 1990. 256 с.
24. **Tsai C.-Y., Tsai K.-C., Li C.-H., Wu C.-C., Lin K.-C., Jhuang S.-J.** Seismic fracture evaluation of diaphragm joints in welded beam-to-box column moment connections // Earthquake engineering and structural dynamics. 2020;49:1344-1362. https://doi.org/10.1002/eqe.3293.
25. **Chen C.-C., Lin C.-C., Tsai C.-L.** Evaluation of reinforced connections between steel beams and box columns // Engineering structures. 2004;26(13):1889-1904. https://doi.org/10.1016/j.engstruct.2004.06.017.
26. **Jian W., Guang T.W.** Experimental seismic behavior of RHS column-to-i beam connection with additional plates // Iranian Journal of Science and Technology Transactions of Civil Engineering. 2022. Vol. 46. P. 2053–2065. https://doi.org/10.1007/s40996-021-00770-0

27. **Chen C.H., Lin K.C., Jhuang S.J., Chang H.-Y.** Seismic performance evaluation of steel box-column connections with ESW stiffeners // International journal of steel structures. 2020;20:766-776. https://doi.org/10.1007/s13296-020-00321-9.
28. Усталость сварных соединений / под ред. **В.И. Труфякова.** Киев: Наукова думка, 1973. 216 с.
29. **Kost, Yu., Dmitrieva, T.** Butt joint with meander outline for box-section column in frame moment connection for seismic // International Journal for Computational Civil and Structural Engineering. 2025, 21(2), 83-98. https://doi.org/10.22337/2587-9618-2025-21-2-83-98 – EDN AMBWUD.

Kost Yurii Sergeevich, Graduate student, Department of Energy Transport and Construction, North-Eastern State University, 13 Portovaya St., Magadan, 685000, Russia, e-mail: kost.svgu@mail.ru

Plyaskin Andrey Sergeevich, PhD in Technical Sciences, Associate Professor, Department of Metal and Wooden Structures, Tomsk State University of Architecture and Building, 2 Solyanaya Sq., Tomsk, 634003, Russia, e-mail: plyaskinandrei@mail.ru

Dmitrieva Tatiana Lvovna, Doctor Science of Engineering, Professor, Department of Mechanics and Strength of Materials, Irkutsk National Research Technical University, Lermontov street, 83, Irkutsk, 664074, Russia, e-mail: dmitrievat@list.ru

Кость Юрий Сергеевич, аспирант, кафедра энергетики транспорта и строительства , ФГБОУ ВО Северо-Восточный государственный университет; 685000, Россия, Магаданская область, г. Магадан, ул. Портовая, д. 13; e-mail: kost.svgu@mail.ru

Пляскин Андрей Сергеевич, кандидат технических наук, доцент, кафедра металлических и деревянных конструкций, ФГБОУ ВО Томский государственный архитектурно-строительный университет; 634003, Россия, Томская область, г. Томск, пл. Соляная, д. 2; e-mail: plyaskinandrei@mail.ru

Дмитриева Татьяна Львовна, доктор технических наук, профессор, кафедра механики и сопротивления материалов, Иркутский Национальный Исследовательский Технический Университет; 664074, Россия, г. Иркутск, ул. Лермонтова, 83; e-mail: dmitrievat@list.ru

International Journal for Computational Civil and Structural Engineering, 22(3) 127–134 (2026)

DOI:10.22337/2587-9618-2026-22-3-127-134

DEVELOPING THE METHOD FOR CREATING THE MAP OF APPLICATION ZONES OF THE BUILDING ENVELOPE BASED ON CALCULATIONS OF PROTECTION AGAINST WATERLOGGING

Kirill P. Zubarev, Yulia A. Sapronova, Vladimir D. Fedoseev

National Research Moscow State University of Civil Engineering, Moscow, RUSSIA

Abstract: The main provisions underlying the creation of a method for the balance of moisture transfer have been given. Based on the balance of moisture transfer, a criterion for waterlogging of the building envelope was derived. The waterlogging criterion was calculated for 81 localities. The results obtained were plotted on a map of Russia, as a result of which three zones of application of the building envelope determining where the structure is permitted to be built were designed. Algorithms for constructing and applying a map of application zones of building enclosing structures have been presented. The effectiveness of the proposed approach is demonstrated for determining the balance of moisture transfer in three cities: Murmansk, Vorkuta and Tomsk. It is noted that the developed method is recommended for implementation in engineering work.

Keywords: humidity regime, moisture transfer equation, resistance to vapor permeation, temperature,map of humidity zones

РАЗРАБОТКА МЕТОДА СОЗДАНИЯ КАРТЫ ЗОН ПРИМЕНЕНИЯ ОГРАЖДАЮЩЕЙ КОНСТРУКЦИИ ЗДАНИЯ НА ОСНОВЕ РАСЧЕТОВ ЗАЩИТЫ ОТ ПЕРЕУВЛАЖНЕНИЯ

К.П. Зубарев, Ю.А. Сапронова, В.Д. Федосеев

[1]Национальный исследовательский Московский государственный строительный университет, г. Москва, РОССИЯ

Аннотация: Приведены основные положения, лежащие в основе создания метода по балансу влагопереноса. На основе баланса влагопереноса был выведен критерий переувлажнения ограждающей конструкции. Был произведен расчет критерия переувлажнения для 81 населенного пункта. Полученные результаты были нанесены на карту России, в результате чего были построены три зоны применения ограждающей конструкции, определяющие где конструкцию можно строить. Приведены алгоритмы построения и применения карты зон применения ограждающих конструкции здания. Эффективность предлагаемого подхода продемонстрирована для определения баланса влагопереноса в трех городах: Мурманск, Воркута и Томск. Отмечено, что разработанный метод рекомендован для внедрения в инженерную работу.

Ключевые слова: влажностный режим, уравнение влагопереноса, сопротивление паропроницанию, температура, карта зон влажности

1. INTRODUCTION

The design of buildings and structures is a complex technological process during which various engineering problems are solved. The main factors influencing the design are the choice of the optimal architectural and planning solution, the use of new and modern technologies, the calculation of various structures by temperature and pressure distribution, etc [1–5].

For the first time, the method of calculating protection against waterlogging was introduced

in 1963 in the Russian regulatory document SNiP II-A.7-62* “Construction Heat Engineering. Design standards". The calculation method was based on the differential equation of moisture transfer proposed by K.F. Fokin [6]:

$$\gamma_0 \cdot \frac{\xi_0(w)}{E_t(t)} \cdot \frac{\partial e(w,t)}{\partial \tau} = \frac{\partial}{\partial x}(\mu \frac{\partial e(w,t)}{\partial x}). \qquad (1)$$

where e, E_t – water vapor partial pressure and saturated water vapor pressure, *Pa*; μ – vapor permeability, *kg/(m·s·Pa)*; ξ_0 – relative vapor capacity, kg/kg; γ_0 – density, kg/m^3; τ – time, *s*; *x* – coordinate, *m*.

Equation (1) was solved in stationary and nonstationary formulations. As a result, formulas for the required vapor permeability resistance have been derived.

$$\begin{cases} R_{n1}^{req} = \frac{(e_{in} - E) \cdot R_{n.o}}{E - e_O} \\ R_{n2}^{req} = \frac{z_0 (e_{in} - E_0)}{\rho_w \cdot \delta_w \cdot \Delta w + \eta} \end{cases} \qquad (2)$$

Then the moisture transfer balance inequality which encompasses the comparison of vapor permeation resistances is used:

$$R_n \geq \mathrm{R}_n^{req} \qquad (3)$$

$$\mathrm{R}_n^{req} = \max[R_{n1}^{req}; R_{n2}^{req}] \qquad (4)$$

where R_n – vapor resistance, $m^2 \cdot s \cdot Pa/kg$; R_{n1}^{req}, R_{n1}^{req}, R_{n2}^{req} – required vapor permeation resistances, $m^2 \cdot s \cdot Pa/kg$.

If inequality (3) is met, then, according to the calculation method, the structure is protected from waterlogging and is allowed to be built. Otherwise, the enclosing structure does not pass the waterlogging test [7–9].

The method of K.F. Fokin entered the modern regulatory framework with the modification of V.G. Gagarin and V.V. Kozlova. The balance of moisture transfer according to equation (3) is reduced relative to the plane of maximum moisture. This method has been introduced into the Russian regulatory document SP 50.13330.2024 "Thermal protection of buildings”.

Despite the effectiveness of the described method, its calculations are quite complex for engineering use. In this regard, development of the new methods of protection against waterlogging, which would let the balance of moisture transfer be assessed in a simplified manner, remains pertinent. In this article, a calculation method that provides the possibility to assess construction of a building envelope using a map of humidity zones has been developed.

2. THE PROBLEM

To develop a method for calculating protection against waterlogging of the external fences of a building using a map of application zones of enclosing structures.

3. MATERIALS AND METHODS

3.1. Derivation of a criterion for waterlogging of the enclosing structure

The analysis of a large number of calculation results for facade solutions of building walls showed that there are two most common options for the location of the plane of maximum moisture: the plane of maximum moisture is either in the insulation layer or at the boundary of the layers [7–9].

The most popular options of locating the plane of maximum moisture in the walls of buildings are presented. The location of the plane in the insulation layer (Figure 1A) and at the boundary between the insulation and the external plaster (Figure 1B) have been demonstrated.

Supposing plane of the greatest moisture is located inside the layer, then the required vapor permeation resistance is found according to formula 2 of the system of equations (2).

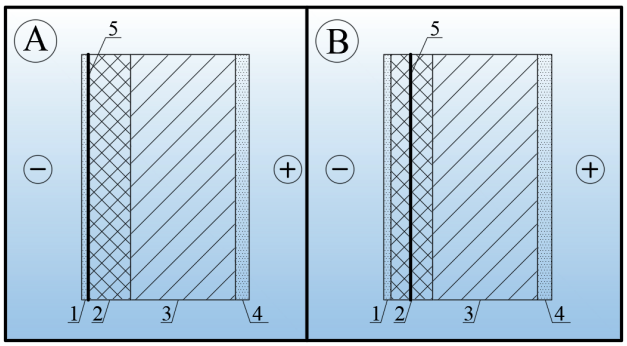


Figure 1. The most common options of the location of the plane of maximum moisture in the walls of buildings (A – position of the plane at the junction of insulation layers and external plaster; B – position of the plane inside the insulation layer; 1 – outer plaster layer; 2 – insulation layer; 3 – base of aerated concrete blocks; 4 – layer of internal plaster; 5 – plane of the greatest moisture)

If the plane of maximum moisture is located at the junction of the layers, the required vapor permeation resistance is determined by the formula:

$$R_{n2}^{req} = \frac{z_0(e_{in} - E_0)}{0.5 \cdot (\rho_{w1} \cdot \delta_{w1} \cdot \Delta w_1 + \rho_{w2} \cdot \delta_{w2} \cdot \Delta w_2) + \eta} \quad (5)$$

In order for the structure to be built, the inequality must be satisfied (3).

Let us divide both sides of equation (3) by R_n:

$$\frac{R_n^{req}}{R_n} \le 1 \quad (6)$$

Let us introduce a new criterion l – the criterion for waterlogging of the enclosing structure:

$$l = \frac{R_n^{req}}{R_n}. \quad (7)$$

We substitute the right side of equation (7) into the left side of inequality (6):

$$l \le 1 \quad (8)$$

Inequality (8) enables us to draw a conclusion about the possibility of building an enclosing structure.

The physical meaning of the waterlogging criterion l is that it indicates whether the structure is waterlogged or not.

The decision about the possibility of construction can be made in accordance with the values of the following system:

$$\begin{cases} l \le 1 - \text{ the structure can be built} \\ l > 1 - \text{ the structure cannot be built} \end{cases} \quad (9)$$

It was found that if the waterlogging criterion l is less than 1, the structure is protected from waterlogging, so it may be built. If the waterlogging criterion l is more than 1, the structure does not pass the waterlogging test, thus, it may not be built.

3.2. Calculation of moisture transfer criteria in different humidity zones in different cities

Let us look at the wall structure (Figure 1).

The physical characteristics of the studied enclosing structure are presented (Table 1).

To analyze the scope of application of the facade solution under consideration (Figure 1), 81 cities located in three different humidity zones have been considered. The cities and their corresponding humidity zones adopted for the study are presented (Table 2).

The waterlogging criterion of the enclosing structure was determined for each locality using formula (7), and the obtained values were plotted on a map of moisture zones. A map of moisture zones is presented with plotted values of the waterlogging criterion (Figure 2).

Table 1. Physical characteristics of the studied enclosing structure

Physical parameter	Value	
1. Layer of external plaster		
Layer thickness, m	0.006	
Density, kg / m^3	1260	
Thermal conductivity, $W / m\ ^\circ C$	А	0.76
	Б	0.93
Vapor permeability, $kg / m \cdot s \cdot Pa$	$3.6 \cdot 10^{-11}$	
2. Insulation made of mineral wool slabs		
Layer thickness, m	0.1	
Density, kg / m^3	150	
Thermal conductivity, $W / m\ ^\circ C$	А	0.04
	Б	0.042
Vapor permeability, $kg / m \cdot s \cdot Pa$	$8.3 \cdot 10^{-11}$	
3. Masonry base made of aerated concrete blocks		
Layer thickness, m	0.3	
Density, kg / m^3	400	
Thermal conductivity, $W / m\ ^\circ C$	А	0.113
	Б	0.117
Vapor permeability, $kg / m \cdot s \cdot Pa$	$6.9 \cdot 10^{-11}$	
4. Layer of internal plaster		
Layer thickness, m	0.011	
Density, kg / m^3	1800	
Thermal conductivity, $W / m\ ^\circ C$	А	0.76
	Б	0.93
Vapor permeability, $kg / m \cdot s \cdot Pa$	$2.5 \cdot 10^{-11}$	

Table 2. Cities and their corresponding humidity zones adopted for the study

Zones according to the "humidity zone map" in accordance with the regulatory document		
Wet	Normal	Dry
Murmansk	Kaliningrad	Belgorod
Saint Petersburg	Smolensk	Rostov-on-Don
Arkhangelsk	Moscow	Astrakhan
Naryan-Mar	Nizhny Novgorod	Volgograd
Petropavlovsk-Kamchatsky	Permian	Penza
Ayan	Vorkuta	Izhevsk
Poronaysk	Surgut	Ekaterinburg
Yuzhno-Sakhalinsk	Dudinka	Orenburg
Yuzhno-Kurilsk	Tomsk	Kurgan
Vladivostok	Tynda	Omsk
	Khabarovsk	Novosibirsk
	Magadan	Kyzyl
	Anadyr	Krasnoyarsk
	Blagoveshchensk	Irkutsk
	Erofey Pavlovich	Yeniseisk
	Okhotsk	Chita
	Keys	Mogocha
	Maykop	Kirensk
	Cherkessk	Bodaibo
	Nalchik	Tura
	Kursk	Lensk
	Vologda	Khatanga
	Cheboksary	Yakutsk
	Tobolsk	Verkhoyansk
	Kazan	Zyryanka
	Syktyvkar	Oymyakon
	Petrozavodsk	Srednekolymsk
	Troitsko-Pechorskoe	Saskylakh
	Urengoy	Olenek
	Dixon	Zhigalovo
	Nikolaevsk-on-Amur	Kosh-Agach
	Igarka	Rubtsovsk
	Aldan	Barnaul
	Totma	Samara
	Ukhta	Chelyabinsk
		Abakan

3.3.Plotting the values of the waterlogging criterion on a map of Russia

Three application zones for the considered building envelope were obtained. The first zone (marked green on the map) is the zone where the balance of moisture transfer (3) is carried out, here $R_{n2}^{req} > R_{n1}^{req}$. The second zone is a zone where the moisture transfer balance (3) is not met, which means that the enclosing structure does not pass the waterlogging test. The third zone is the zone where the moisture transfer balance inequality (3) is satisfied, here $R_{n2}^{req} < R_{n1}^{req}$.

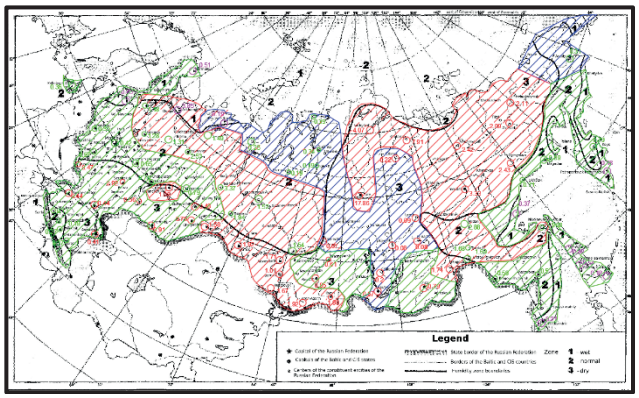


Figure 2. Map of moisture zones with plotted values of the waterlogging criterion (green and blue zones show areas in which the structure has been protected from waterlogging; red zone displays areas where the structure cannot be built)

3.4.Algorithm for applying the proposed approach

To create a map of the application zones of the building envelope based on calculations for protection against waterlogging, the following actions have been taken:

1.The required design has been selected;

2. The criterion for waterlogging of the enclosing structure has been calculated using formula (7);

3. The values of this criterion have been plotted on the map of Russian humidity zones for the cities in accordance with Table 2.

4. 3 zones have been defined on the map: the first green zone and the third blue zone are those where you can construct a building envelope and the second red zone is the zone where the structure under study cannot be built, since it does not pass the waterlogging test.

A number of maps of application zones for various building envelopes are constructed.

To calculate protection against waterlogging using a map of application zones of building envelopes, the following measures have been taken:

1. A map corresponding to the calculated enclosing structure has been selected;

2. The city in which the calculation is performed has been chosen;

3. If the structure falls into the green or blue zone, it means that it has passed the waterlogging test and is allowed to be built. If the structure falls into the red zone, the wall under study does not pass the waterlogging test, therefore, it cannot be built.

4. If the structure falls into the red zone (it has not passed the test for protection against waterlogging), it is necessary to replace the structure with another one or install a vapor barrier on the inner surface of the structure and re-calculate the protection against waterlogging.

4. RESULTS AND DISCUSSION

Options for constructing a building wall with parameters in accordance with Table 1 for three cities, such as Murmansk, Tomsk and Vorkuta were calculated.

4.1.Assessment of the moisture transfer balance using the classical method of calculating the moisture transfer balance

In Murmansk, building envelopes are operated under conditions **A**, whereas in Tomsk and Vorkuta operating conditions are **B**.

It was found that for all three cities, the position of the plane of maximum moisture corresponds to Figure 1A – the junction of external plaster and insulation.

Resistance to vapor permeation from the inner surface to the plane of maximum moisture, as well as the required resistance to vapor permeation for Murmansk is:

$$\begin{cases} R_n = 5.958 \cdot 10^9 \ m^2 \cdot s \cdot Pa / kg \\ \mathrm{R}_{n1}^{req} = 0.608 \cdot 10^9 \ m^2 \cdot s \cdot Pa / kg \\ \mathrm{R}_{n2}^{req} = 3.024 \cdot 10^9 \ m^2 \cdot s \cdot Pa / kg \\ 5.958 \cdot 10^9 \geq \max[0.608 \cdot 10^9; 3.024 \cdot 10^9] \end{cases} \quad (10)$$

Let us determine the values of the waterlogging criterion using the formula (7):

$$l = \frac{3.024 \cdot 10^9}{5.958 \cdot 10^9} = 0.507 \leq 1 \quad (11)$$

Since the waterlogging criterion is less than one, the building envelope in Murmansk has passed the waterlogging rest successfully.

Similar to that, let us determine the same for Vorkuta:

$$\begin{cases} R_n = 5.958 \cdot 10^9 \ m^2 \cdot s \cdot Pa / kg \\ \mathrm{R}_{n1}^{req} = 1.469 \cdot 10^9 \ m^2 \cdot s \cdot Pa / kg \\ \mathrm{R}_{n2}^{req} = -18.612 \cdot 10^9 \ m^2 \cdot s \cdot Pa / kg \\ 5.958 \cdot 10^9 \geq \max[1.469 \cdot 10^9; -18.612 \cdot 10^9] \end{cases} \quad (12)$$

$$l = \frac{1.469 \cdot 10^9}{5.958 \cdot 10^9} = 0.247 \leq 1 \quad (13)$$

Since the waterlogging criterion is less than one, the building envelope in Vorkuta has also passed the waterlogging test successfully.

The difference between the designs for these two cities is that in Murmansk the determining condition for the balance of moisture transfer is the required resistance to vapor permeation R_{n2}^{req}, whereas in Vorkuta the required resistance to vapor permeation is R_{n1}^{req}.

While performing the calculation for Tomsk, we get the following:

$$\begin{cases} R_n = 5.958 \cdot 10^9 \ m^2 \cdot s \cdot Pa / kg \\ \mathrm{R}_{n1}^{req} = 0.328 \cdot 10^9 \ m^2 \cdot s \cdot Pa / kg \\ \mathrm{R}_{n2}^{req} = 9.144 \cdot 10^9 \ m^2 \cdot s \cdot Pa / kg \\ 5.958 \cdot 10^9 \geq \max[0.328 \cdot 10^9; 9.144 \cdot 10^9] \end{cases} \quad (12)$$

$$l = \frac{9.144 \cdot 10^9}{5.958 \cdot 10^9} = 1.535 \geq 1 \quad (13)$$

It was found that the criterion *l is* greater than one, therefore, the wall in Tomsk will be waterlogged, since the balance of moisture transfer is not satisfied.

4.2. Assessment of moisture transfer balance using the proposed approach

We select three cities under study on the map with areas of application of enclosing structures. Three cities under study on the map of areas of application of enclosing structures are presented (Figure 3).

Figure 3 illustrates that Murmansk is located in the green zone (which means that it is possible to build here and $\mathrm{R}_{n2}^{req} > \mathrm{R}_{n1}^{req}$), Vorkuta is located in the blue zone (also allowed to build here and $\mathrm{R}_{n1}^{req} > \mathrm{R}_{n2}^{req}$), whereas Tomsk is in the red zone (no construction allowed).

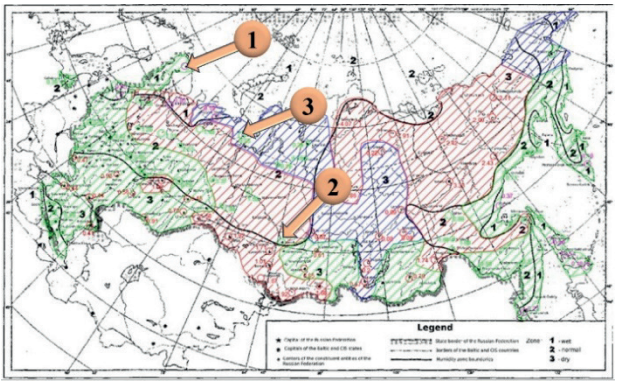


Figure 3. Three cities under study on the map of areas of application of enclosing structures (1 – Murmansk; 2 – Vorkuta; 3 – Tomsk)

A comparison of the classical and proposed approaches demonstrates the superiority of using a map with application zones of the building envelopes. The main advantage of the proposed method is that there is no need to make calculations. This method, in comparison with various methods for assessing the balance of moisture transfer, can be applied by manufacturers of building materials for enclosing structures. The manufacturer can develop a series

of maps of application zones for enclosing structures proposed in this study for their products and implement them into the engineering work of design organizations. This approach will reduce the time spent on designing buildings and structures, eliminate errors in calculations, and make decision support for a particular design more intuitive.
Future work involves a detailed study of three different zones obtained (Figure 1).

5. CONCLUSIONS

In the current study, a new effective method for determining the balance of moisture transfer using a map of application zones of the enclosing structure based on a newly introduced value, namely, the criterion of waterlogging of the enclosing structure, has been developed. The values of the waterlogging criterion have been plotted on the map, then three zones have been identified depending on the value of the criterion and the determining resistance to vapor permeation. An algorithm for constructing and using a map of the applicability of a building envelope is presented. This method can be used by engineers when calculating and assessing the building envelope protection against waterlogging.

6. FUNDING

The research was funded by a grant from the Russian Science Foundation, project number 25-79-00205, https://rscf.ru/en/project/25-79-00205/.

REFERENCES

1. **Akimov P.A., Mozgaleva M.L., Kaytukov T.B.** Numerical Solution of the Problem of Isotropic Plate Analysis with the Use of B-Spline Discrete-Continual Finite Element Method. // International Journal for Computational Civil and Structural Engineering, 2020, Vol. 16, No. 4, pp. 14-28.
2. **Sidorov V.N. Matskevich S.M.** Discrete-analytical solution of the unsteady-state heat conduction transfer problem based on the finite element method. // IDT 2016 - Proceedings of the International Conference on Information and Digital Technologies 2016, 2016, pp. 241-244.
3. **Kotlyarova E.** Improving the methodology for assessing the level of environmental safety of urban areas as the basis of their life cycle // E3S Web of Conferences, 2023, Vol. 389, No. 09062.
4. **Musorina T., Olshevskyi V., Ostrovaia A., Statsenko E.** Experimental assessment of moisture transfer in the vertical ventilated channel // MATEC Web of Conferences, 2016, No. 02002.
5. **Gumerova E., Gamayunova O., Meshcheryakova T.** Energy efficiency upgrading of enclosing structures of mass housing of the Soviet Union // Advances in Intelligent Systems and Computing, 2017, Vol. 692, pp. 432-439.
6. **Arfvidsson, J., Claesson J.** Isothermal moisture flow in building materials: modelling, measurements and calculations based on Kirchhoff's potential. // Building and environment. Vol. 35, Iss. 6, 2000, pp. 519-536.
7. **Gagarin V.G., Akhmetov V.K., Zubarev K.P.** Unsteady-state moisture behavior calculation for multilayer enclosing structure made of capillary-porous materials // IOP Conference Series: Earth and Environmental Science, 2019, Vol. 177(1), pp. 925-932.
8. **Gagarin V.G., Kozlov V.V., Zubarev K.P.** Determination of maximum moisture zone on enclosing structures. // Cold Climate HVAC 2018: Sustainable Buildings in Cold Climates, 2019, pp. 925-932.
9. **Zubarev K.P.** Using discrete-continuous approach for the solution of unsteady-state moisture transfer equation for multilayer building walls. // International Journal for Computational Civil and Structural Engineering, 2021, Vol. 17, No. 2, pp. 50-57.

СПИСОК ЛИТЕРАТУРЫ

1. **Akimov P.A., Mozgaleva M.L., Kaytukov T.B.** Numerical Solution of the Problem of Isotropic Plate Analysis with the Use of B-Spline Discrete-Continual Finite Element Method. // International Journal for Computational Civil and Structural Engineering, 2020, Vol. 16, No. 4, pp. 14-28.
2. **Sidorov V.N. Matskevich S.M.** Discrete-analytical solution of the unsteady-state heat conduction transfer problem based on the finite element method. // IDT 2016 - Proceedings of the International Conference on Information and Digital Technologies 2016, 2016, pp. 241-244.
3. **Kotlyarova E.** Improving the methodology for assessing the level of environmental safety of urban areas as the basis of their life cycle // E3S Web of Conferences, 2023, Vol. 389, No. 09062.
4. **Musorina T., Olshevskyi V., Ostrovaia A., Statsenko E.** Experimental assessment of moisture transfer in the vertical ventilated channel // MATEC Web of Conferences, 2016, No. 02002.
5. **Gumerova E., Gamayunova O., Meshcheryakova T.** Energy efficiency upgrading of enclosing structures of mass housing of the Soviet Union // Advances in Intelligent Systems and Computing, 2017, Vol. 692, pp. 432-439.
6. **Arfvidsson, J., Claesson J.** Isothermal moisture flow in building materials: modelling, measurements and calculations based on Kirchhoff's potential. // Building and environment. Vol. 35, Iss. 6, 2000, pp. 519-536.
7. **Gagarin V.G., Akhmetov V.K., Zubarev K.P.** Unsteady-state moisture behavior calculation for multilayer enclosing structure made of capillary-porous materials // IOP Conference Series: Earth and Environmental Science, 2019, Vol. 177(1), pp. 925-932.
8. **Gagarin V.G., Kozlov V.V., Zubarev K.P.** Determination of maximum moisture zone on enclosing structures. // Cold Climate HVAC 2018: Sustainable Buildings in Cold Climates, 2019, pp. 925-932.
9. **Zubarev K.P.** Using discrete-continuous approach for the solution of unsteady-state moisture transfer equation for multilayer building walls. // International Journal for Computational Civil and Structural Engineering, 2021, Vol. 17, No. 2, pp. 50-57.

Zubarev Kirill Pavlovich, Ph.D. (Candidate of Engineering Sciences), Associate Professor, Associate Professor of the Department of Computer Science and Applied Mathematics of the Moscow State University of Civil Engineering, 129337, Moscow, Yaroslavskoe shosse, 26; e-mail.: zubarevkirill93@mail.ru

Sapronova Yulia Aleksandrovna, laboratory research assistant of the A.B. Zolotov Research and Education Center of Computer Modelling of the National Research Moscow State University of Civil Engineering; 129337, Moscow, Yaroslavskoe shosse, 26; e-mail: ho5metown@gmail.com

Fedoseev Vladimir Dmitrievich, laboratory research assistant of the A.B. Zolotov Research and Education Center of Computer Modelling of the National Research Moscow State University of Civil Engineering; 129337, Moscow, Yaroslavskoe shosse, 26; e-mail: fedosseev.vs@gmail.com

Зубарев Кирилл Павлович, кандидат технических наук, доцент, доцент кафедры информатики и прикладной математики Национального исследовательского Московского государственного строительного университета 129337, г. Москва, Ярославское шоссе, 26; e-mail.: zubarevkirill93@mail.ru

Сапронова Юлия Александровна, лаборант-исследователь научно-образовательного центра компьютерного моделирования уникальных зданий, сооружений и комплексов им. А. Б. Золотова» (НОЦ КМ) Национального исследовательского Московского государственного строительного университета; 129337, г. Москва, Ярославское шоссе, 26; e-mail: ho5metown@gmail.com

Федосеев Владимир Дмитриевич, лаборант-исследователь научно-образовательного центра компьютерного моделирования уникальных зданий, сооружений и комплексов им. А. Б. Золотова» (НОЦ КМ) Национального исследовательского Московского государственного строительного университета; 129337, г. Москва, Ярославское шоссе, 26; e-mail: fedosseev.vs@gmail.com

International Journal for Computational Civil and Structural Engineering, 22(3) 135–143 (2026)

DOI:10.22337/2587-9618-2026-22-3-135-143

NUMERICAL MODELING TECHNIQUE FOR THE HYDRODYNAMIC STABILITY OF SWIRLING FLOWS

Vadim K. Akhmetov

National Research Moscow State University of Civil Engineering, Moscow, RUSSIA

Abstract. A numerical technique is proposed for investigating the hydrodynamic stability of axisymmetric swirling flows of an incompressible viscous fluid within the linear stability theory framework. The associated eigenvalue problem is governed by a system of sixth-order ordinary differential equations. Asymptotic expansions are constructed at both artificial and irregular singular points to facilitate the solution. The system is integrated numerically using a high-order accurate scheme, and the Gram–Schmidt orthonormalization procedure is employed to suppress the rapid growth of particular solutions, thereby ensuring their linear independence. A computational package based on the developed methodology has been implemented and applied to the stability analysis of the Batchelor vortex. Validation tests are conducted to compare the obtained results against available reference data. The existence of a viscous instability mode is established, for which the maximum growth rate is found to decrease monotonically with increasing Reynolds number.

Keywords: hydrodynamic stability, small-disturbance method, swirling flow, viscous mode, growth rate coefficients

МЕТОДИКА ЧИСЛЕННОГО МОДЕЛИРОВАНИЯ ГИДРОДИНАМИЧЕСКОЙ УСТОЙЧИВОСТИ ЗАКРУЧЕННЫХ ТЕЧЕНИЙ

В.К. Ахметов

Национальный исследовательский Московский государственный строительный университет, Москва, РОССИЯ

Аннотация. Представлена методика численного исследования задачи гидродинамической устойчивости осесимметричных закрученных течений вязкой несжимаемой жидкости в рамках линейной теории. Рассматриваемая спектральная задача описывается системой обыкновенных дифференциальных уравнений шестого порядка. Для ее решения в регулярной и иррегулярной особых точках строятся асимптотические разложения. Численное интегрирование системы проводится методом повышенной точности с использованием процедуры ортогонализации Грамма-Шмидта для подавления быстрого роста одного или нескольких решений с целью обеспечения их линейной независимости. Разработанный пакет программ по описанной методике реализован для исследования устойчивости вихря Бэтчелора. Проведены тестовые вычисления для сравнения результатов с имеющимися данными. Показано существование вязкой моды неустойчивости, для которой максимальный коэффициент усиления монотонно убывает с ростом числа Рейнольдса.

Ключевые слова: гидродинамическая устойчивость, метод малых возмущений, закрученный поток, вязкая мода, коэффициенты усиления

1. INTRODUCTION

Swirling flows of liquid and gas are frequently encountered in nature (tornadoes, cyclones, whirlpools) and are widely used in various technical applications. Contemporary areas of application for swirling flows include the following [1,2]: the creation of efficient pulverized coal combustion facilities for modern thermal power plants; optimization of gas turbine engine performance through the use of flow swirl in combustion chambers; the development and design of cyclone-type devices for gas dust removal, particle separation, and liquid mixture separation, for example, for treating produced oil, as well as vortex atomizers for liquid spraying;

and the use of the Ranque–Hilsch effect in vortex tubes for thermal flow separation.

In hydraulic engineering and special construction applications, swirling flows are employed in the design of draft tubes for hydraulic turbines, vortex spillways, antivortex energy dissipators, and antivortex aerators for ecological treatment of natural and artificial water bodies, settling ponds, and storage basins in biological and chemical industries [3].

Investigations into the hydrodynamic stability of swirling flows are extremely relevant. Loss of flow stability often leads to disruption of the designed operating regime, intensification of vibration effects, and damage (or destruction) of the structure.

There are several general stability criteria for swirling flows. For free-vortex type flows, they are formulated in [4, 5]. These criteria are predominantly sufficient in nature and do not allow obtaining precise stability characteristics of the flow.

The primary tool for investigating the hydrodynamic stability of vortex flows is numerical modeling using the perturbation method. For free swirling flows and internal channel flows (excluding the near-wall region), the profiles of the axial U and azimuthal W velocity components can be reasonably well described by expressions

$$U(r) = W_1 + W_2 \exp(-br^2),$$
$$W(r) = \frac{K}{r}[1 - W_2 \exp(-br^2)], \quad (1)$$

where W_1, W_2, K, b are empirically determined constants, and r is the dimensionless distance from the axis. By elementary transformations, profiles (1) can be reduced to the form

$$U = \exp(-r^2), \quad W = \frac{q}{r}(1 - \exp(-r^2)), \quad (2)$$

where q is the flow swirl parameter. Therefore, in recent years, considerable attention has been devoted to the stability investigation of the flow with velocity distribution (2), often referred to as the Q – vortex (or Batchelor vortex).

The inviscid stability of flow (2) with respect to non-axisymmetric perturbations of the form $\exp[i(\alpha z + n\varphi - \alpha ct)]$ was first numerically investigated in [6]. Primary attention was given to perturbations with $n \le -1$, since they proved more unstable than perturbations with positive n. The presented numerical results showed that instability of flow (2) is observed for $q < 1.5$.

The effect of viscosity on the stability of a free vortex was first numerically studied in [7]. The lowest critical Reynolds number corresponded to perturbations with $n = -1$. Two viscous instability modes of the Q-vortex at $n = 0$ and $n = 1$ were found in [8, 9]. In contrast to previously studied inviscid modes, their maximum amplification factor monotonically decreases with increasing Reynolds number $\mathrm{Re} \to \infty$.

The transition from absolute to convective instability in an inviscid formulation for the Batchelor vortex Q was investigated in [10]. In jet flows, absolute instability was observed for modes $n = -1, -2, -3$. For wake-type flows, absolute instability was found only for mode $n = -1$. Generalizations of these studies accounting for flow compressibility were carried out in [11, 12].

Similar investigations in an inviscid formulation for the Rankine vortex are presented in [13], and for shear swirling flows in [14].

Selective calculations of absolute instability for Q vortex accounting for viscosity, performed using direct numerical simulation, were conducted in [15], while systematic and detailed investigations over a wide range of Reynolds numbers are presented in [16].

Experimental results on the stability of swirling flows and the structure of the near-axis recirculation zone during vortex breakdown are presented in [17–19].

Issues of global instability following vortex breakdown are considered in [20]. The relationship between the vortex breakdown phenomenon and swirling flow stability is shown in [21].

With regard to problems of thermal flow separation in Ranque–Hilsch tubes, flow stability was studied in [22], and for stratified media in [23].

The conducted analysis of the scientific literature indicates a strong interest in the stability investigation of swirling flows. The Batchelor vortex has a velocity distribution to which a significant portion of such flows can be reduced. In this connection, the problem of Batchelor vortex stability is an important and pressing issue.

2. PROBLEM STATEMENT AND RESEARCH METHOD

Consider homogeneous axisymmetric flow of a viscous incompressible fluid with a velocity field in an unbounded medium

$$V_z = U(r), \quad V_r = 0, \quad V_\varphi = W(r), \tag{3}$$

where V_z, V_r, V_φ are the axial, radial, and azimuthal velocity components in a cylindrical coordinate system.

Consider small perturbations of the base flow (3) with velocity profiles (2) as solutions of the linearized Navier–Stokes equations in the form of travelling waves (normal modes):

$$\begin{aligned}\{V_z', V_r', V_\varphi', p'\} = \\ = \{F, iS, H, P\}\exp[i(\alpha z + n\varphi - \alpha ct)],\end{aligned} \tag{4}$$

where p is the pressure; α is the wavenumber; n is the perturbation mode $(n = 0; \pm 1; \pm 2; ...)$, with negative values corresponding to wave propagation in the direction opposite to the swirl; c is the wave speed; i is the imaginary unit. For the complex amplitude functions $F(r)$, $S(r)$, $H(r)$, $P(r)$ we obtain the system of equations:

$$\begin{aligned}r^2\gamma F + \alpha r^2 P + r^2 SU' = \\ = \frac{1}{i\,\mathrm{Re}}\left[r(rF')' - (\alpha^2 r^2 + n^2)F\right], \\ r^2\gamma S + 2rHW - r^2 P' = \\ = \frac{1}{i\,\mathrm{Re}}\left[r(rG')' - (\alpha^2 r^2 + n^2 + 1)S - 2nH\right], \\ r^2\gamma H + r^2 S\left(W' + \frac{W}{r}\right) + rnP = \\ = \frac{1}{i\,\mathrm{Re}}\left[r(rH')' - (\alpha^2 r^2 + n^2 + 1)H - 2nS\right], \\ \alpha rF + (rS)' + nH = 0,\end{aligned} \tag{5}$$

where $\gamma = \alpha(U - c) + nW/r$, and the prime denotes differentiation with respect to r. The boundary conditions for system (5) at $r = 0$ are derived from the requirements of regular behavior of the solution near the axis and decay of perturbations at infinity, and have the form:

$$\begin{aligned}S(0) = H(0) = 0, \\ F(0), P(0) \ \ are \ \ limited \ \ for \ \ n = 0; \\ S(0) \pm H(0) = 0, \\ F(0) = P(0) = 0 \ for \ n = \pm 1; \\ S(0) = H(0) = F(0) = P(0) = 0 \ \ for \ \ |n| > 1; \\ S(\infty) = H(\infty) = F(\infty) = P(\infty) = 0.\end{aligned} \tag{6}$$

Consider perturbations (4) that are periodic in z, whose amplitude changes with time. Then α is a real number ($\alpha = 2\pi/\lambda$, where λ is the perturbation wavelength), and $c = c_r + ic_i$ is complex one; c_r represents the speed of perturbation propagation in the direction z (phase velocity), c_i is the temporal growth rate of the perturbation, $\omega_i = \alpha c_i$ is the perturbation amplification factor, and $\omega_r = \alpha c_r$ is the oscillation frequency. If $c_i < 0$, the perturbation amplitudes (4) decay (the flow is stable). And if $c_i > 0$, they grow with time (the flow is unstable). Thus, here it is necessary to determine c_i as a function of α.

In another case, one studies perturbations (4) that are periodic in time with amplitude varying

in the direction z, but independent of time. Then the frequency $\omega = \alpha_r c$ should be considered real (c is the phase velocity), and $\alpha = \alpha_r + i\alpha_i$ is a complex one; α_i determines the spatial growth rate of the perturbation. If $\alpha_i > 0$ the perturbation decays (the flow is stable), and if $\alpha_i < 0$, it grows (the flow is unstable). In this case, it is important to determine the dependence of α_i on ω.

The eigenvalue computation method comprises several stages. Near the singular points $r = 0$ and $r = \infty$, asymptotic solutions are constructed using the Frobenius method [24], which allow the boundary conditions to be transferred to the points $r = r_a$ and $r = r_d$, respectively. Then numerical integration is performed from r_a and r_d into the computational domain towards the point r_c $(r_a < r_c < r_d)$, where the solutions are matched according to the condition

$$\sum_{j=1}^{3} a_j y_{i,j} = \sum_{j=1}^{3} a_{j+3} y_{i,j+3} \quad (i = 1, 2, \ldots, 6), \quad (7)$$

where $y_{i,j}$ are the solutions obtained by integration from r_d to r_c, and $y_{i,j+3}$ are those obtained by integration from r_a to r_c, a_j – произвольные постоянные. The vanishing of the determinant of the linear homogeneous system (7) is achieved by adjusting c_r, c_i (or α_r, α_i) using Newton's method.

In the calculations, $r_a = 0.01$, $r_c = 0.5$ were taken, and the value of r_d was chosen individually for each set of parameters based on the required accuracy of the eigenvalue determination, and varied from $r_d = 2.7$ to $r_d = 150$. The widest integration domain was required for long-wave perturbations, at large Reynolds numbers and swirl parameters. When computing the dependencies of the eigenvalues on the governing parameters, the step in the parameter was determined automatically by the number of iterations k_{it} in Newton's method for solving the characteristic equation. The value of k_{it} was maintained in the interval $3 \le k_{it} \le 7$. If $k_{it} > 7$ or $k_{it} < 3$ for three successively found eigenvalues, the parameter step was correspondingly halved or doubled. To accelerate convergence, the next initial guess for the eigenvalue in Newton's method was determined by linear extrapolation.

It is convenient to represent system (5) for numerical integration as six first-order differential equations $z' = f(r, z)$. To find the solution, we employ the Kutta–Merson method with automatic step-size selection. Denote

$$f_{n+\beta}^{[k]} = f(r_n + \beta h, z_{n+\beta}^{[k]}),$$

where h is the integration step, $z_{n+\beta}^{[k]}$ is the approximate solution found at the point $r_n + \beta h$ with local error h^k. Then the set of calculation formulas can be written as:

$$z_{n+1/3}^{[2]} = z_n^{[5]} + \frac{h}{3} f_n^{[5]},$$

$$z_{n+1/3}^{[3]} = z_n^{[5]} + \frac{h}{6}(f_n^{[5]} + f_{n+1/3}^{[5]}),$$

$$z_{n+1/2}^{[4]} = z_n^{[5]} + \frac{h}{8}(f_n^{[5]} + 3 f_{n+1/3}^{[3]}),$$

$$z_{n+1}^{[4]} = z_n^{[5]} + \frac{h}{2}(f_n^{[5]} - 3 f_{n+1/3}^{[3]} + 4 f_{n+1/2}^{[4]}),$$

$$z_{n+1}^{[5]} = z_n^{[5]} + \frac{h}{6}(f_n^{[5]} + 4 f_{n+1/2}^{[4]} + f_{n+1}^{[4]}).$$

Thus, approximate values $z(r_{n+1})$ are calculated with local errors h^4 and h^5. Comparison of the values $z_{n+1}^{[4]}$ and $z_{n+1}^{[5]}$ provides a practical means to assess the accuracy of the approximate solution $z(r_{n+1})$ during the computation. The integration step h for each computational point is determined from the condition

$$\left| (z_n^{[5]} - z_n^{[4]}) / z_n^{[4]} \right| \le \varepsilon,$$

in which it was assumed that $\varepsilon = 10^{-2}$.

A fundamental difficulty in implementing this method when solving hydrodynamic stability problems is the rapid (parasitic) growth of one or several solutions during integration, as a result of which their linear independence is lost. One of the most effective methods for overcoming these difficulties is the orthogonalization procedure of S.K. Godunov [25].

Such an orthogonalization procedure for the vectors can be performed either at each integration step, or after a certain number of steps when a predefined non-orthogonality criterion is violated. Such a criterion, for example, can be the condition $\max(y^j, y^j)^{1/2} > M$, where the constant M is usually of the order of $10^2 - 10^3$. In the present calculations, orthogonalization was carried out at every computational point.

To compute the complex determinant of system (7), the Gauss elimination method with column pivoting was used. The solution of an equation of the form $F(c) = 0$ was determined by Newton's method.

3. RESULTS AND DISCUSSION

Nontrivial solutions of the homogeneous boundary-value problem (5), (6) with distribution (2) determine the spectrum of complex eigenvalues and eigenfunctions for a given set of parameters Re, q, α, n. The first two parameters characterize the flow, and the latter two describe the perturbation wave.

The results of test calculations of the eigenvalues of the original problem for the viscous mode found in [8] and studied in detail in [9] are presented in Table 1. It can be seen that in all cases there is good agreement. This indicates that the numerical method employed allows obtaining a solution with high accuracy. At the same time, it is simpler in numerical implementation than the spectral collocation method with Chebyshev expansions [8].

In [8], two viscous instability modes with positive azimuthal wavenumbers were identified numerically, for which the maximum amplification factor monotonically decreases as $\mathrm{Re} \to \infty$. One of them corresponds to axisymmetric perturbations $n = 0$, and the other to non-axisymmetric ones with $n = 1$. In both cases, the instability turns out to be weaker compared to the inviscid mode at $n = -1$, and the corresponding critical Reynolds numbers calculated in [9] are higher: $\mathrm{Re}_c = 17.275$; 322.42 for the modes $n = 0; 1$, respectively. These two modes are of significant importance because they confirm the destabilizing effect of viscosity on flow stability.

The present numerical investigations have established that for there also exists an unstable mode of viscous nature (mode 2).

Provide analysis its properties in detail. The critical Reynolds number for it is $\mathrm{Re}_c = 43.934$ at $\alpha_c = 0.5012$, $q_c = 0.6603$. In this sense, it occupies an intermediate position between the viscous modes $n = 0$ and $n = 1$.

Fig. 1 shows the relations $\omega_i = \omega_i(\alpha)$, $\omega_r = \omega_r(\alpha)$ for mode 2 by solid and dashed lines, respectively, calculated at $\mathrm{Re} = 100$, $q = 0.3,\ 0.4,\ 0.5,\ 0.6$ (curves 1–4). It is seen that the amplification factor $\omega_i = \omega_i(\alpha)$ has a peak-shaped distribution. The same character was noted for similar dependencies in [8] when studying viscous modes with $n = 0$ and $n = 1$. The phase velocities of perturbations with wavenumbers corresponding to the maximum amplification factor are negative, i.e., unstable perturbations in this case propagate upstream.

Confirmation that the found mode is viscous in nature is provided by the dependence of the amplification factor on the swirl $\omega_i = \omega_i(q)$ at fixed wavenumber $\alpha = 0.3$ and various $\mathrm{Re} = 300,\ 1000,\ 5000,\ 10000$ (Fig. 2, curves 1–4). It is evident that as the Reynolds number increases, the maximum amplification factor monotonically decreases.

Table 1

Re	α	*q*	$\omega_r \cdot 10^2$	$\omega_i \cdot 10^3$	$\omega_r \cdot 10^2$ [9]	$\omega_i \cdot 10^3$ [9]
25	0.05	0.5	–0.22387	0.98872	–0.22387	0.98851
25	0.05	0.5	0.00374	0.26682	0.00370	0.26618
100	0.3	0.4	1.72806	8.99650	1.72799	8.99607
1000	0.3	0.4	2.34621	0.97904	2.34621	0,97904

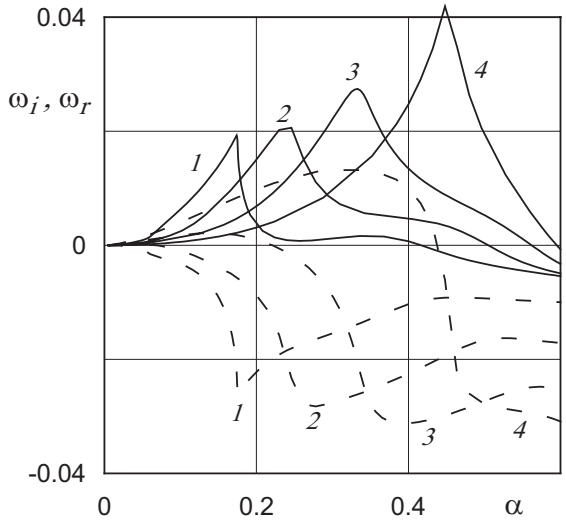


Figure 1. Relation of the amplification factor on the twist angle at Re=100, q=0.3, 0.4, 0.5, 0.6 (curves 1-4)

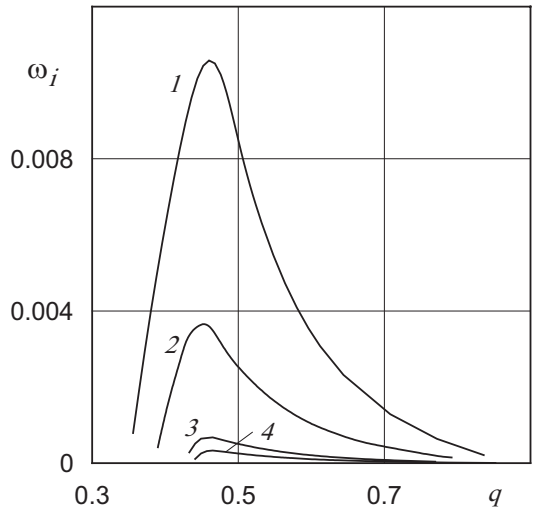


Figure 2. Relation of the amplification factor on the twist angle at α=0.3, Re=300, 1000, 5000, 10000 (curves 1-4)

4. CONCLUSION

An efficient numerical procedure has been developed for investigating the hydrodynamic stability of axisymmetric swirling flows with respect to non-axisymmetric travelling-wave perturbations. Calculations of temporal instability have been performed for the self-similar Batchelor vortex. A viscous instability mode has been found whose amplification factors exceed the values for previously known viscous modes. The application of the considered method is possible for a wide class of flow stability problems with arbitrary velocity profile distributions in various technical applications.

REFERENCES

1. **Gupta A.K, Lilley D.G, Syred N.** Swirl Flows 1984 (Abacus Press)
2. **Lucca-Negro O., O'Doherty T.** Vortex breakdown: a review. Progress in Energy and Combustion Science // 2001. V. 27. Pp. 431–481.
3. **Akhmetov V.K., Volshanik V.V., Zujkov A.L., Orekhov G.V.** Modelirovanie i raschet kontrvihrevyh techenij. Monografiya. M.: Izd-vo ASV, 2012. 252 s.
4. **Leibovich S., Stewartson K. A.** Sufficient condition for the instability of columnar vortices // J. Fluid Mech. 1983. V. 126. P. 335–356.
5. **Stewartson K.; Brown, S.N.** Near–neutral center–modes as inviscid perturbations to a trailing line vortex // J. Fluid Mech. 1985, 156, 387–399.

6. **Lessen M., Singh P.J., Paillet F.** The stability of a trailing line vortex. Part 1. Inviscid theory // J. Fluid Mech. 1974. V.63. P. 753–763.
7. **Lessen M., Paillet F.** The stability of a trailing line vortex. Part 2. Viscous theory // J. Fluid Mech. 1974. V. 65. Pt. 4. P. 769–779.
8. **Khorrami M.R.** On the viscous modes of instability of a trailing line vortex // J. Fluid Mech. 1991. V. 225. P. 197–212.
9. **Mayer E.W., Powell K.G.** Viscous and inviscid instabilities of a trailing vortex // J. Fluid Mech. 1992. V. 245. P. 91–114.
10. **Olendraru C.; Sellier A., Rossi M., Huerre P.** Inviscid instability of the Batchelor vortex: Absolute-convective transition and spatial branches // Phys. Fluids. 1999. 11, 1805–1820.
11. **Yin X.-Y., Sun D.-J., Wei M.-J., Wu J.-Z.** Absolute and convective instability character of slender viscous vortices // Phys. Fuids. 2000. V. 12. № 5. P. 1062–1072.
12. **Yadav N.K., Samanta A**. The stability of compressible swirling pipe flows with density stratification // J. Fluid Mech. 2017. Vol. 823. Pp. 689–715.
13. **Loiseleux T., Chomaz J. M., Huerre P.** The effect of swirl on jets and wakes: Linear instability of the Rankine vortex with axial flow // Phys. Fluids. 1998. V. 10. № 5. P. 1120–1134.
14. **Loiseleux T., Delbende I., Huerre P.** Absolute and convective instabilities of a swirling jet/wake shear layer // Phys. Fluids. 2000. V. 12. № 2. P. 375–380.
15. **Delbende I., Chomas J.-M., Huerre P.** Absolute/convective instabilities in the Batchelor vortex: a numerical study of the linear impulse response // J. Fluid Mech. 1998. V. 355. P. 229–254.
16. **Olendraru C., Sellier A**. Viscous effects in the absolute-convective instability of Batchelor vortex // J. Fluid Mech. 2002. V. 459. P. 371–396.
17. **Blanco-Rodríguez F.J., Rodríguez-García J.O., Parras L., del Pino C.** Optimal response of Batchelor vortex // Physics of Fluids. 2017. Vol. 29. 064108.
18. **Delbende I., Rossi M.** Nonlinear evolution of a swirling jet instability // Physics of Fluids. 2005. Vol. 17. 044103.
19. **Rukes L., Sieber M., Paschereit C., Oberleithner K.** The impact of heating the breakdown bubble on the global mode of a swirling jet: experiments and linear stability analysis // Physics of Fluids. 2016. Vol. 28. 104102.
20. **Oberleithner K.; Paschereit C., Seele, R.; Wygnanski, T.** Formation of turbulent vortex breakdown: intermittency, criticality, and global instability. AIAA J. **2012**, 50, 1437–1452.
21. **Wang, Y.; Wang, X.; Yang, V.** Evolution and transition mechanisms of internal swirling flows with tangential entry // Phys. Fluids. 2018**,** 30, 013601.
22. **Rukes L., Sieber M., Paschereit C., Oberleithner K.** The impact of heating the breakdown bubble on the global mode of a swirling jet: experiments and linear stability analysis // Phys. Fluids**.** 2016, 28, 104102.
23. **Ortiz S., Donnadieu C, Chomaz J.-M.** Three-dimensional instabilities and optimal perturbations of a counter-rotating vortex pair in stratified flows // Phys. Fluids. 2015, 27, 106603.
24. **Akhmetov V.K.** Numerical and asymptotic flow stability analysis of vortex structures // E3S Web of Conferences, 2021, 263, 03003
25. **Godunov S.K.** O chislennom reshenii kraevyh zadach dlya sistemy obyknovennyh differencial'nyh uravnenij // Uspekhi matem. nauk. 1961. T. 16. Vyp. 3. S. 171–174.

СПИСОК ЛИТЕРАТУРЫ

1. **Гупта А., Лилли Д., Сайред Н.** Закрученные потоки. М.: Мир, 1987. 588 с.
2. **Lucca-Negro O., O'Doherty T.** Vortex breakdown: a review. Progress in Energy and Combustion Science // 2001. V. 27. Pp. 431–481.
3. **Ахметов В.К., Волшаник В.В., Зуйков А.Л., Орехов Г.В.** Моделирование и расчет контрвихревых течений. Монография. М.: Изд-во АСВ, 2012. 252 с.
4. **Leibovich S., Stewartson K. A.** Sufficient condition for the instability of columnar vortices // J. Fluid Mech. 1983. V. 126. P. 335–356.
5. **Stewartson K.; Brown, S.N.** Near–neutral center–modes as inviscid perturbations to a trailing line vortex // J. Fluid Mech. 1985, 156, 387–399.
6. **Lessen M., Singh P.J., Paillet F.** The stability of a trailing line vortex. Part 1. Inviscid theory // J. Fluid Mech. 1974. V.63. P. 753–763.
7. **Lessen M., Paillet F.** The stability of a trailing line vortex. Part 2. Viscous theory // J. Fluid Mech. 1974. V. 65. Pt. 4. P. 769–779.
8. **Khorrami M.R.** On the viscous modes of instability of a trailing line vortex // J. Fluid Mech. 1991. V. 225. P. 197–212.
9. **Mayer E.W., Powell K.G.** Viscous and inviscid instabilities of a trailing vortex // J. Fluid Mech. 1992. V. 245. P. 91–114.
10. **Olendraru C.; Sellier A., Rossi M., Huerre P.** Inviscid instability of the Batchelor vortex: Absolute-convective transition and spatial branches // Phys. Fluids. 1999. 11, 1805–1820.
11. **Yin X.-Y., Sun D.-J., Wei M.-J., Wu J.-Z.** Absolute and convective instability character of slender viscous vortices // Phys. Fuids. 2000. V. 12. № 5. P. 1062–1072.
12. **Yadav N.K., Samanta A**. The stability of compressible swirling pipe flows with density stratification // J. Fluid Mech. 2017. Vol. 823. Pp. 689–715.
13. **Loiseleux T., Chomaz J. M., Huerre P.** The effect of swirl on jets and wakes: Linear instability of the Rankine vortex with axial flow // Phys. Fluids. 1998. V. 10. № 5. P. 1120–1134.
14. **Loiseleux T., Delbende I., Huerre P.** Absolute and convective instabilities of a swirling jet/wake shear layer // Phys. Fluids. 2000. V. 12. № 2. P. 375–380.
15. **Delbende I., Chomas J.-M., Huerre P.** Absolute/convective instabilities in the Batchelor vortex: a numerical study of the linear impulse response // J. Fluid Mech. 1998. V. 355. P. 229–254.
16. **Olendraru C., Sellier A**. Viscous effects in the absolute-convective instability of Batchelor vortex // J. Fluid Mech. 2002. V. 459. P. 371–396.
17. **Blanco-Rodríguez F.J., Rodríguez-García J.O., Parras L., del Pino C.** Optimal response of Batchelor vortex // Physics of Fluids. 2017. Vol. 29. 064108.
18. **Delbende I., Rossi M.** Nonlinear evolution of a swirling jet instability // Physics of Fluids. 2005. Vol. 17. 044103.
19. **Rukes L., Sieber M., Paschereit C., Oberleithner K.** The impact of heating the breakdown bubble on the global mode of a swirling jet: experiments and linear stability analysis // Physics of Fluids. 2016. Vol. 28. 104102.
20. **Oberleithner K.; Paschereit C., Seele, R.; Wygnanski, T.** Formation of turbulent vortex breakdown: intermittency, criticality, and global instability. AIAA J. **2012**, 50, 1437–1452.
21. **Wang, Y.; Wang, X.; Yang, V.** Evolution and transition mechanisms of internal swirling flows with tangential entry // Phys. Fluids. 2018**,** 30, 013601.
22. **Rukes L., Sieber M., Paschereit C., Oberleithner K.** The impact of heating the breakdown bubble on the global mode of a swirling jet: experiments and linear

stability analysis // Phys. Fluids**.** 2016, 28, 104102.
23. **Ortiz S., Donnadieu C, Chomaz J.-M.** Three-dimensional instabilities and optimal perturbations of a counter-rotating vortex pair in stratified flows // Phys. Fluids. 2015, 27, 106603.
24. **Akhmetov V.K.** Numerical and asymptotic flow stability analysis of vortex structures // E3S Web of Conferences, 2021, 263, 03003
25. **Годунов С.К.** О численном решении краевых задач для системы обыкновенных дифференциальных уравнений // Успехи матем. наук. 1961. Т. 16. Вып. 3. С. 171–174.

Vadim K. Akhmetov, Doctor of Science, Professor, Department of Computer Science and Applied Mathematics, Moscow State University of Civil Engineering, 26, Yaroslavskoe Shosse, Moscow, 129337, Russia, e-mail: vadim.akhmetov@gmail.com

Ахметов Вадим Каюмович, доктор технических наук, профессор кафедры информатики и прикладной математики Национального исследовательского Московского государственного строительного университета, 129337, г. Москва, Ярославское шоссе, д. 26, e-mail: vadim.akhmetov@gmail.com

DOI:10.22337/2587-9618-2026-22-3-144-154

ANALYSIS OF THE ROUGHNESS PARAMETERS AND CHEMICAL COMPOSITION TRANSFORMATION OF THE PROTECTIVE COATING OF A PIPELINE DURING ITS REPAIR

Vladimir A. Orlov, Sergey P. Zotkin, Maria A. Bolshakova
National Research Moscow State University of Civil Engineering, Moscow, RUSSIA

Abstract. The issues of potential transformation of the surface roughness of solid samples of the sprayed protective coating Subcote FLP, used during the period of trenchless reconstruction of pressure pipelines, are considered. The technique of conducting experiments on the dynamics of changes in the roughness of samples in the time range by immersing them in a container with water, dosing a disinfectant into it and processing water on a magnetic stirrer with subsequent analysis of the surface of samples by methods of lightoscopy and profilometry are presented. Changes in the qualitative characteristics of coating samples and chemical indicators of water are identified and analyzed. The dynamics of changes in the equivalent roughness coefficient of protective coatings and the quality parameters of protective coating samples in water at different temperatures are presented. Based on the results of light spectroscopy, the coefficients of hydraulic friction and equivalent roughness were calculated, as well as an automated calculation using a specially developed program to assess energy savings during water transportation when using the Subcote FLP protective coating during the renovation of a steel pipeline

Keywords: pipeline, protective coating, roughness, light microscopy, profilometry, water quality indicators, energy saving

АНАЛИЗ ТРАНСФОРМАЦИИ ПАРАМЕТРОВ ШЕРОХОВАТОСТИ И ХИМИЧЕСКОГО СОСТАВА ЗАЩИТНОГО ПОКРЫТИЯ ТРУБОПРОВОДА ПРИ ЕГО РЕМОНТЕ

В.А. Орлов, С.П. Зоткин, М.А. Большакова
Национальный исследовательский Московский государственный строительный университет, г. Москва, РОССИЯ

Аннотация. Рассмотрены вопросы потенциальной трансформации шероховатости поверхности твердых образцов напыляемого защитного покрытия Subcote FLP, используемого в период бестраншейной реконструкции напорных трубопроводов. Представлена методика проведения опытов по исследованию динамики изменения шероховатости образцов во временном диапазоне путем их погружения в емкости с водой, дозировании в нее дезинфектанта и обработкой воды на магнитной мешалке с последующим анализом поверхности образцов методами светоскопии и профилометрии. Выявлены и проанализированы изменения качественных характеристик образцов покрытий и химических показателей воды. Представлена динамика изменения коэффициента эквивалентной шероховатости защитных покрытий и качественных параметров образцов защитных покрытий в воде при разной температуре. По результатам светоскопии произведен расчет коэффициентов гидравлического трения и эквивалентной шероховатости, а также автоматизированный расчет по специально разработанной программе для оценки экономии электроэнергии при транспортировке воды в случае использовании защитного покрытия Subcote FLP при реновации стального трубопровода.

Ключевые слова: Трубопровод, защитное покрытие, шероховатость, светоскопия, профилометрия, показатели качества воды, экономия электроэнергии

INTRODUCTION

The issues of determining the roughness of the inner walls of pressure pipelines made of new materials, as well as its possible transformation during the long-term operation of engineering networks, are relevant, as they allow to identify such important characteristics as the values of the coefficients of equivalent resistance and hydraulic friction and, thereby, to substantiate the prospect of possible energy savings during water transportation [1].

An analysis of global experience in the operation and repair of water supply pipeline networks shows that to increase the reliability of pipeline systems, the most promising solution is to rehabilitate them by applying internal protective coatings of various types, including polymer sprayed materials. In the process of developing renovation projects for pipeline transport and their implementation, there is a need to obtain reliable data necessary to ensure the reliability of the restored pipelines by ensuring the appropriate hydraulic and strength characteristics of the restored networks, which acquire a two-layer structure after repair work [2, 3].

An analysis of the results of previously conducted studies shows that there are valid documents in the certification systems that describe the measurement procedures necessary to determine the hydraulic characteristics of pipelines with internal coatings [4]. At the same time, it is very important to determine the ability of protective coatings (internal linings) to maintain their hydraulic characteristics during long-term operation and not to negatively affect the quality of the transported water [5].

Given the significant extent of wear and tear on pipeline systems, where, according to data from the Ministry of Regional Development, more than 40% of water supply networks require immediate repair, the effectiveness of using new types of internal protective coatings for dilapidated pipelines using efficient and prompt trenchless methods becomes extremely relevant [6]. In order to prove the effectiveness of the use of certain types of polymer protective coatings and the absence of potential negative circumstances, such as chemical reactions between the coatings and the transported water, as well as changes in their hydraulic properties (such as changes in surface roughness), it is necessary to conduct a wide range of studies under dynamic conditions using appropriate models and special instruments.

In accordance with the available conformity certificates, protective polymer spray coatings do not change the composition of the pumped medium, maintaining the reliability of pipeline networks at a high level and reducing the negative impact on the urban environment due to repair work. Despite the thin layer of 3-8 mm, these materials can effectively fill in existing defects and increase the wear resistance of pipelines during the rehabilitation process. As a result, the internal surfaces of the restored pipelines tend to become less rough, improving the hydraulic performance of the pipelines. To prove this, the structure of the protective coatings is analyzed using a number of modern contact and optical methods that provide information about their roughness [7].

The objectives of this work were to conduct scientific research that confirms or refutes the noted facts using modern approaches and methods for determining and evaluating the hydraulic performance of protective coating samples.

METHODS AND MATERIALS

The sprayed organic protective coating Subcote FLP was used as the research materials. The coating has a sanitary and epidemiological expert opinion No. 77.01.12.P.014303.09.11 dated 22.09.2011, issued by the Department of the Federal Service for Supervision of Consumer Rights Protection and Human Welfare in Moscow, which allows the coating to be applied to the inner surface of pipelines in domestic and drinking water systems.

In the work, modern tools of contact and optical technologies, respectively profilography and

lightoscopy, were adopted as methods of roughness research. According to the results of these methods, the analysis and comparison of the obtained data was carried out, in particular, on the arithmetic mean deviation of the surface profile, the height of its irregularities, etc. with the subsequent calculation of the values of the coefficients of equivalent roughness of coatings in time before and after their special processing.

The essence of the experiments on studying the dynamics of changes in roughness was to process the samples of the protective coating on a small-sized installation, which was a glass cup (container) of the calculated height and diameter with a measured volume of 1 liter of drinking water (Figure 1). The samples of the protective coatings of certain sizes were rigidly placed in the cup near its wall (at the periphery).

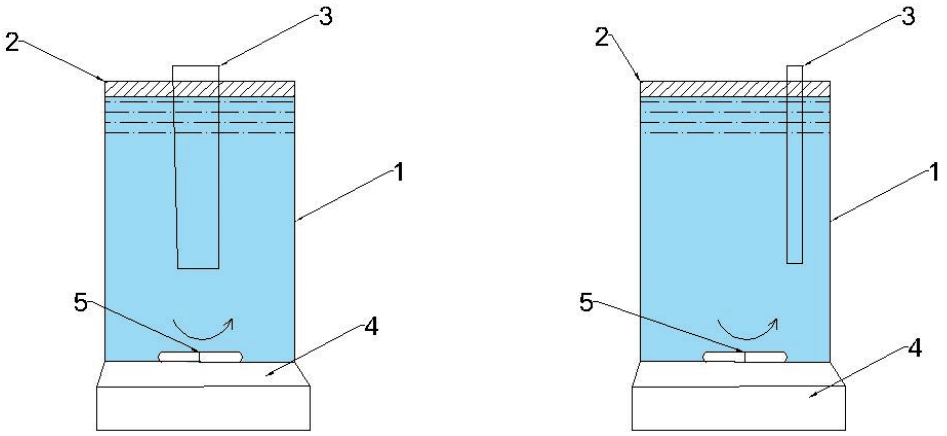


Figure 1. Layout of the apparatus elements on the magnetic stirrer (left – front view of the sample in the container; right – rear view of the sample) 1 - glass cup; 2 - rubber stopper; 3 - sample of a certain size, suspended near the edge of the cup; 4 - magnetic stirrer; 5 – anchor

The beaker was placed on a special device (magnetic stirrer), where the contents were mixed at a specific angular velocity ѡ (converted to linear velocity V or tangential velocity), ensuring a precisely defined contact time between the sample and the water, simulating the identical duration of water flow in a pipeline of the appropriate length and diameter at an optimal velocity of 1 m/s. The conversion of angular velocity to linear (tangential) velocity was performed using an online calculator in the standard program planetcalc.ru.

When conducting experiments on a magnetic stirrer, specially prepared solid samples of the Subcote FLP internal protective coating to be sprayed were examined. The dimensions of the samples were (2.0 x 8.0), and their contact area with the water flow, taking into account the front and back sides, as well as the side surfaces, was 32 cm2. The one-time duration of sample processing in a glass of water on a magnetic stirrer was 2h 47 minutes, which corresponded to (simulated) the presence of water in a pipeline 10 km long and 1200 mm in diameter. These parameters are adopted for the need to ensure approximately equal conditions for the consumption of chlorine in time by a unit of surfaces (1 cm2) of samples and the contact area of the water flow during its transportation through the pipeline. In this case, the consumption of chlorine for the samples was 1/32=0.03125 L and for the simulation of the pipeline 11304000 / 376800000=0.03 L per 1 cm2 of the contact area of the pipeline walls with water.

As mentioned above, two alternative methods were used to study the roughness of the protective coating samples: the probe (contact) method and the optical (non-contact) method,

which have the same range of measured micro-irregularity heights (0.8 – 62.5 μm). These methods are relatively simple to use when processing measurement results.

The scanning electron microscope, the TESCAN MIRA 3 LMU scanning electron microscope and the Olympus GX53 inverted microscope, as well as the TR 100 portable roughness meter, were used as instruments for studying the above parameters. To determine the quality of water, an instrument base was used, including a Primelab PL-HR-atom magnetic stirrer, an ECOSTAB PC 233 analyzer for determining pH, salinity, electrical conductivity and water temperature.

It should be noted that, depending on the regulatory requirements for the disinfectant dose that provides a bactericidal effect during water disinfection, a certain amount of chlorine was artificially added to the water in the form of universal Aquabreeze water disinfection tablets. This ensured that the residual chlorine concentration remained at the required level for water sterilization after it left the water treatment plant, typically at least 1.0 mg/L [8].

The ultimate goal of the research is a comprehensive analysis of the possible transformation of the initial roughness and chemical composition of water over a certain time interval in a magnetic stirrer system, which provides a tangential flow of water as an analogy for the flow of water in linear objects (pressure pipelines) of the appropriate diameter and length. Additionally, the objective is to determine the effect of the duration of the sample's exposure to chlorinated water at a specific dose of the reagent on the roughness [9].

One of the tasks in conducting experiments and processing their results using automated programs was to indirectly assess the energy consumption during water transportation as a result of potential changes in the hydraulic characteristics of the protective coating samples over time and due to the impact of chlorine added to the water.

RESULTS

Below are the results of three research cycles, in particular:

- on the transformation of the equivalent surface roughness coefficients of Subcote protective coating samples based on parallel experiments using profilometry and light microscopy, followed by the calculation of the equivalent surface roughness coefficients of the coatings over time before and after their special treatment, as well as the recording of the arithmetic mean deviation of the surface profile, the height of its irregularities, etc. (I cycle);
- by changing the chemical properties of the surface of the protective coating samples, which leads to changes in the roughness profile heights in the transverse and longitudinal directions, as well as in the morphology (in this case, the structure and elemental chemical composition) of the samples, using electron microscopes to process the data, and by changing the water quality indicators before and after the experiments on the magnetic stirrer (cycle II);
- to assess the energy consumption during water transportation as a result of potential changes in the hydraulic characteristics of protective coating samples over time and due to the impact of chlorine derivatives using modern electronic models (III cycle) [10].

Cycle I.

1. The results of profilometry experiments (on the TR 100 roughness meter) on samples of protective coatings (in cold and hot water) in dynamics and the analysis of the obtained results on the determination of the coefficients of equivalent roughness KE:

- on the initial sample (1) in nature - KE = 0.0386 mm;
- on sample (2) with a chlorine dose of 1.07 mg/L in the initial cold (200 C) water and a processing time of 2 h 47min in the agitator - KE = 0.02428 mm;
- on sample (3) with a chlorine dose of 1.0 mg/L in the initial cold (200 C) water and a double processing time of 2x(2 h 47min) - KE = 0.02085 mm;

- on sample (4) with a chlorine dose of 1.0 mg/l in the initial hot water (500 C) and a treatment duration of 2 h 47m - KE = 0.02225 mm.

The analysis of the data presented above shows a downward trend in the equivalent roughness coefficients as a function of the time spent by the samples in chlorinated water, with the most pronounced effect occurring when the sample is placed in hot water, where the disinfectant dose and the duration of the sample's stay in the magnetic stirrer are the lowest.

2. The results of light microscopy experiments (using an Olympus GX53 microscope) on samples of protective coatings (in cold and hot water) in dynamics and the analysis of the results obtained to determine the equivalent roughness coefficients KE:

- on the original sample (1) in nature - KE = 0.0372 mm;
- on sample (2) with a chlorine dose of 1.07 mg/l in the initial cold (200 C) water and a processing time of 2h 47min in the agitator - KE = 0.0228 mm
- no studies were conducted on sample (3);
- on sample (4) with a chlorine dose of 1.0 mg/l in the initial hot (500 C) water and a processing time of 2h 47m - KE = 0.0217 mm.

As in the previous calculation point, the analysis of the data presented above shows a downward trend in the equivalent roughness coefficients as a function of the time the samples spent in chlorinated water. The greatest reduction in roughness is achieved when the samples are treated with hot water.

When comparing the results of points 1 and 2 for the three samples, it can be noted that the difference in the obtained data for determining the equivalent roughness coefficient KE is as follows:

- for the initial sample (1), the difference in the values of the equivalent roughness coefficient is 0.0386-0.0372 = 0.0014 mm or 3.76%;
- for sample (2), the difference is 0.02428-0.0228=0.00148 mm or 6.5%
- for sample (4), the difference is 0.02225-0.0217=0.00055 mm or 2.53%

Thus, in three experiments, the discrepancy in the KE readings ranged from 2.53% to 6.5%, which indicates that the results of profilometry and light spectroscopy experiments can be used interchangeably to determine the equivalent roughness coefficient of the samples.

The nature of the irregularities (heights) was determined using light microscopy on an inverted Olympus GX53 microscope. There were no roughness protrusions on the samples, respectively, in the longitudinal and transverse directions, which amounted to: 40-120 and 43-103 microns for sample (1), 120-195 and 65-158 for sample (2); 158-210 and 125-208 microns for sample (4). At the same time, the steps for fixing irregularities in samples (1) and (4) were 70, respectively and 200 microns, which can be characterized as a transition from more frequent to more rare, which means that it may indicate some straightening of the roughness of the samples over time during treatment in water with chlorine.

Figure 2 graphs show the transformation of surface irregularities on samples (1) and (4) as sample roughness profiles in the longitudinal direction.

The graphical dependencies presented in Figure 2 indicate that, compared to sample (1), sample (4) exhibits a peculiar "growth" in the average profile height: from (40+120)/2=80.0 μm to (160+210)/2=175 μm. Thus, an increase in the average height of the profiles due to "growths" on the surface of the samples does not lead to an increase in the surface roughness, as the step of the roughness protrusions (irregularities), as noted above, increases from 70 μm to 200 μm, which contributes to the local smoothing of the surface between the peaks of the roughness protrusions.

This phenomenon can be explained by the reaction of chlorine with the sample (see cycle II) or by the deposition of chlorine salts on the surface of the sample, which is a kind of inlay that has a positive effect in this case, as the average deviation of the Ra profile was 9 and 6 μm for samples (1) and (4), respectively.

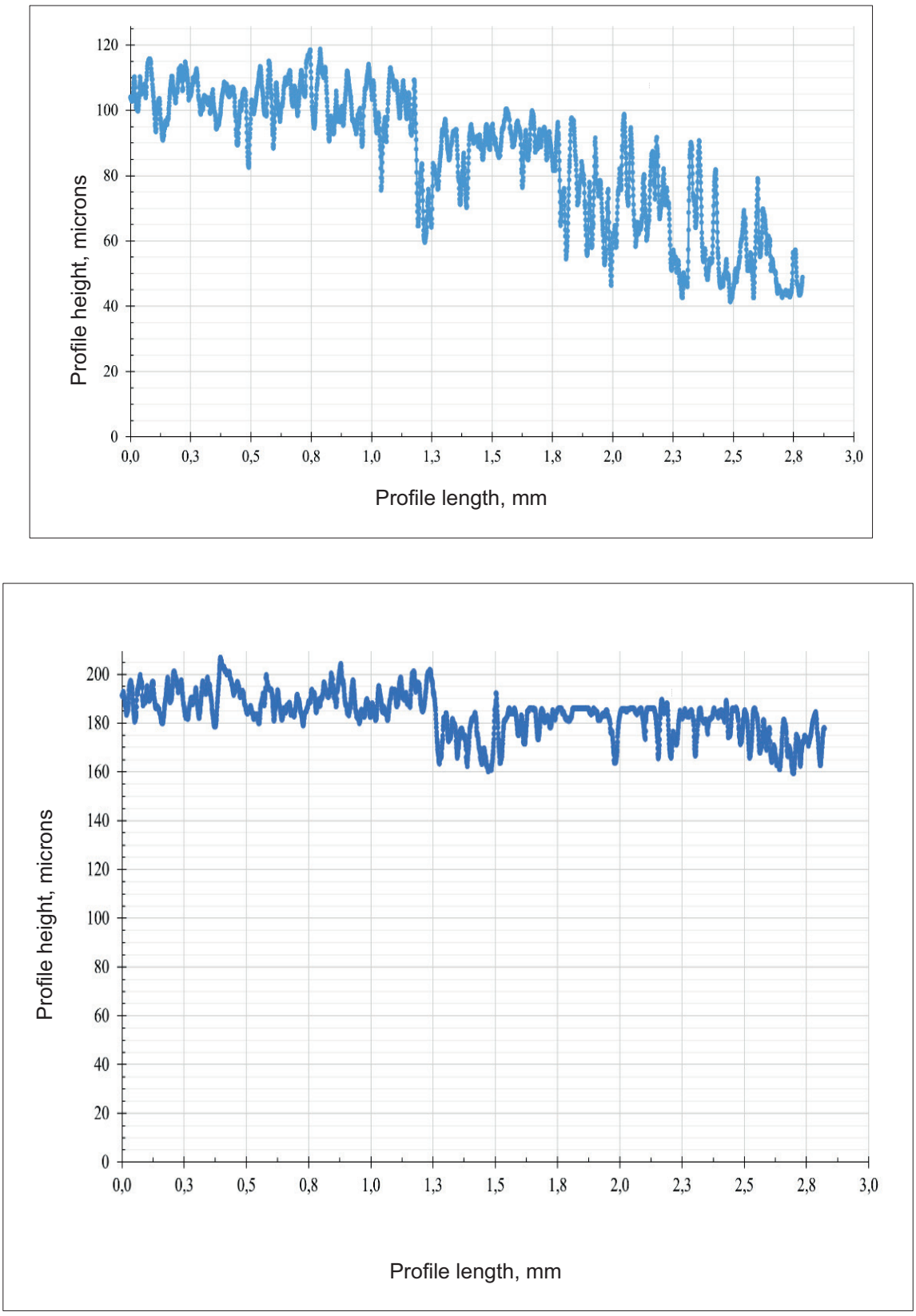


Figure 2. Illustration of the surface profiles of samples (1) and (4), respectively, in the longitudinal direction: from top to bottom before treatment in chlorinated water and after treatment

Thus, it can be concluded that when processing samples on a device with a magnetic stirrer, the possibility of the phenomenon of "straightening" of a rough surface with filling of pores between the peaks of roughness (conditionally called "voids or dips") is not excluded. This suggests that the coefficient of equivalent roughness of the sample may decrease over time, i.e., during long-term operation of a pipeline with a protective coating.

Cycle II.

In this cycle of experiments, the issues of changing the morphology of samples before and after processing in chlorinated water on a magnetic stirrer, as well as the consideration and influence of the quality indicators of water and its temperature on the processes of transformation of the surface of samples, are examined.

In this series of experiments, a TESCAN MIRA 3 LMU scanning electron microscope was used, as well as a device for chemical control of water quality indicators (Ecostab PC 233 analyzer).

The results of experiments with coating samples on an electron microscope showed that there is a change in the Cl (chlorides) indicator on the surface of the samples, with an increase after treatment in water on an apparatus with a magnetic stirrer, and a similar change in the concentration of calcium Ca and the appearance of potassium K.

In the summary Table 1, there are printouts of the output parameters for the presence of chemical elements in the composition of the studied samples, which indicate a change in their chemical composition after treatment on a magnetic stirrer.

Table 1. Illustration of the dynamics of changes in the weight and atomic composition of chemical elements in samples depending on the time and temperature of their processing: on the left, the initial sample (1), in the middle, the sample (2), and on the right, the sample (4)

Element	Weight, %	Atomic, %
C	72.05	78.94
O	23.49	19.32
Na	0.13	0.07
Mg	0.04	0.02
Al	0.15	0.07
Si	1.15	0.68
Cl	0.18	0.07
Ca	2.49	0.82
Results	100	

Element	Weight, %	Atomic, %
C	66.33	74.26
O	27.77	23.33
Na	0.44	0.26
Mg	0.07	0.04
Al	0.18	0.09
Si	1.77	0.85
Cl	0.47	0.18
Ca	2.61	0.88
K	0.36	0.12
Results	100	

Element	Weight, %	Atomic, %
C	65.8	73.94
O	27.91	23.54
Na	0.26	0.15
Al	0.25	0.12
Si	1.82	0.88
Cl	0.76	0.29
Ca	2,98	1,00
K	0.23	0.08
Results	100	

A characteristic feature of the data presented in Table 1 for each sample is:

- sample (1) has a relatively low content of the chemical element chlorine (0.18%) and a predominance of the weight fraction of carbon 72.05% and oxygen 23.49 %;
- in sample (2), compared to sample (1), the concentration of chlorine in the protective coating material increased from 0.18% to 0.47%, i.e., by 2.61 times, while the weight fractions of carbon decreased by 7.94% (72.05-66.33) and the weight fraction of oxygen increased by 15.4% (27.77-23.49), and potassium appeared (0.36%);
- in sample (4), compared to sample (1), the concentration of chlorine in the material increased from 0.18% to 0.76%, i.e., by 4.22 times, while the weight fractions of carbon decreased from 72.05% to 65.8%, i.e., by 1.09 times, and the weight fraction of oxygen

increased by 1.19 times (from 23.49% to 27.91%), while the weight fraction of potassium decreased slightly (0.23%).

It should also be noted that a similar phenomenon of increasing the calcium concentration in the coating material is observed from sample to sample: in sample (2) compared to sample (1), its concentration increased by 4.8%, and in sample (4) by 19.7%.

Below are theoretical calculations illustrating the analysis of changes in the chemical properties of water and samples (2) and (4) after their contact with chlorine water in a beaker on a magnetic stirrer.

Regarding the chlorine reaction with sample (2), it should be noted that the initial value of total chlorine in the water was 1.07 mg/L (before the experiment) and decreased to 0.49 mg/L, remaining in the water as free chlorine that provided water disinfection. Therefore, 1.07-0.49=0.68 mg/L of chlorine should react with sample (2).

On the other hand, the initial value of residual chlorine in the water before the experiments, according to the measurements, was 0.95 mg/L, and after the experiment it decreased to 0.35 mg/L. Then it can be assumed that residual chlorine in the amount of 0.95-0.35=0.6 mg/L reacted with the sample.

Comparing the values obtained from the analysis of the transformation of various forms of chlorine in water, we can note the similarity of the concentration of total chlorine (0.68 mg/L) and residual chlorine (0.6 mg/L), which reacted with the sample. The difference in the results was 11.76%.

Regarding the increase in water mineralization during the experiments, the following can be noted: the initial water mineralization was 282 mg/L (before the experiment), and it increased to 286 mg/L after the experiment, resulting in a slight difference of 4 mg/L. However, this difference is consistent with the formation of chlorides and insoluble calcium salts, which can precipitate on the surface of the sample, leading to incrustation.

In terms of other chemical indicators of water, the following trend should be noted:

- the redox potential (ORP) of the initial water was 20 mV, and after the experiment it was 9 mV;
- the electrical conductivity of the water before the experiment was 397 μS/cm, and after it was 402 μS/cm; the difference of 5 μS/cm indicates an increase in mineralization, including the formation of chlorine salts, which increase the conductivity of the current;
- the pH value of the water before the experiment was 6.8, and after it was 7.02; the difference of 0.22 indicates a near-neutral environment.

Similar trends can be observed in the reaction of chlorine with sample (4), but with some notable differences.

It should be noted that the initial value of total chlorine introduced into the water at a dose of 1 mg /l a few seconds before the experiment was 0.27 mg/l, i.e. there was an almost instantaneous decrease in its concentration at elevated temperature; after the experiment, the concentration of total chlorine decreased to 0.06 mg/l, which may indicate, for example, an active reactions of chlorine with the sample, which confirms the hypothesis of a tendency to increase profile heights due to the growth of precipitating salts (see Figure 2); the initial value of residual chlorine in water was 0.02 mg/l (before the experiment), and the final value of residual chlorine was 0.00 mg/l (after the experiment); thus, all residual chlorine is also reacted with a sample in the amount of 0.02 mg/l and disappeared from the water.

Regarding the increase in water mineralization during the experiments, the following can be noted: the initial water mineralization was 297 mg/L (before the experiment), and it increased to 306 mg/L after the experiment, resulting in a difference of 9 mg/L, which is consistent with the formation of salts (chlorides) that can precipitate on the surface of the sample, contributing to incrustation phenomena.

In other chemical indicators of water, the following trend should be noted:

- the redox potential (ORP) of the initial water was 13 mV, and after the experiment -21 mV, which indicates the ionization of water, i.e. a

sufficient amount of charged ions in it to attract and neutralize the harmful excess acids;
- the electrical conductivity of the water before the experiment was 420 μS/cm, and after it was 430 μS/cm; the difference of 10 μS/cm indicates an increase in mineralization, including the formation of salts in the water, which increase the conductivity of the current;
- the pH value of the water before the experiment was 6.92, and after it was 7.46; the difference of 0.54 indicates a transition of the water from a near-neutral to a slightly alkaline environment.

Cycle III.

The results of the experiments in this cycle were aimed at describing the expected phenomena of inscription as a positive phenomenon that ultimately contributes to reducing the coefficient of hydraulic friction λ and thus leads to a decrease in energy consumption in the case of using the studied coating material for repairing high-pressure steel pipelines that transport drinking water.

Regarding the possible energy savings E (kWh) during water transportation, it can be noted that due to the potential changes in the hydraulic characteristics λ of the protective coatings, the following is observed:
- for the initial period of pipeline operation with a diameter of d (m)

$$\lambda i = 1/(2 \lg d / KEi + 1{,}14)2 = $$
$$=1/(2\lg 1.2 / 0.0000372+1.14)2 = 0.00969 \quad (1)$$
$$Ei = 0.81 \cdot Kt \cdot Q3 \cdot L \cdot \lambda i \cdot 24 \cdot 365 / (d\ 5\ \eta) = $$
$$= 443\ 830.8 \text{ kWh / year} \quad (2)$$

- after a long period of operation of a pipeline with a diameter of d (m) in the future

$$\lambda f=1/(2\lg d/ KEf +1.14)2 = $$
$$=1/(2\lg 1.2/0.0000318+1.14)2 = 0.00943 \quad (3)$$
$$Ef =0{,}81 \cdot Kt \cdot Q3 \cdot L \cdot \lambda f \cdot 24 \cdot 365 / (d\ 5\ \eta) = $$
$$=431\ 922.1 \text{ kWh / year} \quad (4)$$

where Q is the flow rate of water supplied by the pipeline, m3/s; KEi and KEf are the initial and prospective coefficients of equivalent roughness, m, respectively; η is the efficiency coefficient of the pumping unit; 24 is the number of hours the pump operates per day, h; 365 is the number of days in a year; L is the length of the pipeline, m; Kt is the correction factor for the change in water density with temperature.

The presented calculated data were obtained using the Prandtl formula [11], which displays the change in the hydraulic friction coefficient λ for the initial (1) and final (3) periods of operation, and the data from formulas (2) and (4) were obtained using the calculated dependence of energy consumption in the pipeline [6], taking into account the expected values of the hydraulic friction coefficient λ, which were calculated using formulas (1) and (3) using the experimental data obtained from the transformation of the equivalent resistance coefficient KE based on the operation of the small-sized installation.

It should be noted that the calculation of energy consumption E (kWh/year) was performed for a real pressure pipeline with a diameter of d=1.2 (m), a length of L=10000 (m), a water flow rate of Q=1.131 (m3/s), a pump efficiency of η=0.9, a water temperature of T=200 C, and a coefficient of thermal expansion of Kt =0.99923. Thus, it has been calculated that over time, the consumption of electricity during the transportation of water through a pressure pipeline will decrease by 443,830.8-431,922.1=11,908.7 kWh per year due to the reduction in the roughness of the protective coating. For example, if the cost of electricity for industrial enterprises is 1.57 rubles per kWh, the savings in money can amount to 11,908.7·1.57=18 696.7 rubles.

An automated program [12] has been developed and patented for complex energy and hydraulic calculations using the above-described methodology, which includes three cycles of experimental research.

CONCLUSIONS

1. Conducted on a small-sized installation field studies on the assessment of possible transformation of samples of the Subcote FLP polymer coating with reference to the real

conditions of their operation as protective coatings in pipelines during the period of trenchless repair, as well as complex processing of the obtained data using light microscopy and profilometry, allowed to establish a number of dependencies of the change in the coefficients of roughness on temperature conditions.

2. Based on the study of the dynamics of changes in the chemical parameters of water under the conditions of operation of a small-sized installation, assumptions are made about the interaction (reaction) of the samples of protective coatings with chlorine, which leads to a change in their morphology and hydraulic parameters.

3. Based on the results of comprehensive experiments with transformed samples of protective coatings, an energy calculation was performed for the case of their application in a real pressure pipeline during its trenchless renovation, which showed the possibility of saving electricity.

REFERENCES

1. **Averkeev I.A., Zaitseva E.I., Gogina E.S., Orlov V.A.** Development and experimental substantiation of the methodology for determining the coefficient of equivalent roughness by the hydraulic method //Izvestiya vuzov. Stroitelstvo. 2024. No. 12. Pp. 113-122. DOI 10.32683/0536-1052-2024-792-12-113-122
2. **Primin O.G.** Water leaks.-M: Publishing house of FGBOU VO "NRU MGSU". 2022. 167 p.
3. **Aleksandrov V.I., Gvozdev O.B., Karelin A.E., Morozov A.A.** Assessment of the effect of the roughness of the inner surface of hydraulic transport pipelines on the value of specific pressure losses // Journal of Mining Equipment and Electromechanics. 2017. No. 3 (130). Pp. 34-40
4. GOST R 70117-2022 "Surface Roughness. Selection Recommendations" (introduced on January 1, 2023).
5. **Prodous O.A., Yakubchik P.P.** Hydraulic calculation of pipelines made of polymer materials, taking into account the parameters of the roughness of the inner surface of the pipes // Water supply and sanitary engineering. 2020. No. 11. Pp. 55–60
6. **Orlov V.A**. Trenchless technologies and energy saving.-M: ASV Publishing House. 2021. 123 p.
7. **Ravilova V.M.** Modern means and methods of roughness measurement // Scientific Leader Magazine. No. 52 (97), 2022, pp. 20-24
8. **Andrianov A.P. Efremov R.V., Khurgin R.E.** Problems of modern water supply // System technologies. 2022. No. 3 (44). pp. 5 - 13
9. **Houghtalen R., Osman A., Akan A., Hwang N.** Fundamentals of Hydraulic Engineering Systems, 5th edition. Pearson. 2016. 528 p.
10. **Chupin R.V., Melekhov E.S.** Justification of the parameters of developing water supply and sanitation systems based on their electronic models // IOP Conference Series: Materials Science and Engineering, 2020. DOI: 10.1088/1757-899X/880/1/012050
11. **Chugaev R.R.** Hydraulics.-L.: Energiya. 1970. 552 p.
12. **Orlov V.A., Zotkin S.P., Bolshakova M.A.** Simulation of the processes of transformation of water quality indicators and the roughness of the material of pipeline walls during their operation. Certificate of State Registration of Computer Programs dated 25.09.2025

СПИСОК ЛИТЕРАТУРЫ

1. **Аверкеев И.А., Зайцева Е.И., Гогина Е.С., Орлов В.А.** Разработка и экспериментальное обоснование методики определения коэффициента эквивалентной шероховатости гидравлическим способом //Известия вузов. Строительство. 2024. № 12. С. 113-122. DOI 10.32683/0536-1052-2024-792-12-113-122

2. **Примин О.Г.** Утечки воды.-М: Издательство ФГБОУ ВО «НИУ МГСУ». 2022. 167 с.
3. **Александров В.И., Гвоздев О.Б., Карелин А.Э., Морозов А.А.** Оценка влияния шероховатости внутренней поверхности гидротранспортных трубопроводов на величину удельных потерь напора //Журнал Горное оборудование и электромеханика. 2017. № 3 (130). С. 34-40
4. ГОСТ Р 70117-2022 «Шероховатость поверхности. Рекомендации по выбору» (введен с 01.01.2023 г.).
5. **Продоус О.А., Якубчик П.П**. Гидравлический расчет трубопроводов из полимерных материалов с учетом параметров шероховатости внутренней поверхности труб // Водоснабжение и санитарная техника. 2020. № 11. С. 55–60
6. **Орлов В.А.** Бестраншейные технологии и энергосбережение.-М: Издательство АСВ. 2021. 123 с.
7. **Равилова В.М.** Современные средства и методы измерения шероховатости // Журнал «Научный лидер». № 52 (97), 2022, с. 20-24
8. **Андрианов А.П. Ефремов Р.В., Хургин Р.Е.** Проблемы современного водоснабжения // Системные технологии. 2022. № 3 (44). с. 5 - 13
9. **Houghtalen R., Osman A., Akan A., Hwang N.** Fundamentals of Hydraulic Engineering Systems, 5th edition. Pearson. 2016. 528 p.
10. **Chupin R.V., Melekhov E.S.** Justification of the parameters of developing water supply and sanitation systems based on their electronic models // IOP Conference Series: Materials Science and Engineering, 2020. DOI: 10.1088/1757-899X/880/1/012050
11. **Чугаев Р.Р.** Гидравлика.-Л.: Энергия. 1970. 552 с.
12. **Орлов В.А., Зоткин С.П., Большакова М.А.** «Моделирование процессов трансформации качественных показателей воды и шероховатости материала стенок трубопроводов при их эксплуатации». Свидетельство о государственной регистрации программ для ЭВМ от 25.09.2025

Orlov Vladimir A., Professor, Doctor of Technical Sciences; National Research Moscow State Construction University (NIU MSCU), Russia, 129337, Moscow, 26 Yaroslavskoe Shosse, E-mail: OrlovVA@mgsu.ru

Орлов Владимир Александрович, профессор, доктор технических наук; Федеральное государственное бюджетное образовательное учреждение высшего образования «Национальный исследовательский Московский государственный строительный университет» (НИУ МГСУ), Россия, 129337, Москва, Ярославское шоссе, 26; E-mail: OrlovVA@mgsu.ru.

Zotkin Sergey P., Professor, Candidate of Technical Sciences; Russia, National Research Moscow State Construction University (NIU MSCU), Russia, 129337, Moscow, 26 Yaroslavskoe Shosse; E-mail: ZotkinSP@mgsu.ru

Зоткин Сергей Петрович, профессор, кандидат технических наук; Россия, Федеральное государственное бюджетное образовательное учреждение высшего образования «Национальный исследовательский Московский государственный строительный университет» (НИУ МГСУ), 129337, Москва, Ярославское шоссе, 26; E-mail: ZotkinSP@mgsu.ru.

Bolshakova Maria Anatolyevna, Postgraduate Student; Federal State Budgetary Educational Institution of Higher Education "National Research Moscow State University of Civil Engineering" (NRU MGSU), 26 Yaroslavskoye Shosse, Moscow, 129337, Russia; E-mail: haritonova_mariy@mail.ru

Большакова Мария Анатольевна, аспирант; Федеральное государственное бюджетное образовательное учреждение высшего образования «Национальный исследовательский Московский государственный строительный университет» (НИУ МГСУ), Россия, 129337, Москва, Ярославское шоссе, 26; E-mail: haritonova_mariy@mail.ru

International Journal for Computational Civil and Structural Engineering, 22(3) 155–174 (2026)

DOI:10.22337/2587-9618-2026-22-3-155-174

LATERAL-TORSIONAL BUCKLING ANALYSIS OF ASYMMETRIC THIN-WALLED BEAMS

Olga A. Tusnina

National Research Moscow State University of Civil Engineering, Moscow, RUSSIA

Abstract: A review and analysis of domestic and international design codes (Eurocode EN 1993-1-1, American standard ANSI/AISC 360-22 and Russian standard SP 16.13330.2017) regarding the lateral-torsional buckling of flexural elements indicate that current standards lack a universal solution for evaluating the lateral-torsional buckling stability of beams with arbitrary cross-sections under arbitrary loading conditions. The available literature provides design recommendations for the buckling analysis of symmetric and asymmetric I-beams and channels under a limited number of loading configurations and boundary conditions. Therefore, evaluating the buckling stability of non-standard beams (such as strengthened sections, which often exhibit complex and asymmetric geometries) is significantly hindered by the absence of practical engineering methods.

This paper proposes a method for analyzing the elastic lateral-torsional buckling stability of thin-walled steel beams with asymmetric cross-sections under arbitrary loading scenarios and boundary conditions. The method is developed based on the analytical solution to a system of differential buckling equations in accordance with Vlasov's thin-walled beam theory, considering the elastic stage of material behavior. The proposed method is formulated in compliance with the design approaches adopted in SP 16.13330.2017, making it suitable for integration into the regulatory framework. The primary advantage of this method lies in its versatility. The validity of the method is confirmed by calculation examples and verification finite element modeling performed using the Simcenter FEMAP with Nastran software suite.

Keywords: lateral-torsional buckling (LTB), thin-walled steel beam, Vlasov's beam theory, elastic critical moment, finite element analysis (FEA)

РАСЧЕТ ИЗГИБНО-КРУТИЛЬНОЙ УСТОЙЧИВОСТИ НЕСИММЕТРИЧНЫХ ТОНКОСТЕННЫХ БАЛОК

О.А. Туснина

Национальный исследовательский Московский государственный строительный университет, г. Москва, РОССИЯ

Аннотация: Обзор и анализ отечественных и зарубежных нормативных методик (Eurocode EN 1993-1-1, ANSI/AISC 360-22, СП 16.13330.2017) расчета общей устойчивости изгибаемых элементов показывает, что в настоящее время в стандартах отсутствует универсальное решение для оценки устойчивости балок произвольного сечения при произвольном загружении. В технической литературе представлены рекомендации по расчету устойчивости симметричных и несимметричных двутавров, а также швеллеров лишь для ограниченного числа расчетных схем и условий закрепления. Расчет устойчивости балок нетипового профиля (например, усиленных сечений, зачастую имеющих сложную асимметричную форму) затруднен из-за отсутствия инженерных методик.

В статье предложена методика расчета устойчивости плоской формы изгиба тонкостенных стальных балок несимметричного сечения при произвольных граничных условиях и вариантах загружения. Преимуществом предлагаемого подхода является его универсальность. Методика разработана на основе аналитического решения системы дифференциальных уравнений устойчивости в соответствии с теорией тонкостенных стержней В.З. Власова в упругой стадии работы материала. Методика представлена в форме, соответствующей расчетным подходам СП 16.13330.2017, что позволяет внедрить ее в нормативный документ. Достоверность методики подтверждена расчетными примерами и верификационным конечно-элементным моделированием, выполненным с использованием ПК Simcenter FEMAP with Nastran.

Ключевые слова: устойчивость плоской формы изгиба; тонкостенные стальные балки, теория тонкостенных стержней Власова, упругий критический момент, метод конечных элементов (МКЭ)

1. INTRODUCTION

Steel beams are susceptible to lateral-torsional buckling (LTB). At a certain critical bending moment (M_{cr}), the beam loses stability. It undergoes combined lateral deflection and twisting.

Design standards regulate the lateral-torsional buckling resistance of beams. A review of domestic and international codes shows a common approach. The critical buckling moment under uniform bending is taken as the baseline value [1,2]. Then, design codes apply correction factors to account for effects like moment gradients, load height, boundary conditions and restraints at the ends of the unbraced length (L_b) of the beam. The number of these factors varies across different design codes. The American specifications ANSI/AISC 360-22 utilize a single-component equation that contains a single equivalent uniform moment factor (C_b). The following equation for critical buckling moment provided by White and Jung [3] is proposed in AISC 360-22 for monosymmetric I-beam:

$$M_{cr} = C_b \frac{\pi^2 E I_y}{L_b^2}\left(\frac{\beta_y}{2} + \sqrt{\left(\frac{\beta_y}{2}\right)^2 + \frac{I_\omega}{I_y}\left(1 + 0.039\frac{I_t}{I_\omega}L_b^2\right)}\right) \tag{1}$$

The single-component AISC equation accounts for loads applied at the shear center of the profile. It does not consider the effect of load height along the cross-section. This equation overestimates the buckling resistance when the load is applied to the compression flange and underestimates when the load is applied to the tension flange.

The comments on the AISC specification provide a refined equation for the critical buckling moment according to guide [4]. This formula was originally derived by Clark and Hill [5]:

$$M_{cr} = C_1 \frac{\pi^2 E I_y}{\left(K_y L_b\right)^2}\sqrt{\left(\frac{K_y}{K_w}\right)^2 \frac{I_\omega}{I_y} + \frac{\left(K_y L_b\right)^2 G I_t}{\pi^2 E I_y} + \left(C_2 y + C_3\frac{\beta_y}{2}\right)^2} + \left(C_2 y + C_3\frac{\beta_y}{2}\right) \tag{2}$$

where y is the coordinate of the load application point relative to the shear center. The factors C_1, C_2 and C_3 depend on the moment diagram. The effective-length factors K_y and K_w – are the effective-length factors correspond to the lateral bending and warping restraint at the ends of the unbraced length L_b, respectively.

Equation (2) is the so-called three-factor formula. It has the most general form that corresponds to the solution of the differential buckling equations. The general solution allows accounting for the influence of cross-section monosymmetry (Wagner coefficient β_y), moment gradient, end-restraint conditions, and load height effects.

The three-factor formula was provided in previous versions of European standard ENV 1993-1-1:1992 [6]. However, the current version of the Eurocode does not contain rules for determining the critical moment. The three-factor formula is used in the NCCI design guidance [7] but, this implementation does not include the coefficient C_3.

The application of the three-factor formula is limited due to the lack of recommendations for determining the factors C_1, C_2 and C_3. For certain specific cases the values of these coefficients are given in guidelines [7, 8].

There are studies on determining these coefficients for specific cases [9-12]. However, these publications mainly focus on simple design models, typical cross-sections of the beams and loading scenarios for simply supported beams. The factor C_3 remains the least studied parameter. This factor accounts for the cross-sectional asymmetry, as well as the offset between the

shear center and the center of gravity. Research on this coefficient is limited, and it is frequently ignored in engineering practice [13].

Therefore, the development of a universal procedure for determining the coefficients C_1, C_2 and C_3 in the three-factor formula is required. This method should accommodate arbitrary loading scenarios, cross-sectional types and boundary conditions.

The Russian code SP 16.13330.2017 specifies lateral-torsional buckling analysis for symmetric and asymmetric I-beams, and channels. The design procedure covers common beam configurations, boundary conditions, and loading scenarios. It also accounts for the load application point along the cross-section height.

However, the SP formulas apply only to specific design cases. These cases are limited to standard structural models and simple loading conditions. Applying the SP methodology to cases not explicitly covered by the code is difficult. The procedure relies on numerous separate formulas and empirical coefficients. This complexity obscures the physical meaning of the design procedure.

An article [14] introduces a refinement to the standard analysis method implemented in the Russian code SP 16.13330.2017. The author proposes a universal formula for the lateral-torsional buckling reduction factor. However, this formula applies only to single-span symmetric I-beams. Furthermore, it is limited to a specific range of loading scenarios.

An effective approach for practical stability analysis is proposed in paper [15]. The author emphasizes the need to develop a unified equation for the lateral-torsional buckling reduction factor. However, the proposed analytical formulas have explicit structural constraints. Their applicability is limited to specific beam geometries and loading conditions.

A solution for the deformation-based buckling analysis of steel members is proposed in [16]. The analysis utilizes a three-dimensional deformed configuration, taking into account material nonlinearity.

The performed review of articles, design codes, and guidelines shows certain limitations. Current literature lacks a unified and exact solution for the lateral-torsional buckling (LTB) analysis of thin-walled members. Specifically, no existing methods cover arbitrary asymmetric cross-sections under arbitrary boundary and loading conditions. Developing such a method is a necessary task.

2. THEORETIICAL STUDY

Consider an arbitrary asymmetric thin-walled profile subjected to a transverse load q_y (Fig. 1). For practical purposes, it is convenient to use a coordinate system with axes parallel to the webs and flanges of the section (the so-called orthogonal X and Y axes with coordinates x and y). The origin is located at the cross-section centroid. The positive Y-axis points toward the tension fibers and the direction of the X-axis is determined by the left-hand rule. The principal coordinate system (X_0, and Y_0 axes with coordinates x_0 and y_0) is inclined at an angle α_0 relative to the orthogonal axes.

The external load q_y acts through the shear center along the Y-axis, parallel to the web.

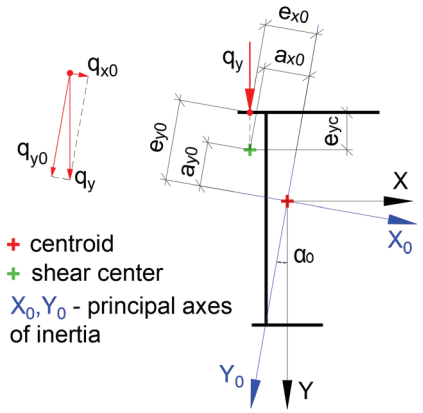


Figure 1. Asymmetric thin-walled profile. Cross-section scheme

Figure 1 defines the geometric and loading parameters of the cross-section: α_0 is the inclination angle of the principal Y_0-axis to the Y-axis; a_{x0} and a_{y0} are the shear center coordinates in

the principal axes of inertia; e_{x0} and e_{y0} are the coordinates of the load application point in the principal axes of inertia; q_{x0} and q_{y0} are the load components parallel to the principal axes, defined as: $q_{xo} = q_y \sin\alpha_0$, $q_{yo} = q_y \cos\alpha_0$.

The transverse load q_y is assumed to act through the shear center thereby eliminating pre-buckling torsion. Thin-walled members with open profiles cross-sections exhibit low torsional stiffness. When a beam is subjected to eccentric transverse loads, its twist angle exceeds he serviceability limit state before reaching the critical buckling load; thus, the serviceability limit state criteria become decisive [17, 18].

For the case under consideration the system of governing linear differential equations for elastic lateral-torsional buckling based on Vlasov's thin-walled beams theory [19] is formulated as follows:

$$\begin{cases} EI_{yo}\xi^{IV} + \left(M_{x0}\theta\right)'' = 0 \\ EI_{yo}\eta^{IV} + \left(M_{y0}\theta\right)'' = 0 \\ EI_{\omega}\theta^{IV} + \left(\left(2\beta_x M_{y0} - 2\beta_y M_{x0} - GI_t\right)\theta'\right)' + \\ + \left(q_{x0}e_{xc0} + q_{y0}e_{yc0}\right)\theta + M_{x0}\xi'' + M_{y0}\eta'' = 0 \end{cases} \quad (3)$$

where I_{x0}, I_{y0} are the principal moments of inertia; I_ω is the warping constant; I_t is the St. Venant torsional constant; β_x, β_y are the monosymmetry constants; $e_{xc0} = e_{x0} - a_{x0}$, $e_{yc0} = e_{y0} - a_{y0}$ are the load application point coordinates relative to the shear center; M_{x0}, M_{y0} are the bending moments about the principal axes: $M_{xo} = M_x \cos\alpha_0$, $M_{yo} = -M_x \sin\alpha_0$.

Equations (3) are formulated with respect to the principal axes of inertia (X_0, Y_0) using the coordinates x_0, y_0. The unknowns in equations (3) are the functions of the shear center displacements: $\xi = \xi(z)$, $\eta = \eta(z)$ are the linear displacements along the X_0 and Y_0 axes, respectively and $\theta = \theta(z)$ is the twist angle about longitudinal axis Z.

The monosymmetry constants βx and βy account for the eccentricity of the centroid relative to the shear center and the additional torque induced by normal bending stresses from the moments M_{y0} and M_{x0} and are defined as follows:

$$\beta_x = \frac{U_{y0}}{2I_{y0}} - a_{x0}, \quad \beta_y = \frac{U_{x0}}{2I_{x0}} - a_{y0} \quad (4)$$

where U_{x0}, U_{y0} are the cross-sectional properties representing the third-order moments of inertia, calculated with respect to the principal axes of inertia:

$$\begin{aligned} U_{x0} &= \int_F y_0^3 dF + \int_F x_0^2 y_0 dF \\ U_{y0} &= \int_F x_0^3 dF + \int_F y_0^2 x_0 dF \end{aligned} \quad (5)$$

The solution to the system of differential buckling equations (3) is described below. From the first and second equations of system (3), the following expressions can be obtained

$$\begin{aligned} \xi'' &= \frac{-M_{x0}}{EI_{y0}} l^2 \cdot \theta = \frac{-M_x \cos\alpha_0}{EI_{y0}} l^2 \cdot \theta \\ \eta'' &= \frac{-M_{y0}}{EI_{x0}} l^2 \cdot \theta = \frac{M_x \sin\alpha_0}{EI_{x0}} l^2 \cdot \theta \end{aligned} \quad (6)$$

By substituting and transforming the system of equations (3), the following buckling equation is obtained:

$$\begin{aligned} &EI_{\omega}\theta^{IV} - 2\beta_{res}\left(M_x\theta'\right)' - GI_t\theta'' + \\ &+ \left(e_{yc} \cdot M_x'' - \frac{M_x^2}{EI_{y0}} l^2 \cdot k_\alpha\right)\theta = 0 \end{aligned} \quad (7)$$

where $k_\alpha = \cos^2\alpha_0 + \frac{EI_{y0}}{EI_{x0}}\sin^2\alpha_0$;

$\beta_{res} = \beta_y \cos\alpha_0 + \beta_x \sin\alpha_0$

Equation (7) can be written in terms of the relative longitudinal coordinate $\zeta = \frac{z}{l}$ (where l is the

unbraced length of the member and z is the absolute longitudinal coordinate).
The following definitions can be defined:

$$\kappa(\zeta)=\frac{l}{EI_{y0}}\cdot M_x(\zeta)$$
$$a=\frac{EI_\omega}{l^2GI_t},\ b_1=\frac{2\beta_{res}EI_{y0}}{lGI_t},\ b_2=\frac{e_{yc}EI_{y0}}{lGI_t}, \quad (8)$$
$$c=\frac{EI_{y0}}{GI_t}k_\alpha$$

Then, the buckling equation (7) is expressed as follows:

$$a\theta^{IV}-\theta''-b_1(\kappa\theta')'+\left(b_2\kappa''-c\kappa^2\right)\theta=0 \quad (9)$$

The components of equation (9) account for the factors affecting lateral-torsional buckling:
- parameter b_1 reflects the effect of cross-sectional asymmetry and the eccentricity between the center of gravity and the shear center;
- parameter b_2 accounts for the load application point along the cross-section height, representing either the destabilizing or restoring effect of the load.
The function $\kappa(\zeta)$ in equation (9) describes the bending moments distribution $M_x(\zeta)$ along the unbraced length of the beam (bending moment diagram). The moment distribution is a function of the external load: $M_x(\zeta)=f(q_y)$. Thus, solving equation (9) yields the critical load value $q_{y,cr}$ at which lateral-torsional buckling occurs.
To solve the equation (9), a sinusoidal distribution of the twist angles is assumed along the unbraced length: $\theta=A\sin\pi\zeta$ $(\zeta\in[0;1])$. Applying the Bubnov–Galerkin method, the differential equation of stability is expressed as follows:

$$\int_0^1\left(\left(b_1+4b_2\right)\kappa+\frac{c}{\pi^2}\kappa^2\right)\cos2\pi\zeta\,d\zeta+$$
$$+\int_0^1\left(b_1\kappa-\frac{c}{\pi^2}\kappa^2\right)d\zeta+\left(a\pi^2+1\right)=0 \quad (10)$$

Equation (10) can be transformed as follows:

$$b_1\left(\int_0^1\kappa\cos2\pi\zeta\,d\zeta+\int_0^1\kappa d\zeta\right)+4b_2\int_0^1\kappa\cos2\pi\zeta\,d\zeta+$$
$$+\frac{c}{\pi^2}\left(\int_0^1\kappa^2\cos2\pi\zeta\,d\zeta-\int_0^1\kappa^2d\zeta\right)+\left(a\pi^2+1\right)=0 \quad (11)$$

The following definitions are introduced:

$$\int_0^1\kappa\cos2\pi\zeta\,d\zeta=\lambda\cdot A_B$$
$$\int_0^1\kappa\cos2\pi\zeta\,d\zeta+\int_0^1\kappa d\zeta=\lambda\cdot C_B \quad (12)$$
$$\int_0^1\kappa^2\cos2\pi\zeta\,d\zeta-\int_0^1\kappa^2d\zeta=\lambda^2\cdot D_B$$

where parameter $\lambda=\frac{l}{EI_{y0}}\cdot q_yl^2$

Thus, equation (11) becomes:

$$\left(b_1\cdot C_B+4A_B\cdot b_2\right)\lambda-\frac{c}{\pi^2}D_B\lambda^2+\left(a\pi^2+1\right)=0 \quad (13)$$

The dimensionless parameters in Equations (12) are given by:

$$A_B=\frac{\int_0^1M_x(\zeta)\cos2\pi\zeta\,d\zeta}{q_yl^2}$$
$$C_B=\frac{\int_0^1M_x(\zeta)\cos2\pi\zeta\,d\zeta+\int_0^1M_x(\zeta)d\zeta}{q_yl^2} \quad (14)$$
$$D_B=\frac{\int_0^1M_x^2(\zeta)d\zeta-\int_0^1M_x^2(\zeta)\cos2\pi\zeta\,d\zeta}{\left(q_yl^2\right)^2}$$

Introducing the parameter $\rho=-4\pi^2A_B$, the final form of the buckling equation can be written as follows:

$$\frac{c}{\pi^2}\lambda^2 - \left(b_1 \cdot \frac{C_B}{D_B} + \frac{1}{D_B} \cdot \rho \cdot \frac{b_2}{\pi^2}\right) \cdot \lambda - \\ - \frac{1}{D_B}\left(a\pi^2 + 1\right) = 0 \tag{15}$$

By solving the quadratic equation (15), the value of λ_{cr} at which the beam buckling occurs is determined:

$$\lambda_{cr} = \left(\frac{\pi^2}{2c} \cdot \left(b_1 \frac{C_B}{D_B} + \frac{1}{D_B}\rho\frac{b_2}{\pi^2}\right) + \right. \\ \left. + \sqrt{\frac{\pi^4}{4c^2} \cdot \left(b_1 \frac{C_B}{D_B} + \frac{1}{D_B}\rho\frac{b_2}{\pi^2}\right)^2 + \frac{1}{D_B}\frac{\pi^2\left(1+\pi^2 a\right)}{c}}\right. \tag{16}$$

Then, the critical load $q_{y,cr}$ and the critical moment M_{cr} can be expressed as follows:

$$M_{cr} = K_1 \cdot q_{y,cr} l^2 = K_1 \cdot \frac{EI_{y0}}{l} \cdot \lambda_{cr} \tag{17}$$

The coefficient K_1 in formula (17) is determined by the bending moment diagram and the specific cross-section along the beam length where the moment value is calculated.

Substituting the values of the parameters a, b_1, b_2, c from (8) into formula (16), we introduce the following coefficients:

$$C_I = \frac{K_I}{\sqrt{D_B}}, C_{II} = \frac{\rho}{\sqrt{D_B}}, C_{III} = \frac{C_B}{\sqrt{D_B}} \tag{18}$$

In its final form, the equation for the elastic lateral-torsional buckling critical moment is expressed as follows:

$$M_{cr} = C_I \left(\frac{\pi^2 EI_{y0}}{k_\alpha l^2}\left(C_{III} \cdot \beta_{res} + \frac{e_{y,c}}{2\pi^2} \cdot C_{II}\right) + \sqrt{\frac{\pi^2 EI_{y0}}{k_\alpha l^2}\left(\frac{\pi^2 EI_{y0}}{k_\alpha l^2}\left(C_{III} \cdot \beta_{res} + \frac{e_{y,c}}{2\pi^2} \cdot C_{II}\right)^2 + \frac{\pi^2 EI_\omega}{l^2} + GI_t\right)}\right) \tag{19}$$

In fact, the derived formula (19) represents an analogue of the three-factor equation for the critical moment (see equation (2)). The key difference is that formula (19) is written in a generalized form and can be applied to any cross-sectional shape, which is highly relevant, for instance, when analyzing strengthened structures. Furthermore, formula (19) enables the analysis of lateral-torsional buckling under unsymmetrical bending, i.e., when the load does not act within a principal plane of inertia.

In the general case, calculating with formula (19) requires knowing the cross-sectional geometric properties, the coordinates of the shear center and the centroid, the inclination angle of the principal axes of inertia, and the load application point coordinates, as well as computing the coefficients C_I, C_{II} и C_{III}.

When applying formula (19) in practice, certain difficulties may arise. These primarily concern the determination of the warping constant I_ω and the parameter β_{res}. Its components β_x and β_y incorporate the geometric properties U_{x0} and U_{y0}, which represent third-order moments of inertia and require the evaluation of integrals over the cross-sectional area. However, existing methods of structural mechanics enable these computations for any cross-sectional shape. For common section types (e.g., asymmetric I-beams and channels), simplified formulas [20] and tabular solutions can be recommended. Standard rolled section catalogs can be supplemented with the respective values.

Furthermore, an automated computational tool for evaluating the geometric properties of arbitrary thin-walled cross-sections will be developed within the framework of future research.

The primary difficulty in applying formula (19) lies in determining the coefficients C_I, C_{II} and C_{III}. These coefficients incorporate the integral parameters A_B, C_B and D_B, that account for both the shape of the bending moment diagram and the buckling mode.

To evaluate the parameters A_B, C_B and D_B, the moment distribution function $M_x(\zeta)$ along the member length must be defined for integration

according to (12). In practice, analytical calculations are hindered by the complexity of deriving moment functions and the labor-intensiveness of manual integration (16). Actual bending moment diagrams are rarely described by simple functions. Therefore, design codes must not be limited only to special loading cases. A universal engineering method for lateral-torsional buckling analysis is required. This methodology must account for arbitrary moment diagrams, any boundary conditions, and diverse buckling modes.

3. ANALYTICAL SOLUTION

The coefficients C_I, C_{II} and C_{III} were analytically determined for various bending moment diagram cases. For this purpose, the actual bending moment diagram within the unbraced segment is approximated by the function $M_x(\zeta)$. Next, by defining the buckling mode shape as a function of the twist angle distribution $\theta = A\sin\pi\zeta$, the integral parameters for the differential equations were evaluated

The most characteristic beam buckling modes were identified using finite element analysis (FEA). As a rule, the lateral-torsional buckling of a beam occurs within the span. This phenomenon involves out-of-plane displacement and twisting toward the compressed top flange. This buckling mode is defined as the "mid-span" buckling mode.

Under specific loading configurations, continuous beams with a less developed bottom flange exhibited a distinct buckling mode. This mode involves out-of-plane displacement of the compressed bottom flange near the support (Fig. 2). This phenomenon is defined as the "support-zone" buckling mode. Here, buckling occurs along the compressed bottom flange within the beam segments on the left and right sides of support.

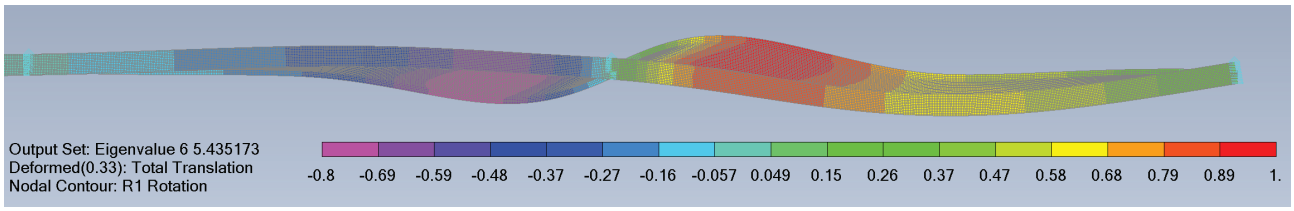
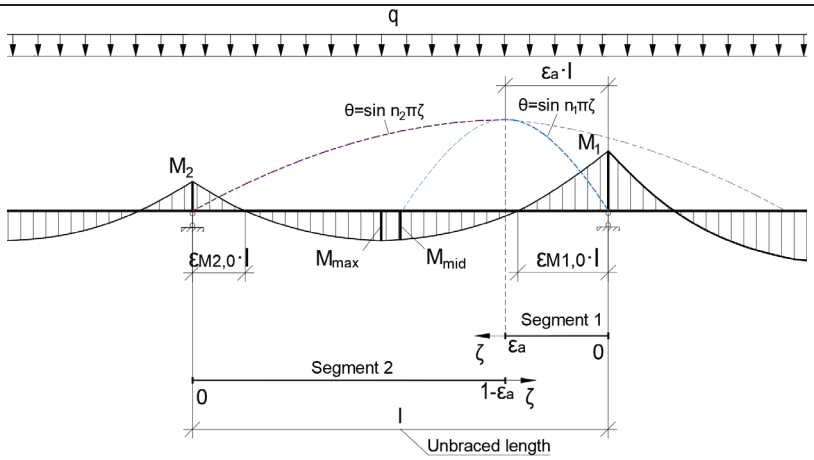


Figure 2. Support-zone buckling mode: lateral-torsional buckling in the bottom-flange compression zones near the support

Table 1. Design models adopted to determine the coefficients C_I, C_{II} and C_{III} for the mid-span buckling mode

Bending moment diagram	Design model and equations for approximating the bending moment diagram
1.1 Non-linear moment diagram	

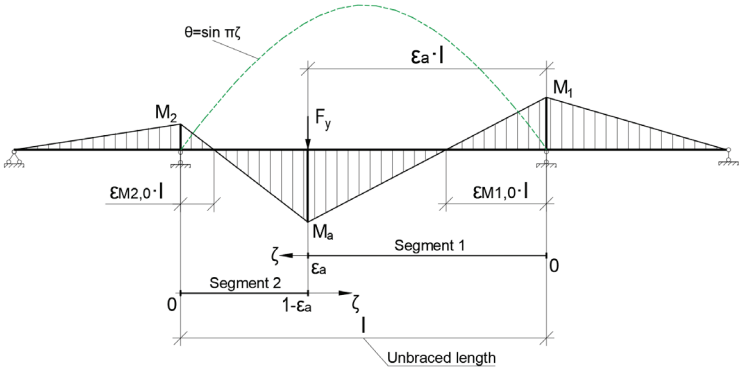
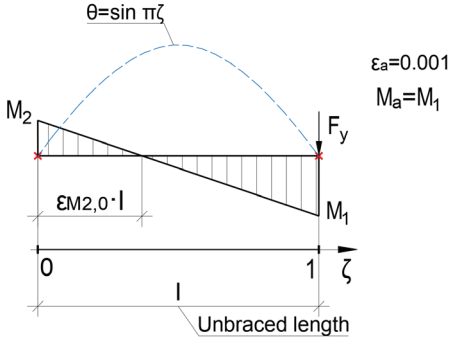
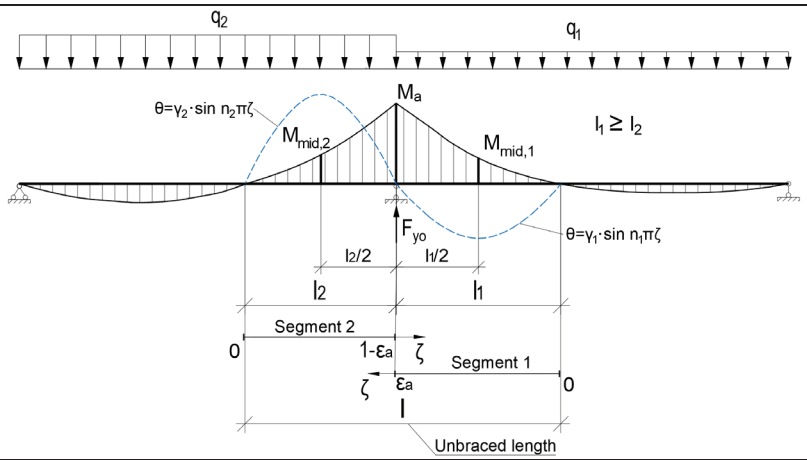
	$$M_x(\zeta)=\begin{cases} q_y l^2\cdot\left(a_{M1}\zeta^2+b_{M1}\zeta+c_{M1}\right),\zeta\in[0;\varepsilon_a](segment\ 1) \\ q_y l^2\cdot\left(a_{M2}\zeta^2+b_{M2}\zeta+c_{M2}\right),\zeta\in[0;(1-\varepsilon_a)](segment\ 2)\end{cases}$$
2.2 Piecewise linear moment diagram with a single kink	 $$M_x(\zeta)=\begin{cases} F_y l\cdot\left(b_{F1}\zeta+c_{F1}\right),\zeta\in[0;\varepsilon_a](segment\ 1) \\ F_y l\cdot\left(b_{F2}\zeta+c_{F2}\right),\zeta\in[0;(1-\varepsilon_a)](segment\ 2)\end{cases}$$
1.3 Linear moment diagram without kinks	 $$M_x(\zeta)=F_y l\cdot\left(b_F\zeta+c_F\right),\zeta\in[0;1]$$

Table 2. Design models adopted to determine the coefficients C_I, C_{II} and C_{III} for the support-zone buckling mode

Bending moment diagram	Design model and equations for approximating the bending moment diagram
2.1 Non-linear moment diagram	

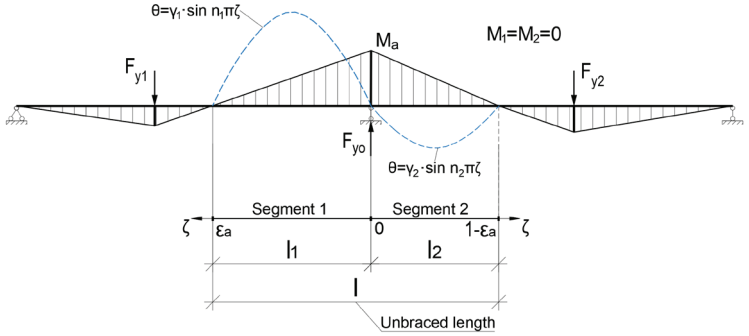
	$$M_x(\zeta)=\begin{cases}F_{yo}l\cdot\left(l_{M1}\zeta^2+d_{M1}\zeta\right),\zeta\in\left[0;\varepsilon_a\right](segment\ 1)\\ F_{yo}l\cdot\left(l_{M2}\zeta^2+d_{M2}\zeta\right),\zeta\in\left[0;\left(1-\varepsilon_a\right)\right](segment\ 2)\end{cases}$$
2.2 Piecewise linear moment diagram	 $$M_x(\zeta)=\begin{cases}F_{yo}l\cdot\left(d_{F1}\zeta+e_{F1}\right),\zeta\in\left[0;\varepsilon_a\right](segment\ 1)\\ F_{yo}l\cdot\left(d_{F2}\zeta+e_{F2}\right),\zeta\in\left[0;\left(1-\varepsilon_a\right)\right](segment\ 2)\end{cases}$$

Table 1 presents the design models adopted to determine the coefficients *C_I, C_{II} and C_{III}* under various bending moment diagrams along the unbraced length for the mid-span lateral-torsional buckling mode. The design models for the support-zone buckling mode are represented in Table 2.

4. PROPOSED ENGINEERING METHOD

For practical application, analytical formulas and tabular solutions have been developed to determine the coefficients *C_I, C_{II} and C_{III}* under various bending moment distributions. Two types of lateral-torsional buckling modes are defined: mid-span and support-zone.

I. Mid-span buckling mode. The following bending moment diagram configurations are considered:

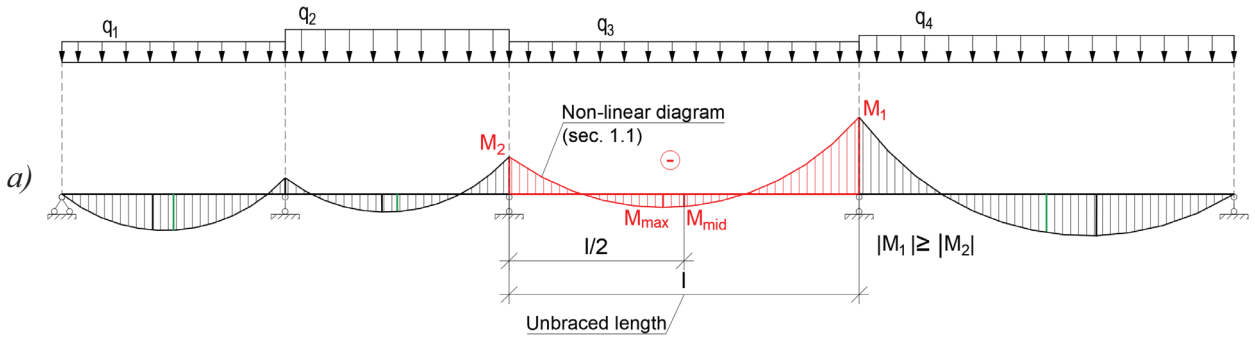
1.1. Non-linear moment diagram.

1.2. Piecewise linear moment diagram with a single kink.

1.3. Linear moment diagram without kinks.

1.4. Piecewise linear moment diagram with two or more kinks.

The design models adopted for the mid-span lateral-torsional buckling check of a continuous beam under various bending moment diagrams are presented in Figure 3.



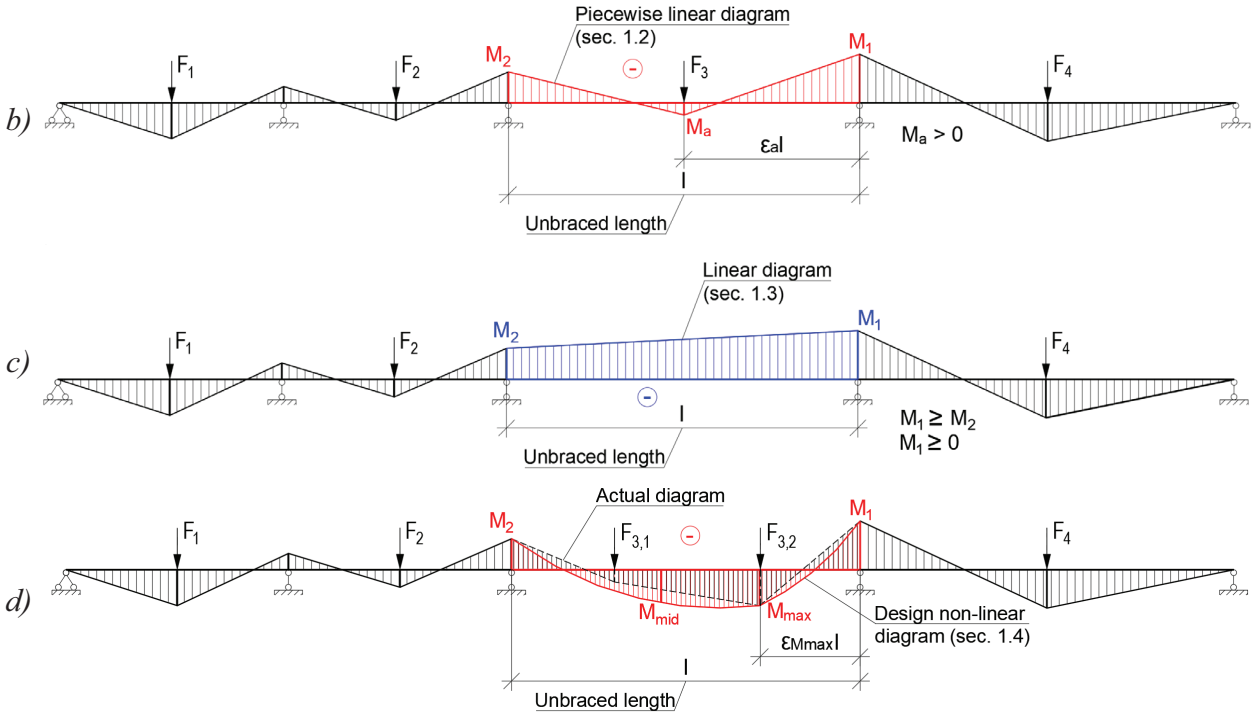


Figure 3. Mid-span buckling mode. Design models for the bending moment diagram: a) non-linear; b) piecewise linear with a single kink; c) linear; d) piecewise linear with two or more kinks

1.1. Non-linear moment diagram (Fig. 3, a).

The coefficients C_I, C_{II} and C_{III} are:

$$C_I = \frac{5.48 \cdot \pi^2 \cdot M_{\max}}{\sqrt{125.5 \cdot \left(M_1^2 + M_2^2\right) + 2278.55 \cdot M_{mid}^2 + 261.81 \cdot \left(M_1 + M_2\right) - 130.91 \cdot M_1 M_2}}$$

$$C_{II} = \frac{21.91 \cdot \pi^2 \cdot \left(2M_{mid} - M_2 - M_1\right)}{\sqrt{125.5 \cdot \left(M_1^2 + M_2^2\right) + 2278.55 \cdot M_{mid}^2 + 261.81 \cdot \left(M_1 + M_2\right) - 130.91 \cdot M_1 M_2}}$$

$$C_{III} = \frac{14.5 \cdot \left(M_1 + M_2\right) + 25.1 \cdot M_{mid}}{\sqrt{125.5 \cdot \left(M_1^2 + M_2^2\right) + 2278.55 \cdot M_{mid}^2 + 261.81 \cdot \left(M_1 + M_2\right) - 130.91 \cdot M_1 M_2}}$$

1.2. Piecewise linear moment diagram with a single kink (Fig. 3, b)

The coefficients C_I, C_{II} and C_{III} are determined using the following formulas:

$$C_I = \frac{K_I}{\sqrt{D_B}}, C_{II} = \frac{\rho}{\sqrt{D_B}}, C_{III} = \frac{C_B}{\sqrt{D_B}}$$

where $K_1 = \dfrac{M_a \cdot \left(1 - \varepsilon_a\right) \cdot \varepsilon_a}{M_a - M_1 \cdot \left(1 - \varepsilon_a\right) - M_2 \cdot \varepsilon_a}$

The parameters D_B, C_B and ρ determined as a function of the relative position of the kink ε_a using the design charts presented in Fig. 4–6.

Parameter D_B is given by: $D_B = D_{B,1} + D_{B,2}$,

$$D_{B,1} = b_{F1}^2 K_{D,bF1} + c_{F1}^2 K_{D,cF1} + b_{F1} c_{F1} K_{D,bF1cF1}$$

$$D_{B,2} = b_{F2}^2 K_{D,bF2} + c_{F2}^2 K_{D,cF2} + b_{F2} c_{F2} K_{D,bF2cF2}$$

Parameter C_B is given by: $C_B = C_{B,1} + C_{B,2}$,

$$C_{B,1} = b_{F1} \cdot K_{C,bF1} + c_{F1} \cdot K_{C,cF1}$$

$$C_{B,2} = b_{F1} \cdot K_{C,bF2} + c_{F1} \cdot K_{C,cF2}$$

The coefficients b_F и c_F characterize the moment distribution and equal:

$$c_{F1} = \frac{M_1 \cdot (1-\varepsilon_a) \cdot \varepsilon_a}{M_a - M_1 \cdot (1-\varepsilon_a) - M_2 \cdot \varepsilon_a};$$

$$b_{F1} = \frac{(M_a - M_1) \cdot (1-\varepsilon_a)}{M_a - M_1 \cdot (1-\varepsilon_a) - M_2 \cdot \varepsilon_a};$$

$$c_{F2} = \frac{M_2 \cdot (1-\varepsilon_a) \cdot \varepsilon_a}{M_a - M_1 \cdot (1-\varepsilon_a) - M_2 \cdot \varepsilon_a};$$

$$b_{F2} = \frac{(M_a - M_2) \cdot \varepsilon_a}{M_a - M_1 \cdot (1-\varepsilon_a) - M_2 \cdot \varepsilon_a};$$

The coefficients K_D и K_C are represented in Fig. 4 and 5. Parameter ρ is given in Table 3 and Fig. 6.

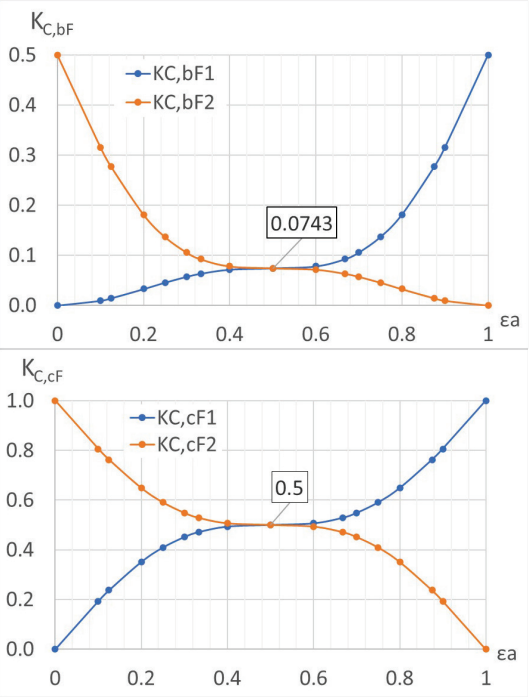


Figure 4. Design charts for the K_C coefficients for a piecewise linear bending moment diagram

Table 3. Parameter ρ for a piecewise linear bending moment diagram with a kink

ε_a	0	0.125	0.25	0.333	0.5	0.667	1
ρ	0	0.293	1	1.5	2	1.5	1

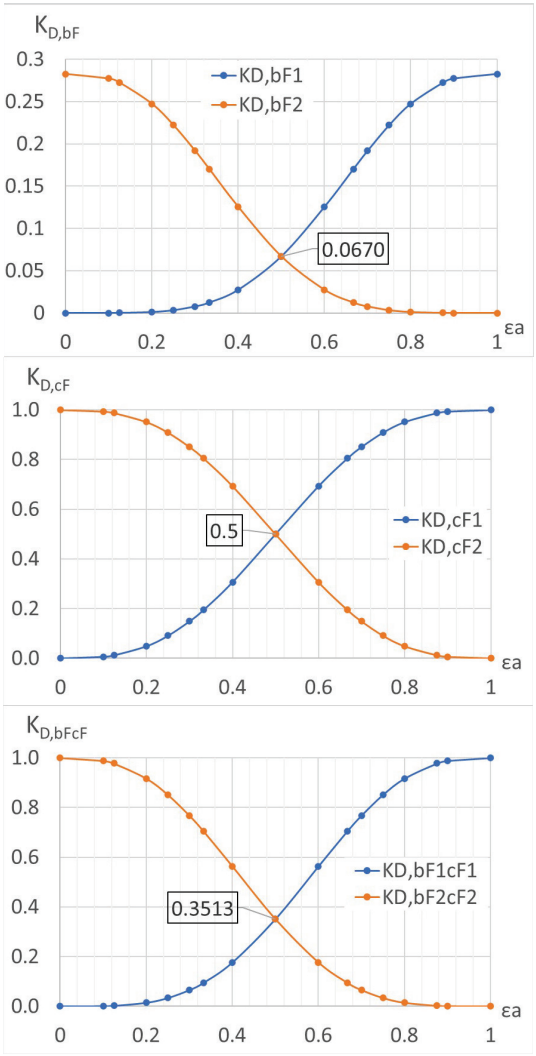


Figure 5. Design charts for the K_D coefficients for a piecewise linear bending moment diagram

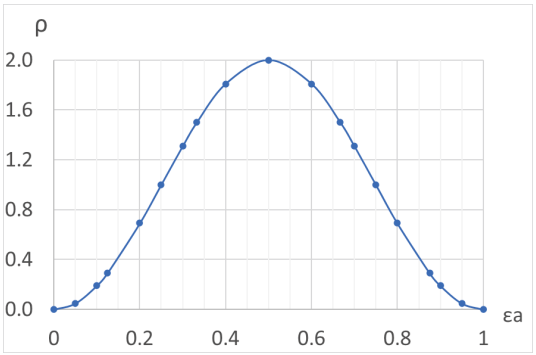
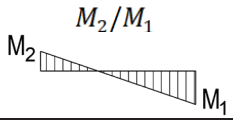


Figure 6. Design chart for the parameter ρ for a piecewise linear bending moment diagram

1.3. Linear moment diagram (Fig. 3, c)

The coefficients C_I, C_{II} and C_{III} are determined as a function of the end-moment ratio M_2 / M_1 and presented in Table 4 and Fig. 7.

Table 4. Coefficients C_I, C_{II} and C_{III} for a linear moment diagram without kinks

M_2/M_1 	C_I	C_{II}	C_{III}
-1	2.765	0	0
-0.5	2.711	0	0.678
-0.25	2.284	0	0.856
0	1.881	0	0.94
0.25	1.564	0	0.977
0.5	1.324	0	0.993
1	1	0	1

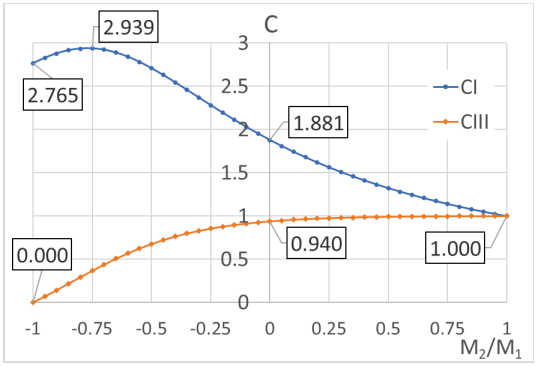


Figure 7. Design charts for the C_I, C_{II} and C_{III} coefficients for a linear moment diagram

1.4. Piecewise linear moment diagram with two or more kinks (Fig. 3, d)

The following initial design data are specified: M_{max} is the maximum moment within the span (at one of the kinks); M_1, M_2 are the support moments (M_1 is the larger of the support moments in absolute value ($|M_1| \geq |M_2|$)).

A piecewise linear bending moment diagram with two or more kinks within the span is reduced to an equivalent non-linear diagram.

For this purpose, the mid-span moment value M_{mid} on the equivalent parabolic bending moment diagram is determined by the formula:

$$M_{mid} = \frac{M_1 \cdot (4\varepsilon_{M\max} - 3) + M_2 \cdot (4\varepsilon_{M\max} - 1)}{8\varepsilon_{M\max} - 1}$$

where ε_{Mmax} is the relative coordinate of the maximum moment (from the end with moment M_1).

The subsequent calculation is performed in accordance with Section 2.1 as for a non-linear bending moment diagram.

II. Support-zone buckling mode

The following bending moment diagram configurations are considered (Fig. 8):

2.1. Non-linear moment diagram.

2.2. Piecewise linear moment diagram.

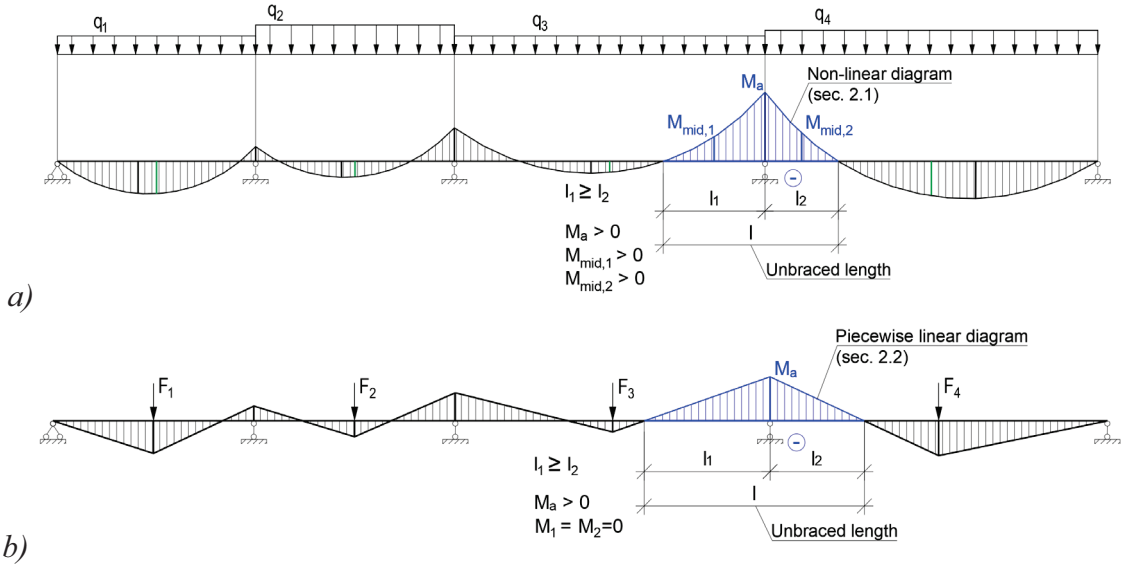


Figure 8. Support-zone buckling mode. Design models for various configurations of the bending moment diagram: a) non-linear; b) piecewise linear with a single kink

2.1. Non-linear moment diagram (Fig. 8, a).
Input data: l_1, l_2 are the lengths of the beam segments with the bottom flange in compression ($l_1 \geq l_2$); M_a is the bending moment at the support; $M_{mid,1}$ and $M_{mid,2}$ are the bending moments at the midpoint of the 1st and 2nd segment correspondingly; $l = l_1 + l_2$ is the equivalent unbraced length; $\varepsilon_a = l_1 / l$ is the relative coordinate.
The coefficients C_I, C_{II} and C_{III} are:

$$C_I = \frac{K_I}{\sqrt{D_B}}, C_{II} = \frac{\rho}{\sqrt{D_B}}, C_{III} = \frac{C_B}{\sqrt{D_B}}$$

where $K_1 = (1-\varepsilon_a)\cdot\varepsilon_a$

$$\rho = \frac{8\cdot(1-\varepsilon_a)\cdot(M_{mid,1} + M_{mid,2} - M_a)}{M_a}$$

Parameter D_B

$$D_B = \left(\frac{\varepsilon_a^4}{5} - \frac{\varepsilon_a^2}{\pi^2} + \frac{3}{2\pi^4}\right)\cdot\frac{4M_{L1}^2}{M_a^2}\cdot\frac{(1-\varepsilon_a)^2}{\varepsilon_a} +$$
$$+\left(\frac{(1-\varepsilon_a)^3\cdot\varepsilon_a}{5} - \frac{(1-\varepsilon_a)^2}{\pi^2} + \frac{3}{2\pi^4}\right)\cdot\frac{4M_{L2}^2}{M_a^2}\cdot\varepsilon_a +$$
$$+\left(\frac{\varepsilon_a^3}{2} - \frac{3\varepsilon_a}{2\pi^2}\right)\cdot\frac{2M_{L1}M_{D1}}{M_a^2}\cdot(1-\varepsilon_a)^2 +$$
$$+\left(\frac{(1-\varepsilon_a)^3\cdot\varepsilon_a}{2} - \frac{3(1-\varepsilon_a)^2}{2\pi^2}\right)\cdot\frac{2M_{L1}M_{D1}}{M_a^2}\cdot\varepsilon_a +$$
$$+\left(\frac{\varepsilon_a^3}{3} - \frac{\varepsilon_a}{2\pi^2}\right)\cdot\frac{M_{D1}^2}{M_a^2}\cdot(1-\varepsilon_a)^2 +$$
$$+\left(\frac{(1-\varepsilon_a)^2\cdot\varepsilon_a}{3} - \frac{(1-\varepsilon_a)}{2\pi^2}\right)\cdot\frac{M_{D2}^2}{M_a^2}\cdot\varepsilon_a\cdot(1-\varepsilon_a)$$

Parameter C_B

$$C_B = \frac{\varepsilon_a\cdot(1-\varepsilon_a)}{2}\cdot\left(\frac{M_{D1}}{M_a}\cdot\varepsilon_a + \frac{M_{D2}}{M_a}\cdot(1-\varepsilon_a)\right) +$$
$$+\left(\frac{\varepsilon_a^2}{3} + \frac{1}{2\pi^2}\right)\cdot\frac{2M_{L1}}{M_a}\cdot(1-\varepsilon_a) +$$
$$+\left(\frac{(1-\varepsilon_a)\cdot\varepsilon_a}{3} + \frac{1}{2\pi^2}\right)\cdot\frac{2M_{L2}}{M_a}\cdot(1-\varepsilon_a)$$

The values of the moments are calculated:

$$M_{D1} = 4M_{mid,1} - M_a,\ M_{D2} = 4M_{mid,2} - M_a;$$
$$M_{L1} = M_a - 2M_{mid,1},\ M_{L2} = M_a - 2M_{mid,2}$$

2.2. Piecewise linear moment diagram (Fig. 8, b). The coefficients C_I, C_{II} and C_{III} are:

$$C_I = \sqrt{\frac{\varepsilon_a}{(0.333\cdot\varepsilon_a - 0.101)}}, C_{II} = 0, C_{III} = 0.5C_I$$

where $\varepsilon_a = l_1 / l$ is the relative coordinate; l_1, l_2 are the lengths of the beam segments adjacent to the support where the bottom flange is in compression (where $l_1 \geq l_2$); $l = l_1 + l_2$ is the equivalent unbraced length.
To identify the governing lateral-torsional buckling mode, the minimum buckling load factor k_{buckl} among those calculated for the different modes must be determined: $k_{buckl} = \frac{M_{cr}}{M_{\max}}$,
where M_{max} is the maximum moment in the span for a mid-span mode and the moment at the support $M_{\max} = M_a$ for a support-zone mode.

5. FINITE ELEMENT VERIFICATION

A lateral-torsional buckling analysis of the continuous beam (Fig. 9) is performed using the developed method. To verify the procedure, a finite element buckling analysis of the beam was performed using the FEMAP software suite. The beam model was built using 4-node shell elements (CQUAD4). The linear elastic buckling analysis was carried out via the Nas-

tran solver using Solution 105 (SOL 105), which determines the critical loads by solving a generalized eigenvalue problem. The SOL 105 solver evaluates the ideal elastic stability (bifurcation buckling). It does not account for the following factors: initial geometric imperfections, residual stresses in the steel due to welding or hot-rolling processes and material non-linearity (plastic deformations and steel yielding).

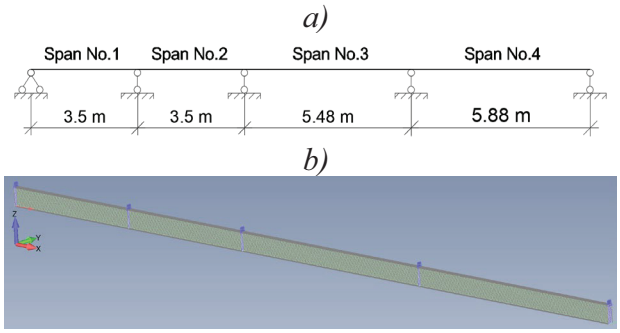


Figure 9. Considered continuous beam a) design model; b) finite element model

Load cases (Fig. 10): 1. L1 – concentrated load F_y=150 kN in each span. 2. L1q – uniformly distributed load q_y=100 kN/m in each span. 3. L2q – uniformly distributed load q_y=100 kN/m in alternative spans (span No. 1 and No. 3).

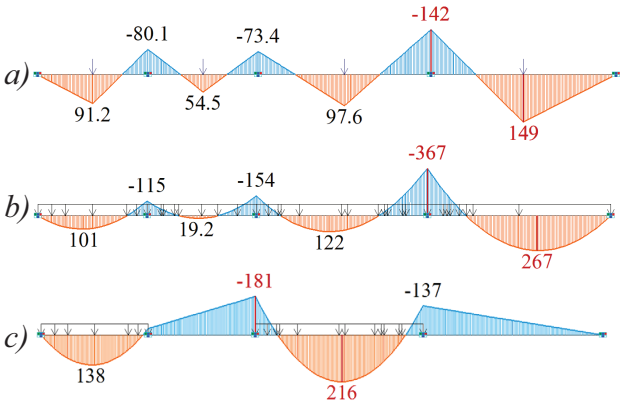


Figure 10. Bending moment diagrams for load case: a) L1; b) L1q; c) L2q

Boundary conditions (Fig. 11). Bottom-flange and top-flange supported beams are considered in the finite element analysis. Various structural configurations of beam supports and bracing are considered, including beams without stiffeners, beams with end bearing stiffeners only, and beams with stiffeners at each support. Double-sided stiffeners with a thickness of 10 mm and a width of 50 mm are modeled.

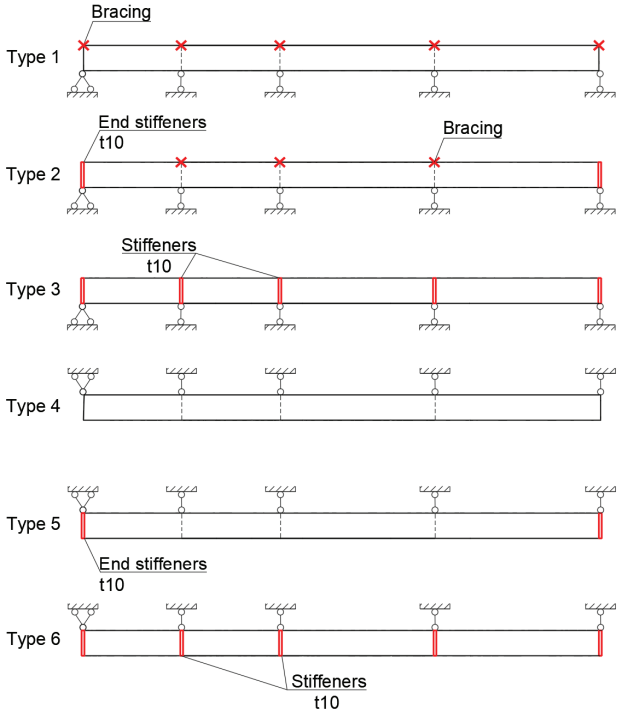


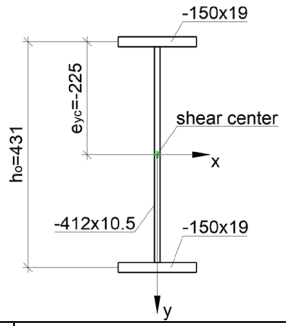
Figure 11. Boundary conditions

For bottom-flange supported beams, lateral bracing at the supports is provided either by stiffeners or by direct lateral restraints applied to the top flange. For beams without bearing stiffeners, the lateral displacement of the top flange at the supports is restricted. No intermediate bracing is provided within the spans.

Tables 5–7 present a comparison of the critical moment values calculated by the proposed method (formula (19)) with the finite element analysis data for the symmetric and monosymmetric I-beams.

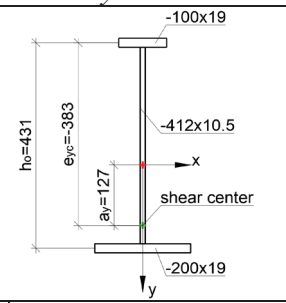
The “FEMAP” column presents the minimum critical moment values obtained from the finite element analysis among all analyzed types of boundary conditions (see Fig. 11).

Table 5. Comparison of Critical Buckling Moments M_{cr}. Symmetric I-beam



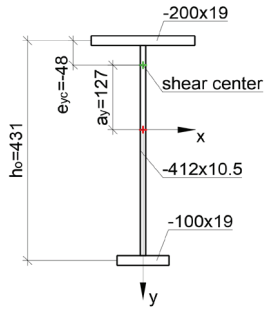
Load case	Span	M_{cr}, kNm (Top flange loaded)		
		Proposed method	FEMAP	Error Δ
L1	No. 1	420	457	8.1%
	No. 2	312	332	6.0%
	No. 3	214	258	17.1%
	No. 4	230	240	4.2%
L1q	No. 1	372	413	9.9%
	No. 2	101	99	-2.0%
	No. 3	151	185	18.4%
	No. 4	199	212	6.1%
L2q	No. 1	407	482	15.6%
	No. 2	852	1048	18.7%
	No. 3	205	226	9.3%
	No. 4	463	614	24.6%
Load case	Span	M_{cr}, kNm (Bottom flange loaded)		
		Proposed method	FEMAP	Error Δ
L1	No. 4	603	635	5.0%
L1q	No. 4	478	496	3.6%
L2q	No. 3	533	652	18.3%
	No. 4	463	617	25.0%

Table 6. Comparison of Critical Buckling Moments M_{cr}. Monosymmetric I-section (type 1)



Load case	Span	M_{cr}, kNm (Top flange loaded)		
		Proposed method	FEMAP	Error Δ
L1	No. 1	227	206	-10.2%
	No. 2	197	196	-0.5%
	No. 3	152	143	-6.3%
	No. 4	156	137	-13.9%
L1q	No. 1	195	191	-2.1%
	No. 2	74	72	-2.8%
	No. 3	106	115	7.8%
	No. 4	133	127	-4.7%
L2q	No. 1	206	225	8.4%
	No. 3	130	126	-3.2%
	No. 4	777	806	3.6%
Load case	Span	M_{cr}, kNm (Bottom flange loaded)		
		Proposed method	FEMAP	Error Δ
L1	No. 4	470	396	-18.7%
L1q	No.1	662	759	12.8%
	No.4	359	300	-19.7%
L2q	No. 1	474	503	5.8%
	No. 3	384	389	1.3%
	No. 4	777	966	19.6%

Table 7. Comparison of Critical Buckling Moments M_{cr}. Monosymmetric I-section (type 2)



Load case	Span	M_{cr}, kNm (Top flange loaded)		
		Proposed method	FEMAP	Error Δ
L1	No. 2	314	325	3.4%
	No. 3	262	312	16.0%
	No. 4	337	330	-2.1%
L1q	No. 1	601	608	1.2%
	No. 2	80	85	5.9%
	No. 3	185	208	11.1%
	No. 4	302	292	-3.4%
L2q	No. 1	729	707	-3.1%
	No. 2	441	569	22.5%
	No. 3	318	363	12.4%
	No. 4	315	372	15.3%
Load case	Span	M_{cr}, kNm (Bottom flange loaded)		
		Proposed method	FEMAP	Error Δ
L1	No. 4	667*	737	9.5%
L1q	No. 4	1027*	1066	3.7%
L2q	No. 2	441	584	24.5%
	No. 4	315	375	0.16

* support-zone buckling mode, M_{cr} is the moment at the support

On average, the calculation error is 12% on the safe side (positive values). The maximum error of the proposed method does not exceed 25%, remaining strictly conservative. Overestimation of the buckling capacity across all cases is limited to less than 10%. The analytically calculated M_{cr} values are obtained assuming no restraints at the ends of the unbraced lengths (μ=1). These results can be refined by taking into account warping and lateral restraints using the effective length factor μ<1.

6. DISCUSSION

The critical buckling moment value M_{cr} is determined when calculating according to the developed method (formula (19)).

For profiles where the load acts along the major principal axis of inertia (i.e. $\alpha_0 = 0$, $k_\alpha = 1$ and $\beta_{res} = \beta_y$), the equation for the critical moment is expressed as follows:

$$M_{cr} = \frac{\pi^2 EI_y}{(\mu l)^2} \cdot C_1 \cdot \left(\left(C_{III} \cdot \beta_y + \frac{e_{y,c}}{2\pi^2} \cdot C_{II} \right) + \sqrt{\left(C_{III} \cdot \beta_y + \frac{e_{y,c}}{2\pi^2} \cdot C_{II} \right)^2 + \frac{I_\omega}{I_y} + \frac{GI_t}{\pi^2 EI_y} \cdot (\mu l)^2} \right) \quad (20)$$

The actual LTB capacity of a beam, considering the structural configuration of its support joints, typically exceeds the analytical solution obtained from an idealized model with free warping boundaries [18, 21] as also demonstrated by the results of the present study (Tables 5–7). To account for the end restraints the effective-length factor μ is provided in the proposed methodology. Future studies aim to evaluate and recommend effective length factors for various boundary conditions to enhance the accuracy of the methodology.

According to the Russian steel design code SP 16.13330.2017, the lateral-torsional buckling analysis of flexural members is performed using the formula: $\frac{M_x}{\varphi_b W_{x,c} R_y \gamma_c} \le 1$,

where $W_{x,c}$ is the section modulus of the compression flange; $\varphi_b = \frac{\sigma_{cr}}{R_y}$ is the LTB reduction factor which relates the critical buckling stress σ_{cr} to the design yield strength of the steel R_y.

To adapt the proposed method to the verification format of SP 16.13330.2017, the critical stresses can be expressed: $\sigma_{cr} = \frac{M_{cr}}{W_{x,c}}$,

where M_{cr} is the critical buckling moment (for the mid-span mode M_{cr} is the maximum moment in the span; for the support-zone mode it is the moment at the support).

7. CONCLUSIONS

Based on theoretical and numerical investigations, and taking into account available experimental data, a practical method for the lateral-torsional buckling analysis of thin-walled beams with open asymmetric cross-sections has been developed. The method is applicable to both simply supported and continuous beams. The key outcomes, assumptions, and future prospects of this research are summarized below:

1. Elastic lateral-torsional buckling is considered.
2. Uniaxial bending within the major principal plane of inertia is considered as the primary case. An analytical solution for biaxial bending is also provided, which is relevant for sections where web-plane loads induce unsymmetrical bending (for example Z-profile).
3. Transverse loads passing through the shear center are considered to eliminate pre-buckling torsion. For eccentric loading, the induced torque makes the serviceability limit state criteria decisive. Due to the low torsional stiffness of open thin-walled sections, the twist angle exceeds the limiting value well before reaching the critical buckling load [17, 18].
4. Channels and similar cross-sections with the shear center located outside the profile are analyzed assuming the load acts centrally. This approach accounts for the structural conditions of

load transfer across the entire flange width. However, a serviceability limit state criteria check must be conducted in addition to the buckling stability assessment

5. The scientific novelty of the research lies in:

- the analytical determination of the C_I, C_{II} and C_{III} coefficients derived directly from the differential buckling equations;
- the derivation of formulas for analyzing thin-walled beams under unsymmetrical bending.

6. The primary advantages of the proposed methodology are as follows:

- versatility across various cross-sectional shapes, arbitrary loading scenarios, and boundary conditions;
- comprehensive consideration of actual bending moment diagrams, load application heights, load directions, and cross-sectional asymmetry;
- compliance with the standard verification formats of SP 16.13330 ensuring seamless integration into national design codes.

7. Future research will focus on the following:

- investigation of end restraint stiffness under actual structural configurations of beam support joints and intermediate braces;
- refinement of the effective-length factor values to account for warping, bending, and lateral restraints at the ends of the unbraced length;
- analysis of the effects of plastic deformations, initial imperfections [22], and residual stresses;
- development of design recommendations for the buckling stability assessment of steel columns and rafters within tapered frames [23];
- implementation of the methodology into a software package, including its application within digital standards and design codes.

REFERENCES

1. **Timoshenko S.P.** (1955) *Ustojchivost' uprugikh sistem* [Stability of elastic systems]. Moscow: Gostekhizdat. (in Russian)
2. **Bleich F.** (1952) *Buckling strength of metal structures*, New York: McGraw-Hill.
3. **White D.V., Jung S.-K**. (2003) *Simplified Lateral Torsional Buckling Equations for Singly-Symmetric I-Section Members*, Structural Engineering, Mechanics and Materials Report No. 03-24b, School of Civil and Environmental Engineering, Georgia Insitutute of Technology, Atlanta, GA
4. **Ziemian R. D.** (2010) *Guide to stability design criteria for metal structures (6th ed.)*. John Wiley & Sons, Inc.
5. **Clark J.W., Hill H.N.** (1960) Lateral Buckling of Beams. *Journal of the Structural Division*, vol. 86, pp. 175-196. doi: 10.1061/JSDEAG.0000540
6. **Andrade A., Camotim D., Costa P.P.** (2007) On the evaluation of elastic critical moments in doubly and singly symmetric I-section cantilevers. *Journal of Constructional Steel Research*, vol. 63 (7), pp. 894–908. doi: 10.1016/j.jcsr.2006.08.015
7. **Bureau A.**, NCCI: Elastic critical moment for lateral torsional buckling. In SN003a-EN-EU NCCI
8. **Boissonade N., Greiner R., Jaspart J. P.** Rules for Member Stability in EN 1993-1-1: Background documentation and design guidelines. (ECCS, Brussels, 2006)
9. **Mathew D.B., Girija K., Nazeer M., Anagha N., Vengadesh J. K. V.** (2024) Experimental and numerical analysis of lateral–torsional bucklingbehaviour of monosymmetric simply supported beam. *Asian Journal of Civil Engineering*, vol. 25, pp. 2471-2482. doi: 10.1007/s42107-023-00920-x.
10. **Mohri F., Brouki A., Roth J.C.** (2003) Theoretical and numerical stability analyses of unrestrained, mono-symmetric thin-walled beams. *Journal of Constructional Steel Research,* vol. 59 (1), pp. 63-90. doi: 10.1016/S0143-974X(02)00007-X.
11. **Mathew D. B., Vengadesh J. K. V., Nazeer M.** (2022) Influence of moment modification factor in lateral torsional buckling of doubly and monosymmetric sections. Proceedings of the *12th Structural Engineering Convention—An International Event (SEC 2022), ASPS Conference Proceedings (Jaipur, India, December 19-22,*

2022), vol. 1, pp. 427–433. doi:10.38208/acp.v1.530.
12. **Bijak R.** (2019) Lateral-torsional buckling moment of simply supported unrestrained monosymmetric beams. *IOP Conference Series: Materials Science and Engineering*, vol. 471 (3), 032074. doi:10.1088/1757-899X/471/3/032074.
13. **Hauksson H., Vilhjalmsson J.B.** (2014) *Lateral-torsional Buckling of Steel Beams with Open Cross Section: Elastic Critical Moment Study and Software Application* (Master's Thesis), Gothenburg: Chalmers University of Technology.
14. **Farfel M.I., Gukova M.I., Svyatoshenko A.E.** (2022) Obshchaya ustoychivost' balok dvutavrovogo postoyannogo secheniya. Razvitie raschetnykh polozheniy [Total stability of two constant section beams. Development of payment provisions]. *Structural Mechanics and Analysis of Constructions,* no. 1, pp. 4–13. doi: 10.37538/0039-2383.2022.1.4.13
15. **Ilyushenkov A.O.** (2025) Razvitie inzhenernoy metodiki rascheta ustoychivosti ploskoy formy izgiba dvutavrovoy balki [Development of engineering methodology for calculating the plane bending stability of an I-beam]. *Bulletin of Science and Research Center of Construction*, vol. 46 (3), pp. 22-42. doi: 10.37538/2224-9494-2025-3(46)-22-42.
16. **Белый Г.И.** Деформационный расчет и устойчивость стержневых элементов стальных конструкций с несимметричным сечением // Вестник гражданских инженеров. 2021. № 4 (87). С. 44-54. doi: 10.23968/1999-5571-2021-18-4-44-53
17. **Туснин А.Р.** Расчет и проектирование конструкций из тонкостенных стержней открытого профиля: дис. … докт. техн. наук. М., 2003. 427 с
18. **Туснина О.А.** Анализ общей устойчивости швеллера при изгибе (2025) Сборник докладов V Национальной научной конференции (г. Москва, 16 декабря 2024 г.)
19. **Vlasov V.Z.** (1959) *Tonkostennye uprugie sterzhni* [Thin–walled elastic members]. Moscow: Fizmatgiz. (in Russian)
20. **Kitipornchai S., Wang C.M., Trahair N.S.** (1986) Buckling of monosymmetric I-beams under moment gradient. *Journal of the Structural Division*, vol. 112 (ST4), pp 781-799. doi: 10.1061/(ASCE)0733-9445(1986)112:4(781)
21. **Lebastard M., Couchaux M., Santana M.V.B., Bureau A., Hjiaj M.** (2022) Elastic lateral-torsional buckling of beams with warping restraints at supports. *Journal of Constructional Steel Research*, vol. 197, 107410. doi: 10.1016/j.jcsr.2022.107410.
22. **Abu Reden G.A., Adany S.** (2025) Elastic lateral-torsional buckling of single-span doubly symmetric I-section beams with intermediate discrete lateral support considering prebuckling deflections. *Thin-Walled Structures*, vol. 212, 113179. doi: 10.1016/j.tws.2025.113179.
23. **Katyushin V.V.** (2018) Zdaniya s karkasami iz stal'nykh ram peremennogo secheniya [Buildings with frames made of tapered steel members]. Moscow: ASV (in Russian).

СПИСОК ЛИТЕРАТУРЫ

1. **Тимошенко С.П.** Устойчивость упругих систем. – М.: Гостехиздат, 1955. – 567 с.
2. **Блейх Ф.** Устойчивость металлических конструкций. – М.: Физматгиз, 1959. – 544 с.
3. **White D.V., Jung S.-K.** Simplified Lateral Torsional Buckling Equations for Singly-Symmetric I-Section Members, Structural Engineering, Mechanics and Materials Report No. 03-24b, School of Civil and Environmental Engineering, Georgia Insitutute of Technology, Atlanta, GA, 2003
4. **Ziemian R.D.** Guide to stability design criteria for metal structures (6th ed.). John Wiley & Sons, Inc., 2010

5. **Clark J.W., Hill H.N.** Lateral Buckling of Beams // Journal of the Structural Division, 1960, Vol. 86, pp. 175-196. doi: 10.1061/JSDEAG.0000540
6. **Andrade A., Camotim D., Costa P.P.** (2007) On the evaluation of elastic critical moments in doubly and singly symmetric I-section cantilevers // Journal of Constructional Steel Research, 2007, Vol. 63 (7), pp. 894–908. doi: 10.1016/j.jcsr.2006.08.015
7. **Bureau A.**, NCCI: Elastic critical moment for lateral torsional buckling. In SN003a-EN-EU NCCI
8. **Boissonade N., Greiner R., Jaspart J. P.** Rules for Member Stability in EN 1993-1-1: Background documentation and design guidelines. (ECCS, Brussels, 2006)
9. **Mathew D.B., Girija K., Nazeer M., Anagha N., Vengadesh J. K. V.** Experimental and numerical analysis of lateral–torsional bucklingbehaviour of monosymmetric simply supported beam // Asian Journal of Civil Engineering, 2024, Vol. 25, pp. 2471-2482. doi: 10.1007/s42107-023-00920-x.
10. **Mohri F., Brouki A., Roth J.C.** Theoretical and numerical stability analyses of unrestrained, mono-symmetric thin-walled beams // Journal of Constructional Steel Research, 2003, Vol. 59 (1), pp. 63-90. doi: 10.1016/S0143-974X(02)00007-X.
11. **Mathew D. B., Vengadesh J. K. V., Nazeer M.** (2022) Influence of moment modification factor in lateral torsional buckling of doubly and monosymmetric sections // Proceedings of the 12th Structural Engineering Convention—An International Event (SEC 2022), ASPS Conference Proceedings (Jaipur, India, December 19-22, 2022), vol. 1, pp. 427–433. doi:10.38208/acp.v1.530.
12. **Bijak R.** Lateral-torsional buckling moment of simply supported unrestrained monosymmetric beams // IOP Conference Series: Materials Science and Engineering, 2019, Vol. 471 (3), 032074. doi:10.1088/1757-899X/471/3/032074.
13. **Hauksson H., Vilhjalmsson J.B.** Lateral-torsional Buckling of Steel Beams with Open Cross Section: Elastic Critical Moment Study and Software Application (Master's Thesis), 2014, Gothenburg: Chalmers University of Technology
14. **Фарфель М.И., Гукова М.И., Святошенко А.Е.** Общая устойчивость балок двутаврового постоянного сечения. Развитие расчетных положений // Строительная механика и расчет сооружений, 2022, № 1. С. 4–13. doi: 10.37538/0039-2383.2022.1.4.13
15. **Ильюшенков А.О.** Развитие инженерной методики расчета устойчивости плоской формы изгиба двутавровой балки // Вестник НИЦ «Строительство», 2025, Том 46, № 3. С. 22-42. doi: 10.37538/2224-9494-2025-3(46)-22-42.
16. **Белый Г.И.** Деформационный расчет и устойчивость стержневых элементов стальных конструкций с несимметричным сечением // Вестник гражданских инженеров, 2021, № 4 (87). С. 44-54. doi: 10.23968/1999-5571-2021-18-4-44-53
17. **Туснин А.Р.** Расчет и проектирование конструкций из тонкостенных стержней открытого профиля: дис. … докт. техн. наук. М., 2003. 427 с
18. **Туснина О.А.** Анализ общей устойчивости швеллера при изгибе // Актуальные проблемы строительной отрасли и образования: сборник докладов V Национальной научной конференции (г. Москва, 16 декабря 2024 г.). М.: Издательство МИСИ – МГСУ, 2025. С. 84-89.
19. **Власов В.З.** Тонкостенные упругие стержни. – М.: Физматгиз, 1959 – 568 с.
20. **Kitipornchai S., Wang C.M., Trahair N.S.** Buckling of monosymmetric I-beams under moment gradient // Journal of the Structural Division, 1986, Vol. 112 (ST4), pp 781-799. doi: 10.1061/(ASCE)0733-9445(1986)112:4(781)
21. **Lebastard M., Couchaux M., Santana M.V.B., Bureau A., Hjiaj M.** (2022) Elastic lateral-torsional buckling of beams with

warping restraints at supports // Journal of Constructional Steel Research, 2022, Vol. 197, 107410. doi: 10.1016/j.jcsr.2022.107410.

22. **Abu Reden G.A., Adany S.** (2025) Elastic lateral-torsional buckling of single-span doubly symmetric I-section beams with intermediate discrete lateral support considering prebuckling deflections // Thin-Walled Structures, 2025, Vol. 212, 113179. doi: 10.1016/j.tws.2025.113179.
23. **Катюшин В.В.** Здания с каркасами из стальных рам переменного сечения. – М.: Издательствово АСВ, 2018. – 1077 с.

Olga A. Tusnina, candidate of technical sciences, docent, associated professor, Department of Steel and Wooden Structures, National Research Moscow State University of Civil Engineering (NRU MGSU), 26, Yaroslavskoe Shosse, Moscow, 129337, Russia, e-mail: tusninaOA@mgsu.ru

Ольга Александровна Туснина, кандидат технических наук, доцент, доцент кафедры Металлических и деревянных конструкций, Национальный исследовательский Московский государственный строительный университет (НИУ МГСУ), д. 26, Ярославское шоссе, г. Москва, 129337, Россия, e-mail: tusninaOA@mgsu.ru

DOI:10.22337/2587-9618-2026-22-3-175-188

EVALUATION OF THE BUCKLING OF FRAME STRUCTURES UNDER DYNAMIC LOADING, TAKING INTO ACCOUNT THE INERTIAL COMPONENTS OF INTERNAL FORCES

Vladimir N. Sidorov*, *Vadim K. Akhmetov, Dmitriy O. Klimushkin
National Research Moscow State University of Civil Engineering, Moscow, RUSSIA

Abstract: An approach to directly assessing the stability of a flat frame structure under unsteady dynamic loading is proposed and numerically investigated. In contrast to the traditional choice of a single static or quasi-static calculation case, at each step of integrating the equation of motion, an instantaneous stability problem is formed, taking into account the inertial components on the left-hand side of the operator equation and in the local forces that determine the geometric rigidity of the calculation model. The contribution of longitudinal and transverse forces, as well as nodal bending moments in resisting the loss of stability of beam elements of the Timoshenko model, is considered together. The method is implemented in the author's finite element program in Python and compared with the nonlinear quasi-static calculation in the Simulia Abaqus/Standard PC environment using the Riks method (Static, Riks). The buckling resistance of the load-bearing frame structure of an industrial building was studied. Its finite element model includes 246 nodes and 369 finite elements. The equation of motion is solved in the time interval 0 – 129.99 sec with a step of 0.01 sec. Analysis of the entire time history showed the presence of single spectral emissions; after checking the temporal stability of the eigenvalues, the physical minimum of the stability margin factor Λ_{min} (SMF) was established at step 7913 (time t = 79.13 s, Λ_{min} = 25.10992). Additionally, the multimode event at step 4138 and time slices selected based on the maximum displacements of nodes in hazardous areas are considered. For two slices generated using the same exact method, SIMULIA Abaqus confirmed the same ranking: the critical value of the load proportionality factor (LPF) obtained using the Ricks method is 48.21736 for t = 41.38 s and 44.42943 for t = 79.13 s. It is shown that the absolute values of the direct SMF and LPF are not identical due to the difference in the formulations of the problem being solved, but the consistency of the dangerous moment in time confirms the diagnostic value of the proposed method.

Keywords: dynamic stability; frame structure; finite element method; Timoshenko beam; inertial forces; geometric stiffness; stability margin; SIMULIA Abaqus; Riks method

ОЦЕНКА УСТОЙЧИВОСТИ РАМНЫХ КОНСТРУКЦИЙ ПРИ ИХ ДИНАМИЧЕСКОМ НАГРУЖЕНИИ С УЧЁТОМ ИНЕРЦИОННЫХ СОСТАВЛЯЮЩИХ ВНУТРЕННИХ УСИЛИЙ

В.Н. Сидоров*, *В.К. Ахметов*, *Д.О. Климушкин, О.А. Туснина
Национальный исследовательский Московский государственный строительный университет, г. Москва, РОССИЯ

Аннотация. Предложен и численно исследован подход к прямой оценке устойчивости плоской рамной конструкции в процессе нестационарного динамического нагружения. В отличие от традиционного выбора одного статического или квазистатического расчётного случая, на каждом шаге интегрирования уравнения движения формируется мгновенная задача устойчивости, учитывающая инерционные компоненты в левой части операторного уравнения и в локальных усилиях, определяющих геометрическую жёсткость расчетной модели. Вклад продольных и поперечных сил, а также узловых изгибающих моментов при сопротивлении потере устойчивости балочных элементов модели Тимошенко рассматривается совместно. Метод реализован в авторской конечно-элементной программе на Python и сопоставлен с нелинейным квазистатическим расчётом в среде ПК SIMULIA Abaqus/Standard методом

Рикса (Static, Riks). Исследовано сопротивление потере устойчивости несущей рамной конструкции промышленного здания. Ее расчетная конечно-элементная модель включает 246 узлов и 369 стержневых элементов. Уравнение движения решается во временном интервале 0 – 129,99 сек с шагом 0,01 сек. Анализ всей временной истории показал наличие одиночных спектральных выбросов; после контроля временной устойчивости собственных значений физический минимум коэффициента запаса устойчивости Λ_{min} (КЗУ (SMF)) установлен на шаге 7913 (момент времени t = 79,13 с, Λ_{min} = 25,10992). Дополнительно рассмотрено многомодовое событие на шаге 4138 и временные срезы, выбранные по максимумам перемещений узлов в опасных зонах. Для двух срезов, сформированных единым точным способом, SIMULIA Abaqus подтвердил одинаковое ранжирование: полученное методом Рикса критическое значение коэффициента пропорциональности нагрузки (LPF) равен 48,21736 для t = 41,38 с и 44,42943 для t = 79,13 с. Показано, что абсолютные значения прямого КЗУ и LPF не являются тождественными вследствие различия постановок решаемой задачи, однако согласованность опасного момента времени подтверждает диагностическую ценность предложенной методики.

Ключевые слова: динамическая устойчивость; рамная конструкция; метод конечных элементов; балка Тимошенко; инерционные силы; геометрическая жёсткость; коэффициент запаса устойчивости; SIMULIA Abaqus; метод Рикса

INTRODUCTION

The development of the finite element method (FEM) transformed the analysis of complex mechanical systems from a collection of particular analytical problems into a general computational procedure. Following the work of R. Clough, which established the term finite element method [1], variational and matrix formulations of the FEM were developed systematically [2, 3]. In stability analysis, this enabled a transition from individual formulae for assessing the stability of a member with an effective length or of a frame to an eigenvalue problem based on global elastic and geometric stiffness matrices.

Two principal static approaches are used in engineering practice. The first, linear bifurcation analysis, determines eigenvalue load multipliers for an idealised prestressed state. The second, nonlinear analysis, traces the equilibrium path with allowance for large displacements, initial imperfections and, where necessary, material nonlinearity [4]. The latter approach underlies the limit-state design procedures specified in Eurocode 3 [5] and SP 16.13330 [6]. The choice of the initial loading remains essential: a static loading scheme contains no information about the distribution of inertia forces at a particular instant of the system's motion.

Dynamic stability is a broader problem. Classical theory addresses parametric excitation, instability regions and the behaviour of systems with varying coefficients in their differential equations [7]. General criteria for the stability of motion originate in the work of A. M. Lyapunov [8] and the development of energy methods for deformable systems [9]. Modern theories emphasise the distinction between the stability of equilibrium and the stability of motion [10]. In civil engineering structures, this problem arises under wind and aeroelastic actions [11], earthquakes, and impulsive or suddenly applied loads [12].

Commercial finite-element packages provide direct dynamic analysis and, separately, linear or nonlinear stability analysis. However, an algorithmic stability assessment of every instantaneous state along the dynamic time history is generally unavailable. The engineer must therefore select one or more instants in advance, transfer the displacements or equivalent forces to a static model, and then perform a quasi-static analysis. Selecting the instant of maximum displacement of an individual node is convenient, but does not guarantee that it coincides with the minimum overall stability margin of the structure.

The choice of beam-element kinematics also affects the result. Euler–Bernoulli theory neglects shear deformation, whereas S. P. Timoshenko's model accounts for independent cross-section rotation and transverse shear [13]. In dynamic analysis, the representation of elastic

stiffness and inertia forces is important, as is the dissipation model. References [14, 15] proposed matrix forms of internal damping for rod elements consistent with an energy-based formulation.

The foundations of the instantaneous stability problem implemented in this study were formulated in [16, 17, 18]. The authors previously developed the inclusion of contributions from axial forces, bending moments and shear forces in the geometric stiffness of rod systems [19]. Earlier publications associated with the present research described the algorithm and model parameters, but did not include numerical modelling of the time history or a comparison of critical states. The aim of this work is to assess whether the direct dynamic stability margin factor can identify unfavourable instants confirmed by an independent nonlinear quasi-static analysis in Abaqus/Standard [20].

The scientific novelty of the study consists in jointly considering: (1) the inertia operator on the left-hand side of the instantaneous eigenvalue problem; (2) the dynamic components of local internal forces used to define the geometric stiffness of the computational model; (3) the complete set of internal-force components N–Q–M of a rod element in stability analysis; (4) the temporal persistence of the spectrum and rejection of isolated eigenvalues; and (5) comparison of the selected critical instants with Riks-method results obtained for the same spatial distribution of dynamic forces.

1. FORMULATION OF THE DIRECT DYNAMIC STABILITY PROBLEM

The motion of the discrete finite-element system is described by the matrix form of d'Alembert's equation:

$$\mathbf{M}\cdot\ddot{\bar{\mathbf{V}}}(t)+\mathbf{D}\cdot\dot{\bar{\mathbf{V}}}(t)+\mathbf{K}\cdot\bar{\mathbf{V}}(t)=\bar{\boldsymbol{F}}(t), \quad (1)$$

where **M**, **D** and **K** are the global mass, damping and elastic stiffness matrices of the computational model; $\bar{\mathbf{V}}$, $\dot{\bar{\mathbf{V}}}$ and $\ddot{\bar{\mathbf{V}}}$ are the displacement, velocity and acceleration vectors; and $\bar{\boldsymbol{F}}$(t) is the external load vector prescribed as a function of time *t*.

To represent the dynamic contributions, diagonal coefficient matrices are introduced that relate the inertia and dissipative forces to the elastic forces at the corresponding global degrees of freedom:

$$\mathbf{A}_{in}=diag((\mathbf{M}\cdot\ddot{\bar{\mathbf{V}}})_{[i]}:(\mathbf{K}\cdot\bar{\mathbf{V}})_{[i]})=diag((\bar{\mathbf{S}}_{in})_{[i]}:(\bar{\mathbf{S}}_{el})_{[i]}), \quad (2)$$

$$\mathbf{A}_{damp}=diag((\mathbf{D}\cdot\dot{\bar{\mathbf{V}}})_{[i]}:(\mathbf{K}\cdot\bar{\mathbf{V}})_{[i]})=diag((\bar{\mathbf{S}}_{damp})_{[i]}:(\bar{\mathbf{S}}_{el})_{[i]}), \quad (3)$$

The ratios of inertia forces to elastic forces are evaluated only when the denominator is sufficiently large and are subjected to regularisation. This prevents division by near-zero components, but does not replace the subsequent verification of the temporal persistence of the eigenvalue spectrum.

The equation of motion can thus be rewritten in operator form:

$$(\mathbf{A}_{din}+\mathbf{E})\cdot\mathbf{K}\cdot\bar{\mathbf{V}}(t)=\bar{\boldsymbol{F}}(t). \quad (4)$$

where $\mathbf{A}_{din} = \mathbf{A}_{in} + \mathbf{A}_{damp}$, and **E** is the identity matrix. The stability formulation adopts the hypothesis that dissipative forces do not produce a potential contribution that directly changes the critical state [17]. Accordingly, only the inertia operator $\mathbf{A}_{in}$ is retained on the left-hand side of the eigenvalue problem.

The instantaneous stability problem at time t is written as:

$$(\mathbf{A}_{din}+\mathbf{E})\cdot\mathbf{K}\cdot\Phi=\mathbf{K}^{\Gamma}\cdot\Phi\cdot\boldsymbol{\Lambda}, \quad (5)$$

Here $\boldsymbol{\Lambda}$ is the diagonal matrix of stability margin factors, and the columns of Φ describe the corresponding buckling modes. The smallest positive real value $\boldsymbol{\Lambda}_{\min}(t)$ is treated as the

minimum instantaneous stability margin factor of the structure.

The complete geometric stiffness matrix of the computational model is assembled as the sum:

$$\mathbf{K}^{\Gamma} = \mathbf{K}_N^{\Gamma} + \mathbf{K}_M^{\Gamma} + \mathbf{K}_Q^{\Gamma}. \qquad (6)$$

where $\mathbf{K}_N^{\Gamma}$ is the conventional contribution of axial forces, $\mathbf{K}_M^{\Gamma}$ is the contribution of nodal bending moments, and $\mathbf{K}_Q^{\Gamma}$ is the contribution of shear forces. The local internal-force vector of a two-node planar rod element has the form [N_1, Q_1, M_1, N_2, Q_2, M_2]. Only the elastic and inertial contributions are included when forming the dynamic internal forces.

Thus, inertia forces are accounted for both on the left-hand side of (5) and in the internal forces that determine the geometric stiffness matrix $\mathbf{K}^{\Gamma}$ on the right-hand side of the eigenvalue problem. This distinguishes the direct dynamic factor from the proportionality factor of a frozen static load. Figure 1 summarises the comparison procedure.

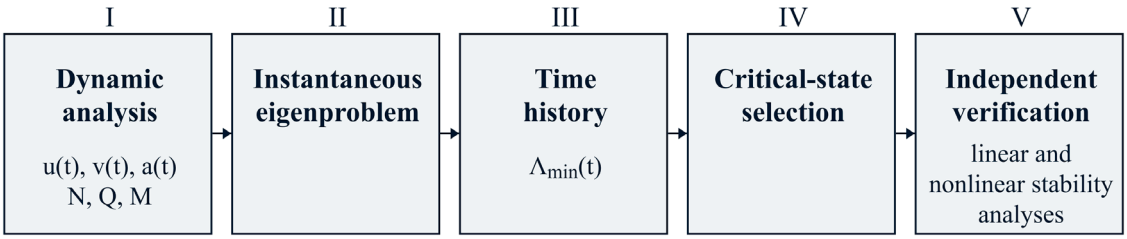


Figure 1. Sequence used to compare the direct dynamic and quasi-static results

2. COMPUTATIONAL MODEL AND NUMERICAL IMPLEMENTATION

2.1. Geometry, Finite Elements, and Material Properties

The stability of a load-bearing planar steel frame of an industrial building was investigated. The frame comprises columns, beams, truss chords and internal working platforms. Its overall dimensions along the coordinate axes are 47.70 × 27.41 m. The finite-element computational model contains 246 nodes and 369 two-node rod elements, with three degrees of freedom per node. Before constraints are applied, the system has 738 degrees of freedom; boundary conditions constrain 27 degrees of freedom at nine nodes. The computational model and control nodes are shown in Figure 2.

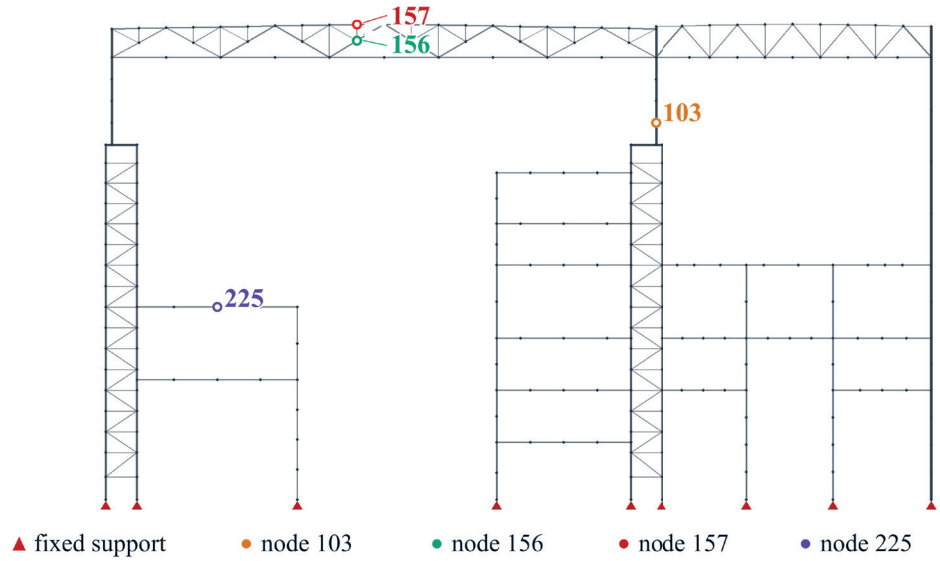


Figure 2. Finite-element model of the investigated frame and control nodes

Inspection of the local element stiffness matrices identified 13 short elements for which the shear contribution resulted in a non-positive-definite local stiffness matrix. Twelve elements were treated using the Euler–Bernoulli model without changing their geometry. One element, 5 mm long, was replaced by a rigid kinematic link between neighbouring nodes. This regularisation preserves the global topology and eliminates artificial local mechanisms.

Table 1. Main parameters of the computational model

Parameter	Adopted value
Model size	246 nodes; 369 elements; 738 nodal degrees of freedom
Overall dimensions	X: −0.05 to 47.65 m; Y: 0 to 27.41 m
Material	E = 210 GPa; ρ = 7850 kg/m³; ν = 0.30; reference yield stress 350 MPa
Cross-sections	15 types; A = 2.12 × 10^{-3} to 5.91 × 10^{-2} m²; I = 2.20 × 10^{-5} to 1.082 × 10^{-2} m⁴
Time grid	Δt = 0.01 s; 13,000 samples; analysis interval 0–129.99 s
Damping	Rayleigh damping ratio ζ = 0.05; calibration against eigenmodes 1 and 111
Stability model	Timoshenko elements; deformed-configuration analysis; N, Q, and M included in the stability equation
Loads	167 components: 130 constant, 28 harmonic, and 9 piecewise-linear
Spectral control	Regularization of ill-conditioned systems; symmetric seven-step temporal window

2.2. Loading and Time Integration of The Equations of Motion

The loading history comprises 167 active components: 92 concentrated and 75 distributed loads. Their time dependence consists of 130 constant, 14 sinusoidal, 14 cosinusoidal and nine piecewise-linear components. Of these, 137 act vertically and 30 horizontally. This time-dependent representation reproduces the combined action of constant operational loads, harmonic actions and transient equipment operating regimes. Representative piecewise-linear load histories applied to the frame are shown in Figure 3.

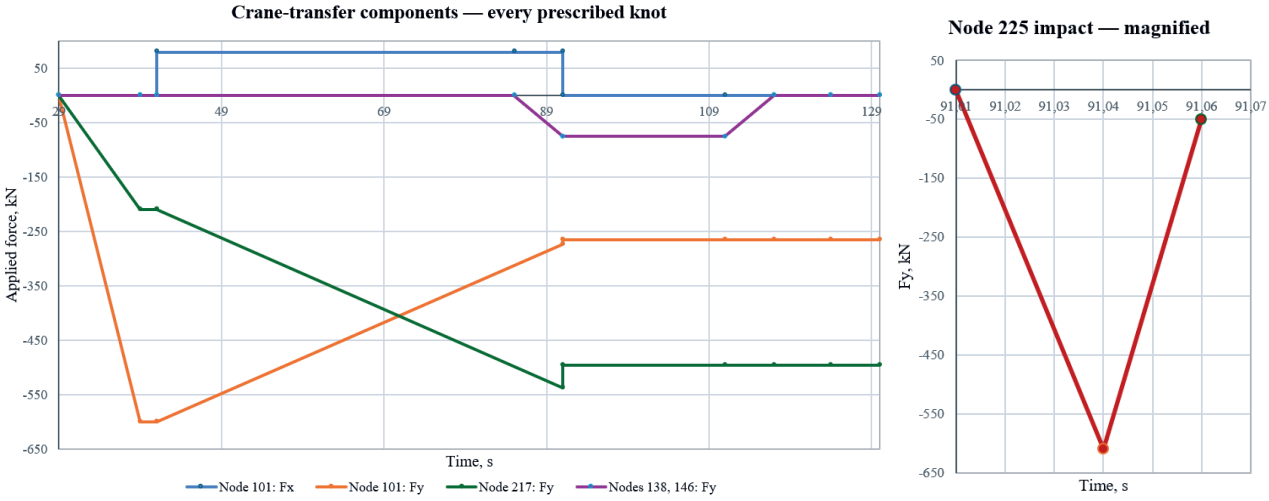


Figure 3. Representative piecewise-linear load histories applied to the frame

Equation (1) is integrated using the Newmark method with a time step of 0.01 s. At each step, a system of linear equations is solved with the following effective coefficient matrix:

$$\mathbf{Z}=\frac{2}{\Delta t^2}\cdot\mathbf{M}+\frac{1}{\Delta t}\cdot\mathbf{D}+\mathbf{K} \quad (7)$$

The acceleration and velocity are then recovered recursively. During direct integration, the nodal coordinates of the computational model are also updated at the new step using the displacements from the previous step. The stiffness, mass and damping matrices are recalculated for the current geometry. The damping coefficients are determined at the first time step and subsequently remain constant.

2.3. Processing of the Stability Spectrum

The eigenvalues are determined for the instantaneous combination of elastic and geometric stiffness. A regularised solution is used when conditioning deteriorates. The final spectrum retains positive, nearly real values associated with physical buckling modes; auxiliary roots are excluded.

A temporal criterion is used to exclude isolated spectral rearrangements: a sequence of neighbouring values and the continuity of the corresponding eigenmodes are examined. The start-up interval is excluded, and the minimum-factor series is additionally processed using a symmetric seven-step window. A physical minimum is identified as a decrease along the same spectral branch that persists over a time interval.

3. QUASI-STATIC ANALYSIS IN SIMULIA ABAQUS

The calculation was performed in Abaqus/Standard using a model assembled from B31 beam elements. An implicit dynamic analysis of the structure is first carried out, and the resulting nodal displacements U, accelerations A and resultant nodal forces are extracted over the prescribed full time interval.

The stability investigation comprised three levels: linear modal analysis, direct implicit dynamic analysis and geometrically nonlinear stability analysis using the Riks method (arc-length method). This combination allows the agreement of mass–stiffness characteristics, dynamic response and limit states to be assessed separately.

The Riks method is an arc-length continuation method for nonlinear equilibrium analysis in the vicinity of a bifurcation. At each increment, the displacement vector and the load multiplier are updated simultaneously, while an additional arc-length constraint defines the step length in load–displacement space. This permits the solution to pass a limit point and trace a descending equilibrium branch, where conventional load control becomes unstable [20, 21].

The maximum load multiplier at the limit point is adopted as the critical result. For the states at t = 41.38 s and t = 79.13 s, the force distributions and deformed geometry were transferred using the same synchronised procedure and used for quantitative comparison. States selected from the displacement maxima of individual nodes were considered additional control cases.

Five states of the dynamic process were used for nonlinear verification: t = 41.38, 41.62, 41.65, 79.13 and 124.04 s. The first and fourth were selected from characteristic values of the global stability factor; the others were selected from displacement maxima at the control nodes. In each case, the static model reproduces the force distribution of the corresponding dynamic state.

The comparison considers the time at which an unfavourable state occurs, the relative ranking of the cases, the critical multiplier and the buckling-mode characteristics. Absolute agreement between the factors is not required, because the direct dynamic and nonlinear quasi-static formulations use different operators.

4. RESULTS

4.1. Minimum Stability Factor Over the Complete Time History

Linear verification was performed by comparing the first ten natural frequencies (Table 2). The mean absolute deviation of the in-house model from Abaqus was 2.87%, and

the maximum deviation was 8.96%. For the first six modes, which are most significant in the dynamic-response range considered, the mean deviation was 1.48%. This confirms the agreement of the global mass and stiffness matrices of the two models.

Table 2. Comparison of the natural frequencies

Mode	In-house model, Hz	Abaqus, Hz	Difference, %
1	0.5931	0.5911	0.34
2	0.8211	0.8265	0.66
3	1.1694	1.1743	0.42
4	1.4475	1.4675	1.36
5	1.7356	1.7630	1.55
6	1.9389	1.9831	2.23
7	2.0621	2.1880	5.75
8	2.3922	2.6275	8.96
9	2.8024	2.9517	5.06
10	3.1217	3.2024	2.52

After isolated spectral rearrangements are excluded, the mean minimum stability margin factor over the working interval is 25.52, the median is 25.61, and the coefficient of variation is 0.899%. A persistent global minimum develops near t = 79.13 s; its lowest original physical value is 25.11. Figure 4 additionally marks only those states for which independent analyses were performed.

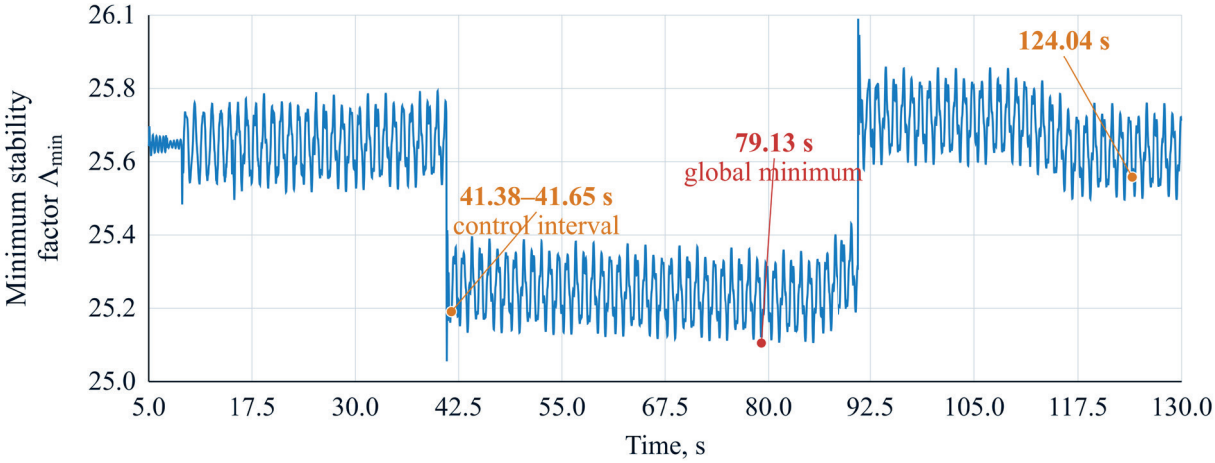


Figure 4. Time history of the minimum stability factor and the investigated states

4.2. Nonlinear Analyses of the Investigated States

At t = 41.38 s, the maximum translational displacement of the dynamic model is 69.994 mm and occurs at node 157. The nonlinear stability analysis yielded a critical load multiplier of 48.217358. After this maximum was reached, a stable descending equilibrium branch developed.

At t = 79.13 s, the maximum translational displacement of node 157 is 71.317 mm, and the critical load multiplier is 44.429428. Thus, relative to the state at t = 41.38 s, both the direct dynamic method and the nonlinear analysis indicate a reduction in the stability margin.

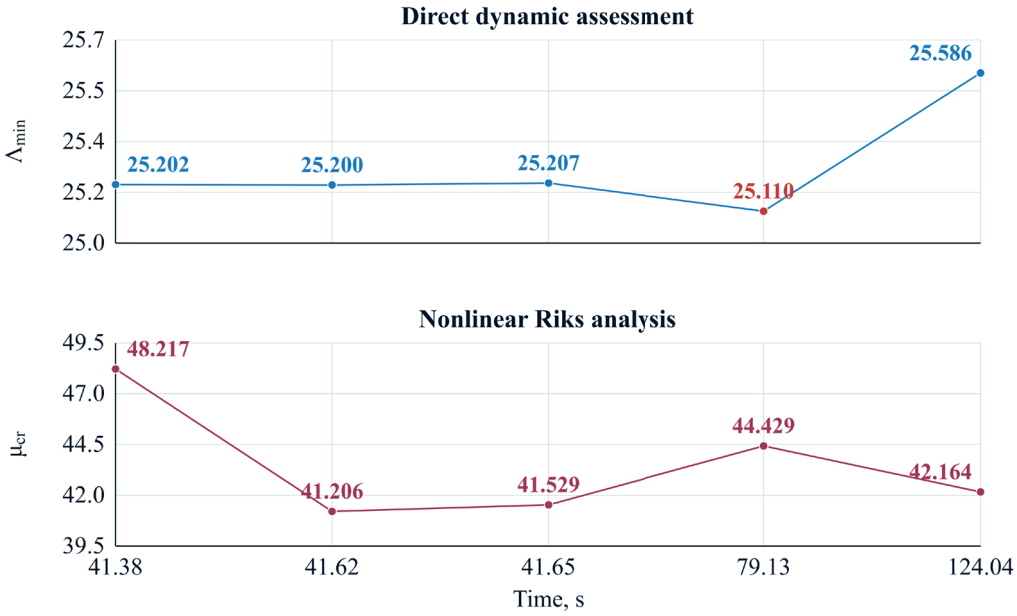


Figure 5. Comparison of the direct and nonlinear stability assessments

The extended series also includes the states at t = 41.62 and 41.65 s, selected from displacement maxima at nodes 103 and 156. Their critical multipliers are 41.206482 and 41.529232, respectively. For the state at t = 124.04 s, the completed analysis reached a critical multiplier of 42.164177 and continued onto a descending branch, ending at 42.103489.

Comparison of the two analyses in Figure 5 shows a mirror-like variation of the principal indicators Λ_{min} (stability margin factor, SMF) and μ_{cr} (load proportionality factor, LPF).

Figures 6–10 show the complete equilibrium paths for the five investigated states. The abscissa gives the translational displacement of the corresponding control node, and the ordinate gives the current load multiplier. All five states, at t = 41.38, 41.62, 41.65, 79.13 and 124.04 s, exhibit a maximum followed by a descending branch. For the state at 124.04 s, the completed calculation establishes the critical multiplier as 42.164177. Large post-critical displacements characterise numerical continuation of the path and are not interpreted as service displacements of the structure.

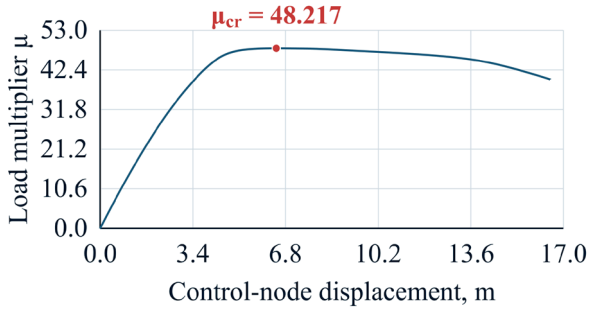


Figure 6. Abaqus equilibrium path obtained by the Riks method at t = 41.38 s (control node 157)

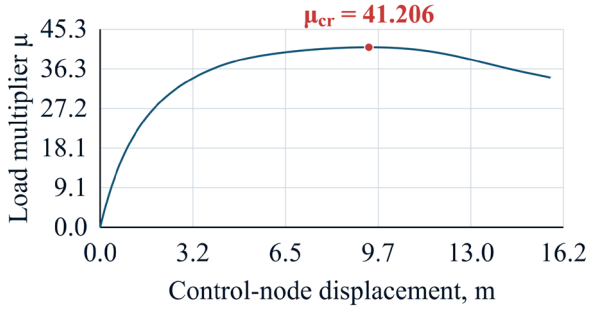


Figure 7. Abaqus equilibrium path obtained by the Riks method at t = 41.62 s (control node 103)

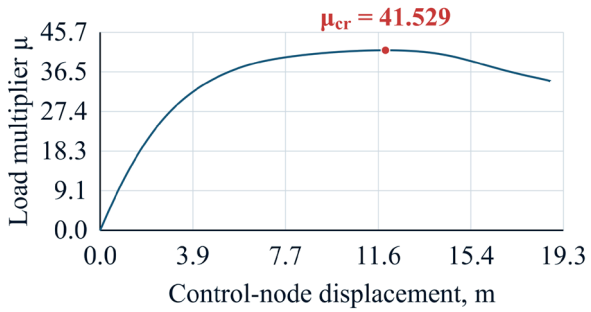


Figure 8. Abaqus equilibrium path obtained by the Riks method at t = 41.65 s (control node 156)

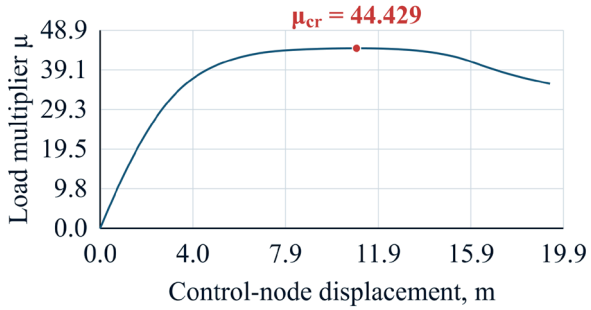


Figure 9. Abaqus equilibrium path obtained by the Riks method at t = 79.13 s (control node 157)

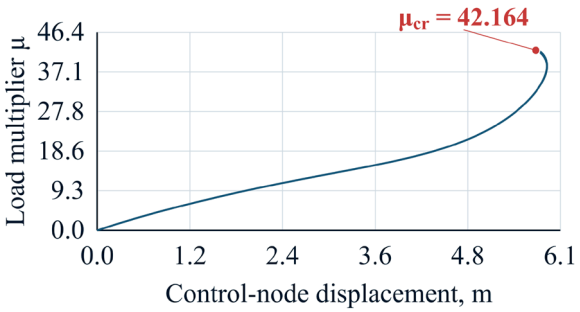


Figure 10. Abaqus equilibrium path obtained by the Riks method at t = 124.04 s (control node 225)

For the two strictly comparable time sections, both methods give the same ranking: the state at t = 79.13 s is more unfavourable than that at t = 41.38 s. The difference between the Python stability margin factors at the two instants is only 0.366%, whereas the corresponding difference in SIMULIA Abaqus is 8.526%. The LPF exceeds the directly calculated SMF by 91.32% at 41.38 s and by 76.94% at 79.13 s (Table 3).

Table 3. Comparison of the direct and nonlinear stability assessments

t, s	Selection criterion	Λ_{min}	μ_{cr}	μ_{cr} higher, %
41.38	Minimum associated with the multimodal response interval	25.202190	48.217358	91.32
41.62	Maximum displacement of node 103	25.246190	41.206482	63.22
41.65	Maximum displacement of node 156	25.261070	41.529232	64.40
79.13	Global minimum of Λ_{min}	25.109920	44.429428	76.94
124.04	Maximum displacement of node 225	25.679420	42.164177	64.19

4.3. Time Sections Associated with Maximum Control-Node Displacements

Quasi-static stability was assessed at time instants selected using a local kinematic criterion from the direct dynamic analysis in SIMULIA Abaqus. This analysis uses Rayleigh damping calibrated against the first and 111th natural frequencies. The extrema of the displacement components at nodes 103, 156 and 225 occur at t = 41.62 s, approximately 41.65 s and 124.04 s, respectively.

At node 103, the maximum U_1 is 29.5477 mm; at node 156, the minimum U_2 is −69.9383 mm; and at node 225, the minimum U_2 is −115.8233 mm.

These states are identified from the single adopted dynamic solution in SIMULIA Abaqus and used as independent control points for quasi-static analysis.

Figure 11 presents fragments of the time histories around the three control extrema. Red points mark the extrema used to select the frozen states. The extrema at nodes 103 and 156 belong to the interval 41.62–41.65 s, whereas the extremum at node 225 occurs during the impulsive change in response at 124.04 s. None of these local kinematic points coincides with the global minimum stability margin factor at 79.13 s.

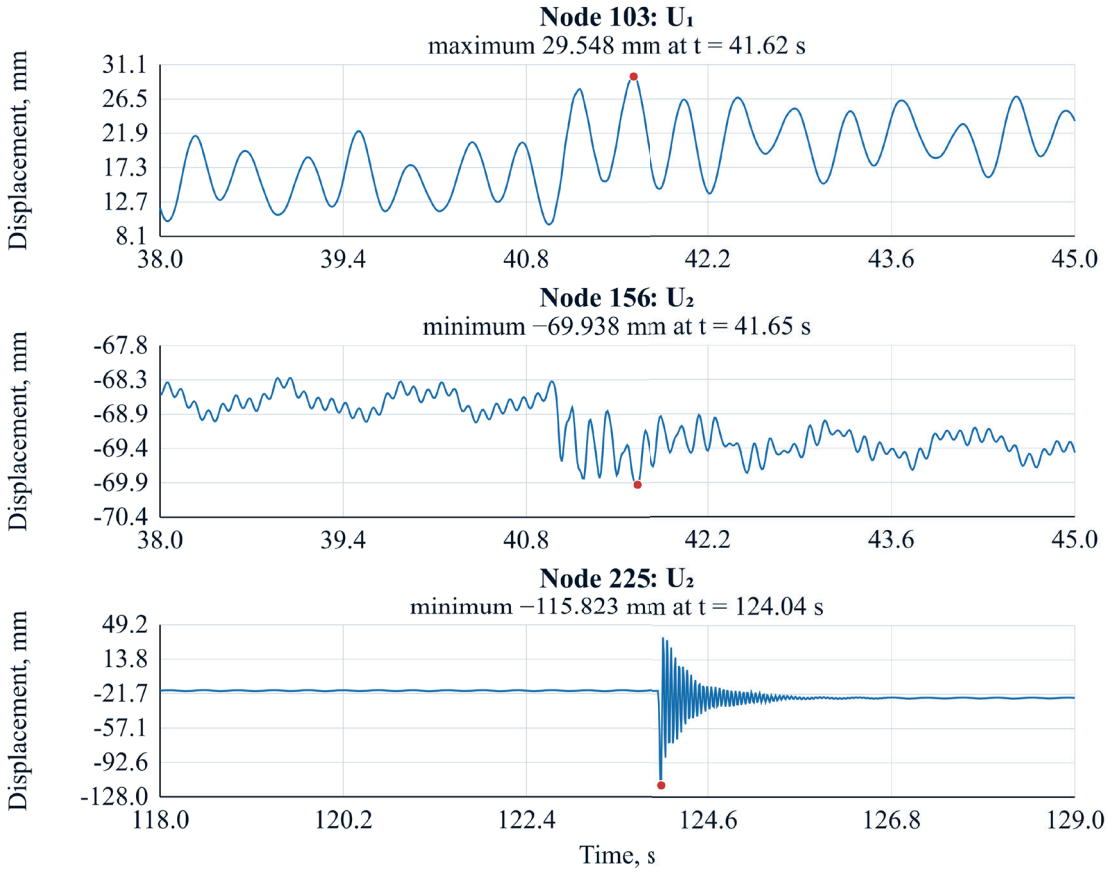


Figure 11. Dynamic response of the Abaqus control nodes with Rayleigh damping calibrated against eigenmodes 1 and 111

5. DISCUSSION

5.1. Interpretation of the Compared Criteria

The proposed factor Λ_{min} and the nonlinear critical multiplier μ_{cr} characterise different mathematical formulations. In the direct method, the inertia contribution simultaneously modifies the instantaneous eigenvalue operator and the local internal forces governing the geometric stiffness of the computational model. In the Riks method, the fixed loading of the selected state is increased proportionally. Their numerical values should therefore be compared in terms of trends and ranking, rather than treating one as a reference value for the other.

The principal comparison criteria are agreement in the unfavourable time interval, ranking of the investigated states and the pattern of change in the stability margin factor. The identical ranking at t = 41.38 and 79.13 s confirms the ability of the proposed direct method to identify the more unfavourable state. Differences across the full series show that incorporating inertia into the instantaneous eigenvalue problem provides information absent from the frozen quasi-static formulation.

5.2. Selection of the Governing Instant

The maximum displacement of an individual node characterises a local kinematic response, whereas Λ_{min} is obtained by solving a global eigenvalue problem for the entire system. The states at t = 41.62, 41.65 and 124.04 s are therefore useful independent control points, but do not replace the search for the minimum stability margin factor over the complete time history. The minimum at t = 79.13 s was found without preselecting a control node.

The resulting series demonstrates the distinction between two ways of selecting an analysis state.

The displacement extrema at nodes 103 and 156 occur within the narrow interval 41.62–41.65 s, whereas the global dynamic minimum occurs substantially later. The proposed method thus extends conventional analysis: it does not discard local control indicators, but supplements them with a global criterion operating over the entire motion trajectory.

5.3. Numerical Robustness and Limitations

Numerical stability of the instantaneous spectrum is an essential part of the direct method. Individual eigenvalues may briefly change order or switch between spectral branches. A physical minimum must therefore be confirmed over a sequence of neighbouring time samples and remain associated with the same eigenmode.

The limitations include linear material elasticity in the direct dynamic model implemented in Python and mixed kinematics for very short beam finite elements. The quasi-static Abaqus model does not include systematic variation of initial imperfections. The Python and Abaqus models use similar, but not identical, methods to form the local finite-element matrices.

Despite these limitations, comparison of the two approaches identifies two robust findings. First, the natural frequencies agree well between the independent models, while the control dynamic extrema in SIMULIA Abaqus provide additional states for nonlinear verification. Second, without preselecting a control node, the direct method identifies an unfavourable time interval and ranks the two principal global states consistently with the nonlinear analysis.

CONCLUSION

- A consistent procedure for instantaneous stability assessment of a frame during time-domain dynamic analysis has been developed. It accounts for inertia forces on the left-hand side of the eigenvalue problem and all local internal-force components N–Q–M.
- Stability of the complete finite-element model of the industrial load-bearing structure, comprising 246 nodes and 369 finite elements, was analysed at 12,498 working time samples with a step of 0.01 s.
- In the adopted direct dynamic analysis in SIMULIA Abaqus, with damping calibrated against the first and 111th natural frequencies, the control extrema were U_1 = 29.5477 mm at node 103 at t = 41.62 s, U_2 = −69.9383 mm at node 156 at t = 41.65 s, and U_2 = −115.8233 mm at node 225 at t = 124.04 s.
- The physical minimum of the first mode occurred at t = 79.13 s, with a stability margin factor $\mathbf{\Lambda}_{min}$ = 25.109920.
- The states at t = 41.38, 41.62, 41.65, 79.13 and 124.04 s were investigated nonlinearly. The critical multipliers were 48.217, 41.206, 41.529, 44.429 and 42.164, respectively. A descending branch was obtained for each state.
- Both methods ranked the two consistently transferred states identically: t = 79.13 s is more unfavourable than 41.38 s. The absolute minimum stability factors differ because of the different approaches to stability analysis and should not be compared as a result and a reference value.
- Selecting a time section solely from the maximum nodal displacement for the Riks method implemented in SIMULIA Abaqus is not a universal procedure.
- Automated identification of an unfavourable instant requires a robust criterion combining median filtering, temporal persistence of the minimum and eigenmode tracking.

The work was supported by the Russian Science Foundation (project No. 25-11-00140).

REFERENCES

1. **Clough R.W.** The finite element method in plane stress analysis. // Proceedings of the 2nd ASCE Conference on Electronic Computation, Pittsburgh, 1960, pp. 345-378.
2. **Zienkiewicz O.C., Taylor R.L.** The Finite Element Method for Solid and Structural Mechanics. 6th ed. Oxford, Butterworth-Heinemann, 2005, 736 pages.

3. **Bathe K.J., Wilson E.L.** Numerical Methods in Finite Element Analysis. Englewood Cliffs, Prentice-Hall, 1976, 528 pages.
4. **Chen W.F., Lui E.M.** Structural Stability: Theory and Implementation. New York, Elsevier, 1987, 608 pages.
5. **EN 1993-1-1:2005.** Eurocode 3: Design of steel structures. Part 1-1: General rules and rules for buildings. Brussels, CEN, 2005, 90 pages.
6. **SP 16.13330.2017.** Steel Structures. Updated Edition of SNiP II-23-81*. Moscow, Standartinform, 2017, 104 pages. (in Russian).
7. **Bolotin V.V.** The Dynamic Stability of Elastic Systems. San Francisco, Holden-Day, 1964, 432 pages.
8. **Lyapunov A.M.** The General Problem of the Stability of Motion. Kharkov, Kharkov Mathematical Society, 1892, 250 pages. (in Russian).
9. **Alfutov N.A.** Fundamentals of the Theory of Stability of Deformable Systems. 2nd ed. Moscow, Mashinostroenie, 1995, 336 pages. (in Russian).
10. **Simitses G.J., Hodges D.H.** Fundamentals of Structural Stability. Burlington, Butterworth-Heinemann, 2006, 389 pages.
11. **Scanlan R.H.** The action of wind on suspension bridges. // Journal of Engineering Mechanics, Volume 117, No. 4, 1991, pp. 813-832. DOI: 10.1061/(ASCE)0733-9399(1991)117:4(813).
12. **Priestley M.J.N., Calvi G.M., Kowalsky M.J.** Displacement-Based Seismic Design of Structures. Pavia, IUSS Press, 2007, 720 pages.
13. **Timoshenko S.P., Gere J.M.** Mechanics of Materials. Moscow, Mir, 1976, 669 pages. (in Russian).
14. **Sidorov V.N., Badina E.S., Detina E.P.** Nonlocal in time model of material damping in composite structural elements dynamic analysis. // International Journal for Computational Civil and Structural Engineering, Volume 17, No. 4, 2021, pp. 14-21. DOI: 10.22337/2587-9618-2021-17-4-14-21.
15. **Sidorov V.N., Badina E.S., Klimushkin D.O.** Modification of the Rayleigh dissipation function for numerical modelling of internal damping in rod structures. // Vestnik MGSU, Volume 19, No. 6, 2024, pp. 960-970. (in Russian). DOI: 10.22227/1997-0935.2024.6.960-970.
16. **Alexandrov A.V., Potapov V.D., Zylev V.B.** Structural Mechanics. Book 2. Dynamics and Stability of Elastic Systems. Moscow, Vysshaya Shkola, 2008, 385 pages. (in Russian).
17. **Alfutov N.A., Kolesnikov K.S.** Stability of Motion and Equilibrium. Moscow, Bauman Moscow State Technical University Press, 2003, 255 pages. (in Russian).
18. **Sidorov V.N., Badina E.S.** The Finite Element Method in Stability and Vibration Problems of Rod Structures: Calculation Examples in Mathcad and MATLAB. Moscow, ASV Publishing House, 2021, 173 pages. (in Russian).
19. **Sidorov V.N., Klimushkin D.O.** Accounting for the complete deformation of rod structural elements in numerical stability analysis. // Proceedings of the International Conference, Saransk, National Research Mordovia State University, 2025, pp. 108-116. (in Russian). ISBN 978-5-7103-4933-5.
20. **Dassault Systèmes SIMULIA Corp.** Abaqus Analysis User's Manual. Version 2024. Providence, RI, Dassault Systèmes SIMULIA Corp., 2024.
21. **Crisfield M.A.** A fast incremental/iterative solution procedure that handles 'snap-through'. // Computers & Structures, Volume 13, No. 1-3, 1981, pp. 55-62. DOI: 10.1016/0045-7949(81)90108-5.

СПИСОК ЛИТЕРАТУРЫ

1. **Clough R.W.** The finite element method in plane stress analysis. // Proceedings of the

2nd ASCE Conference on Electronic Computation, Pittsburgh, 1960, pp. 345-378.
2. **Zienkiewicz O.C., Taylor R.L.** The Finite Element Method for Solid and Structural Mechanics. 6th ed. Oxford, Butterworth-Heinemann, 2005, 736 pages.
3. **Bathe K.J., Wilson E.L.** Numerical Methods in Finite Element Analysis. Englewood Cliffs, Prentice-Hall, 1976, 528 pages.
4. **Chen W.F., Lui E.M.** Structural Stability: Theory and Implementation. New York, Elsevier, 1987, 608 pages.
5. **EN 1993-1-1:2005.** Eurocode 3: Design of steel structures. Part 1-1: General rules and rules for buildings. Brussels, CEN, 2005, 90 pages.
6. **СП 16.13330.2017.** Стальные конструкции. Актуализированная редакция СНиП II-23-81*. М., Стандартинформ, 2017, 104 с.
7. **Bolotin V.V.** The Dynamic Stability of Elastic Systems. San Francisco, Holden-Day, 1964, 432 pages.
8. **Ляпунов А.М.** Общая задача об устойчивости движения. Харьков, Харьковское математическое общество, 1892, 250 с.
9. **Алфутов Н.А.** Основы теории устойчивости деформируемых систем. 2-е изд. М., Машиностроение, 1995, 336 с.
10. **Simitses G.J., Hodges D.H.** Fundamentals of Structural Stability. Burlington, Butterworth-Heinemann, 2006, 389 pages.
11. **Scanlan R.H.** The action of wind on suspension bridges. // Journal of Engineering Mechanics, Volume 117, No. 4, 1991, pp. 813-832. DOI: 10.1061/(ASCE)0733-9399(1991)117:4(813).
12. **Priestley M.J.N., Calvi G.M., Kowalsky M.J.** Displacement-Based Seismic Design of Structures. Pavia, IUSS Press, 2007, 720 pages.
13. **Тимошенко С.П., Гере Дж.М.** Механика материалов. М., Мир, 1976, 669 с.
14. **Sidorov V.N., Badina E.S., Detina E.P.** Nonlocal in time model of material damping in composite structural elements dynamic analysis. // International Journal for Computational Civil and Structural Engineering, Volume 17, No. 4, 2021, pp. 14-21. DOI: 10.22337/2587-9618-2021-17-4-14-21.
15. **Сидоров В.Н., Бадьина Е.С., Климушкин Д.О.** Модификация функции диссипации Рэлея для численного моделирования внутреннего демпфирования в стержневых конструкциях. // Вестник МГСУ, Том 19, № 6, 2024, с. 960-970. DOI: 10.22227/1997-0935.2024.6.960-970.
16. **Александров А.В., Потапов В.Д., Зылев В.Б.** Строительная механика. Книга 2. Динамика и устойчивость упругих систем. М., Высшая школа, 2008, 385 с.
17. **Алфутов Н.А., Колесников К.С.** Устойчивость движения и равновесия. М., Издательство МГТУ им. Н.Э. Баумана, 2003, 255 с.
18. **Сидоров В.Н., Бадьина Е.С.** Метод конечных элементов в задачах устойчивости и колебаний стержневых конструкций. Примеры расчётов в Mathcad и MATLAB. М., Издательство АСВ, 2021, 173 с.
19. **Сидоров В.Н., Климушкин Д.О.** Учёт полного деформирования элементов стержневых конструкций при численном анализе устойчивости. // Материалы международной конференции, Саранск, МГУ им. Н.П. Огарёва, 2025, с. 108-116. ISBN 978-5-7103-4933-5.
20. **Dassault Systèmes SIMULIA Corp.** Abaqus Analysis User's Manual. Version 2024. Providence, RI, Dassault Systèmes SIMULIA Corp., 2024.
21. **Crisfield M.A.** A fast incremental/iterative solution procedure that handles 'snap-through'. // Computers & Structures, Volume 13, No. 1-3, 1981, pp. 55-62. DOI: 10.1016/0045-7949(81)90108-5.

Vladimir Nikolaevich Sidorov – Academician of Russian Academy of Architecture and Construction Science, Dr.Sc, Professor, Head of the Department of Computer Science and Applied Mathematics, National Research University Moscow State University of Civil Engineering, 129337, Russia, Moscow, Yaroslavskoye Shosse,b. 26, Professor of «Building Structures, Buildings and Facilities» Department, Institute of Railway Track, Construction and Structures, Russian University of Transport (MIIT), Professor of Department «Engineering Structures and Numerical Mechanics», Perm National Research Polytechnic University; ORCID: 0000-0001-8812-8022, e-mail: sidorov.vladimir@gmail.com.

Vadim Kayumovich. Akhmetov, Doctor of Science, Professor, Department of Computer Science and Applied Mathematics, Moscow State University of Civil Engineering, 26, Yaroslavskoe Shosse, Moscow, 129337, Russia, e-mail: vadim.akhmetov@gmail.com.

Dmitriy Olegovich Klimushkin – postgraduate student of the Department of Computer Science and Applied Mathematics, National Research University Moscow State University of Civil Engineering; 129337, Russia, Moscow, Yaroslavskoye Shosse,b. 26, e-mail:d.o.klimushkin@gmail.com

Contribution of the authors: all authors made equivalent contributions to the publication.
The authors declare that there is no conflict of interest.

Владимир Николаевич Сидоров — академик РААСН, доктор технических наук, профессор, заведующий кафедрой прикладной математики, Национальный исследовательский Московский государственный строительный университет, Ярославское шоссе, д. 26, Москва, 129337, Россия; ORCID: 0000-0001-8812-80221; e-mail: sidorov.vladimir@gmail.com

Ахметов Вадим Каюмович, доктор технических наук, профессор кафедры информатики и прикладной математики Национального исследовательского Московского государственного строительного университета, 129337, г. Москва, Ярославское шоссе, д. 26, e-mail: vadim.akhmetov@gmail.com

Дмитрий Олегович Климушкин – аспирант кафедры прикладной математики, Национальный исследовательский Московский государственный строительный университет, Ярославское шоссе, д. 26, Москва, 129337, Россия; ORCID: 0009-0007-7147-4595; e-mail: d.o.klimushkin@gmail.com

Вклад авторов: все авторы внесли равноценный вклад в подготовку публикации.
Авторы заявляют об отсутствии конфликта интересов

DOI:10.22337/2587-9618-2026-22-3-189-199

PROBABILISTIC METHOD OF STRUCTURAL RELIABILITY ANALYSIS BY SAMPLING WITH LIMITED STATISTICAL DATA

Sergey A. Solovev, Anastasia A. Soloveva
Vologda State University, Vologda, RUSSIA

Abstract: The article presents an approach to modernizing the data sampling algorithm for structural reliability analysis. This approach enables obtaining more conservative estimates of the failure probability in cases of incomplete or limited statistical data. Numerical examples demonstrate that an incorrect hypothesis regarding the probability distribution type of a random variable in structural reliability problems can lead to estimation errors of up to 5% in the reliability index. Furthermore, neglecting the confidence limits for the parameters of the assumed probability distribution function can result in errors of up to 60% (in a strict mathematical solution). An analysis of scientific and technical publications reveals varying preferred probability distributions for steel yield strength, depending on the steel type and stress-strain conditions. This variability complicates unambiguous selection of a specific probability distribution in real-world tasks during construction site assessments. The proposed data sampling algorithm is based on a modification of the classical Monte Carlo method. It involves selecting a random distribution function and estimating the confidence intervals for its parameters via a bootstrap approach for each generated sample value. The algorithm produces an arbitrary-sized sample containing values representing the lower and upper confidence bounds of the studied parameter. Consequently, the structural element's failure probability is expressed as an interval of values.

Keywords: reliability, probabilistic analysis, safety, sampling, yield strength, failure probability, reliability index, incomplete data

ВЕРОЯТНОСТНЫЙ МЕТОД АНАЛИЗА НАДЕЖНОСТИ СООРУЖЕНИЙ ГЕНЕРАЦИЕЙ ДАННЫХ ПРИ НЕПОЛНОЙ СТАТИСТИЧЕСКОЙ ИНФОРМАЦИИ

С.А. Соловьев, А.А. Соловьева
Вологодский государственный университет, г. Вологда, РОССИЯ

Аннотация: В статье представлен подход к модернизации алгоритма генерации (сэмплинга) данных анализа надежности элементов строительных конструкций, позволяющий получать более достоверные оценки вероятности отказа в случае неполной статистической информации. На численных примерах показано, что неверная гипотеза о типе распределения вероятностей случайной величины в задачах анализа надежности может привести к ошибке в оценке до 5% индекса надежности. В то же время отсутствие учета доверительных границ изменчивости параметров принятой функции распределения вероятностей может привести к ошибкам до 60% (в строгом математическом решении). Анализ научно-технических публикаций показывает различные варианты предпочтительных распределений для предела текучести стали в зависимости от вида стали и условий эксплуатации, что затрудняет принятие однозначного решения о конкретном распределении вероятностей в реальных задачах при обследовании строительных объектов. Предложенный алгоритм генерации данных основывается на модернизации классического метода Монте-Карло и заключается в выборе случайной функции распределения и доверительной оценке ее параметров путем бутстреп-подхода для каждого генерируемого значения выборки. Результатом использования предлагаемого алгоритма является выборка произвольного размера, содержащая значения нижней и верхней доверительной границы значений исследуемого параметра. Вероятность отказа элемента сооружения будет представлена в виде интервала значений.

Ключевые слова: надежность, вероятностный анализ, безопасность, генерация, предел текучести, вероятность отказа, индекс надежности, неполная информация

INTRODUCTION

Reliability is one of the key indicators in substantiating the adopted design decision of the structure. There are many reliability measures, but the failure probability P_f and the reliability index β are most often used in practice of structural design. The calculation of these parameters is based on the principles of probability theory and mathematical statistics.

The fundamental theory of structural reliability in a probabilistic context has been widely developed since the middle of the 20th century [1]. However, the use of many well-developed theoretical provisions faces difficulties in practical application due to limited (incomplete) statistical information and data. It is noted in [2], that "The probability distribution of random variables is usually incomplete owing to a limited amount of data, making it a challenging problem for structural reliability assessments". Modeling of uncertainties in the tasks of assessing and analyzing the reliability of building structures is one of the key problems. As noted in research [3], "despite the highly detailed numerical predictions that can be obtained, these results often do not achieve a satisfactory level of agreement with 'reality', i.e., the actual physical behavior of the considered continuum in the effective operational environment. This discrepancy is caused by epistemic (reducible) and aleatory (caused by variation) uncertainty in the model".

Let's consider a practical problem – the formation of a random variable model for the yield strength of steel of an existing structural steel element. There are several options for selecting a cumulative probability distribution function. In Section 3.02 of Joint Committee on Structural Safety (JCSS) is noted that the log-normal distribution is recommended for yield strength of steel, but bi-modal distributions are preferred in some cases. For the probabilistic description of the yield strength of steel, the normal and lognormal distributions are most often used [4].

Also, an optimal function of probability distribution may change over time and with changing operating conditions. The paper [5] presents the results of studying probability distribution function of yield strength of steel, and it concluded that "the choice of probability distribution for material properties that captures scatter in data over a range of temperatures can influence the simulated structural response" and logistic and beta distribution are suggested. In paper [6], it is noted that "The Shapiro-Wilk test indicates that elastic modulus, yield strength, tensile strength, peak strain, and yield plateau slope of corroded steel with different corrosion loss ratios all fitted the normal distribution".

The authors of research [7] are noted that "according to our experience, the statistic output file is approximated, in the optimal way, by the Hermite four-parameter distribution, which takes into account even the skewness and kurtosis of random yield strength". In the article [8] it is annotated that "the yield stress as well as ultimate steel strength random parameters do not follow a Gaussian distribution".

So, the above literature review shows that there are many possible probabilistic models for the yield strength of steel. The choice of a specific probability distribution function in the real task of structural reliability analysis imposes a certain responsibility on the civil engineer. The problem becomes more complicated when you have to analyze a small statistical sample size. In conditions of limited statistical data, the parameters of the probability distribution functions are confidence intervals. The use of common complexes in which data sampling tasks are solved is based on a specific function with precise parameters. Using the parameters of a sample data set in this case leads to a decrease in the accuracy of the results and a difficult-to-estimate calculation error.

In this study, it is proposed to consider an algorithm for structural reliability analysis with incomplete statistical information, when data is obtained by the new approach of sampling.

METHODS

The key task of probabilistic reliability analysis of structures is the preliminary formation of random variable models that will describe the variability of calculated parameters. As a rule, classical probability distribution functions of random variables known from mathematical statistics and probability theory are used for this purpose. Choosing an unsuitable distribution function can lead to significant errors in estimating the reliability index or the probability of failure. This problem is particularly acute in practical tasks, when statistical samples of only a few dozen values are available based on the results of tests/studies. Let's first analyze how big relative errors can be if an analytical engineer selects a suboptimal probability distribution function or its statistical parameters.

Let us consider the problem of selecting a random variable model for the yield strength of steel based on the results of its tests. Let C255 steel be given, and its statistical characteristics are obtained from the study [9].

The following 30 samples were obtained when sampling values from the normal distribution with parameters: expected value (mean) $\mu_x = 288.18$ MPa and standard deviation $\sigma_x = 20.17$ MPa (the coefficient of variation is 7 percent): $x \in$ {303.49, 293.85, 290.28, 286.92, 272.97, 282.52, 254.03, 286.20, 268.24, 265.92, 291.81, 316.26, 306.70, 256.50, 268.22, 307.16, 268.36, 283.65, 299.27, 268.65, 290.31, 261.27, 276.05, 294.63, 256.05, 297.06, 287.78, 299.32, 292.70, 315.69} MPa.

Let's also assume that the task is to evaluate the reliability index β when a stress equal to the normative value of the yield strength $R_{y,n} = 255$ MPa.

If the true probability distribution function and its exact parameters are known, then the reliability index can be expressed as:

$$\beta = \frac{\mu_x - R_{y,n}}{\sigma_x}. \quad (1)$$

Using eq. (1), it is possible to estimate the true reliability index $\beta = 1.645$ and following no-failure probability $P = \Phi(\beta = 1.645) = 0.95$, where Φ(.) denotes Laplace function (the Z table). But in practice, the probability distribution function and its parameters are unknown in advance.

There are various approaches for choosing the most appropriate probability distribution function for a data sample. For example, the Kolmogorov–Smirnov statistic D_n quantifies a distance between the empirical distribution function of the sample $F_n(x)$ and the cumulative distribution function of the reference distribution $F(x)$ as:

$$D_n = \sup_x \left| F_n(x) - F(x) \right|. \quad (2)$$

The lower the value of the statistic D_n, the more likely it is that the sample values are derived from the function $F(x)$. The critical value of the Kolmogorov-Smirnov statistic for 30 values is $D_{cr} = 0.248$ (with the confidence probability $\alpha = 0.05$) or $D_{cr} = 0.223$ (with the confidence probability $\alpha = 0.10$).

The choice of the optimal distribution for the available statistical data sample is related to the selection of both the probability distribution function and its parameters. The Distribution Fitter App of the MATLAB mathematical software package or the SciPy library of the Python programming language can be used to assign the parameters.

It is possible to obtain following parameters of different types of distributions (Table 1). Using the value of the distribution function at $F(0.05)$, as well as the inverse normal distribution $P = \Phi(\beta)$, it is possible to estimate the non-failure probability and the reliability index β of the yield strength of steel at the point of characteristic value.

The cumulative distribution functions plots are presented in Figure 1.

Table 1. Analysis of different distribution functions for steel yield strength

Type of the probability distribution function	Fitted parameters*	K-S statistics D_n	Reliability index β	ε, %
Normal	$\mu_x = 284.73$ MPa; $\sigma_x = 17.32$ MPa	0.123454	1.716766	4.18
Lognormal	$s = 0.0611$; loc = 0 MPa; scale = $\ln(\mu_x) = 5.6497$ MPa	0.121157	1.716777	4.18
Logistic	$\mu_x = 285.13$ MPa; $S_x = 10.33$ MPa	0.131419	1.632292	0.78
GEV	$c = 0.379$; loc = μ_x =279.422 MPa; scale = σ_x =17.877 MPa	0.121072	1.650278	0.32
Gamma	$a = 268.49$; scale = 1.05 ($\mu_x = 284.3$ MPa; $\sigma_x = 17.34$ MPa)	0.121829	1.732762	5.06

*The parameters fitted in Python using SciPy library

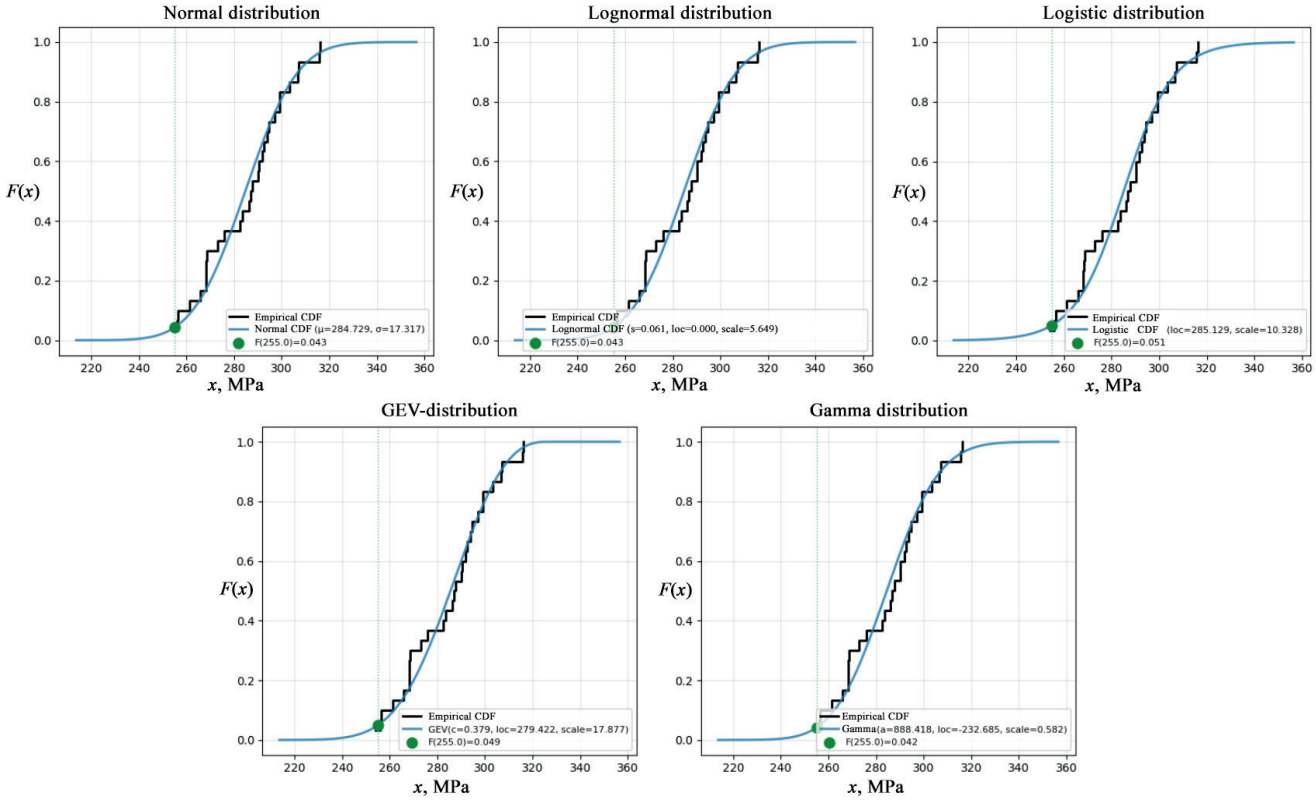


Figure 1. Cumulative distribution functions (CDF) plots of different probability distributions

As can be seen from Table 1, preferred distributions for above sample dataset are Generalized Extreme Value (GEV) with $D_n = 0.121$. The lognormal and gamma distributions also have similar values of Kolmogorov-Smirnov statistics and can be assumed, but in this case the error (which in practice cannot be estimated, since we know the real probability distribution function and parameters only in the current conditional example) would be 4-5%.

Let's assume that an analytical engineer reliably knows the probability distribution function based on a long-term analysis of a random variable at a steel manufacturing plant. According to probability theory and mathematical statistics, the values of the parameters of the general data set can be estimated from a sample population at confidence intervals. Fig. 2 shows the boundaries of the confidence intervals for the mean and standard deviation normal distribution and the above data sample with different confidence levels.

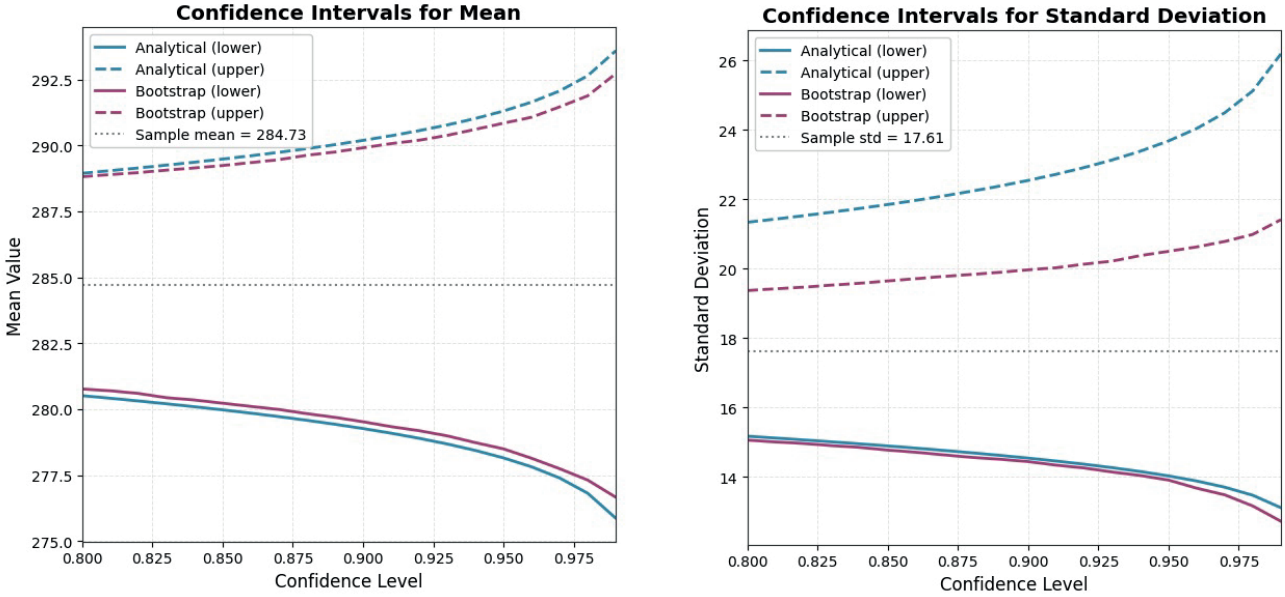


Figure 2. Confidence intervals for mean (a) and standard deviation (b) depending on confidence level

Confidence intervals for the reliability index β at various levels can be calculated based on confidence estimates of statistical parameters and equation (1). The best-case (maximum mean and minimum standard deviation) and worst-case (minimum mean and maximum standard deviation) scenarios are considered (Table 2) [10].

Table 2. Confidence intervals for reliability index β

Confidence level	0.80	0.90	0.95	0.99
Analytical β	[1.202; 2.238]	[1.077; 2.421]	[0.998; 2.590]	[0.780; 2.944]
[min ε, max ε], %	[-26.5, 36.9]	[-32.1, 59.7]	[-36.5, 68.3]	[-44.1, 105.7]
Bootstrap β	[1.330; 2.246]	[1.229; 2.418]	[1.146; 2.577]	[1.012; 2.966]
[min ε, max ε], %	[-26.7, 23.7]	[-31.9, 33.9]	[-36.2, 43.6]	[-44.5, 62.6]

As a rule, the lowest value of β is taken and confidence level 0.95. The difference in this case is about 30-60% between real and estimated value of the reliability index β (in a strict mathematical solution).

Thus, a preliminary analysis shows the importance of choosing a random variable distribution function and assigning its parameters. The following algorithm is proposed to modernize the random variable model in practical problems:

1. Five (k=1, 2, …, 5) cumulative distribution functions (CDFs) of random variables are selected based on scientific and technical analysis of previous experience in statistical data analysis of the random parameter under study;
2. Samples of random variables $x = \{x_1,\ x_2,\ ...,\ x_n\}$ are obtained by measuring/testing. At least $n = 20$ values are recommended;
3. Values of K-S statistics D_n are estimated for every CDFs by eq. (2). Parameters of CDFs are fitted using Distribution fitter in MATLAB or SciPy in Python;
4. Weights of CDFs $w_{KS,k}$ are estimated based on the K-S statistics D_n as $w_{KS,1} = \dfrac{1/D_{n,1}}{1/\sum_{k=1}^{5} D_{n,k}}$, where $\sum_{k=1}^{5} w_{KS,k} = 1$;
5. Weights of CDFs $w_{emp,k}$ are estimated based on empirical data. These weights are assigned by an expert, depending on the scientific and technical analysis, the data of the manufacturing plant, the characteristics of the material, etc. The assignment of weights for design parameters during design is considered as a general decision of the engineering community, approved in the design recommendations. As a result $\sum_{k=1}^{5} w_{emp,k} = 1$;
6. Based on the data from points 3-4, a weight $w_k = \dfrac{w_{KS,k} + w_{emp,.k}}{2}$ is assigned to each probability distribution function;
7. The bootstrap method [11] estimates confidence intervals for the parameters of the selected distribution functions;
8. Confidence intervals for probability distribution functions are constructed using probability boxes [12, 13] approach based on the confidence intervals of CDFs parameters;
9. Then the values of the random variable are sampled as follows:
9.1. A random cumulative distribution function is selected according to its weight according to p. 6 (a uniform distribution is used);
9.2. One value is sampled for the lower confidence bound of this CDF and one value for the upper bound. The reverse transformation method is used for sampling;
9.3. Paragraphs 9.1-9.2 are repeated as many times as samples need to be obtained for reliability analysis, depending on the required accuracy;
10. As a result of the implementation of the algorithm, the results are obtained in the form of the required number of samples N for the lower and upper confidence bounds of the cumulative distribution function of a random variable x.

Using the above algorithm, it is possible to obtain the confidence bounds for cumulative distribution functions for all random variables for which a sample set of data is given (snow load, steel/concrete strength measurements, etc.).

Further reliability analysis can be performed using the Interval Monte Carlo (IMC) method [14, 15]. The limit state function $g(\mathbf{X})$ is formed, where N samples are performed for each random variable in the vector of random variables $\mathbf{X}$ (according to the above algorithm or based on known cumulative distribution functions). In the case of confidence interval estimates, the vector will also be represented in interval form $\underline{\mathbf{X}}$ and $\overline{\mathbf{X}}$. Then the probability of failure is calculated as follows:

$$\underline{P}_f \approx \frac{1}{N}\sum_{j=1}^{N} I\left[g\left(\underline{\mathbf{X}}\right) \le 0\right], \tag{3}$$

$$\overline{P}_f \approx \frac{1}{N}\sum_{j=1}^{N} I\left[g\left(\overline{\mathbf{X}}\right) \le 0\right], \tag{4}$$

where is an indicator function that has a value of 1 if I[.] is equal to "true", and the value is 0 if I[.] is equal to "false".

There are various approaches to assigning the required probability of failure, for example [16, 17, etc.]

RESULTS AND DISCUSSION

For the above data, based on the bootstrap method (1000 samples and a confidence probability of 0.95), the following interval estimates of the parameters of probability distributions were obtained:

- Normal distribution: $\mu_x \in \lfloor 278.39,\ 290.66 \rfloor$ MPa, $\sigma_x \in \lfloor 13.76,\ 20.09 \rfloor$ MPa;
- Lognormal distribution: $s \in \lfloor 0.0488,\ 0.0703 \rfloor$, $\mu_x \in \lfloor 277.98,\ 289.94 \rfloor$ MPa;
- Logistic distribution: $\mu_x \in \lfloor 277.74,\ 291.89 \rfloor$ MPa, $S_x \in \lfloor 7.75,\ 12.21 \rfloor$ MPa;
- GEV distribution: $loc = \mu_x \in \lfloor 273.67,\ 285.95 \rfloor$ MPa, $scale = \sigma_x \in \lfloor 13.88,\ 20.71 \rfloor$ MPa, $c = 0.3789$;
- Gamma distribution: $scale \in \lfloor 1.0380,\ 1.0846 \rfloor$, $a = 268.5$.

Based on the interval estimations of parameters, following probability boxes [12] can be constructed (Fig. 3).

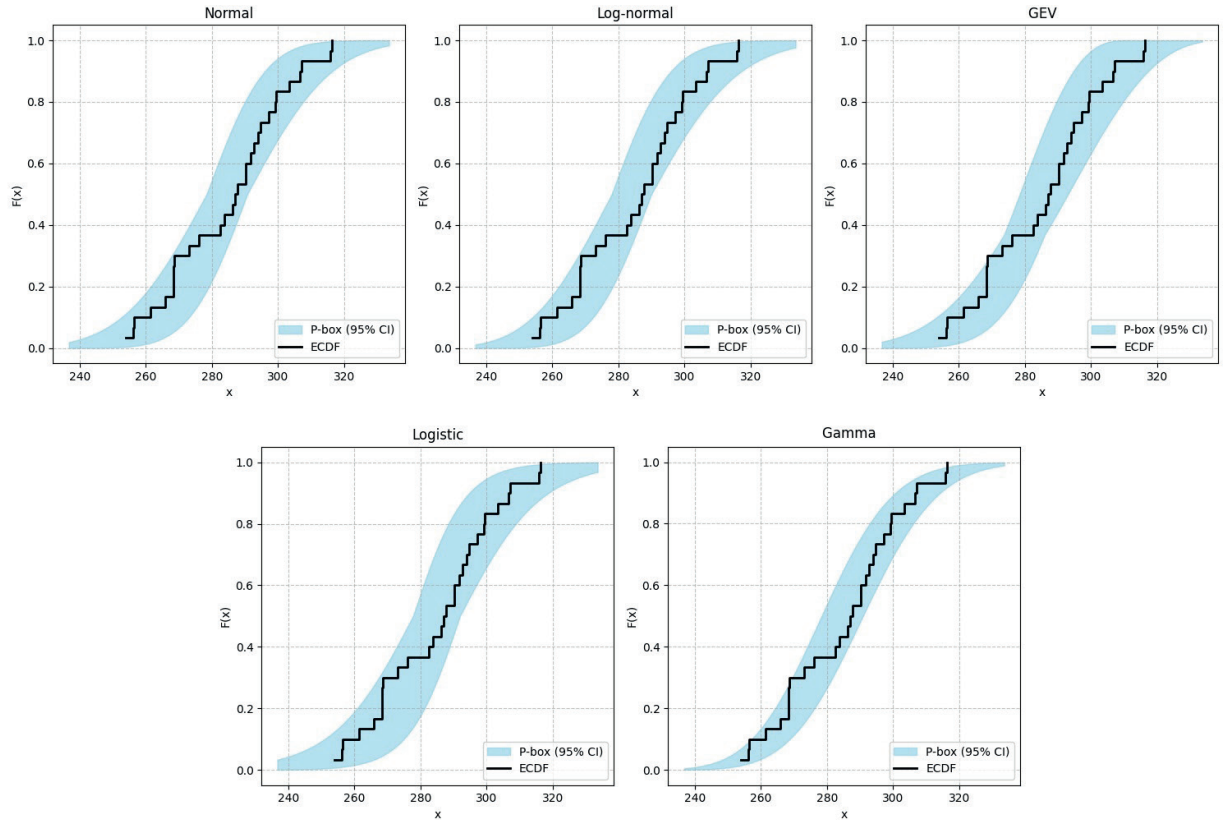


Figure 3. Probability boxes for different types of cumulative distribution functions

Probability box is a confidence interval for the real cumulative distribution function. The left and right boundaries of the functions are accepted as the possible worst and best options for various combinations of interval parameters, and are not always accepted for all the smallest and largest values of the interval.

Let's assume that based on a priori data, as well as Kolmogorov-Smirnov statistics, the following weights were obtained for probability distributions: GEV-distribution $w_{GEV} = 0.30$, lognormal distribution $w_{\ln} = 0.30$, normal distribution $w_{norm} = 0.20$, logistic $w_{\log} = 0.10$, gamma distribution $w_{gamma} = 0.10$.

Further, according to the calculated statistical parameters and weights of the probability

distribution functions, sampling of 1 million values for the lower and upper boundary functions of the probability distribution was performed using the above algorithm. Graphs of these functions, as well as empirical and theoretical ones, are shown in Fig. 4.

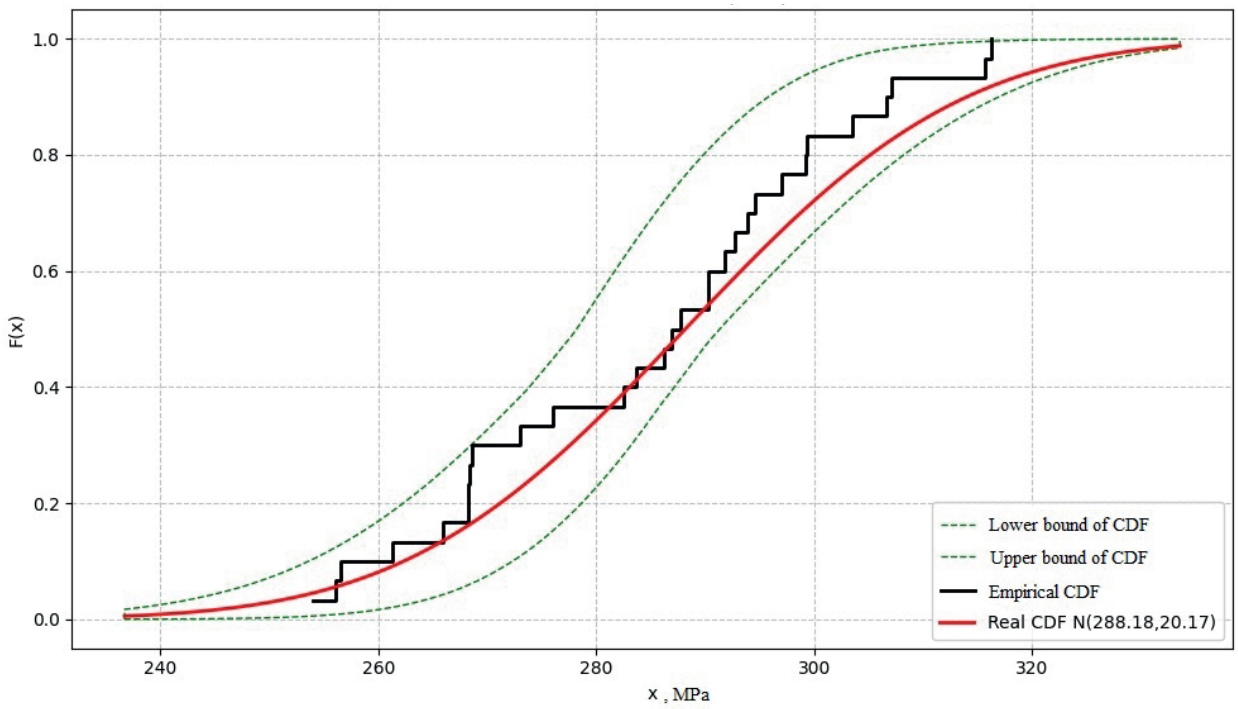


Figure 4. Graphs of confidence bounds for CDF by proposed algorithm, empirical CDF and true CDF

As can be seen from Figure 4, the confidence bounds for the cumulative distribution function according to the proposed algorithm completely cover both the real cumulative distribution function and the empirical one (the sample from which was obtained using the true distribution function).

In cases of complex mathematical models of the limit state, including numerical models, modern approaches can be used to reduce the required number of calculations based on meta-models and surrogate models [18-20].

CONCLUSION

1. Choosing a not optimal cumulative distribution function or its parameters can lead to significant errors (up to 60%) in estimating the reliability index or the probability of failure. This problem is particularly acute in practical tasks, when statistical samples of only a few values are available based on the results of tests/experimental research.

2. The proposed algorithm for modeling random variables for probabilistic reliability analysis of building structures is based on a mixture of probability distribution functions with interval estimation of its parameters by bootstrapping. A numerical example shows the efficiency of using the algorithm – the confidence domain covers both the real distribution function and the empirical one.

3. The estimate of the probability of failure or the reliability index will be presented in an interval form. For a narrower interval response, it is necessary to increase the quantity/quality of available statistical information. If it is impossible to obtain the necessary information, reliability can be improved using classical methods – increasing cross-sections, increasing strength, reducing loads, etc.

ACKNOWLEDGEMENTS

The research was funded by the Russian Science Foundation (RSF), Project No. 25-79-00112, https://rscf.ru/project/25-79-00112/.

REFERENCES

1. **Saleh J. H., Marais K.** Highlights from the early (and pre-) history of reliability engineering // Reliability engineering & System safety. 2006. vol. 91. no. 2. pp. 249-256.
2. **Ni P., Yuan Z., Han Q., Du X., Fu J.** Reliability assessment of civil structures with incomplete probability distribution information // Probabilistic Engineering Mechanics. 2023. vol. 74. 103541.
3. **Faes M. G., Daub M., Marelli S., Patelli E., Beer M.** Engineering analysis with probability boxes: A review on computational methods // Structural Safety. 2021. vol. 93. 102092.
4. **Nadol′skij V. V., Martynov Yu. S.** Veroyatnostnoe modelirovanie soprotivleniya stal′nykh elementov [Probabilistic modeling of resistance of steel elements]. Vestnik Polotskogo gosudarstvennogo universiteta. Seriya F. Stroitel′stvo. Prikladnye nauki. 2015. no. 8. pp. 44-49
5. **Stephani A., Van Coile R., Khorasani N. E., Gernay T., Hopkin D.** Probabilistic model for steel yield strength retention factor at elevated temperatures. In Proc., 16th Int. Probabilistic Workshop. Berlin: Ernst & Sohn, 2018. pp. 1-6.
6. **Wang Y., Zhou X., Wang H., Kong D., Xu S.** Stochastic constitutive model of structural steel based on random field of corrosion depth. Case Studies in Construction Materials. 2022. vol. 16. e00972.
7. **Melcher J., Kala Z., Holický M., Fajkus M., Rozlívka L.** Design characteristics of structural steels based on statistical analysis of metallurgical products. Journal of Constructional Steel Research. 2004. vol. 60(3-5). pp. 795-808.
8. **Konečný P.** Correlation of Steel Yield Stress and Ultimate Strength-Monte Carlo Simulation via Non-Gaussian Random Variables // Materials Science Forum. Trans Tech Publications Ltd, 2017. vol. 893. pp. 223-228.
9. **Solovyev SA, Kopeykin O.E., Solovyeva A.A.** Veroyatnostnyj metod proektirovaniya stal'nyh ferm na zadannyj uroven' nadezhnosti i dolgovechnosti **[**Probabilistic method of designing steel trusses for a given level of reliability and durability] // Vestnik MGSU [Monthly Journal on Construction and Architecture]. 2025. vol. 20. no. 5. pp. 655-666.
10. **Qiu Z., Yang D., Elishakoff I.** Combination of structural reliability and interval analysis // Acta Mechanica Sinica. 2008. vol. 24. no. 1. pp. 61-67.
11. **Marks C. E., Glen A. G., Robinson M. W., Leemis L. M.** Applying bootstrap methods to system reliability. The American Statistician. 2014. vol. 68. no. 3. pp. 174-182.
12. **Soloveva A. A., Solovev S. A.** Reliability analysis of RHS steel trusses joints based on the p-boxes approach // International Journal for Computational Civil and Structural Engineering. 2021. vol. 17. no. 1. pp. 87-97.
13. **Xie H., Li J., Liao D.** A new structural reliability analysis method under non-parameterized probability box variables // Structural and Multidisciplinary Optimization. 2022. vol. 65. no. 11. p. 322.
14. **Zhang H., Mullen R. L., Muhanna R. L.** Interval Monte Carlo methods for structural reliability // Structural Safety. 2010. vol. 32. no. 3. pp. 183-190.
15. **Zhang H., Dai H., Beer M., Wang W.** Structural reliability analysis on the basis of small samples: an interval quasi-Monte Carlo method // Mechanical Systems and

Signal Processing, 2013. vol.37. no.1-2. pp. 137-151.
16. **Fischer K., Viljoen C., Köhler J., Faber, M.H.** Optimal and acceptable reliabilities for structural design // Structural Safety. 2019. vol. 76. pp. 149-161.
17. **Diamantidis D., Holický M., Sýkora M.** Target reliability levels based on societal, economic and environmental consequences of structural failure // 12th International Conference on Structural Safety and Reliability (ICOSSAR). 2017. pp. 644-653.
18. **Schöbi R., Sudret B.** Structural reliability analysis for p-boxes using multi-level meta-models // Probabilistic Engineering Mechanics. 2017. vol. 48. pp. 27-38.
19. **Su G., Peng L., Hu L.** A Gaussian process-based dynamic surrogate model for complex engineering structural reliability analysis // Structural Safety. 2017. vol. 68. pp. 97-109.
20. **Gaspar B., Teixeira A. P., Soares C. G.** Assessment of the efficiency of Kriging surrogate models for structural reliability analysis // Probabilistic engineering mechanics. 2014. vol. 37. pp. 24-34.

СПИСОК ЛИТЕРАТУРЫ

1. **Saleh J. H., Marais K.** Highlights from the early (and pre-) history of reliability engineering // Reliability engineering & System safety. 2006. vol. 91. no. 2. pp. 249-256.
2. **Ni P., Yuan Z., Han Q., Du X., Fu J.** Reliability assessment of civil structures with incomplete probability distribution information // Probabilistic Engineering Mechanics. 2023. vol. 74. 103541.
3. **Faes M. G., Daub M., Marelli S., Patelli E., Beer M.** Engineering analysis with probability boxes: A review on computational methods // Structural Safety. 2021. vol. 93. 102092.
4. **Надольский В. В., Мартынов Ю. С.** Вероятностное моделирование сопротивления стальных элементов // Вестник Полоцкого государственного университета. Серия F. Строительство. Прикладные науки. 2015. №8. С. 44-49.
5. **Stephani A., Van Coile R., Khorasani N. E., Gernay T., Hopkin D.** Probabilistic model for steel yield strength retention factor at elevated temperatures. In Proc., 16th Int. Probabilistic Workshop. Berlin: Ernst & Sohn, 2018. pp. 1-6.
6. **Wang Y., Zhou X., Wang H., Kong D., Xu S.** Stochastic constitutive model of structural steel based on random field of corrosion depth. Case Studies in Construction Materials. 2022. vol. 16. e00972.
7. **Melcher J., Kala Z., Holický M., Fajkus M., Rozlívka L.** Design characteristics of structural steels based on statistical analysis of metallurgical products. Journal of Constructional Steel Research. 2004. vol. 60(3-5). pp. 795-808.
8. **Konečný P.** Correlation of Steel Yield Stress and Ultimate Strength-Monte Carlo Simulation via Non-Gaussian Random Variables // Materials Science Forum. Trans Tech Publications Ltd, 2017. vol. 893. pp. 223-228.
9. **Соловьев С. А., Копейкин О. Е., Соловьева А. А.** Вероятностный метод проектирования стальных ферм на заданный уровень надежности и долговечности // Вестник МГСУ. 2025. Т. 20. №. 5. С. 655-666.
10. **Qiu Z., Yang D., Elishakoff I.** Combination of structural reliability and interval analysis // Acta Mechanica Sinica. 2008. vol. 24. no. 1. pp. 61-67.
11. **Marks C. E., Glen A. G., Robinson M. W., Leemis L. M.** Applying bootstrap methods to system reliability. The American Statistician. 2014. vol. 68. no. 3. pp. 174-182.
12. **Soloveva A. A., Solovev S. A.** Reliability analysis of RHS steel trusses joints based on the p-boxes approach // International Journal for Computational Civil and

Structural Engineering. 2021. vol. 17. no. 1. pp. 87-97.
13. **Xie H., Li J., Liao D.** A new structural reliability analysis method under non-parameterized probability box variables // Structural and Multidisciplinary Optimization. 2022. vol. 65. no. 11. p. 322.
14. **Zhang H., Mullen R. L., Muhanna R. L.** Interval Monte Carlo methods for structural reliability // Structural Safety. 2010. vol. 32. no. 3. pp. 183-190.
15. **Zhang H., Dai H., Beer M., Wang W.** Structural reliability analysis on the basis of small samples: an interval quasi-Monte Carlo method // Mechanical Systems and Signal Processing, 2013. vol.37. no.1-2. pp. 137-151.
16. **Fischer K., Viljoen C., Köhler J., Faber, M.H.** Optimal and acceptable reliabilities for structural design // Structural Safety. 2019. vol. 76. pp. 149-161.
17. **Diamantidis D., Holický M., Sýkora M.** Target reliability levels based on societal, economic and environmental consequences of structural failure // 12th International Conference on Structural Safety and Reliability (ICOSSAR). 2017. pp. 644-653.
18. **Schöbi R., Sudret B.** Structural reliability analysis for p-boxes using multi-level meta-models // Probabilistic Engineering Mechanics. 2017. vol. 48. pp. 27-38.
19. **Su G., Peng L., Hu L.** A Gaussian process-based dynamic surrogate model for complex engineering structural reliability analysis // Structural Safety. 2017. vol. 68. pp. 97-109.
20. **Gaspar B., Teixeira A. P., Soares C. G.** Assessment of the efficiency of Kriging surrogate models for structural reliability analysis // Probabilistic engineering mechanics. 2014. vol. 37. pp. 24-34.

Sergey Alexandrovich Solovev — candidate of technical sciences, docent, head of the industrial and civil engineering department of Vologda State University (VSU), 15 Lenina street, Vologda, 160000, Russian Federation, solovevsa@vogu35.ru, 88172518396

Anastasia Andreevna Soloveva — candidate of technical sciences, lecturer of the industrial and civil engineering department of Vologda State University (VSU), 15 Lenina street, Vologda, 160000, Russian Federation, solovevaaa@vogu35.ru, 88172518396

Соловьев Сергей Александрович — кандидат технических наук, доцент, заведующий кафедрой промышленного и гражданского строительства ФГБОУ ВО «Вологодский государственный университет» (ВоГУ), д. 15, ул. Ленина, г. Вологда, 160000, Россия, solovevsa@vogu35.ru, 88172518396

Соловьева Анастасия Андреевна — кандидат технических наук, старший преподаватель кафедры промышленного и гражданского строительства ФГБОУ ВО «Вологодский государственный университет» (ВоГУ), д. 15, ул. Ленина, г. Вологда, 160000, Россия, solovevaaa@vogu35.ru, 88172518396